National Library
of Canada

Bibliothèque nationale
du Canada

Canadian Theses Service

Service des thèses canadiennes

Ottawa, Canada
K1A 0N4

NOTICE

The quality of this microform is heavily dependent upon the quality of the original thesis submitted for microfilming. Every effort has been made to ensure the highest quality of reproduction possible.

If pages are missing, contact the university which granted the degree.

Some pages may have indistinct print especially if the original pages were typed with a poor typewriter ribbon or if the university sent us an inferior photocopy.

Reproduction in full or in part of this microform is governed by the Canadian Copyright Act, R.S.C. 1970, c. C-30, and subsequent amendments.

AVIS

La qualité de cette microforme dépend grandement de la qualité de la thèse soumise au microfilmage. Nous avons tout fait pour assurer une qualité supérieure de reproduction.

S'il manque des pages, veuillez communiquer avec l'université qui a conféré le grade.

La qualité d'impression de certaines pages peut laisser à désirer, surtout si les pages originales ont été dactylographiées à l'aide d'un ruban usé ou si l'université nous a fait parvenir une photocopie de qualité inférieure.

La reproduction, même partielle, de cette microforme est soumise à la Loi canadienne sur le droit d'auteur, SRC 1970, c. C-30, et ses amendements subséquents.

NL-339 (r. 88/04) c

Canada

UNIVERSITY OF ALBERTA

RADIO FREQUENCY HEATING OF POROUS, MOISTURE BEARING MATERIALS IN A COAXIAL GUIDING STRUCTURE

BY

MIKE NACHAI ©

A THESIS

SUBMITTED TO THE FACULTY OF GRADUATE STUDIES AND RESEARCH IN
PARTIAL FULFILLMENT OF THE REQUIREMENTS FOR THE DEGREE OF
MASTER OF SCIENCE

DEPARTMENT OF ELECTRICAL ENGINEERING

EDMONTON, ALBERTA
FALL 1991

National Library of Canada
Bibliothèque nationale du Canada

Canadian Theses Service
Service des thèses canadiennes

Ottawa, Canada
K1A 0N4

The author has granted an irrevocable non-exclusive licence allowing the National Library of Canada to reproduce, loan, distribute or sell copies of his/her thesis by any means and in any form or format, making this thesis available to interested persons.

The author retains ownership of the copyright in his/her thesis. Neither the thesis nor substantial extracts from it may be printed or otherwise reproduced without his/her permission.

L'auteur a accordé une licence irrévocable et non exclusive permettant à la Bibliothèque nationale du Canada de reproduire, prêter, distribuer ou vendre des copies de sa thèse de quelque manière et sous quelque forme que ce soit pour mettre des exemplaires de cette thèse à la disposition des personnes intéressées.

L'auteur conserve la propriété du droit d'auteur qui protège sa thèse. Ni la thèse ni des extraits substantiels de celle-ci ne doivent être imprimés ou autrement reproduits sans son autorisation.

ISBN 0-315-70165-X

Canada

UNIVERSITY OF ALBERTA

RELEASE FORM

NAME OF AUTHOR:	MIKE NACHAI
TITLE OF THESIS:	RADIO FREQUENCY HEATING OF POROUS LOSSY MATERIALS IN A COAXIAL GUIDING STRUCTURE
DEGREE:	MASTER OF SCIENCE
YEAR THIS DEGREE GRANTED:	FALL, 1991

PERMISSION IS HEREBY GRANTED TO THE UNIVERSITY OF ALBERTA LIBRARY TO REPRODUCE SINGLE COPIES OF THIS THESIS AND TO LEND OR SELL SUCH COPIES FOR PRIVATE, SCHOLARLY OR SCIENTIFIC RESEARCH PURPOSES ONLY.

THE AUTHOR RESERVES OTHER PUBLICATION RIGHTS, AND NEITHER THE THESIS NOR EXTENSIVE EXTRACTS FROM IT MAY BE PRINTED OR OTHERWISE REPRODUCED WITHOUT THE AUTHOR'S WRITTEN PERMISSION.

Mike Nachai
(Student's Signature)

3511 Ellerslie Road, 9th Avenue S.W.
Edmonton, Alberta, Canada
T6H 4N6
(Student's Permanent Address)

DATED: AUGUST 16, 1991

UNIVERSITY OF ALBERTA

FACULTY OF GRADUATE STUDIES AND RESEARCH

THE UNDERSIGNED CERTIFY THAT THEY HAVE READ, AND RECOMMEND TO THE FACULTY OF GRADUATE STUDIES AND RESEARCH FOR ACCEPTANCE, A THESIS ENTITLED "RADIO FREQUENCY HEATING OF POROUS MOISTURE BEARING MATERIALS IN A COAXIAL GUIDING STRUCTURE" SUBMITTED BY MIKE NACHAI IN PARTIAL FULFILLMENT OF THE REQUIREMENTS FOR THE DEGREE OF MASTER OF SCIENCE.

S Chute
Dr. F. S. Chute (Supervisor)

F.E. Vermeulen
Dr. F. E. Vermeulen (Supervisor)

Ronald P W Lawson
Dr. R. P. W. Lawson

John Stephenson
Dr. J. S. Stephenson

J F Vaneldik
Dr. J. F. Vaneldik

DATED: August 16, 1991

Abstract

The mathematical modelling of the guided wave radio frequency heating of oil sand, or other similar lossy media, is studied. A coaxial waveguide two dimensional simulation routine is developed for this purpose, both with and without the assumption that only transverse electromagnetic (TEM) fields exist inside the coaxial waveguide. The assumption of TEM fields facilitates simplified numerical simulation. It is also assumed, for the purposes of simplified numerical simulation, that the flow of fluids within the lossy medium does not significantly affect the electromagnetic heating scenario, and is therefore neglected. An investigation into the validity of these physical assumptions is carried out. The computer simulation routine is used in conjunction with scaled laboratory experiments in order to investigate and optimize the guided wave radio frequency heating process.

Acknowledgement

I wish to express my appreciation to the following individuals:

My supervisors, Dr. F.S. Chute and Dr. F.E. Vermeulen for their assistance throughout my graduate program, and for always giving me enough rope.

Jim Fearn, for superb technical expertise during my experimental work.

Dr. S.M. Farouq Ali for his advice on linear systems inversion techniques.

Dr. W.R. Tinga for instrumentation assistance.

Dr. C.P. Stroemich, for data acquisition assistance.

David Ellinger, for electric field measurement help, and for the RF power amplifier.

Richard Maslowski and David Goulbourne for the career guidance.

The execution of this study was made possible by funding provided by the Alberta Oil Sands Technology and Research Authority.

This thesis was produced by electronic means. The digital medium was not compromised during the writing, illustrating, editing, or printing phases. Special acknowledgement is given to Dr. Edmund Sumbar for his assistance in this area.

Table of Contents

Page

Chapter 1. Introduction 1

  1.1 The Electrical In Situ Heating Process 1

  1.2 Investigational Method 6

Chapter 2. Formulation of the Mathematical Model for TEM COPTER 10

  2.1 The Electrical Problem 10
    2.1.1 The TEM Approximation 10
    2.1.2 The TEM Electrical Model 13

  2.2 The Thermal Problem 15

Chapter 3. Numerical Solution of the Mathematical Model for TEM COPTER 24

  3.1 The Grid Structure 24

  3.2 The Electrical Equivalent Circuit 25

  3.3 Conservation of Energy and Solution of the Thermal Problem 34

  3.4 The Computational Algorithm 43

Chapter 4. Testing and Verification of COPTER 45

  4.1 Verification of the Intrinsic Operation of COPTER 45

  4.2 Verification of the "Steam Disappears" Fluid Flow Approximation. 46

  4.3 Comparison of TM COPTER and TEM COPTER 64
    4.3.1 TM COPTER 64
    4.3.2 Numerical Comparison 70

  4.4 Comparison With Physical Models 83

Chapter 5. Summary of Results Using the Guided Wave Heating Process 91

  5.1 The Self Coating Action 91

  5.2 Uniform Heating in Low Loss Cases 98

  5.3 The Use of Axial Electric Fields for the Promotion of Uniform Heating 98

  5.4 "Total Evaporation Boring" 102

Chapter 6. Conclusions 116

References 119

Appendix A. Selected Results from the TEM Experiment.................................. 121

Appendix B. Electrical and Thermal Properties of the Model Medium............ 131

Appendix C. TEM COPTER Program Listing... 133

Appendix D. Sample Output From TEM COPTER.. 145

List of Tables

Page

Table 4.1 Single axial cell COPTER experiment medium parameters at 14 MHz.......... 46

Table 4.2 Simulated medium parameters for TEM assumption examination simulations.......... 71

Table 4.3 Full RF heating experiment medium parameters.......... 84

List of Figures

Page

Figure 1. Typical radio frequency guided wave in-situ heating arrangement. 3

Figure 2.1 TEM experiment apparatus interconnection.................................. 12

Figure 2.2 Coaxial geometry.. 13

Figure 2.3 Section j of transmission line equivalent circuit model................. 15

Figure 2.4a Representative conductivity versus temperature plot.................... 18

Figure 2.4b Representative conductivity versus time plot............................... 18

Figure 2.5 Hoop structure.. 20

Figure 2.6 Thermal equivalent circuit network.. 22

Figure 3.1 Simulation grid... 24

Figure 3.2 Single cell "hoop".. 25

Figure 3.3 Simulation grid seen as a surface of revolution............................ 25

Figure 3.4 Jth section of equivalent circuit discretization of transmission line 26

Figure 3.5 Practical transverse impedance electrical representation............... 27

Figure 3.6 Series RC equivalent circuit scheme for cell (i,j)........................... 30

Figure 3.7a Transverse impedance prediction of single RC circuits.................. 33

Figure 3.7b Transverse impedance prediction of double RC circuits................. 33

Figure 3.8 Thermal equivalent circuit array for cell....................................... 35

Figure 3.9 Temperature matrix... 37

Figure 3.10 Flow diagram of the computational algorithm.............................. 44

Figure 4.1 Single axial cell COPTER experiment apparatus interconnection. 47

Figure 4.2a Net input power for simulations.. 51

Figure 4.2b Brine sand "A" real component of input impedance....................... 52

Figure 4.2c Brine sand "B" real component of input impedance....................... 52

Figure 4.2d Brine sand "A" imaginary component of input impedance.............. 53

Figure 4.2e Brine sand "B" imaginary component of input impedance.............. 53

Figure 4.2f Brine sand "A" temperature at inner conductor (r = 0.05 m).......... 54

Figure 4.2g Brine sand "B" temperature at inner conductor (r = 0.05 m).......... 54

Figure 4.2h Brine sand "A" temperature at midpoint between conductors (r = 0.1 m).. 55

Figure 4.2i Brine sand "B" temperature at midpoint between conductors (r = 0.1 m).. 55

Figure 4.2j Brine sand "A" temperature at outer conductor (r = 0.15 m).......... 56

Figure 4.2k Brine sand "B" temperature at outer conductor (r = 0.15 m).......... 56

Figure 4.2l Brine sand "A" simulated heat loss to inner conductor.................. 57

Figure 4.2m Brine sand "B" simulated heat loss to inner conductor.................. 57

Figure 4.2n Brine sand "A" temperature at inner conductor (r = 0.05 m) with simulated heat loss to inner conductor.. 58

Figure 4.2o Brine sand "B" temperature at inner conductor (r = 0.05 m) with simulated heat loss to inner conductor.. 58

Figure 4.2p Brine sand "A" temperature between conductors (r = 0.1 m) with simulated heat loss to inner conductor.. 59

Figure 4.2q Brine sand "B" temperature between conductors (r = 0.1 m) with simulated heat loss to inner conductor.. 59

Figure 4.3 Input impedances of power down test.. 63

Figure 4.4 Electromagnetic fields in simulation cell...................................... 65

Figure 4.5 Simulation cell as viewed from termination end.......................... 66

Figure 4.6 Simulation cell in three dimensions as viewed from termination end.. 68

Figure 4.7a TEM COPTER simulation mass percent water content vs. position. Initial conductivity = 0.00205 S/m. Time = 15000 sec.. 72

Figure 4.7b TM COPTER simulation mass percent water content vs. position. Initial conductivity = 0.00205 S/m. Time = 15000 sec................. 73

Figure 4.7c TEM COPTER simulation mass percent water content vs. position. Initial conductivity = 0.0205 S/m. Time = 15000 sec..... 74

Figure 4.7d TM COPTER simulation mass percent water content vs. position. Initial conductivity = 0.0205 S/m. Time = 15000 sec................. 75

Figure 4.7e TEM COPTER simulation mass percent water content vs. position. Initial conductivity = 0.052 S/m. Time = 15000 sec....... 76

Figure 4.7f TM COPTER simulation mass percent water content vs. position. Initial conductivity = 0.052 S/m. Time = 15000 sec..................... 77

Figure 4.7g TEM COPTER simulation mass percent water content vs. position. Initial conductivity = 0.069 S/m. Time = 15000 sec....... 78

Figure 4.7h TM COPTER simulation mass percent water content vs. position. Initial conductivity = 0.069 S/m. Time = 15000 sec..................... 79

Figure 4.7i TEM COPTER simulation mass percent water content vs. position. Initial conductivity = 0.205 S/m. Time = 15000 sec....... 80

Figure 4.7j TM COPTER simulation mass percent water content vs. position. Initial conductivity = 0.205 S/m. Time = 15000 sec..................... 81

Figure 4.8 Full RF heating experiment apparatus interconnection................. 85

Figure 4.9a TM COPTER simulation temperature (°C) vs. position. Initial water saturation level = 20 %. Time = 25000 sec.......................... 87

Figure 4.9b TM COPTER simulation temperature (°C) vs. position. Initial water saturation level = 10 %. Time = 22000 sec.......................... 88

Figure 4.10 TM COPTER simulation mass percent water content vs. position. Initial water saturation level = 20 %. Time = 25000 sec............... 89

Figure 5.1a TM COPTER simulation mass percent water content vs. position. Initial conductivity = 0.205 S/m. Time = 0 sec. Frequency = 100 MHz.. 92

Figure 5.1b TM COPTER simulation mass percent water content vs. position. Initial conductivity = 0.205 S/m. Time = 402 sec. Frequency = 100 MHz.. 93

Figure 5.1c TM COPTER simulation mass percent water content vs. position. Initial conductivity = 0.205 S/m. Time = 1171 sec. Frequency = 100 MHz.. 94

Figure 5.1d TM COPTER simulation mass percent water content vs. position. Initial conductivity = 0.205 S/m. Time = 2445 sec. Frequency = 100 MHz.. 95

Figure 5.2a Representative attenuation factor versus coating radius plot......... 97

Figure 5.2b Representative wavelength versus coating radius plot.................. 97

Figure 5.3a TEM COPTER simulation mass percent water content vs. position. Initial conductivity = 0.00205 S/m. Time = 15000 sec. Termination = open circuit... 99

Figure 5.3b TEM COPTER simulation mass percent water content vs. position. Initial conductivity = 0.00205 S/m. Time = 15000 sec. Termination = short circuit... 100

Figure 5.3c TEM COPTER simulation mass percent water content vs. position. Initial conductivity = 0.00205 S/m. Time = 15000 sec. Termination = alternate open / short circuit.................................. 101

Figure 5.4a TM COPTER simulation mass percent water content vs. position. Initial conductivity = 0.205 S/m. Time = 0 sec. Frequency = 100 Mhz 104

Figure 5.4b TM COPTER simulation mass percent water content vs. position. Initial conductivity = 0.205 S/m. Time = 107 sec. Frequency = 100 Mhz 105

Figure 5.4c TM COPTER simulation mass percent water content vs. position. Initial conductivity = 0.205 S/m. Time = 888 sec. Frequency = 100 Mhz 106

Figure 5.4d TM COPTER simulation mass percent water content vs. position. Initial conductivity = 0.205 S/m. Time = 3040 sec. Frequency = 100 Mhz 107

Figure 5.4e TM COPTER simulation mass percent water content vs. position. Initial conductivity = 0.205 S/m. Time = 4843 sec. Frequency = 100 Mhz 108

Figure 5.4f TM COPTER simulation mass percent water content vs. position. Initial conductivity = 0.205 S/m. Time = 8788 sec. Frequency = 100 Mhz 109

Figure 5.5a TM COPTER simulation mass percent water content vs. position. Initial conductivity = 0.205 S/m. Time = 0 sec 111

Figure 5.5b TM COPTER simulation mass percent water content vs. position. Initial conductivity = 0.205 S/m. Time = 471 sec 112

Figure 5.5c TM COPTER simulation mass percent water content vs. position. Initial conductivity = 0.205 S/m. Time = 9711 sec 113

Figure 5.5d TM COPTER simulation mass percent water content vs. position. Initial conductivity = 0.205 S/m. Time = 14706 sec 114

Figure 5.5e TM COPTER simulation mass percent water content vs. position. Initial conductivity = 0.205 S/m. Time = 19706 sec 115

Figure A.1a Relative field magnitudes [1E-3 S/m|50 MHz|9.563 mm] 122

Figure A.1b Relative field magnitudes [1E-3 S/m|50 MHz|9.931 mm] 123

Figure A.1c Relative field magnitudes [1E-3 S/m|50 MHz|12.700 mm] 124

Figure A.2a Relative field magnitudes [1.29 S/m|20 MHz|9.563 mm] 125

Figure A.2b Relative field magnitudes [1.29 S/m|50 MHz|9.931 mm] 126

Figure A.2c Relative field magnitudes [1.29 S/m|80 MHz|9.931 mm] 127

Figure A.3a Relative field magnitudes [1E-3 S/m|2 MHz|9.931 mm] 128

Figure A.3b Relative field magnitudes [0.66 S/m|2 MHz|9.931 mm] 129

Figure A.3c Relative field magnitudes [1.29 S/m|2 MHz|9.931 mm]........................ 130

List of Plates

		Page
Plate 2	TEM Experiment apparatus	11
Plate 4.1	Single axial cell COPTER experiment	46
Plate 4.2	Full RF heating experiment apparatus	84
Plate 4.3	Inner conductor encrusted sand formation	90

Nomenclature (rms quantities)

D	electric flux density vector (coulombs / square meter)
B	magnetic flux density vector (tesla)
E	electric field intensity vector (volts / meter)
H	magnetic field intensity vector (amperes / meter)
ρ	charge density (coulombs / cubic meter)
σ	conductivity (siemens / meter)
ε	permittivity (farads / meter)
μ	permeability (henries / meter)
ω	angular frequency (radians / second)
E_r	radial electric field intensity phasor (volts / meter)
E_z	axial electric field intensity phasor (volts / meter)
H_ϕ	azimuthal magnetic field intensity phasor (amperes / meter)
V	phasor voltage (volts)
I	phasor current (amperes)
L	inductance per unit length (henries / meter)
C	capacitance per unit length (farads / meter)
G	conductance per unit length (siemens / meter)
R	resistance per unit length (ohms / meter)
RS	real component of cell transverse impedance (ohms)
Z	impedance per unit length (ohms / meter)
Q_{inst}	volumetric instantaneous heating rate (watts / cubic meter)
Q	time averaged volumetric heating rate (watts / cubic meter)
S	steam energy (joules)
P	power (watts)
M_{VOL}	volumetric heat capacity (joules / cubic meter degree celsius)
C_v	heat of vaporization (joules / gram)

v	volume (cubic meters)
k	thermal conductivity (watts / meter degree celsius)
t	time (sec)
T	temperature (degrees celsius)
T_{steam}	boiling temperature (degrees celsius)
H	heat flow (watts)
A	surface area (square meters)
G_R	radial thermal conductance (watts per degree celsius)
G_Z	axial thermal conductance (watts per degree celsius)
S_W	moisture saturation (fractional)
W	mass percent moisture content
m_w	mass of moisture in grid (grams)
m_s	mass of sand in grid (grams)
α	temperature dependence factor (1 / degrees celsius)
K_{1A}	measured moisture dependence factor
K_{1B}	measured moisture dependence factor (1 / percent)
K_{1C}	measured moisture dependence factor (1 / percent squared)
K_A	measured moisture dependence factor
K_B	measured moisture dependence factor (1 / percent)
K_C	measured moisture dependence factor (1 / percent squared)
ϕ	porosity (fractional)

1. Introduction

1.1 The Electrical In Situ Heating Process

Alberta's in-place crude bitumen reserves are estimated to contain 1000 million barrels of oil, or nearly half as much as the world's total conventional supply of oil discovered to date. Because of its intrinsically high viscosity, however, bitumen cannot be simply drawn to the surface and refined for use like a conventional light or medium gravity oil. In fact, at in-situ temperatures, bitumen is essentially immobile.

Because the majority of bitumen rich oil sand lies from between 75 m to 750 m beneath the surface of the earth, surface mining is impractical as well as environmentally destructive. Instead, many forms of in-situ processing have been developed which reduce the viscosity of the bitumen within the underground payzone such that recovery may take place. Underground fluid injection, combustion, and hot gas addition are all means by which heat is transferred to the oil sand, thereby enhancing its fluidity. Flowing oil is then pushed to the surface by a suitable driving agent. Due to low thermal conductivity and fluid permeability of the underground formations, however, heat transfer using these techniques is very inefficient and difficult to control. Typically, large amounts of energy are wasted for each barrel of oil that is produced.

The idea of using electromagnetic radiation to heat the in-situ oil has gained considerable attention in recent years[1]. Because electrical currents heat the formation from within, electromagnetic heating completely bypasses many of the traditional reservoir energy deposition problems. Poor thermal conductivity and low fluid permeability are not electrical properties and do not impede the propagation of electromagnetic waves into an oil sand payzone.

Frequencies which have been considered in electrically assisted recovery operations range from near DC (60 Hz power, for example) to much higher radio frequencies. Low frequency heating has obvious advantages in low initial capital costs and ease of implementation over its RF counterpart. Indeed, working full scale 60 Hz bitumen recovery systems have been successfully built and tested[2]. In certain instances, however, such schemes are rendered ineffective by the nature of the medium to be heated. The low frequency conduction currents that heat the formation cannot penetrate into the formation without the presence of moisture to establish ionic conductivity between electrode pairs. Obviously, the low frequency technique may not be employed in oil sand regions with particularly low moisture contents, such as the Utah deposits. Even in moist, highly conductive media there are problems with low frequency heating operations because of high electrode temperatures resulting from localized heating at the electrodes. Oil sand material immediately surrounding these electrodes will lose water content due to subsequent water evaporation. As a result, low frequency electromagnetic signals are effectively decoupled from the remaining payzone, thus terminating the heating process. Various electrode configurations have been designed to prevent this loss of coupling by restricting the evaporation[3]. At the expense of greatly increased cost and complexity, a 60 Hz electrode can be physically enlarged by underreaming the well bore region which is occupied by the electrode, and then filling the underreamed region with a highly conductive material such as metal shot and brine. Even with the lower electrode surface current densities which are afforded by such a design, electrode temperatures can become extremely high, and means must be provided for circulating cooling fluid around the well bore. Some elaborate 60 Hz schemes have been proposed which employ large numbers of electrode arrays buried in the oil sand payzones[4]. Alternate rows of these electrode arrays are excited at various duty cycles in order to avoid electrode overheating by way of thermal heat conduction during the "off" portions of the duty cycles.

Alternately, radio frequency heating could be used without such expensive electrode configurations. High electrode temperatures and subsequent moisture evaporation eventually occur regardless of applied frequency, but RF fields generate displacement currents as well as conduction currents. Because these displacement currents can flow regardless of moisture conditions, the electromagnetic wave is capable of propagating beyond the dried barrier and into the remaining payzone. Essentially, the moisture deficient region resembles a large cylindrical capacitor. At radio frequencies, this capacitor presents less of an impedance to the electromagnetic currents than it does at low frequencies, thus allowing the signals to penetrate beyond the dried barrier.

Radio frequency heating of lossy media has been attempted by merely lowering individual antennas into the lossy formation[5,6]. In highly conductive media, the application of power becomes quite difficult using this technique, since the applied electromagnetic wave tends to reflect away from the application point in the lossy medium, back towards the antenna. Moreover, it is not readily possible to penetrate the formation to any significant depth with individual antenna power applications, resulting in localized, non uniform heating only. In consideration of energy efficiency of the heating process, it can be mathematically shown[7] that heat deposition inhomogeneities generally result in less than optimal energy deposition.

Improved radio frequency heating performance can be achieved by utilizing configurations that guide electromagnetic energy into the formation[8-10]. A possible electrode arrangement consists of an array of horizontal wells penetrating the formation as suggested in figure 1.

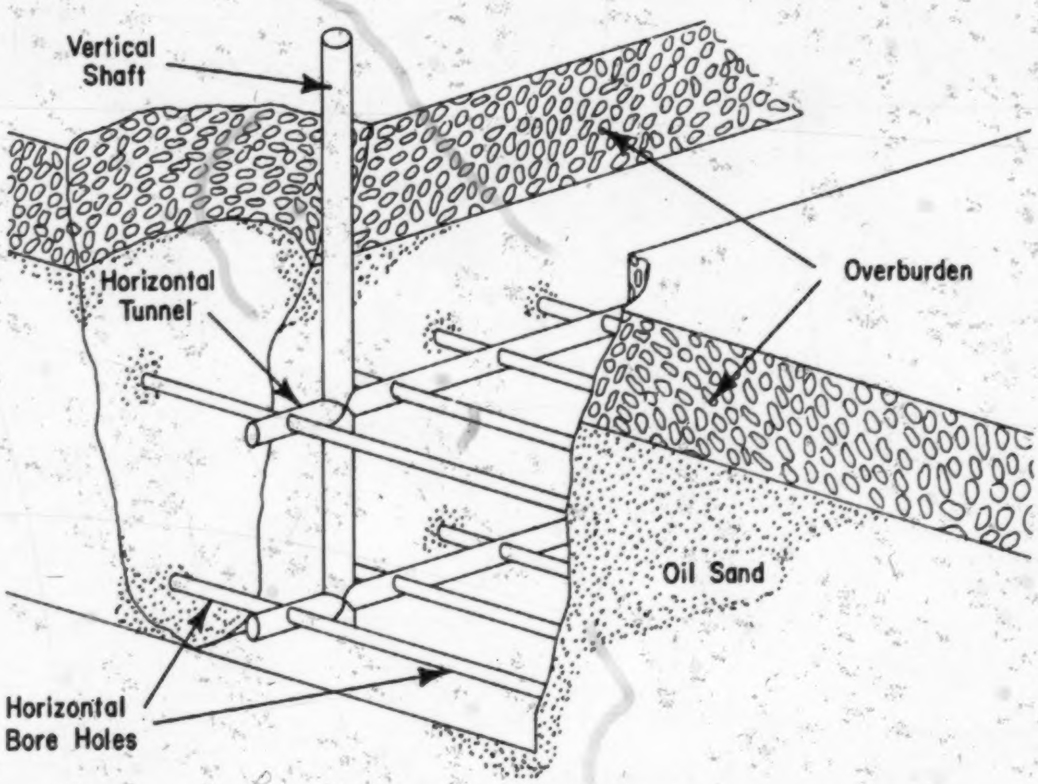

Figure 1. Typical radio frequency guided wave in-situ heating arrangement.

Energy is guided into the formation along these pairs of wells, each pair consisting of an upper and lower well, which behave as an electromagnetic transmission line. By controlling the excitation, the termination, and the dimensions of the line itself, a great deal of control and optimization of the heating process is possible[11]. In addition, very little electromagnetic energy is wasted or leaked to surrounding regions because of the inherent shielding properties of the transmission waveguide.

The IIT Research Institute (IITRI)[12] has conducted a number of guided wave heating studies and field experiments in the low moisture oil sands of Utah. The IITRI triplate heating array is an example of the possible performance of the guided wave heating process. The triplate array is similar to the guiding structure of figure 1 except that an additional horizontal row of electrodes is used in the triplate array in order to minimize leaked radiation. The electrical characteristics of the Utah oil sands and the excitation fields used by IITRI were such that important wavelength effects were experienced, and insight into the guided wave heating process was gained. In examining the application of guided wave heating to moist, more highly conductive earth type materials such as the Athabasca oil sands, different phenomena are experienced due to different physical and electrical properties of these materials. The technology developed by IITRI is not directly applicable in these cases.

Consider the heating of moist, lossy materials whose moisture content is sufficiently small that it is not possible for water to migrate through the material. When a radio frequency wave is initially excited on a transmission line which penetrates into such a medium, the heating rate at high frequencies is significant only near the power input point due to line attenuation. As a result, the material which is in close proximity to the source conductors tends to dry rapidly due to water evaporation. A decrease in the electrical conductivity of this material then obviously occurs and progressively smaller currents are passed between the transmission line conductors in this region. This shifts the deposition of power along the line to the adjacent material in the axial direction. Heating and evaporation are experienced progressively further from the power input point as time passes. Typically, a thin dried coating is quickly formed along the entire length of the waveguide well before the temperatures between the conductors have increased significantly. Subsequent heating of the material between the conductors of the transmission line is now governed by the altered electrical characteristics along this coated waveguide.

Coated waveguide conductors, whether formed by manually applying a dielectric coating or self generated in the manner described above, drastically reduce the attenuation of the propagating wave along the line such that overheating near the source is reduced. A launched wave may then traverse the line several times, alternately reflecting off either end of the line, until its energy is dissipated by the remaining lossy medium. If the line length is small compared to the electrical wavelength, the attenuation may be reduced to the point where relatively uniform heating of the material between the conductors occurs once the coating has been formed. However, when the attenuation is small, the forward and backward travelling waves will alternately interfere with each other in constructive and destructive manners such that significant heating is produced only at half wavelength intervals along the line. The resulting energy deposition inhomogeneities can be quite detrimental on longer lines[12]. In some cases it is possible to modify these "standing wave" inhomogeneities by "moving" the positions of the peaks along the waveguide[11].

In porous lossy materials of high fluid mobility, the formation of the self generated dried conductor coatings referred to above is dependent on the level of excitation. At lower power densities, the region immediately surrounding the conductors may not completely dry out as evaporated moisture is continually being replaced by fluid transported from more remote regions. Attenuation remains high and the entire volume of material between the transmission line conductors near the source is gradually raised to the steam point. Only when virtually all of the water in this region has been converted to steam will the wave progress along the line to heat deeper into the material. The heated zone between the conductors gradually and progressively expands down the length of the waveguide. This heating process has been referred to as "total evaporation boring"[8,13]. The evolution of heating in this case is in distinct contrast to that observed in the preceding low moisture content case where significant heating of the bulk of the material between the conductors only takes place after a thin dried coating has developed along the entire length of the line.

At higher power densities, a partially dried region can be formed that is also of sufficient extent to decouple the currents and shift the power dissipation to further along the line even if mobile fluids exist within the material. Flowing fluids are flashed to steam and driven off before they effect total resaturation of the drying regions. In this case, the decoupling process generally takes longer than for a material where the moisture is not free to migrate. Temperatures between the conductors increase in a manner that exhibits features of both total evaporation boring and self coating action. Collectively, these transmission line heating processes in moist, lossy materials have been referred to as "electromagnetic flooding" or EMF[8,13].

The precise nature of the "flood" that results in a particular application depends in a complex manner on the fluid flow properties of the material and on the conductor diameters and separation as well as on the actual power level. Since the decoupling process depends on how the signal attenuation along the line changes with the growing moisture depleted zone, heating will also vary significantly with the electrical properties of the material and the operating frequency. Indeed, total evaporation boring can be observed, even in the absence of water migration, if the operating frequency is sufficiently high.

A number of experiments have been conducted to illustrate electromagnetic flooding[14] but to date no detailed analysis of the process has been attempted. The purpose of this thesis is to provide a basis for describing electromagnetic flooding and other guided wave heating phenomena. The physical relationships involved are introduced and a computer code is developed to numerically solve the equations which ultimately govern the evolution of temperature and the evaporation of moisture in the region between the guiding electrodes.

1.2 Investigational Method

Assuming unlimited time and resources are at one's disposal, full scale experimental heating tests and actual RF bitumen recovery pilot plants present themselves as possible investigational means. Information regarding the RF heating process may, however, be much more efficiently obtained through analytical calculations, by scaled laboratory experimentation, and by numerical simulation.

Analytical solution of a guided wave RF heating problem involves the solution of Maxwell's equations for the electrical portion of the problem. The general field solution is transverse magnetic (TM) in nature, and is comprised of transverse electromagnetic (TEM) field components and an axial electric field component. This electrical solution must be obtained simultaneously with the solution of the heat conduction equation, which regulates the thermal aspects of the overall problem. The electrical conductivity of the lossy medium is very strongly dependent on temperature, which implies that a highly non-linear coupling also exists between the governing electrical and thermal equations. In addition, when electromagnetic power flows into a volume of oil sand or similar lossy material, it is in general also necessary to account for fluid flow and the attendant mass and heat transfer through the medium. The flow of fluids, the evolution of steam, along with the interdependent medium parameters, virtually eliminate the possibility of analytic solutions to all but the most trivial of guided wave RF heating problems.

Physical scale modelling represents a viable alternate means of studying the complete guided wave RF heating problem. The most applicable reference to this point lies with the laboratory experimentation of R.G. McPherson[14]. McPherson has conducted scaled laboratory experiments of electromagnetic flooding in moist, Athabasca oil sand type media. All of the important phenomena which govern the guided wave heating process in high moisture content media, such as evaporation boring, and the formation of dielectric coatings on conductor surfaces, were first observed by McPherson in his experiments. However, his means of investigation was, for the most part, experimental in nature, and he could not readily investigate the various phenomena contributing to the heating of the material.

As a means of investigation, numerical simulation represents the ultimate in labor efficiency, when repeated simulations must be performed in order to isolate and study a particular phenomenon, or to optimize the heating process by examining the effects of various permutations of medium parameters, for example. This thesis concentrates on the development of a numerical simulator to examine the guided wave heating process. Since the simulator, and hence any knowledge one acquires from its operation, is only as competent as is the theoretical model upon which it is based, a rather extensive amount of laboratory experimentation (approximately one half of the time spent on this project) was undertaken to complement and verify the numerical simulation results. To the author's knowledge no such simulator currently exists although IITRI[5] has developed an RF heating model, Z NET, which models single antenna heating schemes but does not directly address the problems of fluid and heat flow.

The numerical simulation process is complicated by the same problems which have made any analytical approach virtually impossible. Fortunately, the guided wave RF heating process exhibits some characteristics which permit approximate models to be developed that will satisfactorily account for the salient features of the process. The basic phenomena which characterize the heating process are themselves not determined by physical waveguide configurations. It is possible to employ, for example, a coaxial waveguide instead of some arbitrary array of parallel wells, with little compromise in the ability to study the fundamental RF guided wave heating processes. The azimuthal symmetry which is afforded by the coaxial geometry enables the simulations to be performed within a two dimensional framework instead of within a three dimensional one. Obviously, this yields an enormous saving in the time which is required to develop the simulation code, and to perform the simulations. A coaxial geometry is, in fact, realized in the immediate vicinity of the individual conductors of guiding structures such as the one depicted in figure 1. Additional simplification of the simulation process was achieved by assuming that the flow of fluids and gases other than steam is not significant and may be neglected. This is often the case in practical situations as will be demonstrated experimentally in this thesis. The simulation routine COPTER was developed in order to simulate the guided wave RF heating of lossy materials in a coaxial geometry, under the assumption that except for the evolution of steam, the flow of fluids and gases does not significantly effect the process and may be neglected.

Under certain circumstances, such as low loss conditions, high operating frequencies, or electrically short lines with open circuited loads, it is possible to assume that essentially TEM wave components are present within the guide, as opposed to the generalized TM fields. These circumstances are discussed in detail in the following chapters. Based on the various fields which are encountered in guided wave heating problems, two versions of COPTER have been developed. The first version, TEM COPTER, assumes that only TEM fields are present throughout the heating process. Where this assumption is valid, it is possible to employ very simple transmission line analysis for the solution of the electrical problem, which obviously decreases the difficulty of the simulation process still further. Because of its economical operating costs, TEM COPTER was instrumental in the development and verification of those portions of the COPTER routine (which do not depend on the actual nature of the fields) that accounted for the manner in which steam evolves in the model. Another version, TM COPTER, was developed with a full finite difference electrical solver in place of the simple transmission line solver for those cases involving general TM field components. The various simplifying assumptions and strategies made possible the development of the COPTER routine in a format that permitted execution on a Macintosh microcomputer.

COPTER is capable of running simulations using any desired excitation and line termination. Dielectric inner conductor coatings and any physical dimension of coaxial line may be input to the program, as computer memory permits. COPTER is written such that only initially homogeneous media may be modelled. It was thought that this would be adequate, since on a scale comparable to typical interwell spacings, the majority of oil sand deposits can be modelled as homogeneous media. Moreover, COPTER was written so that future accommodations of initially inhomogeneous materials could be easily implemented. The features which were installed in COPTER are designed to facilitate the simulation of the various important physical phenomena which occur during guided wave heating runs, as described in section 1.1. Of course, the accuracy of the simulator is compromised, once any of the basic simplifying assumptions upon which the operation of COPTER is based are violated.

2. Formulation of the Mathematical Model for TEM COPTER

2.1 The Electrical Problem

The solution of all time harmonic electromagnetic field problems in lossy media, regardless of the frequencies of operation or boundary conditions, is universally governed by Maxwell's equations:

$$\nabla \bullet \mathbf{D} = \rho \tag{2.1}$$

$$\nabla \bullet \mathbf{B} = 0 \tag{2.2}$$

$$\nabla \times \mathbf{E} = -j\omega\mu \mathbf{H} \tag{2.3}$$

$$\nabla \times \mathbf{H} = (\sigma + j\omega\varepsilon)\mathbf{E} \tag{2.4}$$

D is the phasor electric flux density in coulombs per square meter, **B** is the phasor magnetic flux density in teslas, **E** is the phasor electric field intensity in volts per meter, and **H** is the phasor magnetic field intensity in amperes per meter. In the above equations ρ represents the charge density in coulombs per cubic meter, σ is the conductivity in siemens per meter, ε is the permittivity in farads per meter, μ is the permeability in henries per meter, and ω is the angular frequency in radians per second. It is not readily possible to arrive at a solution for the electromagnetic fields, and hence the heating rates, of a guided wave RF heating scenario, as a function of time, due to the complex electrical nature of the system. The full solution of Maxwell's equations in a generalized coaxial geometry would yield axial and radial electric field components, as well as azimuthal magnetic field components. Instead, some form of simplification is sought in order to facilitate a more practical field solution which would reflect all the essential elements of the original problem.

2.1.1 The TEM Approximation

If a coaxial waveguide with perfectly conducting boundaries is filled with a homogeneous material, the dominant electromagnetic fields which will result upon the application of RF excitation to the waveguide are of a very elementary nature. These fields contain only TEM components (no axial electromagnetic fields), and are thus of the form of the fields which are commonly excited on simple two conductor transmission lines. After the excitation has been applied for some time such that significant energy has been dissipated in the lossy material, the material which is near the inner conductor will typically begin to dry, forming a low loss dielectric coating. With this developing inhomogeneity, the fields which then exist are no longer strictly TEM in nature. With the onset of axial fields as a result of the inner conductor coating, one must question the use of a simple TEM electrical model as the proper means of obtaining the field solutions and the subsequent heating patterns.

The conditions under which a TEM approximation would be justified were examined experimentally, by quantitatively and qualitatively examining the presence of the axial electric fields. Electric field probes[15] developed by D. Ellinger were employed in order to directly measure the axial and radial electric field components at all positions within a coaxial guiding structure, as shown in plate 2 and figure 2.1, under a variety of electrical conditions. Numbers 1 through 4 in plate 2 and figure 2.1 relate the actual and schematic representations of the experimental apparatus. The 0.91 m long, 0.3 m diameter electrically

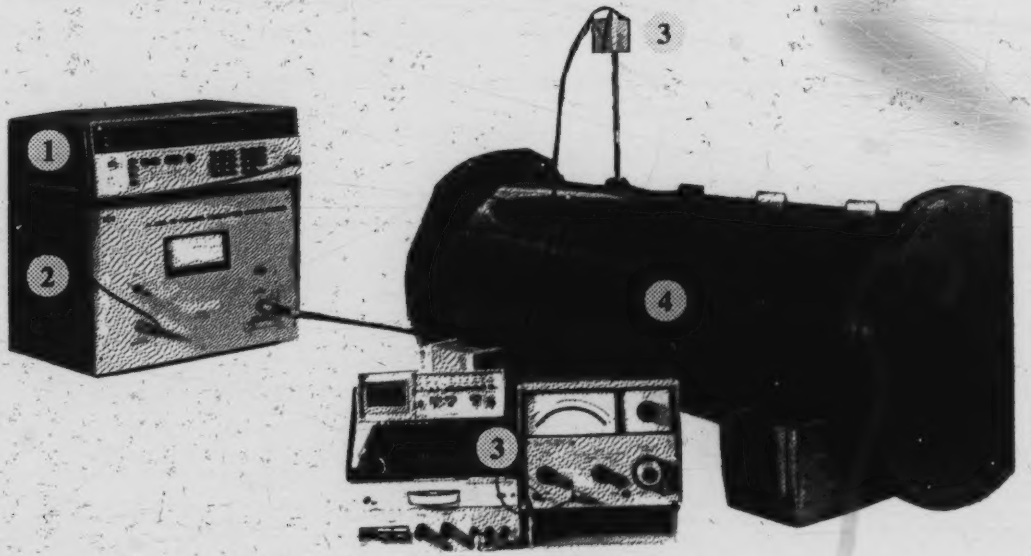

Plate 2. TEM experiment apparatus.

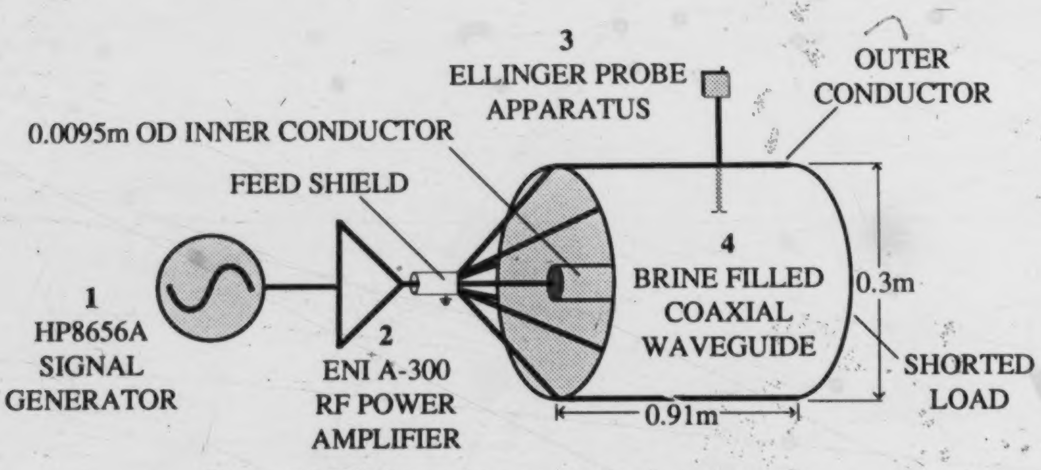
3
ELLINGER PROBE
APPARATUS
OUTER
CONDUCTOR
0.0095m OD INNER CONDUCTOR
FEED SHIELD
4
BRINE FILLED
COAXIAL
WAVEGUIDE
0.3m
1
HP8656A
SIGNAL
GENERATOR
2
ENI A-300
RF POWER
AMPLIFIER
SHORTED
LOAD
0.91m

Figure 2.1 TEM experiment apparatus interconnection.

shorted coaxial tube (item 4 in plate 2 and figure 2.1) was completely filled with distilled water, whose conductivity was adjusted from 10^{-3} S/m to 12 S/m by the selective addition of NaCl crystals. An HP8656A signal generator (item 1) and an ENI model A-300 power amplifier (item 2) excited the coaxial structure at frequencies ranging from 500 kHz to 80 MHz. Excitation levels were chosen such that the dynamic range of the probes (item 3) was not exceeded. To create a two layer medium in the coaxial tube in order to produce an axial field component within the water, the 0.0095 m diameter inner conductor was coated with a urethane layer, whose radial thickness was varied from 19 μm (sprayed on) to 1.6 mm (urethane tubing). To conform to the electrical boundary condition of a short circuited load, a TEM field node and an axial field antinode must occur at the short circuit. A shorted load was therefore used in order to provide the largest magnitude (worst case) axial electric field in the lower frequency runs, and to minimize fringing. As shown in figure 2.1, multi-point input feed shielding was used in order to provide, as much as possible, a distortionless excitation field at the input. The experimental data is given in Appendix A.

A number of observations were made from the experimental data:

1. The larger the coating thickness, the stronger the axial field, as expected. No axial field could be observed when the coating was removed.

2. The higher the frequency of the applied wave, the weaker the axial field, since the decreasing impedance across the coating is equivalent to reducing the coating thickness itself.

3. Higher brine conductivities tended to increase the strength of the axial field, for fixed frequencies and coating thicknesses.

Based on the results of the TEM experiment, it is possible to conclude that the TEM approximation should be valid in low loss media, or if very high excitation frequencies are employed in the heating process. Common waveguide theory also suggests that validity would be maintained in electrically short guides with open circuited loads since the load then coincides with an axial field minimum regardless of material properties or operating frequencies.

2.1.2 The TEM Electrical Model

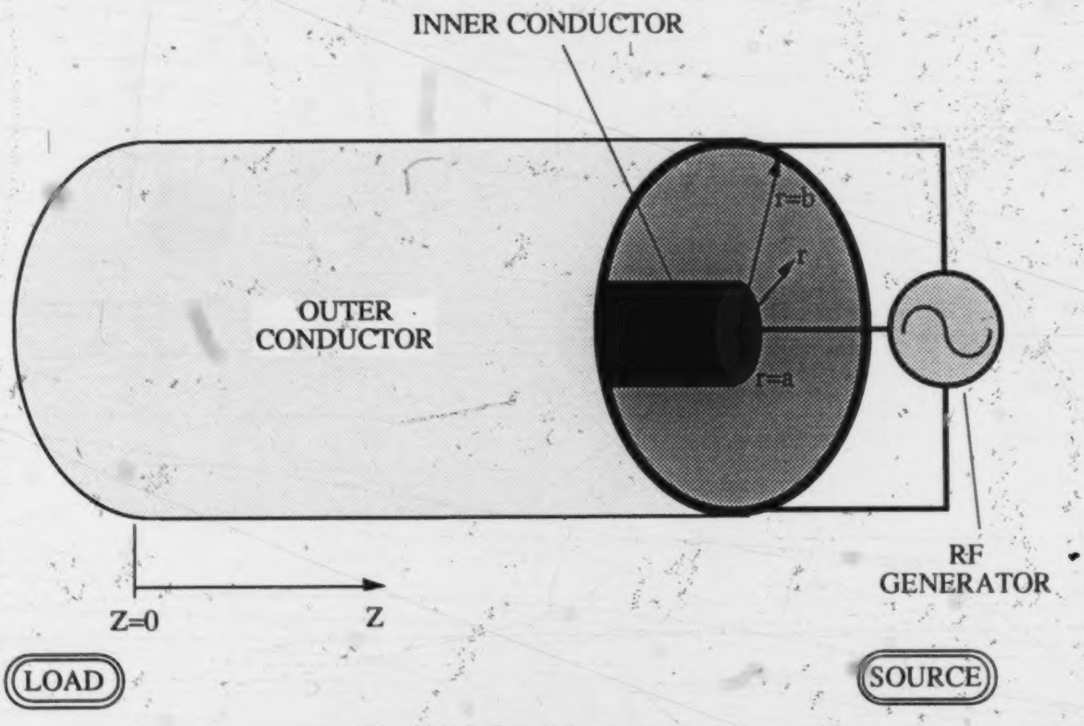

Figure 2.2 Coaxial geometry.

For TEM fields in the azimuthally symmetric coaxial geometry of figure 2.2, equations 2.1 to 2.4 reduce to:

$$\frac{\partial E_r}{\partial z} = -j\omega\mu H_\phi \qquad (2.5)$$

$$\frac{\partial H_\phi}{\partial z} = -(\sigma + j\omega\varepsilon)E_r \qquad (2.6)$$

where E_r and H_ϕ represent the radial electric field and the circumferential magnetic field components respectively. These field components may be specified in terms of the phasor voltage V, in volts, between the conductors and the phasor axial current I, in amps, in the conductors:

$$E_r = \frac{V}{r \ln\frac{b}{a}} \qquad (2.7)$$

$$H_\phi = \frac{I}{2\pi r} \qquad (2.8)$$

Substituting these expressions into 2.5 and 2.6, one obtains:

$$\frac{\partial V}{\partial z} = -j\omega L_o I \qquad (2.9)$$

$$\frac{\partial I}{\partial z} = -(G_o + j\omega C_o)V \qquad (2.10)$$

which represent the TEM electrical problem. In these equations,

$$L_o = \frac{\mu_o}{2\pi} \ln\frac{b}{a} \qquad (2.11)$$

which is the inductance per unit length of the coaxial line in henries per meter ($\mu = \mu_o$ since the medium is assumed to be non magnetic), and

$$C_o = \frac{2\pi\varepsilon}{\ln\frac{b}{a}} \qquad (2.12)$$

which is the shunt capacitance per unit length of the coaxial line in farads per meter. Also,

$$G_o = \frac{2\pi\sigma}{\ln\frac{b}{a}} \qquad (2.13)$$

is the shunt conductance per unit length of the coaxial line in siemens per meter. Equations 2.9 to 2.13 are consistent with the electrical ladder network representation of the coaxial line shown in figure 2.3.

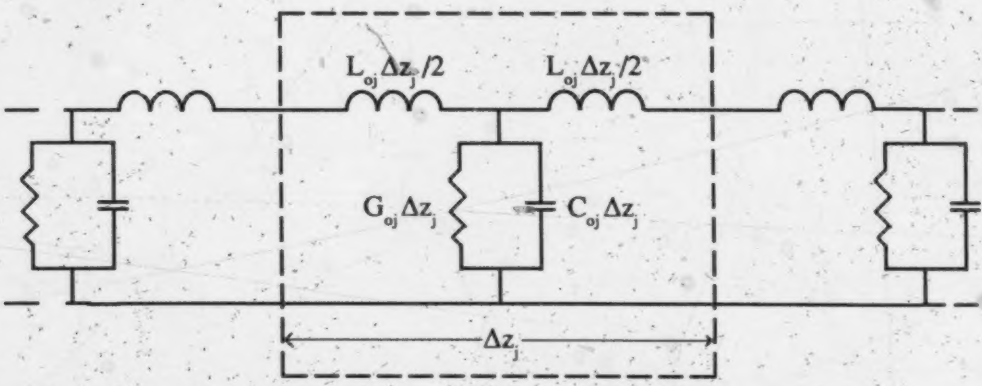

Figure 2.3 Section j of transmission line equivalent circuit model.

The network is composed of many infinitesimally small line sections. Each network section electrically models a corresponding portion of the transmission line, once the lumped element parameters are chosen for the portion, using equations 2.11, 2.12, and 2.13. It is easily shown, via simple circuit analysis and differential theory, that equations 2.9 and 2.10 are equivalent to this network. It is this ladder network that will form the basis of the electrical solver for TEM COPTER.

2.2 The Thermal Problem

Once the electrical model has been established such that the electric fields may be found for a given problem excitation and medium, it is necessary to determine the physical changes to the medium which result from the heating process. In addition to the temperature changes, the thermal model which is employed by COPTER also accounts for the change of phase which occurs when a body of moisture bearing medium is heated to the boiling point. As the boiling temperature is approached, the vapor pressure begins to increase as changes occur to the saturation levels, the relative permeabilities, the viscosities, and the densities of the constituents. Less of the dissipated power is consumed in the raising of the temperature of the medium, and more is consumed to supply the heat of vaporization. In addition, the flow of fluids by both gravity and vapor pressures may promote resaturation of the drying regions. Throughout the simulation process, conservation of energy, individual mass conservation of the medium constituents, as well as the appropriate phase equilibria, must be maintained. Clearly, the simulation of these events is a complex task.

Simulations which were performed using the simulator TCTM-EPEIOS[16] (which models low frequency heating with full multi-phase, multi-component fluid flow) indicated that under certain circumstances, the flow of fluids may be neglected in oil sand heating situations. This is often the case in porous lossy materials such as oil sand, if the water saturation level (percentage of pore volume which is occupied by the water) is less than approximately 20 %. As energy is deposited into such materials so that the temperature is brought to near the boiling point of the pore water, the evolution of steam is accompanied by a sharp increase in vapor pressure in the medium. Significant fluid movements and resaturations will not arise from this pressure or from capillary action, however, since reasonable applied power levels will evaporate minor fluid movements before they become significant. Alternately, the fluid saturation level may be extremely low such that the fluid is essentially immobile within the pores of the medium. In either case, the steam is driven off under its own pressure while the medium temperature is held at the boiling point, and little resaturation occurs. The use of perforated electrodes, which in practice permits the injection and production of fluids at the electrodes, also facilitates the escape of the steam to the atmosphere. The water saturation level within the medium can thus be progressively reduced to some near zero value, especially in the vicinity of the electrodes.

As discussed in Appendix B, the electrical conductivity of the medium may be calculated as:

$$\sigma(W,T) = [1+a(T-24)][K_{1C}W^2+K_{1B}W+K_{1A}] \qquad (2.14)$$

where W is the mass percent water content, T is temperature in degrees celsius, and a is the temperature dependence factor, with the dimension $^{\circ}C^{-1}$. The measured constants K_{1C} and K_{1B} have the units $\%^{-2}$ and $\%^{-1}$ respectively, while K_{1A} is dimensionless. Upon initial application of power to the lossy material, the approximately linear increase in the temperature of the material results in a linear increase in the conductivity of the material. Then, as water is removed by the evolution of steam, the conductivity drops rapidly, predominantly as the square of the mass percent water content, until some residual conductivity value is reached. This residual value is based on the conductivity of the moisture depleted lossy material. A representative conductivity variation, under the application of power, is given in figure 2.4.

In order to accommodate the phase change which occurs in the medium as a result of the heating process, without developing a full fluid flow simulation section, the "steam disappears" approximation was developed. Under the guise of this approximation, it is assumed that once the boiling temperature has been reached in an elemental volume of the medium, the temperature of the volume remains fixed at the boiling temperature, as long as moisture is contained within the volume. It is then assumed that energy which is deposited in a volume at the steam temperature is directed exclusively towards evaporation of the connate water within the volume, and not towards any further increase in the temperature of the volume. Conservation of energy with respect to the specific heat of vaporization of the water is used to estimate the mass of water m_w converted to steam, ignoring any associated pressurization effects:

$$m_w = S / C_v \qquad (2.15)$$

m_w is in grams. S represents steam energy in joules and C_v is heat of vaporization in joules per gram. It is assumed that the steam simply "disappears" to the atmosphere via pores in the medium and electrode perforations. During this process, changes to the conductivity of the volume are determined by the decreasing water content terms in equation 2.14. Once the water has been removed, the conductivity of the volume is set permanently to a small residual value. Obviously, the range of validity of the "steam disappears" fluid flow approximation corresponds to those cases in which resaturating fluid flow may be neglected.

With the phase change modelling in place, the thermal problem requires a means of mathematically modelling the heat flows and temperature changes which also result from the RF stimulation process. Within the lossy medium, it is possible to calculate the volumetric instantaneous rate Q_{inst} at which electromagnetic energy is converted to heat in the

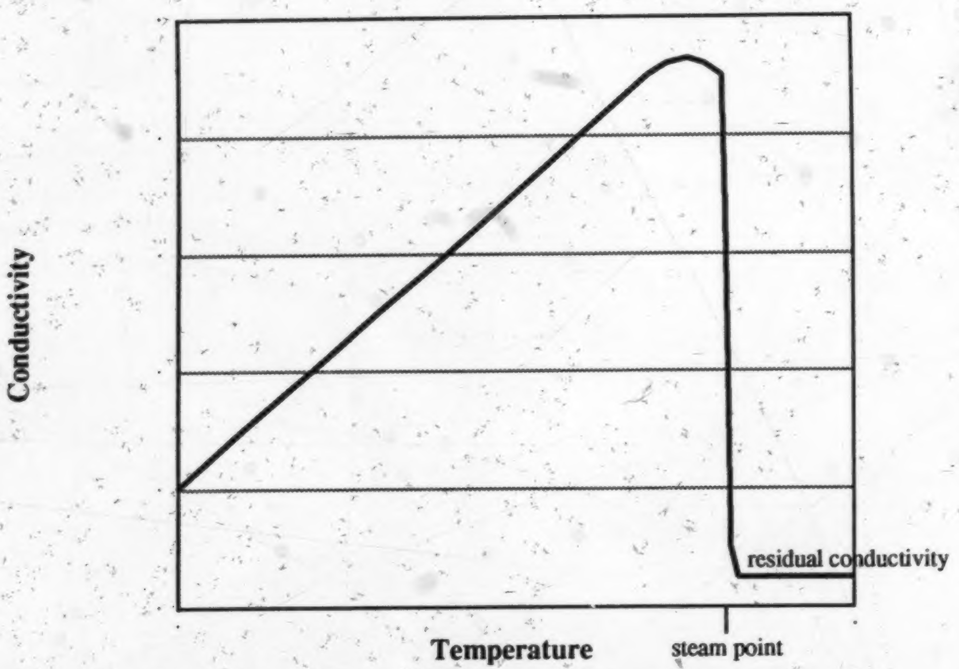

Figure 2.4a Representative conductivity versus temperature plot.

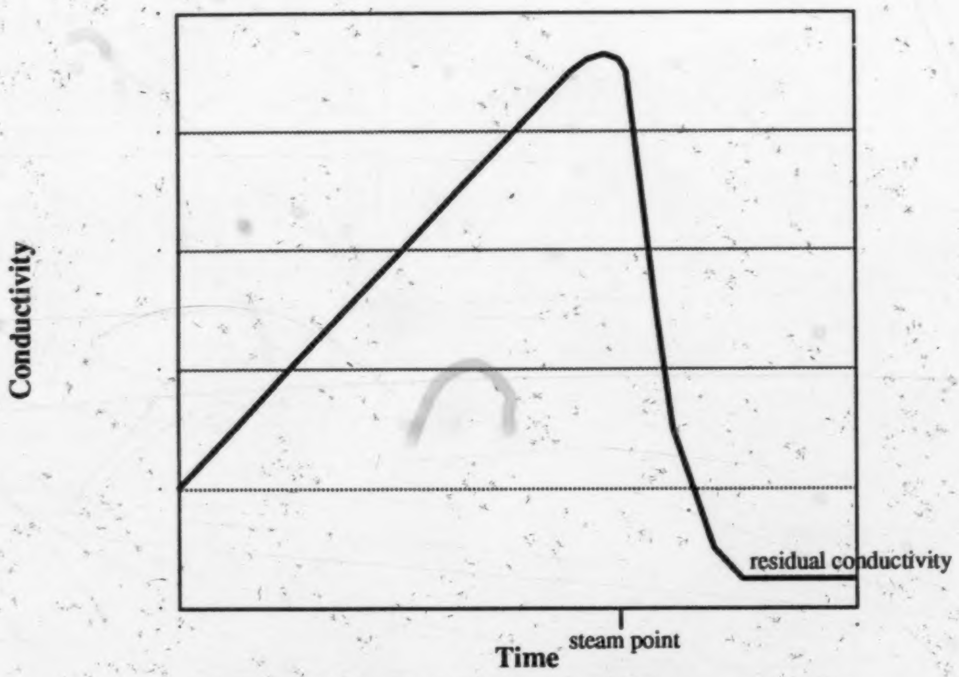

Figure 2.4b Representative conductivity versus time plot.

presence of an electric field:

$$Q_{inst} = \sigma\ E(t) \bullet E(t) \tag{2.16}$$

in watts per cubic meter, where E(t) represents the instantaneous value of the electric field intensity. Instantaneous fluctuations in the temperature which result from fluctuations in Q_{inst} during each cycle of the electric field are not important on the much larger time scale of the simulation process. In order to model the thermal events on the macroscopic time scale on which they would normally be observed, it is the time averaged volumetric heating rate Q of the fields which is of relevance. Assuming rms field quantities:

$$Q = \sigma |E|^2 \tag{2.17}$$

The known heating rates are then forcing terms in the equation which governs the resulting thermal changes in the medium. This equation is known as the heat conduction equation:

$$M_{VOL} \frac{\partial T}{\partial t} = \nabla \bullet (k \nabla T) + \sigma |E|^2 \tag{2.18}$$

where M_{VOL} is the volumetric heat capacity of the medium in joules per cubic meter per degree celsius, k is the thermal conductivity in watts per meter per degree celsius, and t is time in seconds. The heat conduction equation is used to determine the temperature change in a medium which results from both heat flow into the medium and electrical power dissipation in the medium. Energy is conserved in this process, as $M_{VOL} \frac{\partial T}{\partial t}$ represents the power equivalent of the temperature increase, while $\nabla \bullet (k \nabla T)$ and $\sigma |E|^2$ represent the heat flow power into, and electrical power dissipation in the medium, respectively.

When a region of thermally conductive material is exposed to a temperature gradient, heat will flow across the medium, from the higher temperature location toward the lower one. The magnitude of the heat flow is directly proportional to the thermal conductivity of the medium and to the magnitude of the gradient. This is directly analogous to Ohm's law, or the proportionality between the current flow and the resistance of a lossy medium in the presence of a voltage gradient. In previous discussions of the TEM electrical model, resistors and capacitors represented this proportionality, thereby governing the steady state flow of current in the medium. In a similar fashion, it is possible to develop a lumped element thermal model for axial and radial heat flow.

In order to formulate the thermal equivalent circuit which is used in order to solve equation 2.18 within the problem domain, consider the structure illustrated in figure 2.5.

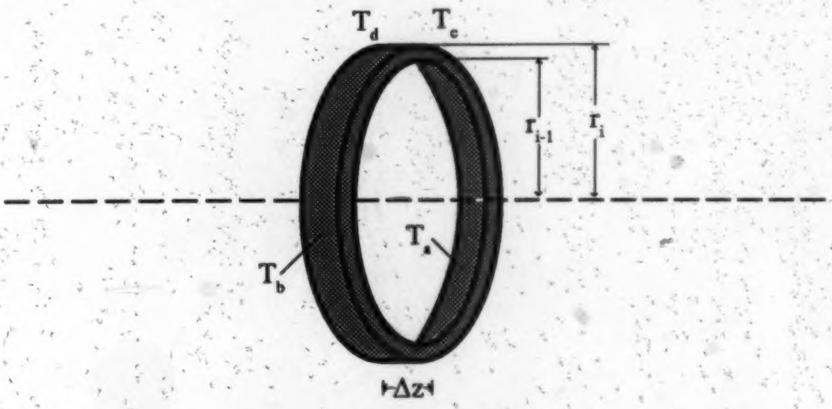

Figure 2.5 Hoop structure.

Suppose that the inner radius r_{i-1} of the structure is held at a constant temperature T_a and that the outer radius r_i is held at a constant temperature T_b. Further suppose that the remaining edges are insulated such that only radial heat flow is possible. In steady state conditions, equation 2.18 for this problem becomes:

$$\nabla^2 T=0$$

or,

$$\frac{1}{r}\frac{\partial}{\partial r}\left(r\frac{\partial T}{\partial r}\right)=0$$

Solving this equation by simple integration and evaluation of constants yields:

$$T(r)=T_a+\frac{(T_b-T_a)}{\ln\frac{r_i}{r_{i-1}}}\ln\frac{r}{r_{i-1}}$$

The heat flow, in watts, in analogy to Ohm's law, is written as:

$$H = -kA\nabla T \tag{2.19}$$

A is the surface area, in m^2, across which the heat flow is to be determined. For the structure in question, the radial heat flow is calculated as:

$$H = -k2\pi r\Delta z\frac{\partial T}{\partial r}$$

Differentiating the T(r) expression and substituting into the above yields the expression for the steady state heat flow from the inner radius to the outer radius of the structure:

$$H = \frac{-k2\pi\Delta z(T_b - T_a)}{\ln\frac{r_i}{r_{i-1}}} \tag{2.20}$$

Here, a thermal conductivity constant of proportionality relates the temperature gradient to the heat flow term as a resistance relates a voltage gradient to a current flow. Alternately, if the inner and outer radii were thermally insulated, and if the right and left axial bounds of the structure were held at the temperatures T_c and T_d respectively, then it is easily shown that the steady state axial heat flow to the right is written as:

$$H = \frac{k\pi(r_i^2 - r_{i-1}^2)(T_d - T_c)}{\Delta z} \tag{2.21}$$

It will become advantageous, for purposes of clarity, to define thermal "conductances" which are equal to the constants of proportionality of equations 2.20 and 2.21. For the hoop structure under discussion, equation 2.20 may therefore be rewritten as:

$$H = G_R\,(T_a - T_b) \tag{2.22}$$

where

$$G_R = \frac{k2\pi\Delta z}{\ln\frac{r_i}{r_{i-1}}} \tag{2.23}$$

in watts per degree celsius. Similarly, equation 2.21 may be rewritten as:

$$H = G_Z\,(T_d - T_c) \tag{2.24}$$

where

$$G_Z = \frac{k\pi(r_i^2 - r_{i-1}^2)}{\Delta z} \tag{2.25}$$

Using the thermal conductance concept, one may readily calculate the steady state heat flows which occur in the presence of a temperature gradient within a coaxial geometry. As shown in figure 2.6, this is done in a manner which is similar to using Ohm's law for the calculation of currents in the presence of voltage gradients.

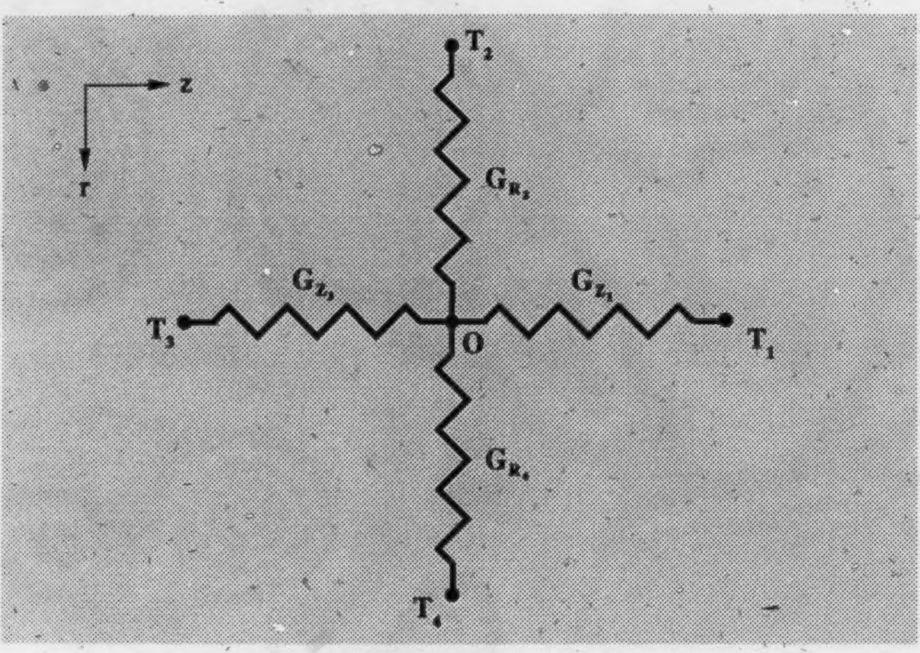

Figure 2.6 Thermal equivalent circuit network.

The net flow of heat into node O is then written as:

$$H_0 = G_{Z_1}(T_1 - T_0) + G_{R_2}(T_2 - T_0) + G_{Z_3}(T_3 - T_0) + G_{R_4}(T_4 - T_0) = 0$$

in steady state conditions, which is analogous to Kirchoff's current law. This heat flow calculation model will form the basis for the numerical solution of the thermal problem, which will be described in the following chapter.

For purposes of the thermal problem, all boundaries of the waveguide are modelled as thermal insulators. Specifically, it is assumed in this study that the outer conductors of the coaxial waveguides under discussion are surrounded by thermal insulation. The outer conductor will be assumed to be a thin metallic surface that possesses a very high thermal conductivity, and because of its limited volume, requires little heat energy to significantly increase its temperature. Thus, for practical purposes, insulating the outer radial boundary of the model will result in the outer electrode being maintained at the temperature of the adjacent lossy material. The inner conductor of the coaxial waveguide will also be assumed to absorb negligible heat energy from the surrounding material and will likewise remain at the temperature of the lossy material immediately surrounding the inner electrode. Because it is assumed that no temperature gradient exists between the conductors and the media adjacent to either of them, the conductors themselves are considered to be part of the thermal insulation.

3. Numerical Solution of the Mathematical Model for TEM COPTER

A numerical solution to the electromagnetic heating problem discussed in the preceding chapter was achieved by dividing the heated zone into a large number of small regions, within each of which it is possible to assume constant values for the electrical and thermal properties. The flow of electric current and heat within these regions is then assumed to be characterized by the equivalent circuit methods which were also introduced in the preceding chapter.

3.1 The Grid Structure

Based on the chosen azimuthally symmetric coaxial geometry, the problem domain of COPTER is discretized as shown in figure 3.1.

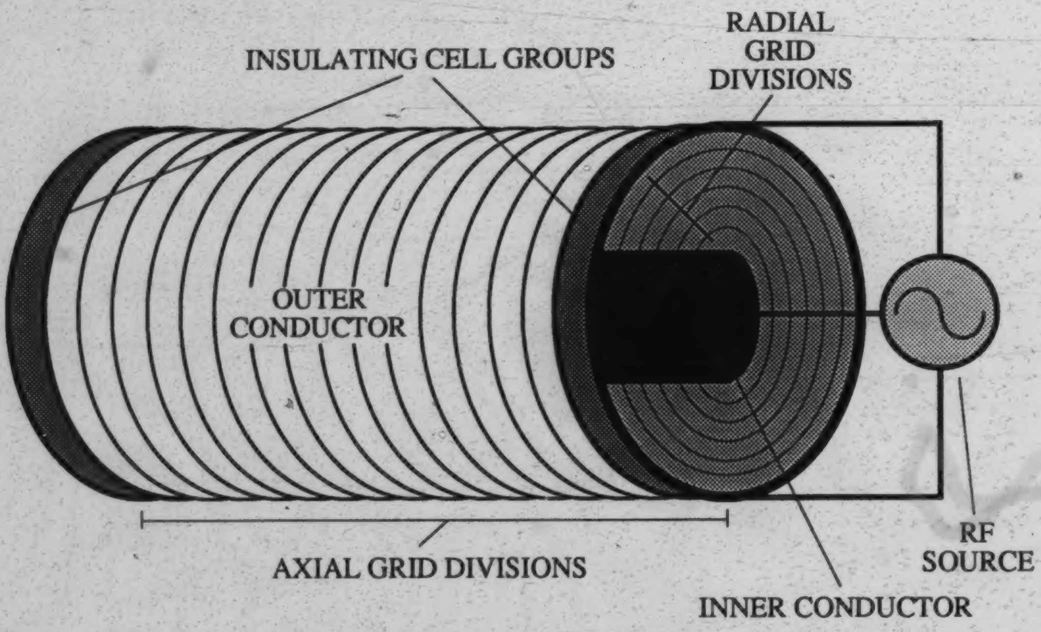

Figure 3.1 Simulation grid.

From this diagram, it is clear that a single region or cell from the complete domain would resemble the hoop introduced in the preceding chapter (figure 2.5) and repeated here in figure 3.2. Because of the azimuthal symmetry of the coaxial model, it is not necessary to subdivide this ring or hoop in the azimuthal direction. The grid structure shown in figure 3.1 is thus represented in cross section, as shown in figure 3.3.

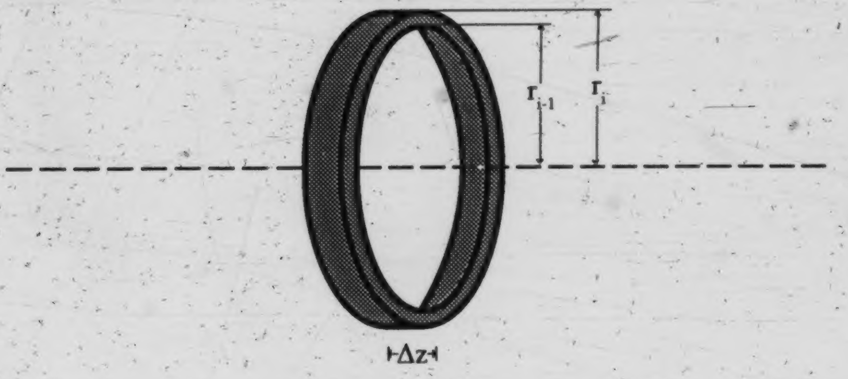
r_{i-1}
r_i
Δz

Figure 3.2 Single cell "hoop".

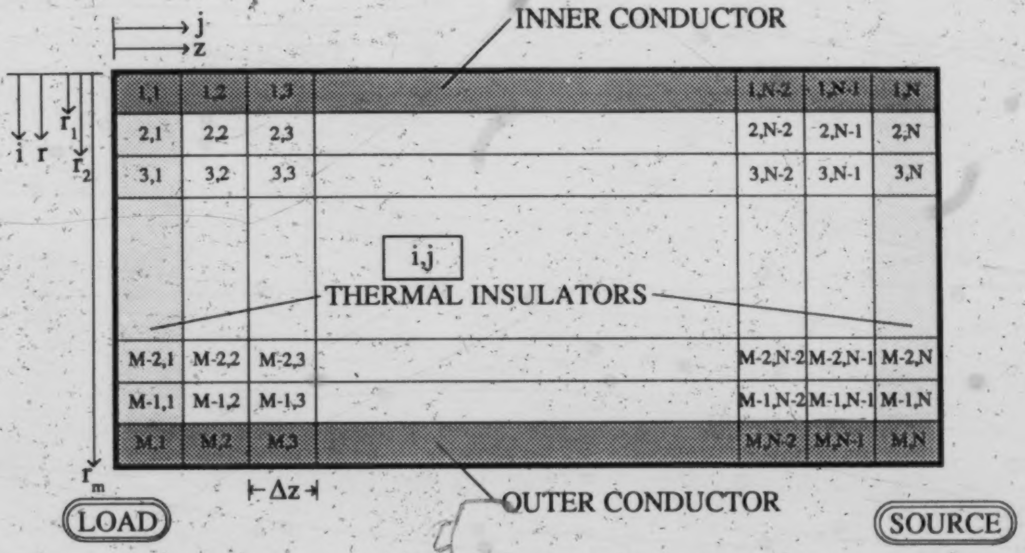
j
z
INNER CONDUCTOR
i
r
r_1
r_2
r_m
1,1
1,2
1,3
1,N-2
1,N-1
1,N
2,1
2,2
2,3
2,N-2
2,N-1
2,N
3,1
3,2
3,3
3,N-2
3,N-1
3,N
i,j
THERMAL INSULATORS
M-2,1
M-2,2
M-2,3
M-2,N-2
M-2,N-1
M-2,N
M-1,1
M-1,2
M-1,3
M-1,N-2
M-1,N-1
M-1,N
M,1
M,2
M,3
M,N-2
M,N-1
M,N
Δz
OUTER CONDUCTOR
LOAD
SOURCE

Figure 3.3 Simulation grid seen as a surface of revolution.

3.2 The Electrical Equivalent Circuit

As has been shown, an incremental axial section of a TEM transmission line model may be discretized as indicated in figure 3.4. The transmission line model is thus represented in its entirety by many such sections, all of length Δz, cascaded together. With modifications, this will form the electrical portion of the overall discretization indicated in figure 3.3. L_{oj} represents the inductance per unit length which is provided by the line conductors over the length Δz. Similarly, G_{oj} and C_{oj} represent the electrical conductances

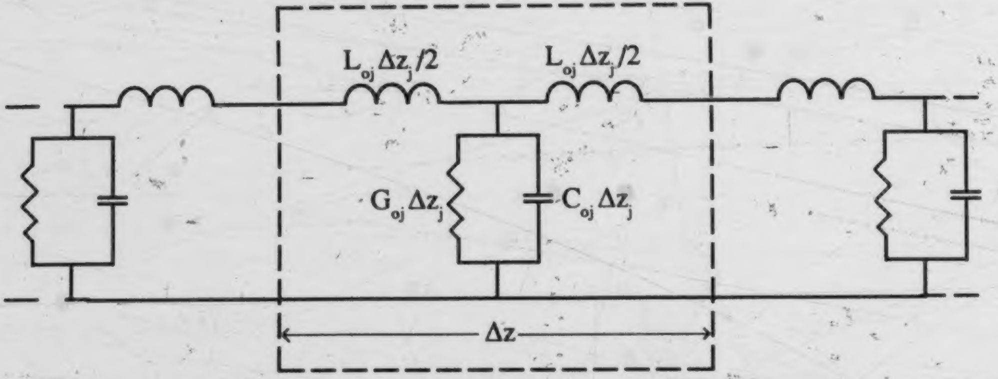

Figure 3.4 Jth section of equivalent circuit discretization of electrical transmission line.

and capacitances per unit length, associated with a TEM field between the inner and outer conductors, for section j of the line. Obviously, the values of each of these parameters are dependent upon the conductivities and the dielectric constants of the material within section j of the coaxial tube. Conductivity and dielectric constant gradients will develop in the material at various physical positions, as the heating process occurs. Axial gradients are accommodated by choosing the appropriate circuit parameters for each axial Δz section. However, the single parallel combination of $G_{oj}\,\Delta z$ and $C_{oj}\,\Delta z$ cannot represent the shunt conductance and capacitance of material within the jth section with adequate resolution, as this material becomes electrically inhomogeneous in the radial direction as well. In order to properly model the radial inhomogeneities, the radial section between the inner and outer conductors is divided into the subsections shown in figure 3.3. The single parallel combination is correspondingly replaced by multiple parallel subcombinations, arranged in series, as shown in figure 3.5. The component values of each subcombination are determined by the electrical properties (Appendix B) of the medium which is contained within the corresponding radial subsection. With this additional refinement, the electrical equivalent circuit representation may be employed as the electrical portion of the overall physical discretization of figure 3.3. The transverse impedance between the inner and outer radii of the hoop of figure 3.2 is represented by one of the new parallel RC combinations illustrated in figure 3.5. The values of R and C of these parallel RC combinations are dictated by the electrical parameters of the medium within the hoop, by the size of the hoop itself, and are given for the ith radial division of the jth axial section by:

$$R_{i,j} = \frac{\ln \frac{r_i}{r_{i-1}}}{2\pi\sigma_{i,j}\Delta z} \tag{3.1}$$

$$C_{i,j} = \frac{2\pi\varepsilon_{i,j}\Delta z}{\ln \frac{r_i}{r_{i-1}}} \tag{3.2}$$

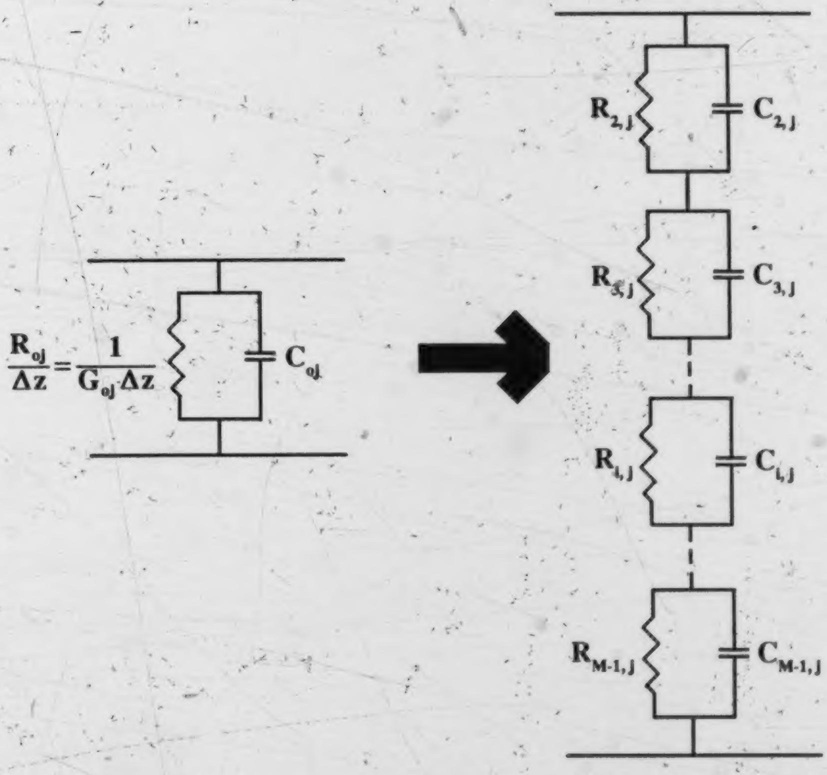

Figure 3.5 Practical transverse impedance electrical representation.

If sufficient quantities of cells are employed in both the radial and the axial directions such that the medium electrical inhomogeneities are properly resolved and such that there are at least 20 axial sections per wavelength in the material, this electrical circuit discretization will accurately characterize the TEM electrical model solution.

The parallel RC electrical equivalent circuit is closely analogous to the actual microscopic electrical behavior of the medium within the hoop of figure 3.2. The parallel circuit representation is not without drawbacks, however. The complex impedance of each of the parallel RC combinations is written as follows:

$$Z_{i,j}=\frac{R_{i,j}}{1+\omega^2C_{i,j}^2R_{i,j}^2}-j\frac{\omega R_{i,j}^2C_{i,j}}{1+\omega^2C_{i,j}^2R_{i,j}^2} \tag{3.3}$$

Suppose an electrically short, open circuited coaxial waveguide (or a single Δz portion of a long guide) is filled with a homogeneous, moist lossy material. Further suppose that this coaxial waveguide is then placed into an oven, whose temperature is programmed to increase at a very slow rate. With the temperature increasing at such a slow rate, the temperature and water content of the entire mass of lossy material would change in a uniform fashion, thus maintaining its electrical homogeneity throughout the warming period and into the moisture evaporative phase. Assuming that the uniform temperature and water content is known at all times, a single parallel RC circuit could be employed along with equations 3.1, 3.2, and 3.3 in order to exactly predict the impedance of the coaxial section. The coaxial section could be represented by a single hoop because of the electrical homogeneity of the material. Typically, for very moist materials, the initial impedance is quite small and is almost purely resistive. Because of the dominance of the ionic conductivity, $R_{i,j}$ is much smaller than $C_{i,j}$ in the parallel RC combination. The $\omega^2C_{i,j}^2R_{i,j}^2$ term in the denominator of the real portion of equation 3.3 is initially much smaller than one, thus allowing the $R_{i,j}$ term to dominate the real portion, and the entire transverse impedance as well. As the uniform heating process is applied to the material in the coaxial tube, the conductivity of the material begins to increase according to the temperature dependent portion of equation B.1. Clearly, the real portion of the transverse impedance will increase its dominance as $R_{i,j}$ decreases. As soon as the boiling point is reached, however, water begins to evaporate and the situation begins to change. The water content dependent portion of equation B.1 now becomes the conductivity controlling mechanism, since the temperature remains constant at the boiling point. Since the parabolic term of the water content dependent portion of equation B.1 dominates over the linear and constant terms during the evaporative phases of practical heating cases, the conductivity of the material drops according to the square of the water content. This, in turn, causes the as yet predominantly resistive transverse impedance, which still equals $R_{i,j}$, to rise according to the square of the mass percent water content. Finally, the rising $R_{i,j}$ term eventually causes the $\omega^2 C_{i,j}^{\ 2} R_{i,j}^{\ 2}$ term to rise to the point that it becomes greater than one and cannot be neglected. The real portion of the transverse impedance then drops rather abruptly as the reciprocal of $R_{i,j}$, or as the reciprocal of the square of the mass percent water content, as further evaporation occurs. A large, abrupt spike is thus actually observed in the real portion of the transverse impedance, as would be measured on a vector impedance meter. The RC equivalent circuit correctly predicts this spike. Because the moisture in the uniformly heated coaxial chamber has essentially been driven off, displacement currents are then dominant in the material, and a reactive transverse impedance is observed.

Consider again the same electrically short coaxial container filled with a moist material, but this time assume heating occurs by the application of radio frequency energy. Because of the coaxial geometry, the deposition of energy into the material will occur first in the region which is nearest to the inner conductor. The subsequent heating and drying of the remaining material will occur progressively, with time, in a radially outward manner. It is not possible to employ a single parallel RC electrical equivalent circuit in order to solve for the impedance of this coaxial cell, due to the electrical inhomogeneities which develop in the radial direction, as a result of the inherently non uniform heating. One might believe that by using several interconnected parallel RC circuits, as suggested in figure 3.5, such that each circuit represents a hoop which is thin enough to contain relatively homogeneous material, the impedance could then be predicted. Practically speaking, however, the use of the multiple parallel RC circuits is extremely sensitive to the discretization process. Unless an extremely fine radial grid partition and a subsequently large number of circuits is employed in order to predict the transverse impedance of the electrically short coaxial section, false spikes will be predicted in the real portion of the impedance. One spike is generated by each of the parallel RC circuits of figure 3.5 as each of the cells which is represented by the circuits is progressively evaporated, in the radially outward direction, during heating. Each spike is produced in the same manner as described in the uniform coaxial heating example, since the simulator incorrectly assumes that the medium within each grid remains perfectly homogeneous at all times. The radial grid structure which must be chosen in order to properly predict the transverse impedance is, in fact, such that virtually uniform material does exist in each hoop throughout the course of the heating. The inordinately large number of radial cells called for by this criterion will often exceed the capabilities of the simulation computer. One may therefore conclude that the circuit of figure 3.5 is not the optimal choice for the representation of the transverse impedance when the change of phase of the connate water in the material must be simulated.

In order to facilitate a proper representation of the transverse impedance of the hoop cells during a COPTER simulation, a direct replacement for the parallel RC circuit was devised. The purpose of this new equivalent circuit is to predict the transverse impedance properly during all phases of the simulation. It was proposed that each cell contain an imaginary radial partition, which would move radially between the inner radius and the outer radius of the cell. The position of this imaginary partition is chosen while steam is evolving during a simulation, based on the ratio of the remaining moisture mass in the cell to the initial moisture mass in the cell. The cell is thus divided by the partition into two concentric cell portions; one ostensibly "dry", the other "wet". The physical dimensions of the concentric portions change with the radial movement of the partition. Instead of assigning one parallel RC circuit to each cell in figure 3.3, the new scheme employs one parallel RC circuit for each portion. The two circuits are themselves interconnected in series in order to represent the transverse impedance of one cell, as shown in figure 3.6. The "dry" parallel RC circuit represents the transverse impedance of the inner cell portion, while the "wet" RC parallel circuit represents the impedance of the outer cell portion. The impedance which is predicted by the wet parallel RC circuit depends on the overall cell temperature and on the physical dimensions of the outer cell portion. The imagined water content of the wet portion is

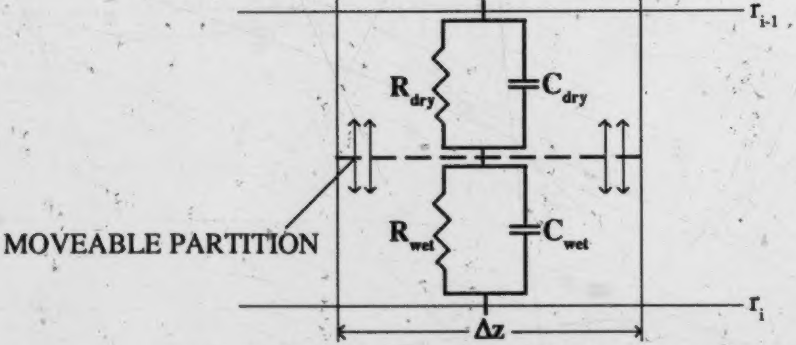

Figure 3.6 Series RC equivalent circuit scheme for cell (i,j).

assumed to remain at the initially saturated level throughout the simulation. The dry parallel RC circuit is imagined to be at all times devoid of moisture. The position of the partition is continually adjusted so that the volume of the dry region grows in accordance to the amount of water evaporated and the water saturation levels in the material.

At the beginning of heating, when the cell is fully saturated with moisture, the partition rests at the inner radial boundary of the cell. The transverse impedance of the cell is therefore predicted using the wet circuit, a single parallel RC circuit as before. This does not change until the boiling point is reached in the cell. After some evaporation is simulated in the cell and the ratio of the remaining moisture mass to the initial moisture mass of the cell becomes less than one, the partition moves away from the inner radial cell boundary. Both wet and dry cell portions are subsequently employed to predict the transverse impedance of the cell. The partition is positioned such that the mass of moisture in the wet portion of the cell is equal to the remaining mass of moisture in the entire cell. Again this assumes that the wet portion remains at the initial moisture saturation level at all times. The slightly depleted overall cell is electrically approximated by the two discrete artificial cell portions, placed in series. As the evaporative process continues, the partition moves further towards the outer radial boundary of the cell, thus progressively emphasizing the dry parallel RC impedance. Once the total cell moisture has been driven off, only the dry parallel RC circuit is used to predict the transverse impedance of the cell.

Except for the spikes, the double RC circuit representation almost duplicates the impedance of the single parallel RC circuit at all phases of the heating. By using the double equivalent circuit instead of the single equivalent circuit, one effectively linearizes the spike producing parabolic water content conductivity dependence. Employing the double RC circuit, with its dynamic rediscretization process, is equival[illegible] to using the single RC circuit with an infinitely fine radial grid discretization.

One drawback of the double RC circuit is that unlike the single RC circuit, its mechanism of operation is not directly based on the physical process of the phase change. The concept of the moving moisture partition represents an unphysical oversimplification of the evaporation process. Because of this oversimplification, the double RC circuit tends to incorrectly predict the presence of large capacitive impedance components at earlier times during the [illegible] than is actually observed. If, for example, only 10 % of the moisture of a cell has been driven off due to evaporation, one would experimentally measure a resistive impedance for the cell. This is due to the fact that 90 % of the remaining moisture would typically be sufficient to sustain substantially ionic coupling across the cell. If the double RC circuit was employed to predict the impedance at this instant in time, however, the small dry cell portion which would arise as part of the double circuit methodology would lead to an incorrect evaluation of the reactive component. Effectively, a very small dielectric portion is all that is needed in order to electrically decouple the cell. In practical simulations, however, a large number of double RC circuits are employed to predict the shunt impedance of an axial slice of the coaxial line. As evaporation occurs during the simulation, only two or three of these cells in the slice will simultaneously possess moving grid partitions. The excess reactive impedance which is intermittently provided by these few cells is always masked by the reactive impedance of the totally dried cells which lie closer to the inner conductor. The superiority of the double RC method over the single RC method is illustrated in figure 3.7. Clearly, the double equivalent circuit represents the method of choice as part of the electrical portion of the overall numerical solution in the TEM COPTER routine.

Once the lumped element parameters are known, the TEM electrical solver calculates the total transverse impedance of each axial group of cells. An arbitrarily assumed solution is chosen for the load voltage (or load current, depending on the impedance of the load), and simple network "ladder" analysis is then employed in order to calculate the voltage and current levels for each of the cell groups, in succession, towards the source. As this "ladder" solution progresses, a source excitation level is calculated based on the assumed voltage or current level at the load. This calculated level at the source is compared to the actual excitation level at the source, and a ratio between the calculated source level and the actual source level is subsequently derived. The voltage and current levels for each of the cell groups are scaled accordingly and the resulting power dissipation is determined for each of the cells.

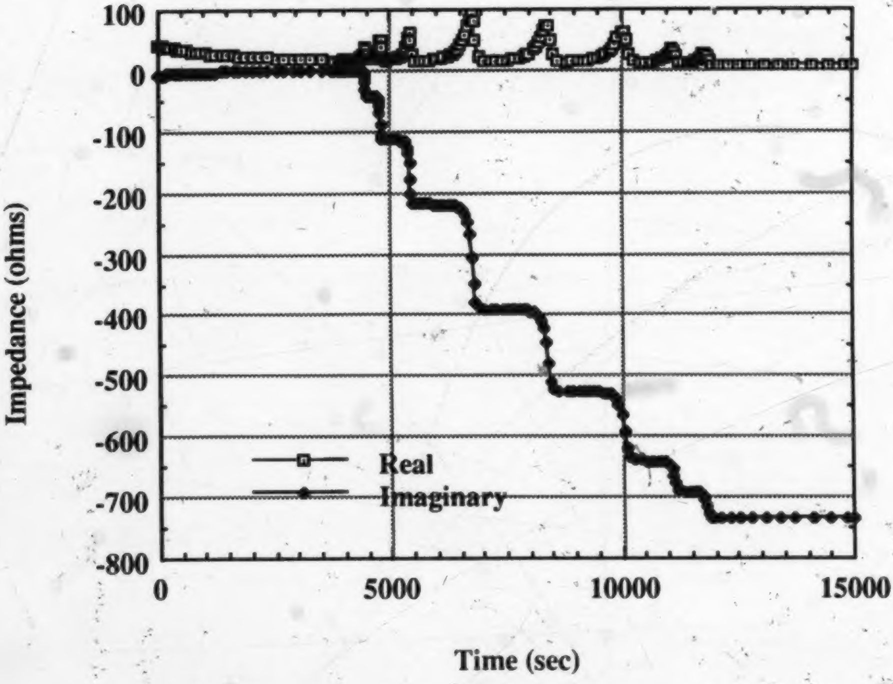

Figure 3.7a Transverse impedance prediction of single RC circuits.

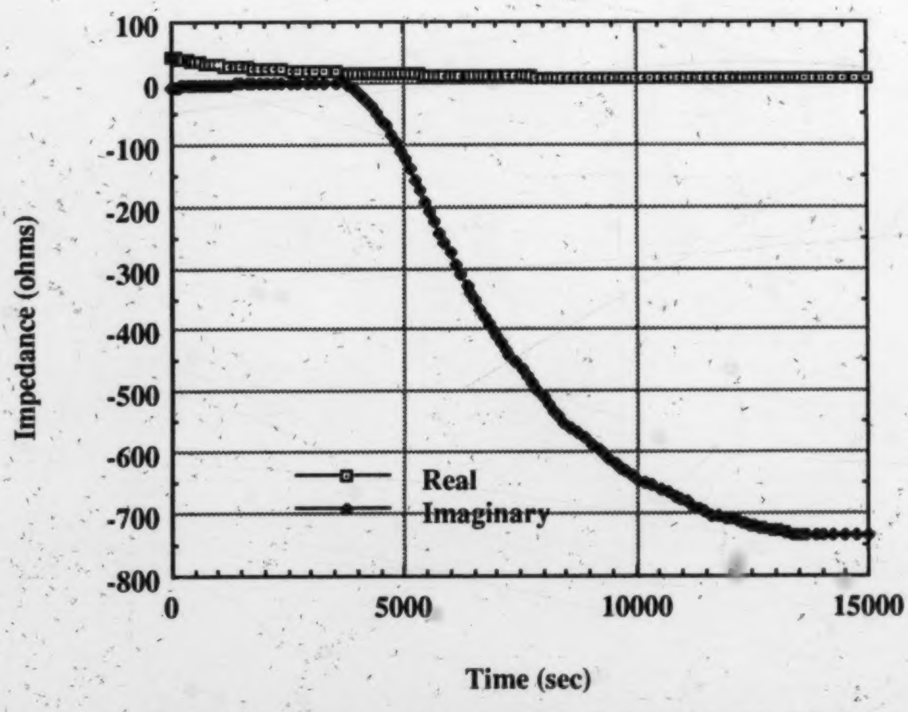

Figure 3.7b Transverse impedance prediction of double RC circuits.

3.3 Conservation of Energy and Solution of the Thermal Problem

Solution of the thermal problem in each of the small cell hoops of figure 3.2 as a function of time must be accomplished for two cases. The first case involves those instances in which a phase change is not occurring (no steam is evolving) in any of the cells, while the second involves those instances in which a phase change does occur. If no phase change is occurring, the thermal problem is solved by first writing equation 2.18 specifically for the volume $v_{i,j}$ of the cell hoop i,j:

$$M_{VOL_{i,j}} \frac{\partial T_{i,j}}{\partial t} v_{i,j} = \nabla \bullet (k_{i,j} \nabla T_{i,j}) v_{i,j} + \sigma_{i,j} \left| E_{i,j} \right|^2 v_{i,j}$$

In terms of inward heat flows $H_{\text{in radial } i,j}$, $H_{\text{in axial } i,j}$ (see Chapter 2) and assuming TEM fields:

$$M_{VOL_{i,j}} \frac{\partial T_{i,j}}{\partial t} v_{i,j} = H_{\text{in radial } i,j} + H_{\text{in axial } i,j} + \left| I_j \right|^2 RS_{i,j}$$

where I_j represents the phasor transverse current in rms amps, and $RS_{i,j}$ represents the real component of the transverse impedance of cell i,j in ohms. If the temperature of cell i,j changes by an amount $\Delta T_{i,j}$ in a small time period Δt, the equation becomes:

$$\begin{aligned} & M_{VOL_{i,j}} \Delta T_{i,j} v_{i,j} \\ & = \left[H_{\text{in radial } i,j} + H_{\text{in axial } i,j} + \left| I_j \right|^2 RS_{i,j} \right] \Delta t \end{aligned} \qquad (3.4)$$

Equation 3.4 is a physical statement of the conservation of energy which is written for each cell. The energy required to raise the temperature of the cell volume i,j by an amount $\Delta T_{i,j}$ in Δt seconds equals the net heat energy flowing into the volume in time Δt plus the electrical energy dissipated in the volume in time Δt.

The numerical solution to the thermal problem is effected by breaking the total heating time into many small time steps, and by solving equation 3.4 for all the cells during each time step, beginning at $t = 0$. The durations of the time steps are small, such that the thermal problem is effectively linearized, thus facilitating its solution within the time span of each step. Once the solutions for each of the time steps are successively combined, the total thermal solution is complete for the entire heating period. The time step size must be chosen small enough such that proper simulator "tracking" takes place, but not so small as to unnecessarily prolong the run time of the simulation. By examining the degree of heating in each cell from the electrical solution, along with the degree of thermal heat flow into each cell based on cell temperatures from the previous time step, COPTER examines the approximate net power input to each cell. Obviously, higher energy inputs lead to greater changes in cell temperatures and moisture contents. Proportionately smaller time steps are therefore chosen in order to maintain proper simulation of the more quickly developing physical changes. Observation has shown that errors in the simulation process will also result if differences in the durations of successive time steps exceed approximately five percent of the time step sizes themselves.

The thermal conductance model of the previous chapter is used in the solution of equation 3.4 for each cell, during each time step. A cross sectional view of the cell of figure 3.2, along with the appropriate thermal conductances, is given in figure 3.8.

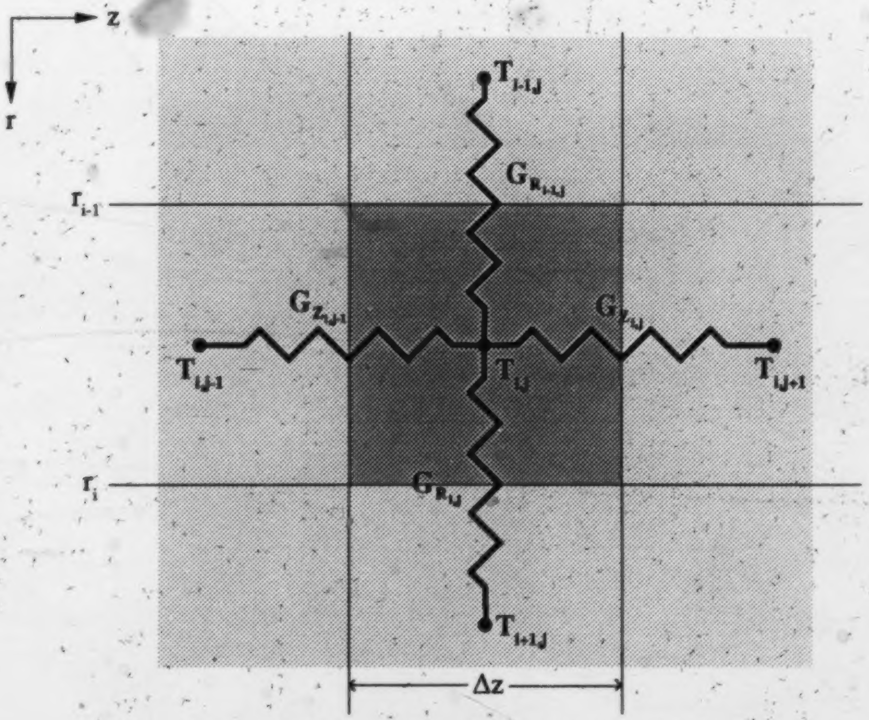

Figure 3.8 Thermal equivalent circuit array for cell.

Equation 3.4 can be written as:

$$\begin{aligned} &M_{VOL_{i,j}}(T_{i,j}^{n+1}-T_{i,j}^{n})\pi(r_i^2-r_{i-1}^2)\Delta z \\ &=(G_{R_{i-1,j}}(T_{i-1,j}^{n+1}-T_{i,j}^{n+1})+G_{Z_{i,j-1}}(T_{i,j-1}^{n+1}-T_{i,j}^{n+1}) \\ &+G_{R_{i,j}}(T_{i+1,j}^{n+1}-T_{i,j}^{n+1})+G_{Z_{i,j}}(T_{i,j+1}^{n+1}-T_{i,j}^{n+1}))\Delta t \\ &+\left|I_j\right|^2 RS_{i,j}\Delta t \end{aligned} \tag{3.5}$$

where n indicates the time step index. $T_{i,j}{}^{n}$ is the temperature of cell i,j at the beginning of time step n, while $T_{i,j}{}^{n+1}$ indicates the temperature of cell i,j at the end of time step n, or at the beginning of time step n+1. Each thermal conductor in figure 3.8 is formed as a series combination of one thermal conductor from cell i,j plus another thermal conductor from the respective adjacent cell. Each of the individual thermal conductors which comprise the combined conductors of figure 3.8 were calculated according to the thermal conductor model of the previous chapter. The thermal conductors of figure 3.8 are therefore written as:

$$G_{R_{i,j}}=\frac{2\pi\Delta z k_{i,j}k_{i+1,j}}{k_{i,j}\ln\left[\frac{r_{i+1}+r_i}{2r_i}\right]+k_{i+1,j}\ln\left[\frac{2r_i}{r_{i-1}+r_i}\right]} \tag{3.6}$$

$$G_{R_{i-1,j}}=\frac{2\pi\Delta z k_{i-1,j}k_{i,j}}{k_{i-1,j}\ln\left[\frac{r_i+r_{i-1}}{2r_{i-1}}\right]+k_{i,j}\ln\left[\frac{2r_{i-1}}{r_{i-2}+r_{i-1}}\right]} \tag{3.7}$$

$$G_{Z_{i,j}}=\frac{2\pi(r_i^2-r_{i-1}^2)}{\Delta z}\left[\frac{k_{i,j}k_{i,j+1}}{k_{i,j}+k_{i,j+1}}\right] \tag{3.8}$$

$$G_{Z_{i,j-1}}=\frac{2\pi(r_i^2-r_{i-1}^2)}{\Delta z}\left[\frac{k_{i,j-1}k_{i,j}}{k_{i,j-1}+k_{i,j}}\right] \tag{3.9}$$

The discrete heat conduction equation 3.5 is written for each cell. The cell temperatures which are used in the right hand terms of each of these written equations are the cell temperatures which exist at the end of the time step, as opposed to those cell temperatures which exist at the beginning of the time step. In other words, the heat flows are calculated in terms of temperatures existing at the end of the time step in question. Since these end of time step cell temperatures are not known, and since one unknown cell temperature exists for each application of equation 3.5 to each cell, and since there are as many unknown cell temperatures as there are cells, a linear system of equations is generated and must be solved in order to determine the end of time step cell temperatures. This is known as an implicit thermal solution, since knowledge of the unknown end of time step temperatures is implied during each writing of equation 3.5 for each cell. Alternately, one could explicitly effect the thermal solution by employing beginning of time step cell temperatures in the right hand terms of equation 3.5. The end of time step cell temperatures are then determined directly from equation 3.5 without requiring the solution of a linear system of equations. Because the explicit method does not update the cell temperatures with the more recent (albeit unknown) end of time step cell temperatures, unmanageable sacrifices are made to simulation accuracy and stability if the explicit method is used[17,18]. The implicit method is preferable, and is therefore used in the thermal solution portion of COPTER. The linear system of temperature equations is assembled as shown:

$$
\begin{bmatrix}
A_{2,2} & C_{2,2} & & & & & E_{2,2} & & & & & & & & \\
B_{3,2} & A_{3,2} & C_{3,2} & & & & & E_{3,2} & & & & & & & \\
 & B_{4,2} & A_{4,2} & C_{4,2} & & & & & E_{4,2} & & & & & & \\
 & & & \ddots & & & & & & \ddots & & & & & \\
 & & & & B_{M1,2} & A_{M1,2} & C_{M1,2} & & & & & E_{M1,2} & & & \\
D_{2,3} & & & & & B_{2,3} & A_{2,3} & C_{2,3} & & & & & E_{2,3} & & \\
 & D_{3,3} & & & & & B_{3,3} & A_{3,3} & C_{3,3} & & & & & E_{3,3} & \\
 & & D_{4,3} & & & & & B_{4,3} & A_{4,3} & C_{4,3} & & & & & E_{4,3} \\
 & & & \ddots & & & & & & \ddots & & & & & \\
 & & & & & D_{M1,3} & & & & & B_{M1,3} & A_{M1,3} & C_{M1,3} & & \\
 & & & & & & \ddots & & & & & & \ddots & & \\
 & & & & & & & & D_{M1,N1} & & & & & B_{M1,N1} & A_{M1,N1}
\end{bmatrix}
\begin{bmatrix}
T_{2,2}^{n+1} \\ T_{3,2}^{n+1} \\ T_{4,2}^{n+1} \\ \vdots \\ T_{M1,2}^{n+1} \\ T_{2,3}^{n+1} \\ T_{3,3}^{n+1} \\ T_{4,3}^{n+1} \\ \vdots \\ T_{M1,3}^{n+1} \\ \vdots \\ T_{M1,N1}^{n+1}
\end{bmatrix}
=
\begin{bmatrix}
F_{2,2} \\ F_{3,2} \\ F_{4,2} \\ \vdots \\ F_{M1,2} \\ F_{2,3} \\ F_{3,3} \\ F_{4,3} \\ \vdots \\ F_{M1,3} \\ \vdots \\ F_{M1,N1}
\end{bmatrix}
$$

Figure 3.9 Temperature matrix.

where

$$
\begin{aligned}
A_{i,j} = {} & M_{VOL_{i,j}}\, \pi(r_i^2 - r_{i-1}^2)\Delta z \\
& + \left[G_{R_{i-1,j}} + G_{Z_{i,j-1}} + G_{R_{i,j}} + G_{Z_{i,j}}\right]\Delta t
\end{aligned}
\qquad (3.10)
$$

$$
B_{i,j} = -G_{R_{i-1,j}}\,\Delta t \qquad (3.11)
$$

$$C_{i,j} = -G_{R_{i,j}} \Delta t \qquad (3.12)$$

$$D_{i,j} = -G_{Z_{i,j-1}} \Delta t \qquad (3.13)$$

$$E_{i,j} = -G_{Z_{i,j}} \Delta t \qquad (3.14)$$

$$F_{i,j} = \left|I_j\right|^2 RS_{i,j} \Delta t + M_{VOL_{i,j}} T^n_{i,j} \pi (r_i^2 - r_{i-1}^2) \Delta z \qquad (3.15)$$

Since the medium boundaries are assumed to be thermal insulators, the appropriate thermal conductance terms become zero for cells which are adjacent to the boundaries.

During a time step in which no phase change is occurring, COPTER solves the linear system of temperature equations in figure 3.9, thereby effecting a fully implicit solution to the thermal problem, using the highly efficient ADI (Alternating Direction Implicit) method[19]. In this method, the time step is divided into two half time steps. All cell temperatures are updated at the end of the first half time step using a partially implicit technique. During the first half time step, equation 3.5 is first written for each cell in the group of cells with indices i=2, j=2 to N-1 (figure 3.3) which lies immediately adjacent to the inner conductor. However, while writing equation 3.5 for a given cell in the group, end of first half time step (implicit) temperatures are used on the left side of equation 3.5 for the temperatures of the two adjacent cells in the i=2 group which appear there. The remaining temperature terms corresponding to radially adjacent cells are taken explicitly from temperature data existing at the beginning of the first half time step. Since the G_R coupling terms do not appear in the resulting temperature matrix for the i=2 group, the matrix itself is of a very elementary "tridiagonal" form, lacking the far off diagonal bands. Inversion of this matrix and subsequent determination of the end of first half time step temperatures for the i=2 cell group is accomplished with the very efficient TRIDAG algorithm[20]. Proceeding radially outwards towards the outer conductor, each of the remaining i=3 to M-1 cell group temperatures is then updated to the end of the first half time step, one group at a time, using this partially explicit technique. During its update, a cell group then uses, as some of its explicit temperatures, end of first half time step temperatures from the radially inward adjacent cell group which was updated just prior to it. Remaining explicit temperatures, which are required from the radially outward adjacent cell group, are taken from temperature data at the beginning of the first half time step as before, since the outer adjacent cell group has yet to be updated to the end of the first half time step. Once this process is completed, the updated end of first half time step cell temperatures will be in error due to the significant degree of explicitness which was employed in the solutions. A similar process then uses these approximate temperatures as the beginning of second half time step temperatures and proceeds to calculate the end of overall time step temperatures in the cells, except that columns of cells, i=2 to M-1 for each j, are used as the cell groups, proceeding axially, one group at a time, from the load to the source. Implicitness is this time observed in only the radial direction, with G_z coupling terms missing in each of the group temperature matrices. Despite its partially explicit operational nature, ADI is capable of effecting virtually fully implicit solutions of the temperature matrix of figure 3.9 because errors which are deduced from the radial explicitness of the first half time step are effectively nullified by errors which appear as a result of the axial explicitness of the second half time step. This assumes, of course, that the time steps are small enough to provide "symmetrical" time step halves, which promote complete nullification. ADI becomes mathematically implicit only when the time step sizes become incrementally small, but during non boiling time steps, virtual implicitness is usually achieved if differences in the durations of successive time steps does not exceed five percent of the time step sizes.

Electrical cell parameters for each time step, conductivities and dielectric constants and the associated impedances and heating rates, are determined explicitly using cell information which exists at the beginning of the time step. Thus $RS_{i,j}$, which depends on $\sigma_{i,j}$, which is in turn temperature dependent, is calculated in terms of the temperature at the beginning of the time step. More specifically, the power dissipation in a cell during a time step is determined from the temperature at the beginning of the time step and not from the temperature at the end of the time step. In this case, it was found that explicitness does not hamper the simulation process as long as the time step size restrictions are observed.

A second case of the thermal solution must be considered with the onset of phase changes. If a moisture bearing cell has reached the boiling point during the simulation, it is assumed that the cell continues to boil for the duration of the time step in question. As a result, any electrical or thermal energy which is deposited into the boiling cell during the time step is directed only towards the evolution of steam, and not towards the increasing of the cell temperature. Thermal conductances model the heat flows as before and equation 3.5 is written for each non-boiling cell. Of course, once a cell begins to boil, its end of time step temperature (the "boiling point") is not an unknown quantity. As a result, the boiling cells are not represented in the temperature stiffness matrix, but do appear in the forcing terms. The change of phase which must be simulated, as a result of the evolution of steam, requires significant attention during the total thermal system solution process. Moreover, the total linear system can become quite large, once an adequate number of simulation cells is chosen for a properly resolved grid discretization.

The earliest versions of COPTER employed various relaxation methods rather than ADI in order to solve the thermal system. These iterative methods functioned properly, albeit slowly, during the simulation until the boiling point was reached. Simulating the phase change involves holding the temperatures of water bearing boiling cells at the boiling temperature if these cell temperatures would otherwise exceed the boiling point in the absence of the phase change effect. From the point of first boiling onward, the numbers of iterations which were required by the various iterative thermal solvers to invert the total thermal matrix during each time step would increase by orders of magnitude because of the temperature fixing. Due to the extremely poor run time efficiency of the early COPTER thermal solvers, full TEM COPTER simulations required several days of continuous computing in order to complete. No amount of time step size or relaxation modification could alleviate this problem.

A high performance thermal solver was required in order to invert the total thermal matrix efficiently during a phase change. During the subsequent investigation of possible numerical methods, it was observed that the inversion efficiency of the evaporative thermal linear system responded dramatically to those numerical system solution techniques which possess greater degrees of implicitness. The ADI method, which is used to solve the system and update the cell temperatures during the non evaporative time steps, was modified to attempt to solve the system during evaporative periods as well. The ADI algorithm is carried out as previously explained, except that immediately after the temperatures of each of the cell groups are updated during either half time step, the end of half time step temperatures of water bearing cells which exceed the boiling temperature are held at the boiling temperature. Although this method provided a physically viable means of solving the thermal system during boiling time steps, and thereby simulating the phase change, calculations revealed that in this case, conservation of energy was not maintained as boiling progressed. Decreasing the time step size appeared to partially solve this problem since this increased the degree of implicitness, but impractical time step durations resulted when more favorable energy balances were achieved.

The optimal technique which is employed in COPTER for the inversion of the thermal linear system is still based on the ADI method. During the non-boiling phases of the COPTER simulations, pure ADI is used. As boiling begins, the modified version of ADI is used to calculate an approximate end of time step temperature for each cell. Because ADI is not perfectly implicit, however, it is followed in the same time step by lightly accelerated iterative PSOR[21] during the evaporative portions of the simulation to restore full implicitness and energy balance to the thermal solution process. Both ADI and PSOR stages are modified to hold the temperatures of boiling cells at the boiling temperature during the solution. Solution presented by the ADI stage alone contains significant inaccuracy, but it is close enough to the fully implicit solution such that it provides an excellent "first guess" for the PSOR stage. Because few iterations of PSOR are then required for the final solution during boiling, the efficiency of the ADI is not compromised. In practical situations, these methods resulted in more than an order of magnitude improvement in the run time efficiency of the COPTER thermal solver.

Non uniform grid dimensioning is employed in the radial direction, since heating events will always occur much more quickly near the inner conductor of the coaxial guiding structure, and finer grid resolution is therefore required in these areas. When COPTER simulations are performed using the TEM electrical solver, the radial dimension of the cell which is nearest to the inner conductor must be chosen such that it is no larger than the radius of the inner conductor itself. Proceeding radially outwards towards the outer conductor, each of the radial dimensions of the remaining cells should be chosen to be successively larger in a logarithmically increasing fashion. The differences in the radial dimensions of radially adjacent cells should not exceed a factor of two. The quantity of axial cells must be chosen such that more than twenty axial cells are present within one wavelength at all times during the simulation.

Once the end of time step cell temperatures have been determined during a time step for the boiling case, the water content arrays are adjusted for the water bearing cells whose temperatures have reached the boiling point. This is accomplished by simply depleting the moisture content variables of each of the water bearing, boiling cells based on the heat of evaporation of water and the calculated steam energies of each of the cells as shown in equation 3.16:

$$m_{w_{i,j}} = m_{w_{i,j}} - \frac{S_{i,j}}{C_v} \qquad (3.16)$$

where $G_{w\,i,j}$ is the mass of moisture in cell i,j in grams, and C_v is the heat of vaporization of the moisture in joules per gram. $S_{i,j}$ is the steam energy in cell i,j in joules and is given by:

$$\begin{aligned} S_{i,j} = (&G_{R_{i-1,j}}(T^{n+1}_{i-1,j} - T_{steam}) + G_{Z_{i,j-1}}(T^{n+1}_{i,j-1} - T_{steam}) + G_{R_{i,j}}(T^{n+1}_{i+1,j} - T_{steam}) \\ &+ G_{Z_{i,j}}(T^{n+1}_{i,j+1} - T_{steam}))\Delta t + \left|I_j\right|^2 RS_{i,j}\Delta t \qquad (3.17) \end{aligned}$$

Strangely, the five percent time step duration criterion is relaxed for high moisture content media during the boiling phases of the simulation. For wet materials, it is possible to employ simulation time steps which are several orders of magnitude larger after the boiling begins, with no loss in simulation accuracy. Although the rationale behind this discovery is not clear, this "boost code" does realize a tremendous saving in the simulation run time of high medium moisture cases.

COPTER is formatted to run on various versions of the Macintosh II microcomputer under the MPW FORTRAN compiler shell[22]. A minimum 2MB of ram is required when large numbers of cells are employed during the simulations. Throughout the development of COPTER and during the execution of all simulations, no requirement for a machine precision greater than single precision was present. Typical full simulations which employ the TEM electrical solver require a few hours of computing time on a Macintosh II.

3.4 The Computational Algorithm

In order to solve the overall model and determine the heating and moisture patterns which develop as a result of the application of RF energy to the coaxial guide, the electrical and thermal problems must be solved on an ongoing basis, as time progresses during the heating process. A flow diagram of the computational algorithm is given in figure 3.10. After initialization is completed, the simulation algorithm is specifically executed on a per time step basis as follows:

1. As discussed in Appendix B, the electrical conductivities and dielectric constants are first calculated for each of the cells based on the temperature and moisture contents of the cells. These are the temperatures and moisture contents which are present at the start of the time step, since the time step duration has yet to be chosen by the simulator. The thermal conductivities within the cells are calculated in a similar manner. Lumped element parameters for each of the cells are subsequently calculated.

2. The electrical solution is effected, as described in section 3.2, and the power dissipation levels are determined for each cell.

3. A time increment Δt is determined which is inversely proportional to the net power flowing into the cell with the largest net power input.

4. Discrete energy balance equation 3.5 is written for each cell.

5. The resulting linear system of equations is inverted using ADI.

6. During phase change time steps, full implicitness of the thermal solution, which is only partially maintained by the ADI scheme, is restored by the implicit recovery scheme. During the restoration, the end of time step steam energies of the boiling cells are calculated.

7. The water content of the boiling cells is updated, based on the steam energies of these cells for the time step.

8. As described in the next chapter, a complete energy balance calculation is performed as one means of evaluating the ongoing accuracy of the simulator.

9. After outputting relevant electrical and thermal data to a file, the simulation elapsed time is compared to the specified end time. If simulation time remains, the process is cycled back to point 1.

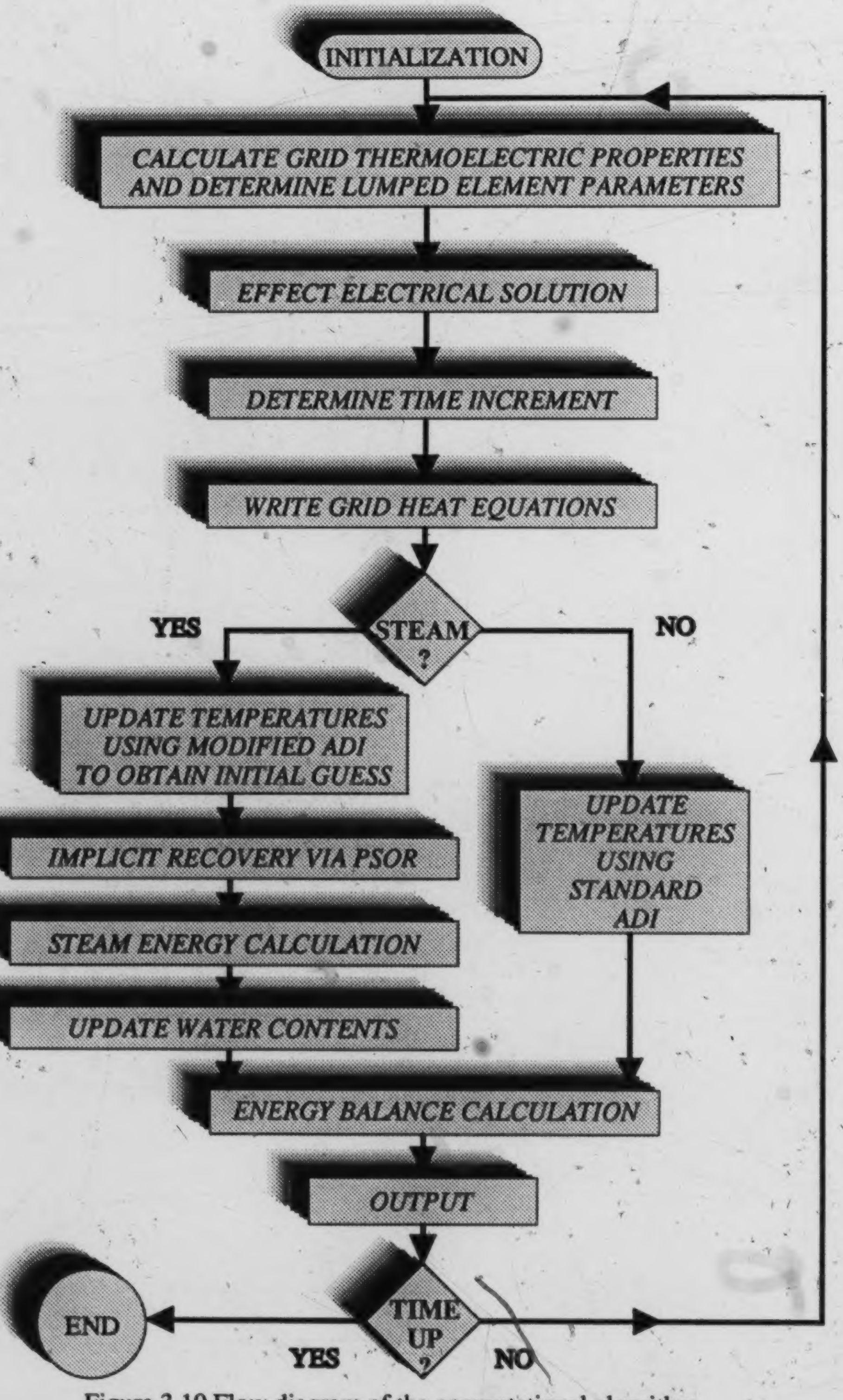
INITIALIZATION
CALCULATE GRID THERMOELECTRIC PROPERTIES AND DETERMINE LUMPED ELEMENT PARAMETERS
EFFECT ELECTRICAL SOLUTION
DETERMINE TIME INCREMENT
WRITE GRID HEAT EQUATIONS
STEAM ?
YES
NO
UPDATE TEMPERATURES USING MODIFIED ADI TO OBTAIN INITIAL GUESS
IMPLICIT RECOVERY VIA PSOR
STEAM ENERGY CALCULATION
UPDATE WATER CONTENTS
UPDATE TEMPERATURES USING STANDARD ADI
ENERGY BALANCE CALCULATION
OUTPUT
TIME UP ?
END
YES
NO

Figure 3.10 Flow diagram of the computational algorithm.

4. Testing and Verification of COPTER

Before the results of COPTER mathematical model solutions could be viewed with a degree of reliability, verification of the complete operation of the COPTER simulator, including the validity of the assumptions on which the solutions are based, was conducted.

4.1 Verification of the Intrinsic Operation of COPTER

COPTER was developed with some initial uncertainty regarding the relative importance of axial electric field components and flowing fluids. The basic operation of the simulator, ignoring the margins of error associated with the uncertainty, had to be deemed reliable before investigations into the uncertainty itself (and subsequently into the complete RF guided wave heating process) could occur. This was accomplished in several ways. Firstly, the employment of ongoing energy balance verifications during the running of the simulations was used, as outlined in equation 4.1:

$$P_{in}^{n}\Delta t_{n} = \sum_{n}\sum_{i,j}\left[S_{i,j}^{n} + M_{VOL_{i,j}}^{n} v_{i,j}(T_{i,j}^{\prime n} - T_{i,j}^{n})\right] \qquad (4.1)$$

where n represents the time step number and P_{in} represents the net input power to the guide, in watts. By cumulatively calculating the total steam energy S in joules and the total temperature rise energy for all the cells, and by comparing the sums of these energies against the cumulative input energy as the simulation progresses, one effectively performs a complete energy throughput analysis on the simulation process. If, during some point in the simulation, equation 4.1 cannot be satisfied to a reasonable extent, it is then apparent that some error in the simulation process (typically an excessively large time step or inadequate numerical precision) has occurred. All of the results and conclusions which are presented in this thesis were drawn from properly energy balanced COPTER simulations. COPTER was also verified against the analytic solutions of various electrical and thermal problems. By performing low frequency, non evaporative simulations in open circuited coaxial geometries, COPTER results could also be compared against the very reliable MEGAERA[23] simulation routine. These comparisons are of some merit, since they indicate that COPTER will reliably simulate the heating of lossy materials in coaxial geometries whenever the absence of axial field components and the lack of fluid movement are absolutely known.

4.2 Verification of the "Steam Disappears" Fluid Flow Approximation

In order to evaluate the validity of the "steam disappears" fluid flow approximation and the performance of the evaporative coding, several experimental RF heating operations were performed. RF power at 14 MHz was applied to a thermally insulated, electrically short, open circuited section of coaxial waveguide, as shown in plate 4.1 and in figure 4.1. The circled numbers in plate 4.1 identify the various components of the experimental apparatus

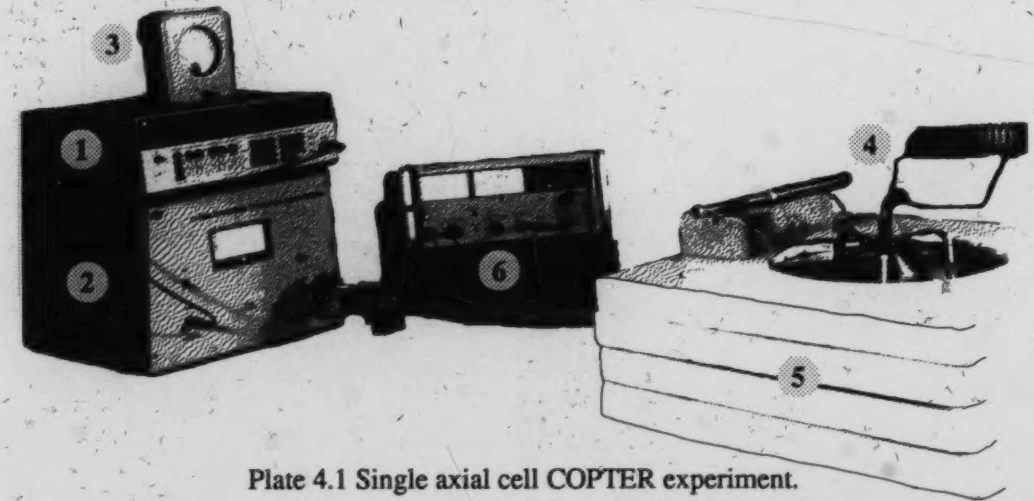

Plate 4.1 Single axial cell COPTER experiment.

	Brine Sand A	Brine Sand B
Sand Porosity (%)	37	37
Sand Density (g/cm^3)	1.56	1.56
Brine Sand Initial Thermal Conductivity (W/m°C)	1.35	1.73
Brine Sand Initial Heat Capacity (J/g°C)	0.83	0.91
Brine Sand Initial Water Saturation (%)	10	20
Brine Sand Initial Density (g/cm^3)	1.60	1.64
Brine Sand Initial Mass Water Content (%)	2.31	4.52
Brine Conductivity @24°C (S/m)	12	3
Brine Sand Initial Conductivity @24°C (S/m)	0.032	0.039
Brine Sand Initial Relative Dielectric Constant @24°C	7	10
Sand Conductivity @24°C (S/m)	$2x10^{-5}$	$2x10^{-5}$
Sand Relative Dielectric Constant @24°C	3	3
Initial Brine Sand Loss Tangent	6	5
Smallest Wavelength (m)	2.8	2.5

Table 4.1 Single axial cell COPTER experiment medium parameters at 14 MHz.

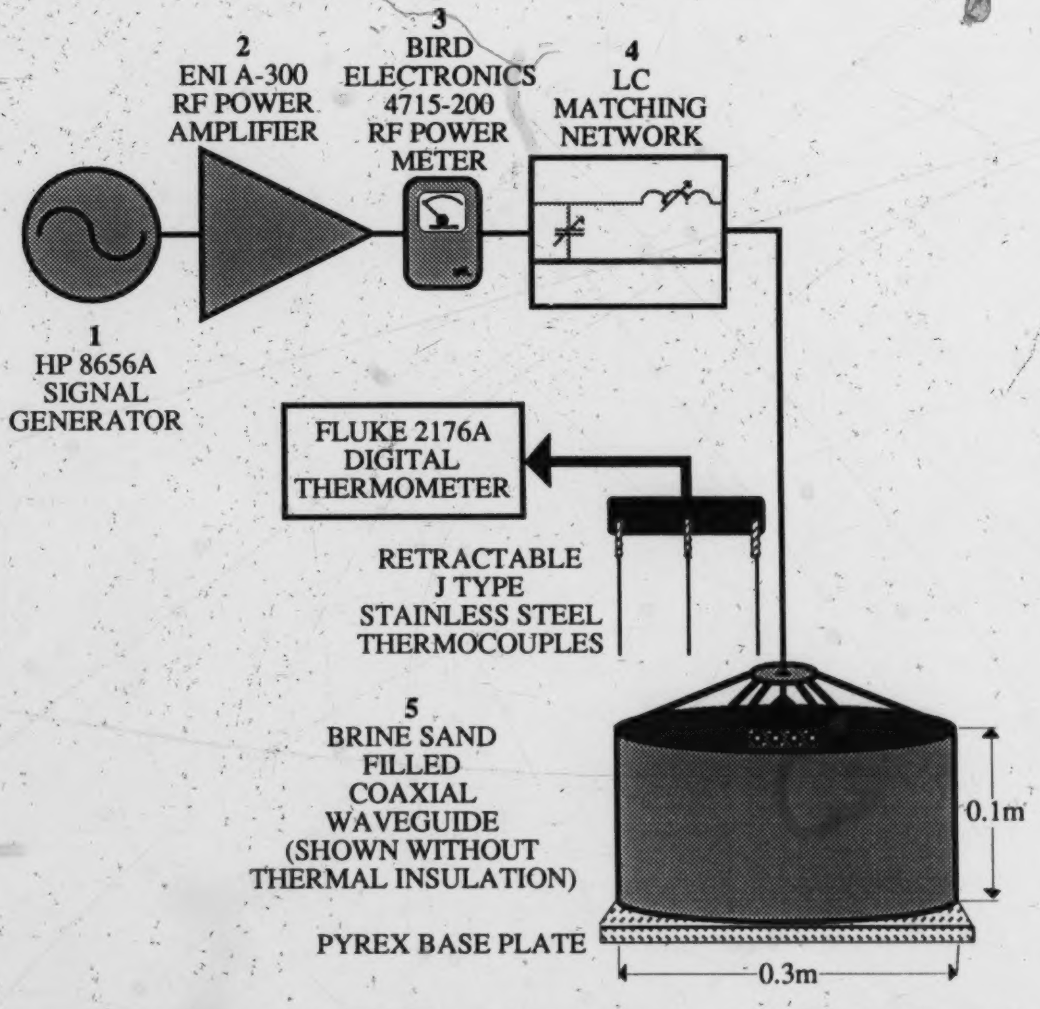
1
HP 8656A
SIGNAL
GENERATOR
2
ENI A-300
RF POWER
AMPLIFIER
3
BIRD
ELECTRONICS
4715-200
RF POWER
METER
4
LC
MATCHING
NETWORK
FLUKE 2176A
DIGITAL
THERMOMETER
RETRACTABLE
J TYPE
STAINLESS STEEL
THERMOCOUPLES
5
BRINE SAND
FILLED
COAXIAL
WAVEGUIDE
(SHOWN WITHOUT
THERMAL INSULATION)
PYREX BASE PLATE
0.1m
0.3m

Figure 4.1 Single axial cell COPTER experimental apparatus. 0.1 m OD, 0.0032 m wall thickness inner conductor is perforated with one 1 mm hole per cm^2 for escaping steam.

in figure 4.1. For purposes of this test the moisture rich material filling the coaxial section was a mixture of sand and brine referred to as brine-sand. Brine-sand was chosen as the lossy medium since it is structurally typical of the earth type materials which would most likely be heated using RF methods. Also, the thermal and electrical properties of brine-sand, as discussed in Appendix B, are easily controlled for modelling purposes. No elaborate preparation procedures are necessary for brine-sand, except that a new mixture should be stored overnight in a sealed container before use so that homogeneity is improved via capillary action of the brine. Two variations of brine-sand were chosen, since different water saturation levels in each brine-sand provided a means of evaluating the importance of water content on the fluid flow approximation. The appropriate parameters for each of these brine-sands are shown in table 4.1. Temperature and input impedance measurements were taken, since these parameters are easily measured, are of practical significance, and provide adequate means of comparison of the experimental results with the results of COPTER simulations.

The experimental procedure warranted special attention due to the dynamic nature of the experiment. Initially, the input impedance of the coaxial waveguide was essentially resistive. The salinity levels of the brine-sands were chosen such that the real components of the input impedances were consistently less than 50 ohms. Matching could therefore be maintained with the common LC technique alone, as illustrated in figure 4.1. As power was continually applied to the brine-sand and a dielectric layer was formed on the inner conductor, a large capacitive component would then dominate the input impedance, with the real component itself becoming smaller. In order to maintain the match, the series inductor of the matching network had to be increased to cancel the capacitive component. Effectively, this series resonant circuit provided the enormous voltage magnification which was necessary to continue to force power into the increasingly reactive load. In the presence of high voltages, complete shielding could not be maintained along the feed apparatus due to persistent arcing between the shielding and the center conductor. Heavy gauge binding post input terminals and teflon insulation, instead of coaxial connectors, prevented dielectric breakdown within the feed apparatus, but the compromise in shielding resulted in large amounts of electromagnetic radiation leaking to the surroundings. Radiation monitoring equipment indicated that field intensity was not hazardous at distances greater than at least 1 m from the waveguide during heating periods, but separate shielding was required for nearby electronic equipment.

Temperature measurement also required special attention. Standard stainless steel thermocouples could not remain in the sand during power application periods. Alcohol based thermometers, on the other hand, can be left within the waveguide as power is applied since they do not perturb the electromagnetic fields, but they do not provide sufficient temperature range. Fiber optic thermometers are also transparent to electromagnetic fields, but were prohibitively expensive for this project. Temperature measurements were attained by installing thin dielectric teflon tubes into the medium at the desired measurement positions. Power was shut down periodically such that stainless steel thermocouples could be inserted into the medium via the teflon tubes and the temperature could be recorded. Matching network adjustments and proper equipment operation were also facilitated by the absence of radiation during these periods.

The input impedance was measured with an HP 4815A RF Vector Impedance Meter (item 6 on plate 4.1) during the power off periods. Because it was difficult to resolve the small real portion of the input impedance in the presence of the capacitive component during later portions of the experiments, special impedance measurement procedures were developed. A number of high quality reference coils were designed in order to cancel the capacitive component of the input impedance, such that the real component could be observed. The resistive and reactive components of these coils were accurately determined using several independent measurement techniques. The real component of the input impedance of the waveguide was obtained by series resonating the waveguide at 14 MHz with an appropriate reference coil and subtracting the coil resistance and the HP 4815A probe resistance from the resulting reading.

As heating continued, larger coils were required to maintain a match in the presence of the increasing capacitive component of the waveguide input impedance. Because the real component of the input impedance would decrease until it became comparable to the resistive drop of the coil, an increasing portion of the applied power was dissipated by the coil. Although this was minimized through optimal coil design procedures, some means of determining the net input power to the waveguide was ultimately necessary. After the impedance components of the matching coils were accurately determined, the net input power was derived from a simple power division calculation made from the real components of the matching coil impedance and the waveguide input impedance. Power dissipation would also occur in the base on which the packed waveguide was placed if the base material was of a lossy nature. A PVC plastic base became deformed from direct heating from the load end fields during preliminary experimental runs. PVC is among many lossy plastics which would provide a significant waveguide real input impedance component with no sand in the waveguide. Pyrex glass was eventually selected as the base material, since it combines virtually lossless electrical characteristics with thermal cycling capabilities.

It has previously been mentioned that the COPTER simulation routine was written under the assumption that all medium boundaries are perfect thermal insulators. As a result, styrofoam insulation was used extensively on all boundaries of the experimental waveguide apparatus. This insulation must not be compromised at any time, including the power off periods. In practise, significant heat flows were difficult to prevent. Ventilation holes in the inner conductor which allowed the escape of steam also resulted in significant heat losses from the interior region of the conductor. Generally, however, if the experiment could be completed in no more than a few hours, experience dictated that it was possible to assume that the insulation was satisfactory for the purposes of simulation.

Because the axial dimension of the open circuited coaxial waveguide was chosen such that it spanned only a small fraction of a wavelength at 14 MHz, the presence of only TEM fields was assured. Since the TEM version of COPTER will reliably simulate problems which involve purely TEM fields with no fluid flow, one may conclude that if TEM COPTER could not predict the heating of these single cell experiments, the performance of the evaporative coding (based on the "steam disappears" fluid flow approximation) must then remain in question. The results of these single cell experiments and the corresponding TEM COPTER simulations are presented in figure 4.2. Figure 4.2a illustrates the simulated input power, which was virtually the same for both brine-sand experiments. This simulation input power was determined by time averaging the net experimental input power over the successive duty cycles which were observed as a result of the power off periods used for temperature measurements and equipment adjustments.

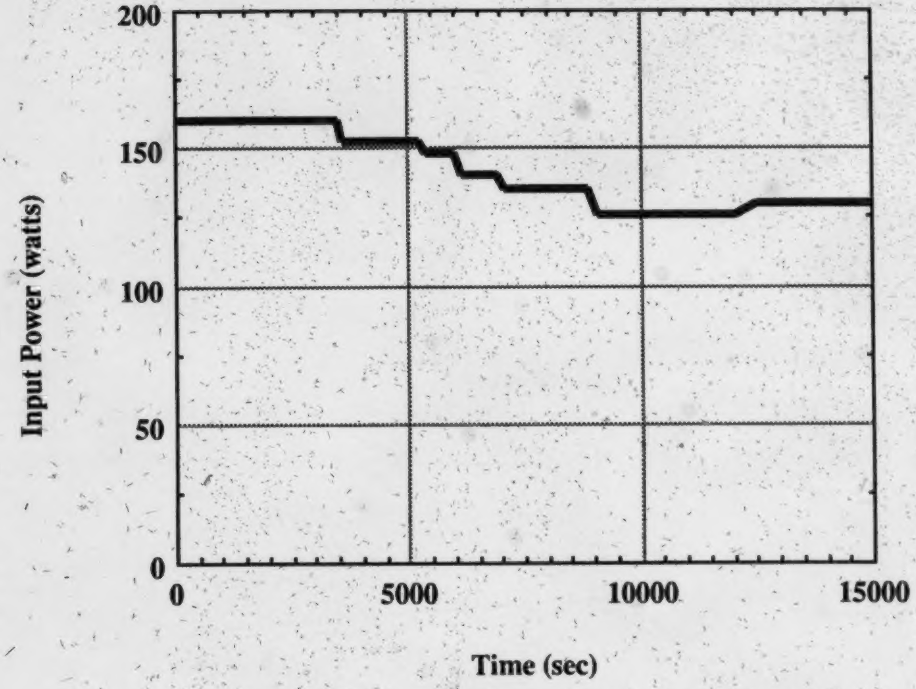

Figure 4.2a Net input power for simulations.

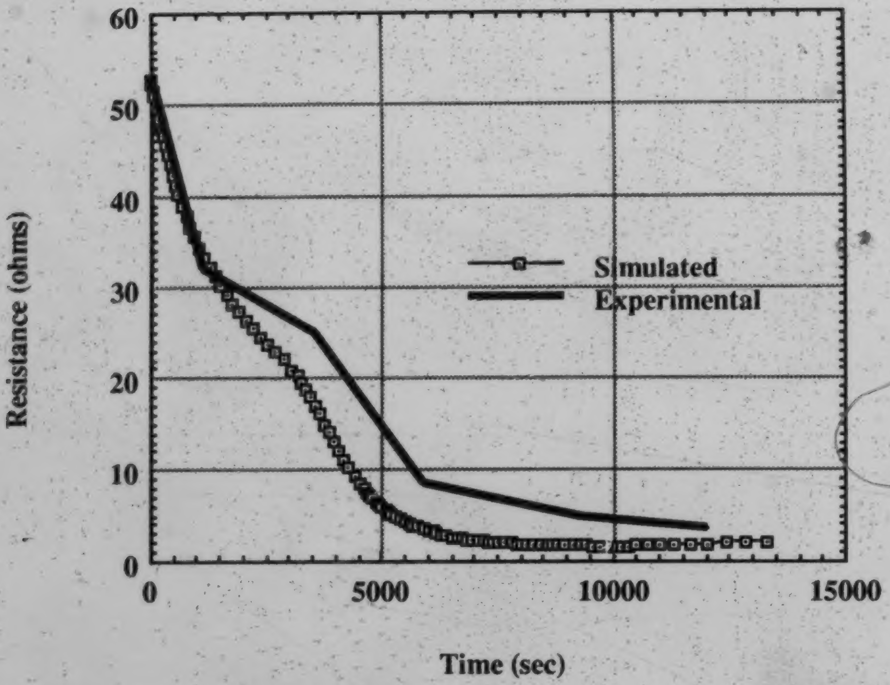

Figure 4.2b Brine sand "A" real component of input impedance.

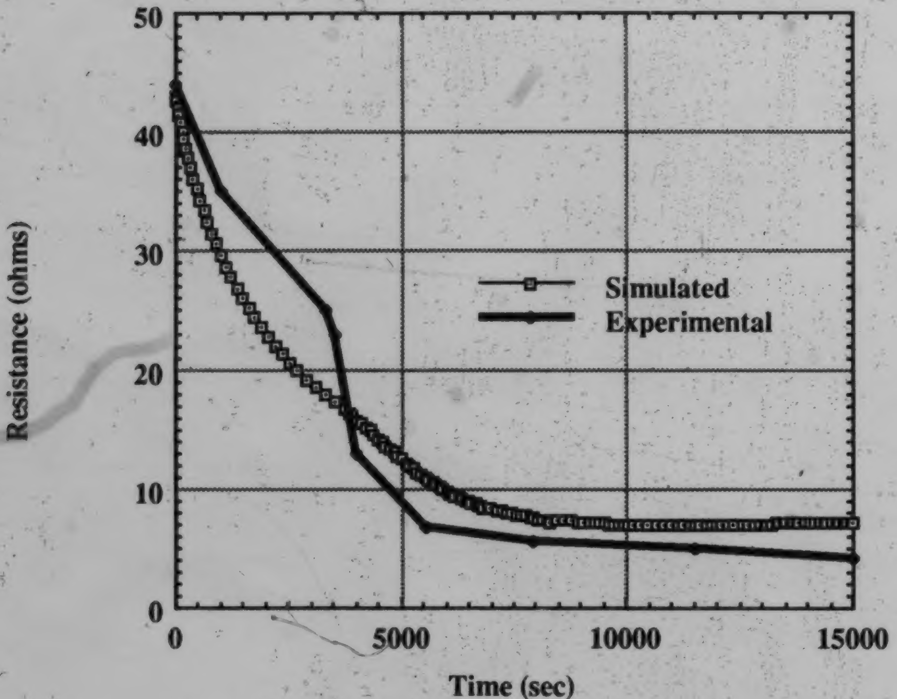

Figure 4.2c Brine sand "B" real component of input impedance.

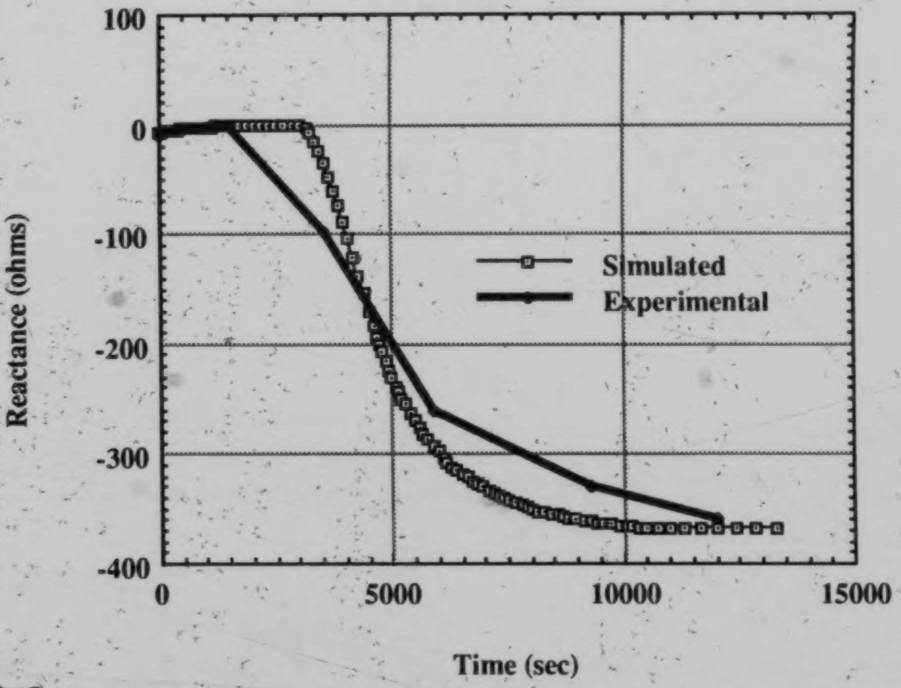

Figure 4.2d Brine sand "A" imaginary component of input impedance.

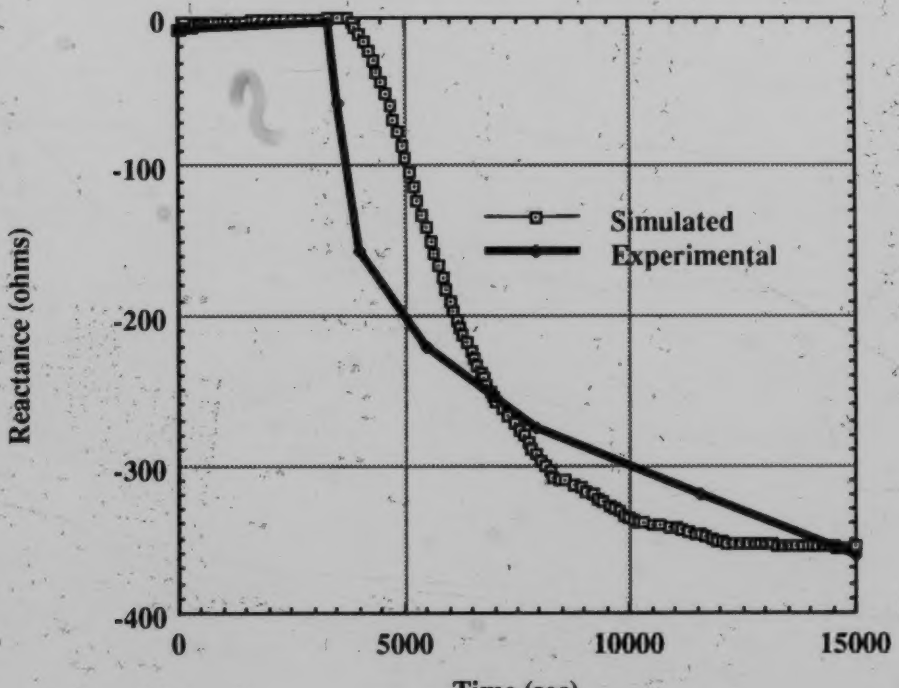

Figure 4.2e Brine sand "B" imaginary component of input impedance.

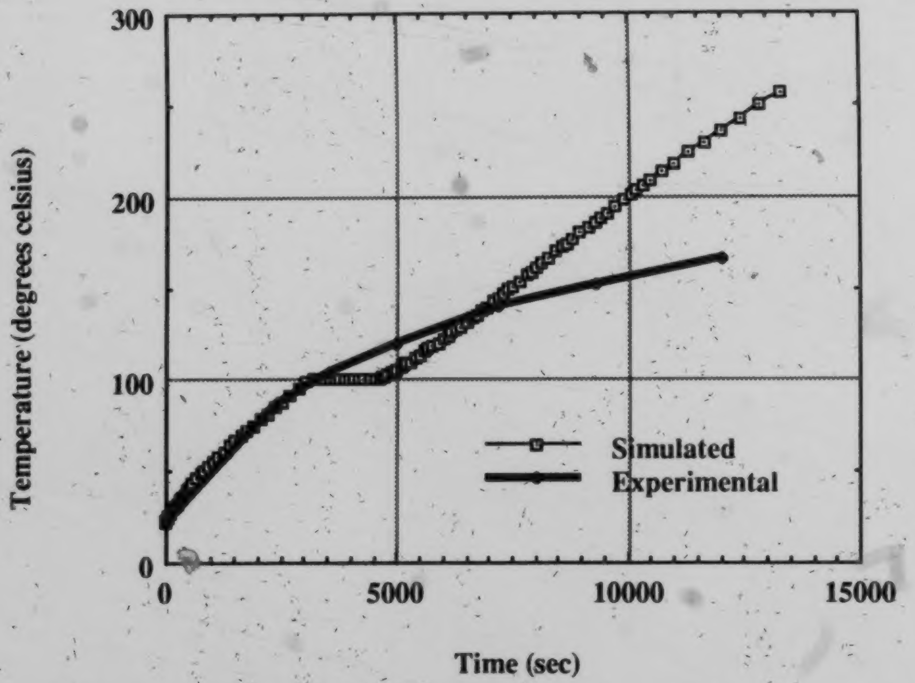

Figure 4.2f Brine sand "A" temperature at inner conductor (r = 0.05 m).

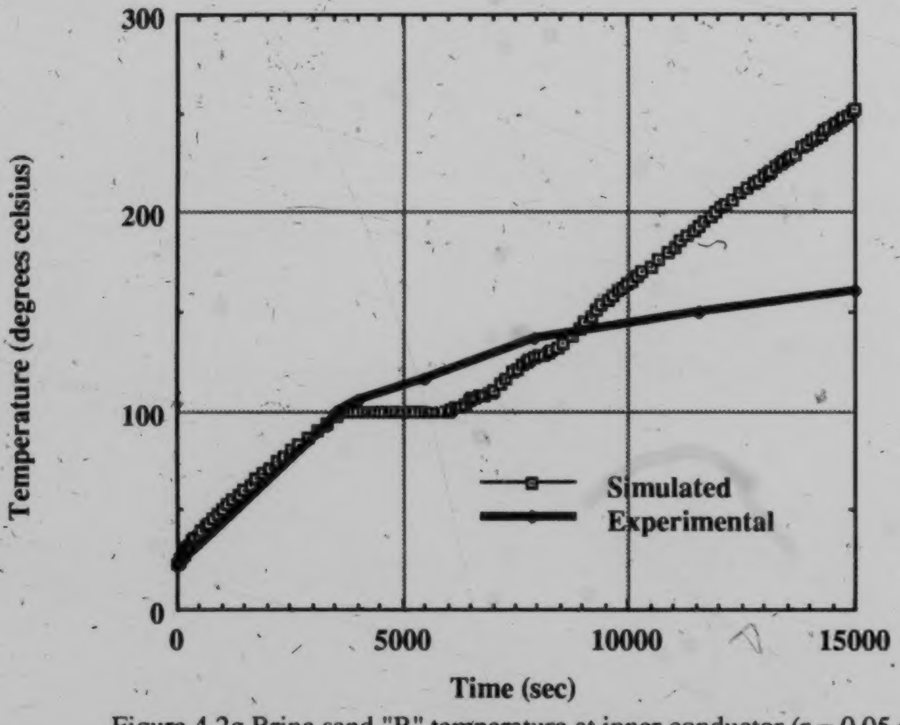

Figure 4.2g Brine sand "B" temperature at inner conductor (r = 0.05 m).

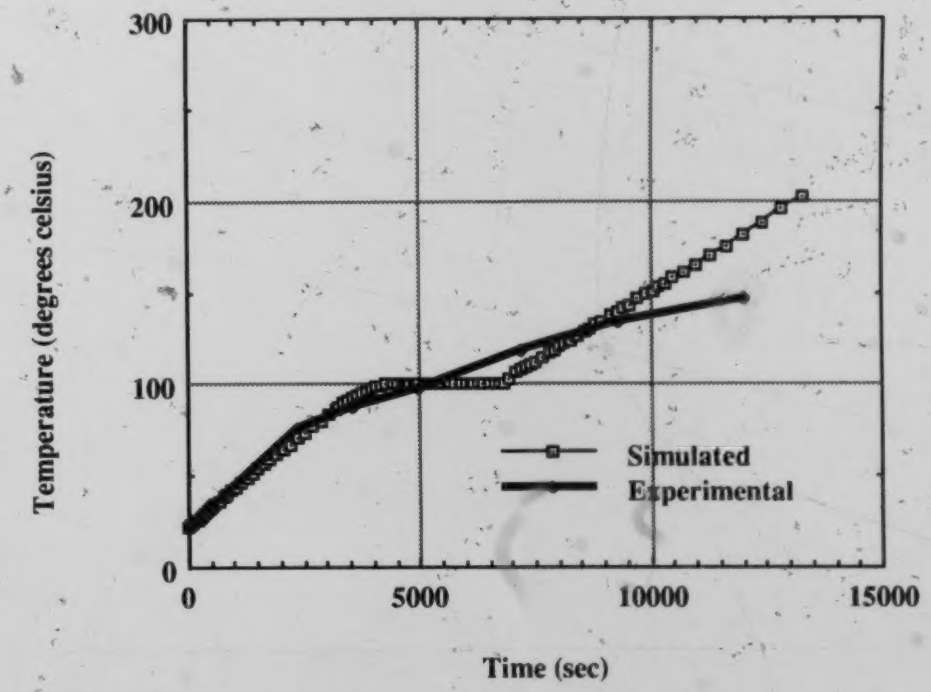

Figure 4.2h Brine sand "A" temperature at midpoint between conductors (r = 0.1 m).

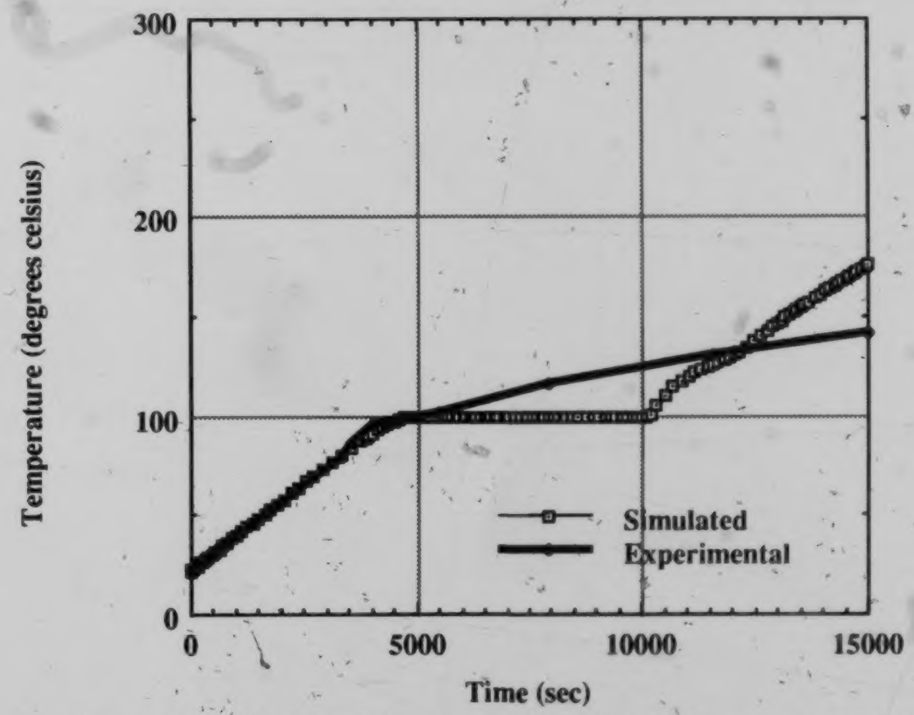

Figure 4.2i Brine sand "B" temperature at midpoint between conductors (r = 0.1 m).

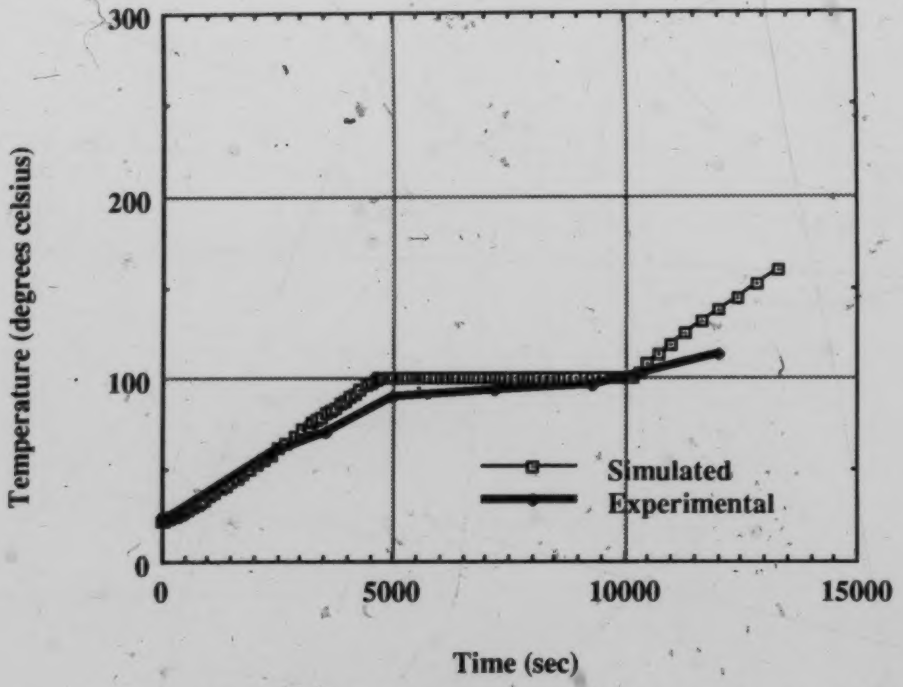

Figure 4.2j Brine sand "A" temperature at outer conductor (r = 0.15 m).

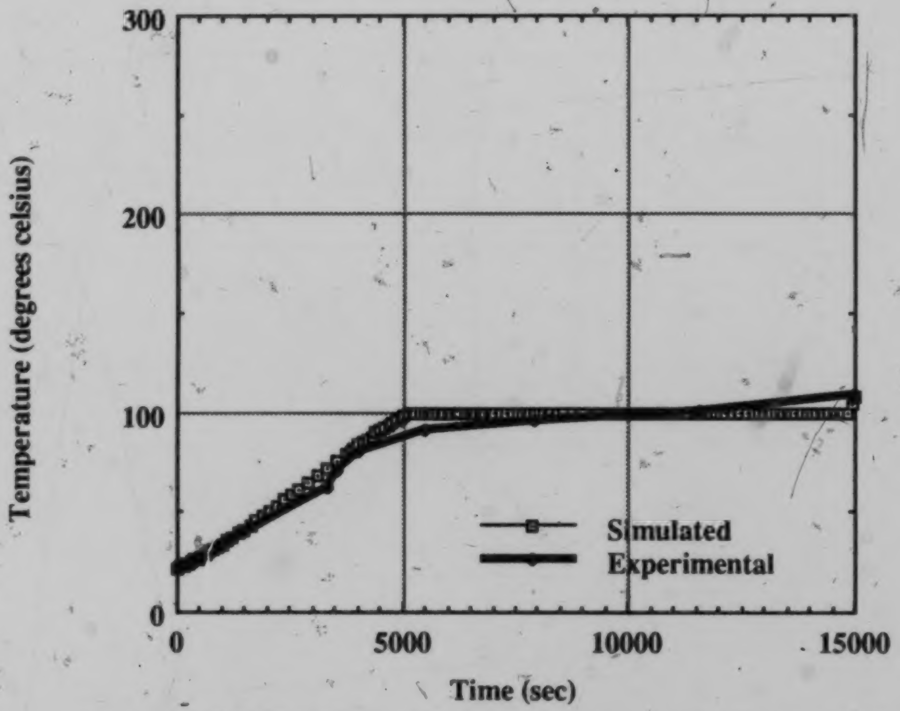

Figure 4.2k Brine sand "B" temperature at outer conductor (r = 0.15 m).

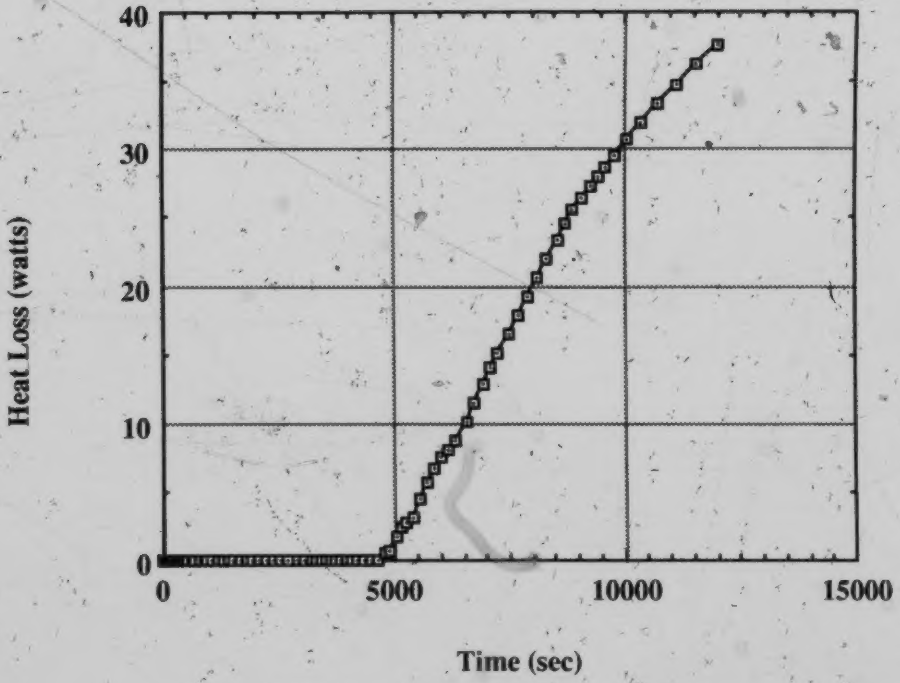

Figure 4.2l Brine sand "A" simulated heat loss to inner conductor.

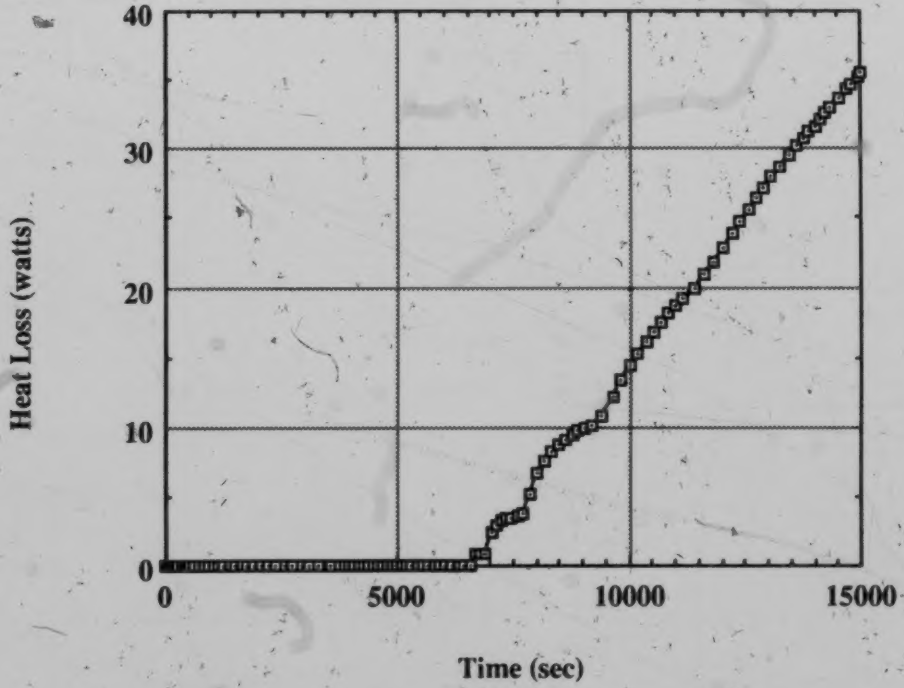

Figure 4.2m Brine sand "B" simulated heat loss to inner conductor.

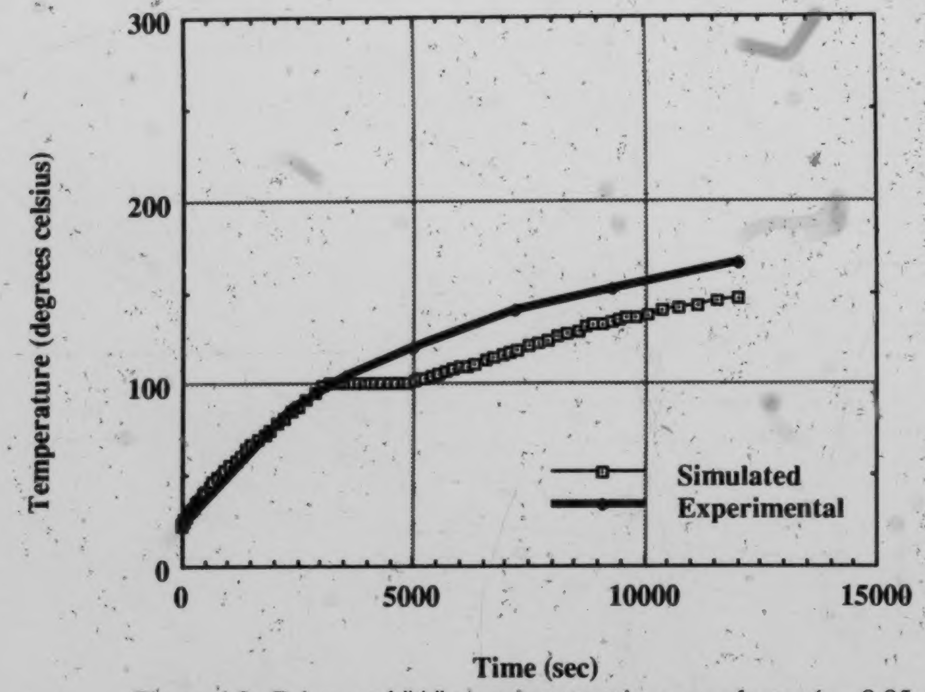

Figure 4.2n Brine sand "A" temperature at inner conductor (r = 0.05 m) with simulated heat loss to inner conductor.

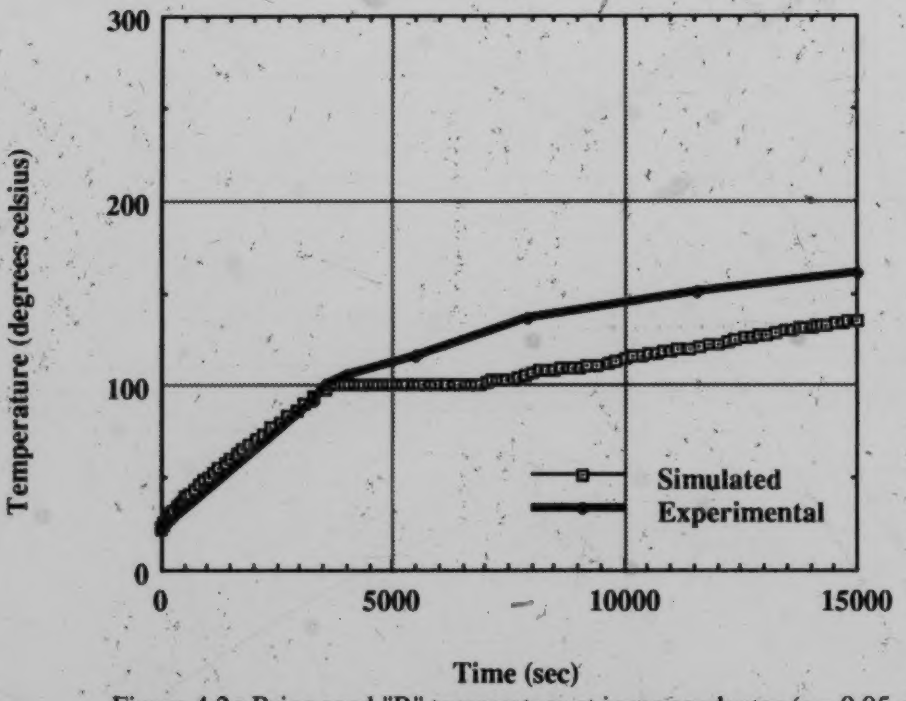

Figure 4.2o Brine sand "B" temperature at inner conductor (r = 0.05 m) with simulated heat loss to inner conductor.

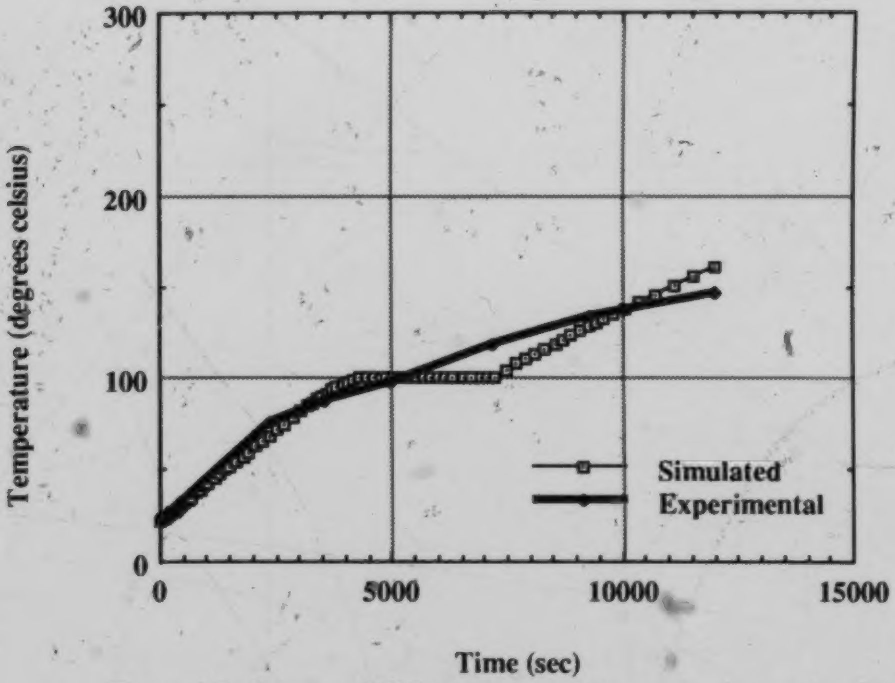

Figure 4.2p Brine sand "A" temperature between conductors (r = 0.1 m) with simulated heat loss to inner conductor.

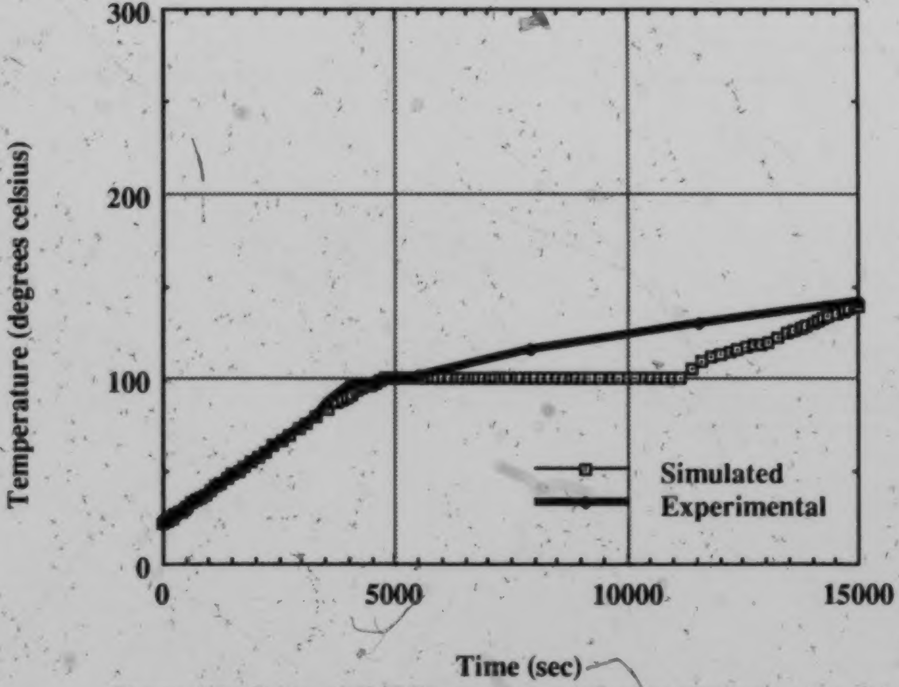

Figure 4.2q Brine sand "B" temperature between conductors (r = 0.1 m) with simulated heat loss to inner conductor.

The results of the single axial cell experiments indicate that the "steam disappears" fluid flow approximation is valid in brine-sand materials with the reasonably low levels of liquid saturation used in the two experiments described above. Discrepancies between the experimental and simulated versions of the real input impedance components (figures 4.2b and 4.2c) can be attributed to the measurement inaccuracies due to the difficult measurement procedure, discussed earlier, which was used while dielectric coatings were formed on the inner conductor. A similar rationale is applied to the discrepancies in the imaginary impedance results of figure 4.2c and 4.2d. In these cases, however, accurate measurements became increasingly difficult once the area near the inner conductor began to dry. Reactive impedance fluctuations of two orders of magnitude would then typically occur within a period of a few minutes, which made the impedance measurements rather sensitive to the measurement times. Nevertheless, general agreement between experimental and simulated results was observed.

Temperature measurements were slightly hampered by the rapid changes which took place when boiling was initiated. Also, evaporation did not occur at a constant temperature. Figures 4.2f and 4.2g display both experimental and simulated inner conductor temperatures as functions of time. Agreement was virtually perfect until evaporation began, which attests to the satisfactory performance of the basic thermal model of COPTER. Differences which then appeared during phase change periods are partly attributed to vapor pressure build up within the heated medium as the boiling point was reached, which would initiate the early migration of fluids out from the sand and into the perforated inner conductor and also result in an increased saturated steam temperature. A reduced fluid presence within the sand as the boiling point was then attained would explain why the experimental temperature did not remain at the boiling point for a longer period of time before rising above it as total drying was achieved. Increased temperature discrepancy appeared in figure 4.2g due to higher initial water concentration and subsequently more mobile fluids. Small errors are inherent in the "steam disappears" approximation because it neglects the pressure build up and the subsequent flow of fluids with the onset of evaporation. An evaporating cell is assumed to remain at the boiling temperature of the brine until enough net energy is transferred into the cell to equal the energy which would mathematically be required to evaporate the brine originally within that cell into an open atmosphere. Finally, as the area near the inner conductor becomes devoid of moisture and reaches still higher temperatures, significant heat losses can be expected due to the increasing temperature gradient between this region and the nearby atmosphere, because of the less than perfect insulating properties at the inner conductor. Temperature results which were taken at the midpoint between the conductors (figures 4.2h and 4.2i) are similarly rationalized, except that the thermal events occur later in time than at the inner conductor, and that less heat loss is evident in the later phases due to the improved insulating properties of the adjacent sand. The final temperature graphs, figures 4.2j and 4.2k, depict the outer conductor temperatures, which were the slowest to reach the boiling point due to the lower current densities in this area. It is likely that the reduced heating activity generated little fluid movement near the outer conductor, as the experimental temperature adhered much more accurately to the fixed boiling temperature of the simulator during the evaporative period. Due to excessively high temperatures which appeared near the inner conductor, it was not possible to observe temperatures at the outer conductor beyond the evaporative phase. Heat loss is noticeable in the results of the single axial cell experiment, but in practical terms, it was not large enough to invalidate the comparisons to the simulated temperatures which were determined assuming perfect thermal insulation. The simulated and experimental temperatures of the more moist brine-sand B require slightly longer to reach the same temperatures as brine-sand A due to the increased heat capacity of brine-sand B resulting from the extra moisture contained within brine-sand B.

As a preliminary means of modelling the loss of heat from the inner conductor, additional simulation was performed with manually programmed heat loss to the inner conductor occurring as shown in figures 4.2l and 4.2m. The inner conductor was the least insulated medium boundary and displayed the highest temperature gradient to the outer atmosphere which justifies the assumption that heat loss to the inner conductor accounted for most of the total heat loss. The programmed heat loss was chosen to become increasingly significant at higher temperatures just as it did experimentally. The resulting inner conductor temperature graphs of figures 4.2n and 4.2o indicate better agreement between experimental and simulated temperatures during later stages of heating. The middle temperature plots of figures 4.2p and 4.2q display somewhat improved agreement since the simulated heat loss at the inner conductor had less effect at the middle location.

Less formal testing has indicated that for the same approximate power input levels, COPTER was less capable of predicting the results of experiments which involved initial water saturation levels of 35 % or greater. In these cases, it was observed that COPTER would consistently predict the correct temperatures and input impedances only until the temperature at the inner conductor reached the boiling point. COPTER would then predict a decoupling (dried insulating layer near the inner conductor and a subsequently capacitive input impedance) which occurred much earlier in time than what was observed experimentally.

During one experimental run which was conducted with an initial water saturation level of 100 %, it was observed that the entire medium seemed to lose water uniformly during the initial portions of the evaporation. Moisture and temperature gradients in the radial direction appeared only after most of the moisture had uniformly evaporated. This is in contrast to the very obvious radial moisture gradients which were observed during the evaporative phases of the 10 % and 20 % water saturation cases.

Based on these events, it is postulated that the radially inward flow of liquid does occur to varying extents during the evaporative phases of all but the initially dryest experiments. Unless the level of water saturation is low enough such that the attractive forces between the sand grains and the water molecules exceed the driving pressures of evaporation, it is thought that upon evaporation of water near the inner electrode, the highly conductive brine from more remote regions moves radially inwards towards the inner conductor, thus replenishing with liquid the drying area near the inner conductor. This, in turn, maintains a resistive electrical input impedance for a longer period of time. As an aside, a special version of the 20 % water saturation brine-sand experiment was devised in order to qualitatively examine the presence of the radial liquid flow phenomenon. The 20 % water saturation experiment was conducted as before, except that power was removed at 4260 seconds - immediately after decoupling was first observed. From that point in time onward, the input impedance to the electrically short coaxial section was carefully monitored. If radial liquid flow was occurring, it would continue long enough after the power was removed such that some indication of recoupling would then be provided. The results of this experiment are presented in figure 4.3.

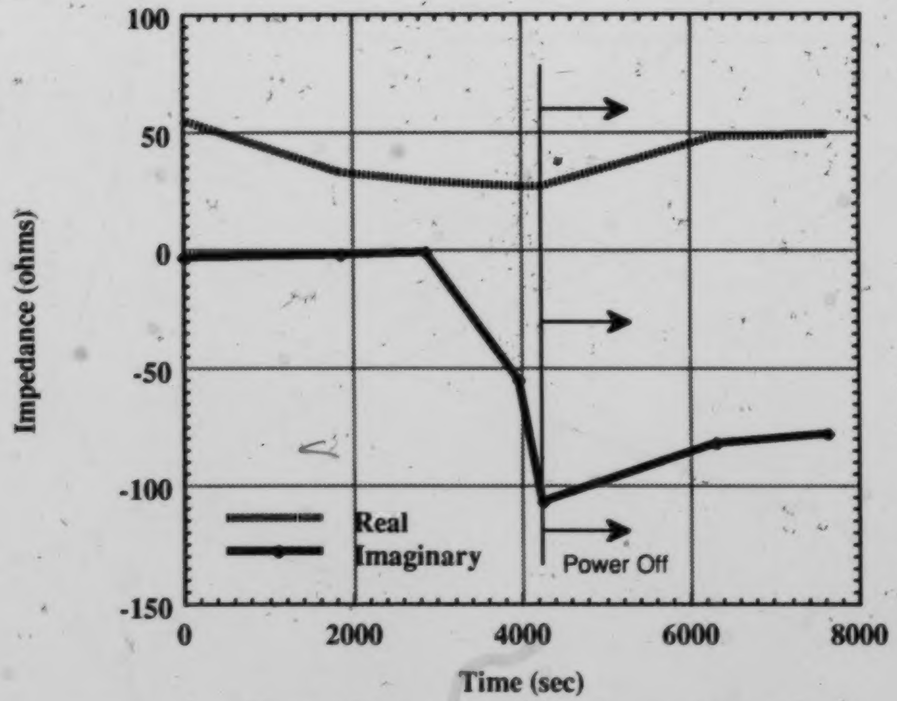

Figure 4.3 Input impedances of power down test.

Recoupling is clearly indicated by the decreasingly capacitive input impedance which is apparent in figure 4.3 after the power was removed. Because of the radially inward flow of liquid which was occurring under the pressure of the phase change even after the power was removed, and due to gravity to a lesser extent, replenishment of the drying medium near the inner conductor was occurring. This phenomenon was observed in the 10 % water saturation cases as well, but to a substantially lesser degree. Nevertheless, COPTER, using the "steam disappears" approximation, is capable of simulating the results of both the 20 % and the 10 % water saturation experiments to a reasonable degree of accuracy. In reality, the water does not simply change to steam and then "disappear" through the pores of the sand without resulting in any liquid flow, but it is obvious that some radial flow may exist without negating the validity of the "steam disappears" fluid flow assumption. It is believed that if sufficient power is applied to the initially evaporating medium under the presence of subsequently radially flowing liquids, the liquids are in fact driven off to steam more quickly than they can effect recoupling at the inner conductor.

The results of the single axial cell COPTER experiment indicate that under certain conditions, the "steam disappears" fluid flow assumption is a valid means of simulating the fluid flows which occur during the heating of porous, water wet, lossy materials. These conditions state that *the connate water content within the material must be low enough such that evaporatively driven liquid flow does not occur to a significant extent. If the medium moisture level is high enough to facilitate fluid flow under the pressures of fluid evaporation, then the "steam disappears" assumption may still be employed if the liquid is evaporated more quickly than it can perpetuate the flow.* For the power densities which were applied to the brine-sand in the single axial cell COPTER experiments, the "steam disappears" approximation will maintain its validity for water saturation levels to approximately 20 %. In many practical oil sand situations, the water saturation level is low enough that the "steam disappears" approximation should be valid.

4.3 Comparison of TM COPTER and TEM COPTER

The results of the TEM experiment (Appendix A) indicate that in many cirrcumstances significant axial fields will be present during the guided wave heating process. For many of the various permutations of heating scenarios which one may wish to consider, the onset of the dried dielectric conductor coatings, which cause the axial fields to appear, is a virtual certainty. The use of a purely TEM electrical solver, for the wide variety of operating conditions that would be required of a commercial version of COPTER, is questionable.

4.3.1 TM COPTER

As mentioned in the Chapter 1, a version of the COPTER routine, TM COPTER, was developed with fully generalized electromagnetic field solution capabilities for the coaxial geometry. Essentially, the TEM ladder electrical solution coding in TEM COPTER was replaced with a full finite difference field solution code, based on the program HERZ[24].

HERZ solves the general electromagnetic problem within a coaxial geometry based on a finite difference approximation, for the azimuthal component of the phasor magnetic field intensity H_ϕ, and for the radial and axial phasor electric field components E_r and E_z.

The electromagnetic problem solution begins with equation 2.3 in integral form:

$$\oint \mathbf{E}\bullet\mathbf{dl} = -j\omega\mu\int_{\mathbf{s}} \mathbf{H}\bullet\mathbf{ds} \qquad (4.2)$$

Using this equation as indicated in figure 4.4, one first performs a line integration with the electric fields which are along the boundary of the arbitrary cell i,j, and a surface integral on the surface "S" with the magnetic field contained within the boundary.

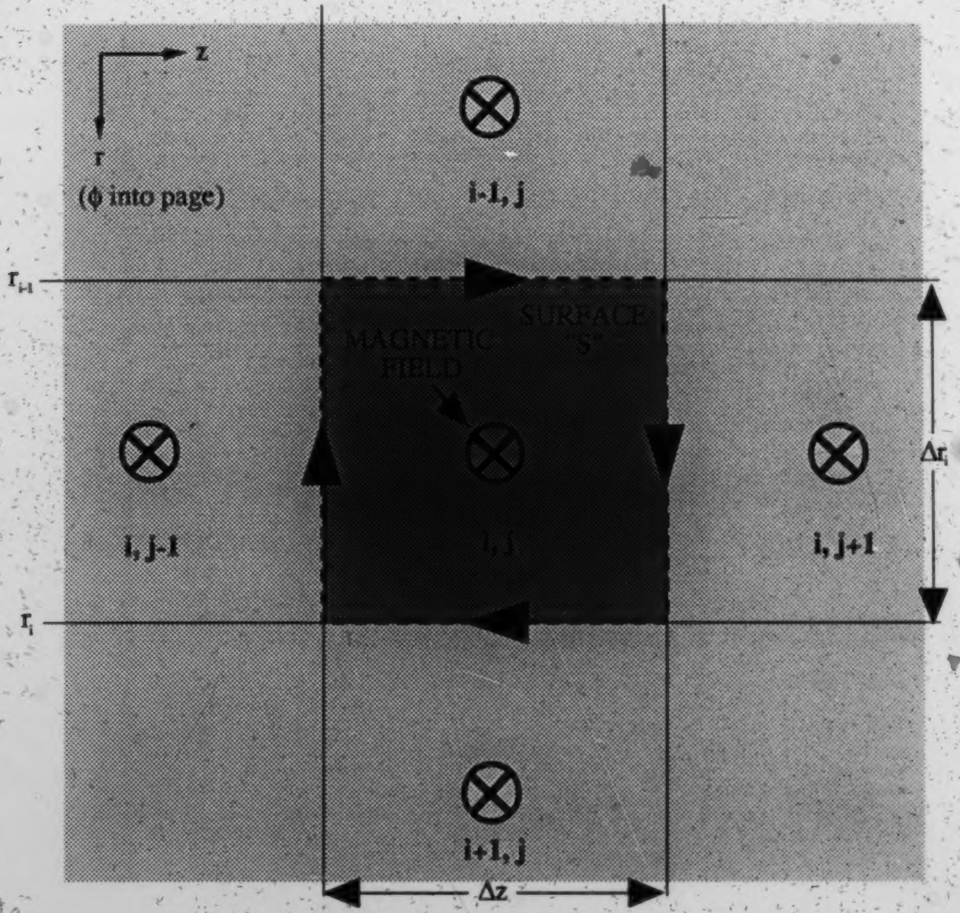

Figure 4.4 Electromagnetic fields in simulation cell.

$$
\begin{aligned}
&E_{r_{i,j+\frac{1}{2}}}\Delta r_i - E_{z_{i+\frac{1}{2},j}}\Delta z - E_{r_{i,j-\frac{1}{2}}}\Delta r_i + E_{z_{i-\frac{1}{2},j}}\Delta z \\
&= -j\omega\mu H_{\phi_{i,j}}\Delta r_i \Delta z
\end{aligned}
\tag{4.3}
$$

Equation 2.4 in integral form becomes:

$$\oint \mathbf{H} \bullet \mathbf{dl} = \int_{S} (\sigma + j\omega\varepsilon)\mathbf{E} \bullet \mathbf{ds} \tag{4.4}$$

From this equation, a line integral of the azimuthal magnetic field is performed around the perimeter of the surface "S" shown in figure 4.5, followed by a surface integral with the axial electric field on the surface "S".

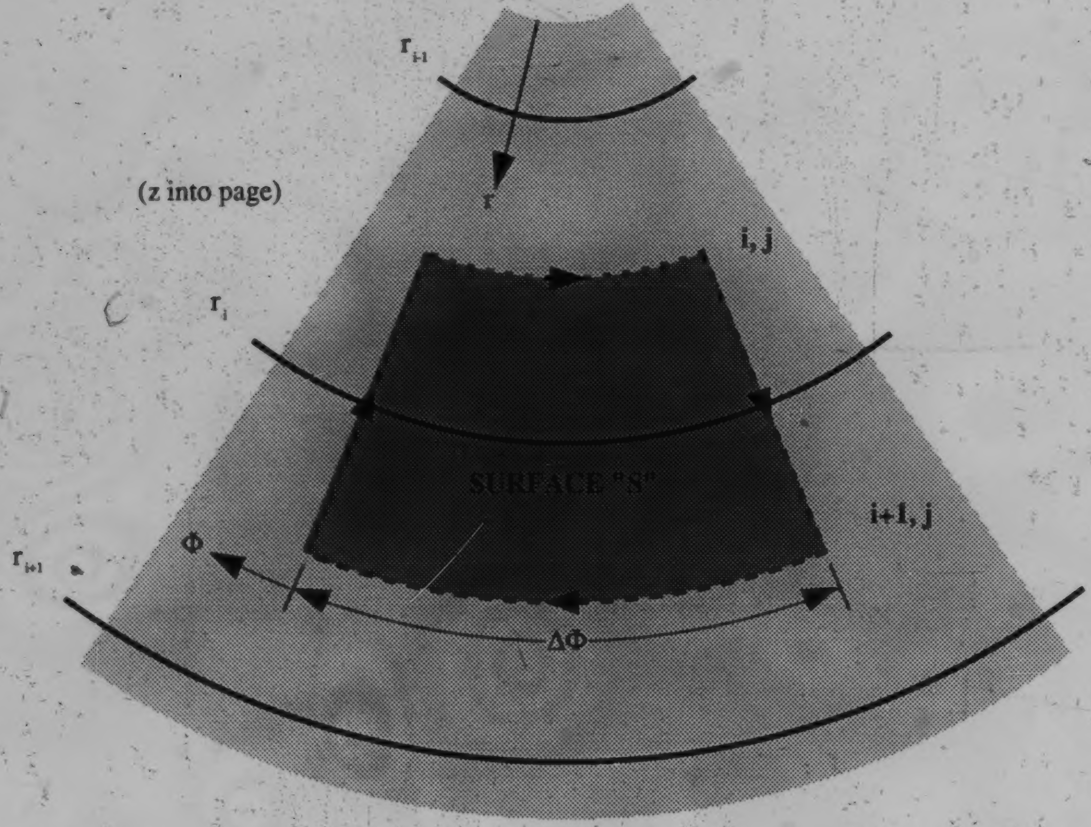

Figure 4.5 Simulation cell as viewed from termination end.

$$
\begin{aligned}
&H_{\phi_{i+1,j}}\left[\frac{r_{i+1}+r_i}{2}\right]\Delta\phi - H_{\phi_{i,j}}\left[\frac{r_i+r_{i-1}}{2}\right]\Delta\phi \\
&=(\sigma_{i,j}+j\omega\varepsilon_{i,j})E_{z_{i+\frac{1}{2},j}}\left[r_i^2-\left(\frac{r_i+r_{i-1}}{2}\right)^2\right]\frac{\Delta\phi}{2} \\
&+(\sigma_{i+1,j}+j\omega\varepsilon_{i+1,j})E_{z_{i+\frac{1}{2},j}}\left[\left(\frac{r_i+r_{i+1}}{2}\right)^2-r_i^2\right]\frac{\Delta\phi}{2}
\end{aligned}
\qquad (4.5)
$$

Moving radially inward to the next cell, the same operation is performed.

$$
\begin{aligned}
&H_{\phi_{i,j}}\left[\frac{r_i+r_{i-1}}{2}\right]\Delta\phi - H_{\phi_{i-1,j}}\left[\frac{r_{i-1}+r_{i-2}}{2}\right]\Delta\phi \\
&=(\sigma_{i-1,j}+j\omega\varepsilon_{i-1,j})E_{z_{i-\frac{1}{2},j}}\left[r_{i-1}^2-\left(\frac{r_{i-1}+r_{i-2}}{2}\right)^2\right]\frac{\Delta\phi}{2} \\
&+(\sigma_{i,j}+j\omega\varepsilon_{i,j})E_{z_{i-\frac{1}{2},j}}\left[\left(\frac{r_i+r_{i-1}}{2}\right)^2-r_{i-1}^2\right]\frac{\Delta\phi}{2}
\end{aligned}
\qquad (4.6)
$$

The surface in figure 4.6 is also subjected to line and surface integration according to equation 4.4.

$$
\begin{aligned}
&H_{\phi_{i,j}}\left[\frac{r_i+r_{i-1}}{2}\right]\Delta\phi - H_{\phi_{i,j+1}}\left[\frac{r_i+r_{i-1}}{2}\right]\Delta\phi \\
&=(\sigma_{i,j}+j\omega\varepsilon_{i,j})E_{r_{i,j+\frac{1}{2}}}\left[\frac{r_i+r_{i-1}}{2}\right]\frac{\Delta\phi\,\Delta z}{2} \\
&+(\sigma_{i,j+1}+j\omega\varepsilon_{i,j+1})E_{r_{i,j+\frac{1}{2}}}\left[\frac{r_i+r_{i-1}}{2}\right]\frac{\Delta\phi\,\Delta z}{2}
\end{aligned}
\qquad (4.7)
$$

Once again, this operation is also performed on the next cell to the right in the axial direction.

$$
\begin{aligned}
&H_{\phi_{i,j-1}}\left[\frac{r_i+r_{i-1}}{2}\right]\Delta\phi - H_{\phi_{i,j}}\left[\frac{r_i+r_{i-1}}{2}\right]\Delta\phi \\
&=(\sigma_{i,j-1}+j\omega\varepsilon_{i,j-1})E_{r_{i,j-\frac{1}{2}}}\left[\frac{r_i+r_{i-1}}{2}\right]\frac{\Delta\phi\,\Delta z}{2} \\
&+(\sigma_{i,j}+j\omega\varepsilon_{i,j})E_{r_{i,j-\frac{1}{2}}}\left[\frac{r_i+r_{i-1}}{2}\right]\frac{\Delta\phi\,\Delta z}{2}
\end{aligned}
\qquad (4.8)
$$

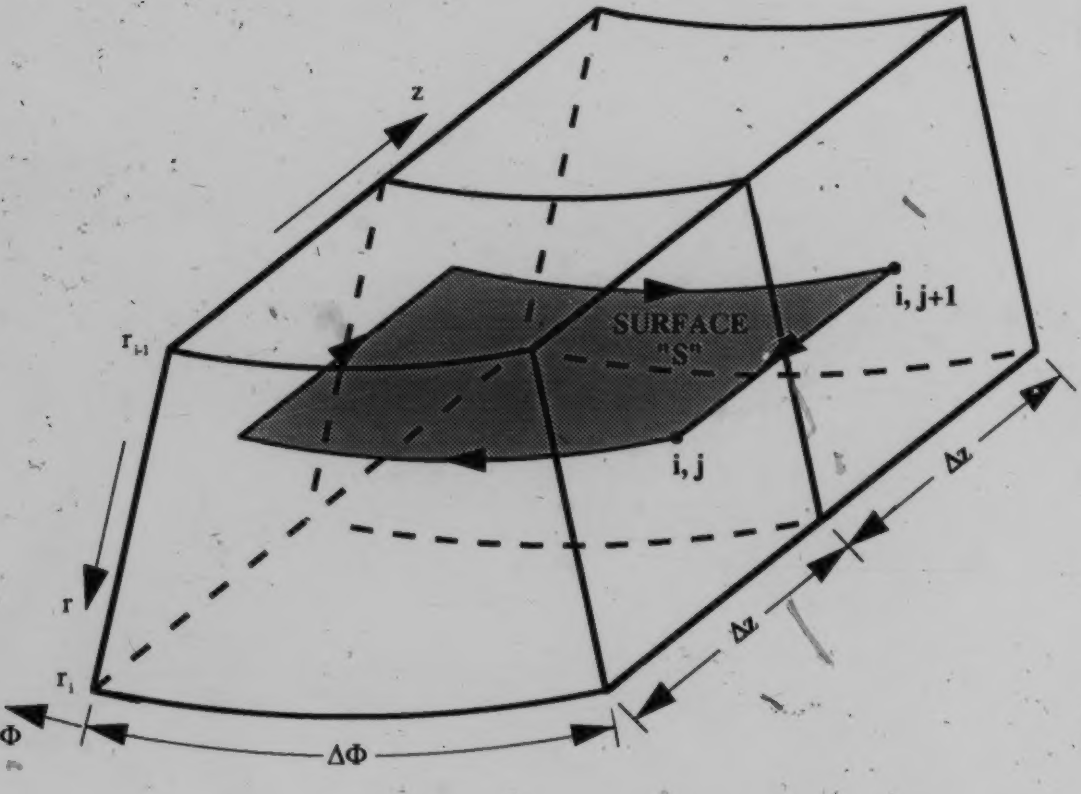
z
r_{i-1}
SURFACE "S"
i, j+1
i, j
r
r_i
Φ
ΔΦ
Δz
Δz

Figure 4.6 Simulation cell in three dimensions as viewed from termination end.

Equations 4.5 to 4.8 inclusive are then substituted into equation 4.4 in order to eliminate the electric field terms. The resulting equation is the electrical analog of equation 3.5.

$$\begin{aligned} &A_{i,j}H_{\phi_{i,j}} + B_{i,j}H_{\phi_{i-1,j}} + C_{i,j}H_{\phi_{i+1,j}} + D_{i,j}H_{\phi_{i,j-1}} \\ &+E_{i,j}H_{\phi_{i,j+1}} = 0 \end{aligned} \tag{4.9}$$

where

$$\begin{aligned} A_{i,j} = &\frac{2\Delta r_i}{\Delta z(\sigma_{i,j} + j\omega\varepsilon_{i,j} + \sigma_{i,j+1} + j\omega\varepsilon_{i,j+1})} \\ &- \frac{(r_i + r_{i-1})\Delta z}{(\sigma_{i,j} + j\omega\varepsilon_{i,j})\left[r_i^2 - \left(\frac{r_i + r_{i-1}}{2}\right)^2\right] + (\sigma_{i+1,j} + j\omega\varepsilon_{i+1,j})\left[\left(\frac{r_i + r_{i+1}}{2}\right)^2 - r_i^2\right]} \\ &+ \frac{2\Delta r_i}{\Delta z(\sigma_{i,j} + j\omega\varepsilon_{i,j} + \sigma_{i,j-1} + j\omega\varepsilon_{i,j-1})} \\ &- \frac{(r_i + r_{i-1})\Delta z}{(\sigma_{i-1,j} + j\omega\varepsilon_{i-1,j})\left[r_{i-1}^2 - \left(\frac{r_{i-1} + r_{i-2}}{2}\right)^2\right] + (\sigma_{i,j} + j\omega\varepsilon_{i,j})\left[\left(\frac{r_i + r_{i-1}}{2}\right)^2 - r_{i-1}^2\right]} \\ &+ j\omega\mu\,\Delta r_i\Delta z \end{aligned}$$

$$B_{i,j} = \frac{(r_{i-1} + r_{i-2})\Delta z}{(\sigma_{i-1,j} + j\omega\varepsilon_{i-1,j})\left[r_{i-1}^2 - \left(\frac{r_{i-1} + r_{i-2}}{2}\right)^2\right] + (\sigma_{i,j} + j\omega\varepsilon_{i,j})\left[\left(\frac{r_i + r_{i-1}}{2}\right)^2 - r_{i-1}^2\right]}$$

$$C_{i,j} = \frac{(r_i + r_{i+1})\Delta z}{(\sigma_{i,j} + j\omega\varepsilon_{i,j})\left[r_i^2 - \left(\frac{r_i + r_{i-1}}{2}\right)^2\right] + (\sigma_{i+1,j} + j\omega\varepsilon_{i+1,j})\left[\left(\frac{r_i + r_{i+1}}{2}\right)^2 - r_i^2\right]}$$

$$D_{i,j} = \frac{-2\Delta r_i}{\Delta z(\sigma_{i,j} + j\omega\varepsilon_{i,j} + \sigma_{i,j-1} + j\omega\varepsilon_{i,j-1})}$$

$$E_{i,j} = \frac{-2\Delta r_i}{\Delta z(\sigma_{i,j} + j\omega\varepsilon_{i,j} + \sigma_{i,j+1} + j\omega\varepsilon_{i,j+1})}$$

Writing equation 4.9 for each cell results in the formation of a complex linear system of equations. HERZ[24] determines the electromagnetic field values within the coaxial boundary during each time step by solving this system. The electric field values at the centers of the cells are determined by a simple averaging of the electric fields on the cell boundaries. Assuming rms field quantities, computation of volumetric cell powers then becomes:

$$Q_{i,j} = \sigma_{i,j}|E_z|^2 + \sigma_{i,j}|E_r|^2 \tag{4.10}$$

Grid selection rules are unchanged from TEM COPTER, except that radial grid dimensioning must be chosen with at least twice the resolution of the TEM COPTER requirements. *Several days of continuous run time* are usually required for TM COPTER simulations on current state of the art Macintosh equipment, due to the increased number of cells, and to the additional run time of the full electrical solver.

4.3.2 Numerical Comparison

In order to examine the range of validity of the TEM approximation under practical circumstances, the TEM and TM electrical solver versions of COPTER were both employed to simulate the RF heating of several brine-sands in an open circuited coaxial waveguide at 100 MHz, with each brine-sand exhibiting different electrical conductivities. According to the results of the TEM experiment, the presence of the axial fields which would appear in lossy materials as a result of dielectric conductor coating is influenced by varying the value of the initial electrical conductivity of the materials. Both versions of COPTER were first used to simulate the full heating process of a low loss brine-sand. The initial conductivity of the sand was then progressively increased by increasing the brine salinity of the sand, and the simulations were repeated with the changed conductivity levels. For the sand with the lowest initial conductivity, no axial fields were expected to develop in the sand for the duration of the procedure, according to the results of the TEM experiment (Appendix A). Conversely, for the highest initial conductivity sand, strong axial fields were expected to be present in the sand throughout most of the heating cycle. By comparing the results of the TEM COPTER and the TM COPTER simulations for each of the initial conductivity cases, a practical evaluation of the TEM approximation was possible. The simulation parameters, including the physical dimensions of the waveguide, and the properties of the brine-sand, are given in table 4.2. These simulation parameters were selected to closely coincide with actual experimental heating scenarios, such as those performed by McPherson[14].

Frequency of Operation (MHz)	100
Power Level (W)	800
Load	Open Circuit
Coaxial Waveguide Length (m)	0.91
Coaxial Waveguide Diameter (m)	0.30
Inner Conductor Diameter (m)	0.0095
Brine Sand Initial Density (g/cm^3)	1.62
Brine Sand Initial Mass Water Content (%)	4.15
Brine Sand Initial Relative Dielectric Constant @24°C	5.8
Sand Conductivity (S/m)	2×10^{-5}
Sand Relative Dielectric Constant	3

Table 4.2 Simulated medium parameters for TEM assumption examination simulations.

Operating frequency and guide length were chosen so that the guide was electrically long, thus not constraining the fields to only TEM as in an electrically short case. The results of the simulations are given in figure 4.7. Sporadic wet spots which appear in radially spaced groups reflect inaccuracy which is inherent in the plotting software and should not be interpreted as results of the simulations.

As illustrated in figures 4.7a and 4.7b, both versions of COPTER predict the same simulated mass percent water content results after 15000 seconds of heating. Initial conductivity was 0.00205 S/m for this case, while initial wavelength was 1.24 m. Clearly, the effect of any axial electric field components is negligible during this low loss heating test. Here, the TEM approximation is entirely adequate even though the initial and observed final wavelengths indicate that the waveguide was at no time electrically short. This is also true for the case in which the initial conductivity was raised to 0.0205 S/m with an initial wavelength of 1.19 m, as shown in figures 4.7c and 4.7d. As simulations were performed with still higher initial conductivities, however, one begins to notice some discrepancy. Figures 4.7e and 4.7f depict the results of a case with conductivity initially at 0.052 S/m, and an initial wavelength of approximately 1.03 m. Here, the TEM result depicts the usual standing wave moisture pattern, which is due to the non uniform heating resulting from an analogous

Figure 4.7a TEM COPTER simulation mass percent water content vs. position.
Initial conductivity = 0.00205 S/m. Time = 15000 sec.

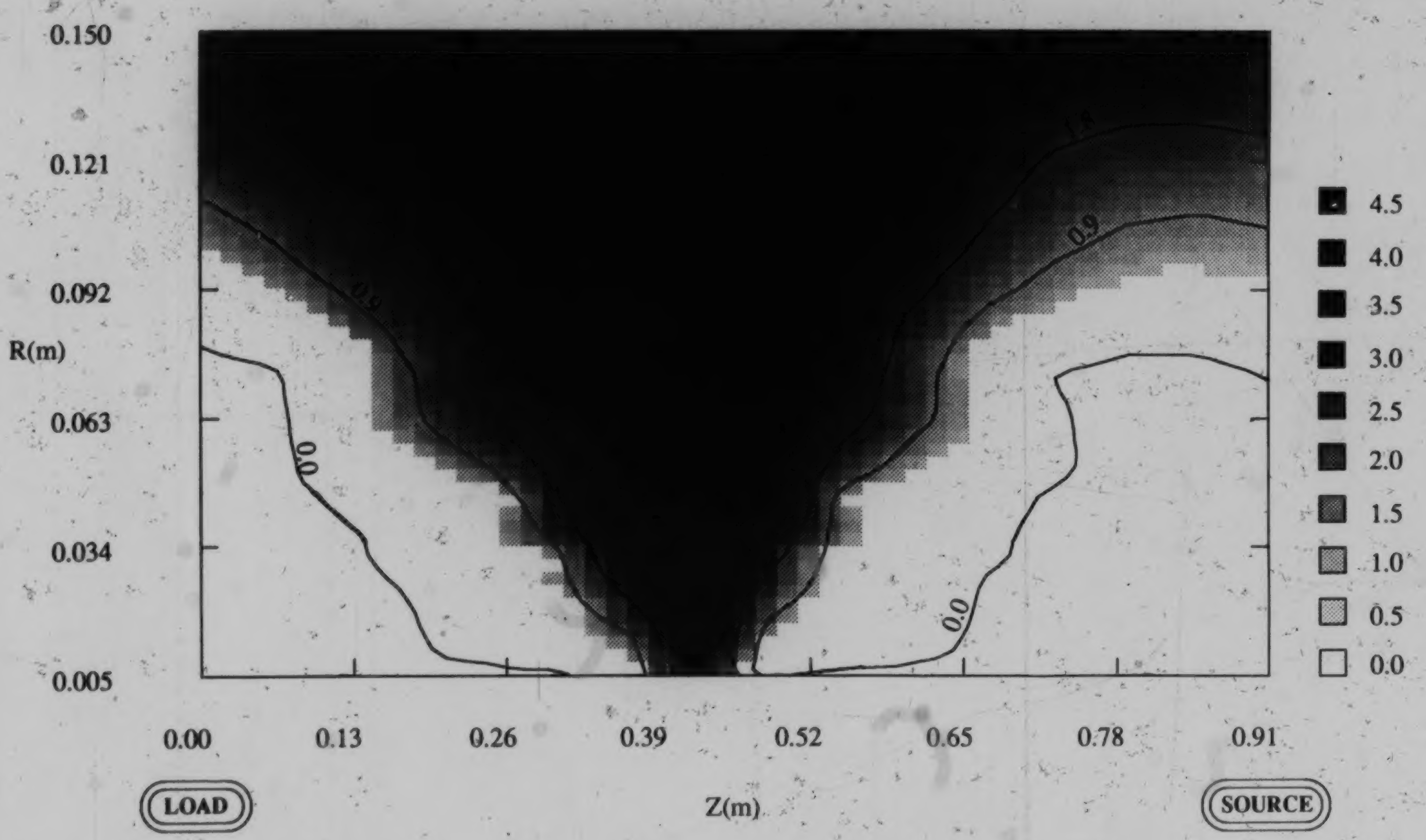

Figure 4.7b TM COPTER simulation mass percent water content vs. position.
Initial conductivity = 0.00205 S/m. Time = 15000 sec.

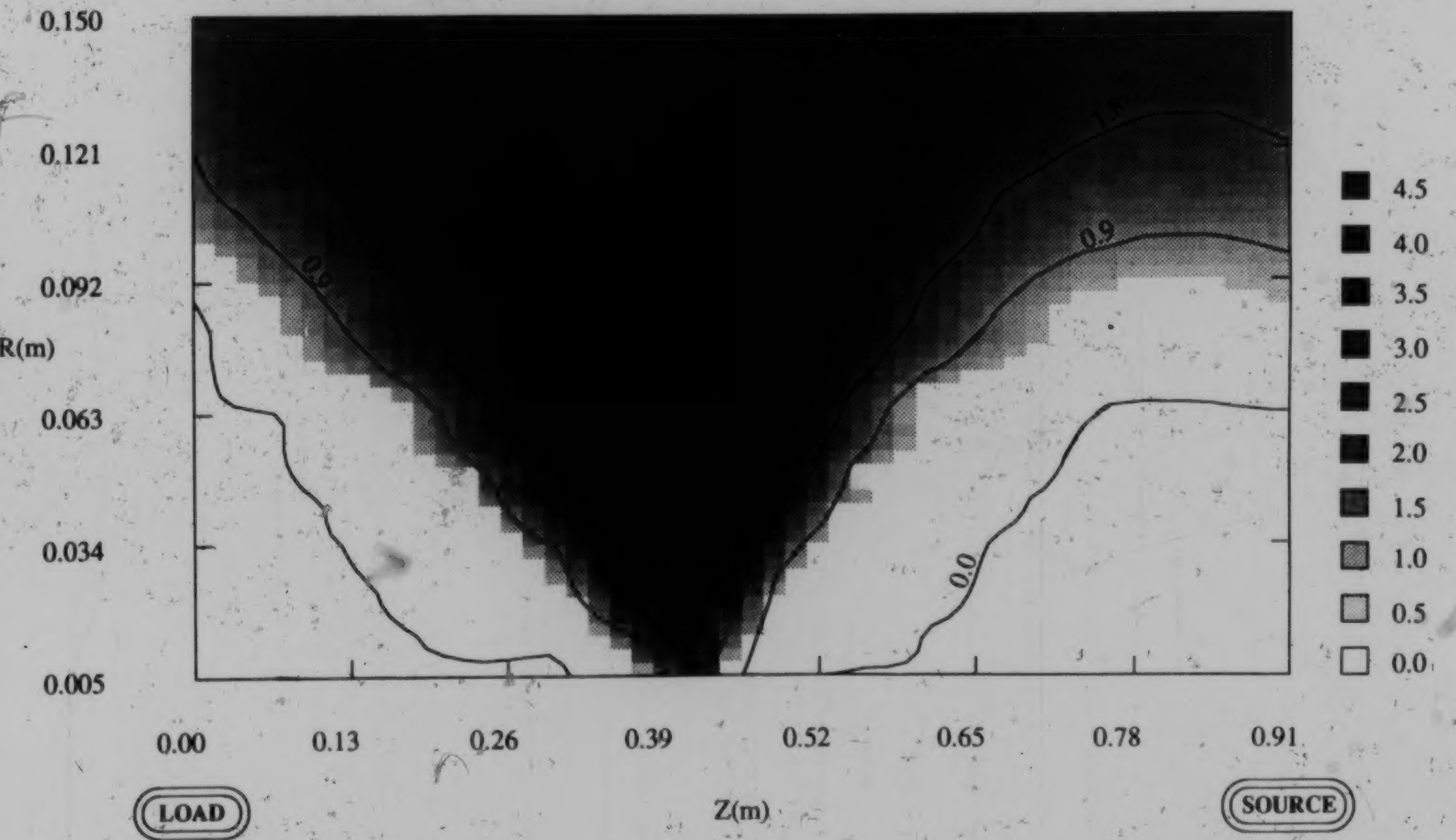

Figure 4.7c TEM COPTER simulation mass percent water content vs. position. Initial conductivity = 0.0205 S/m. Time = 15000 sec.

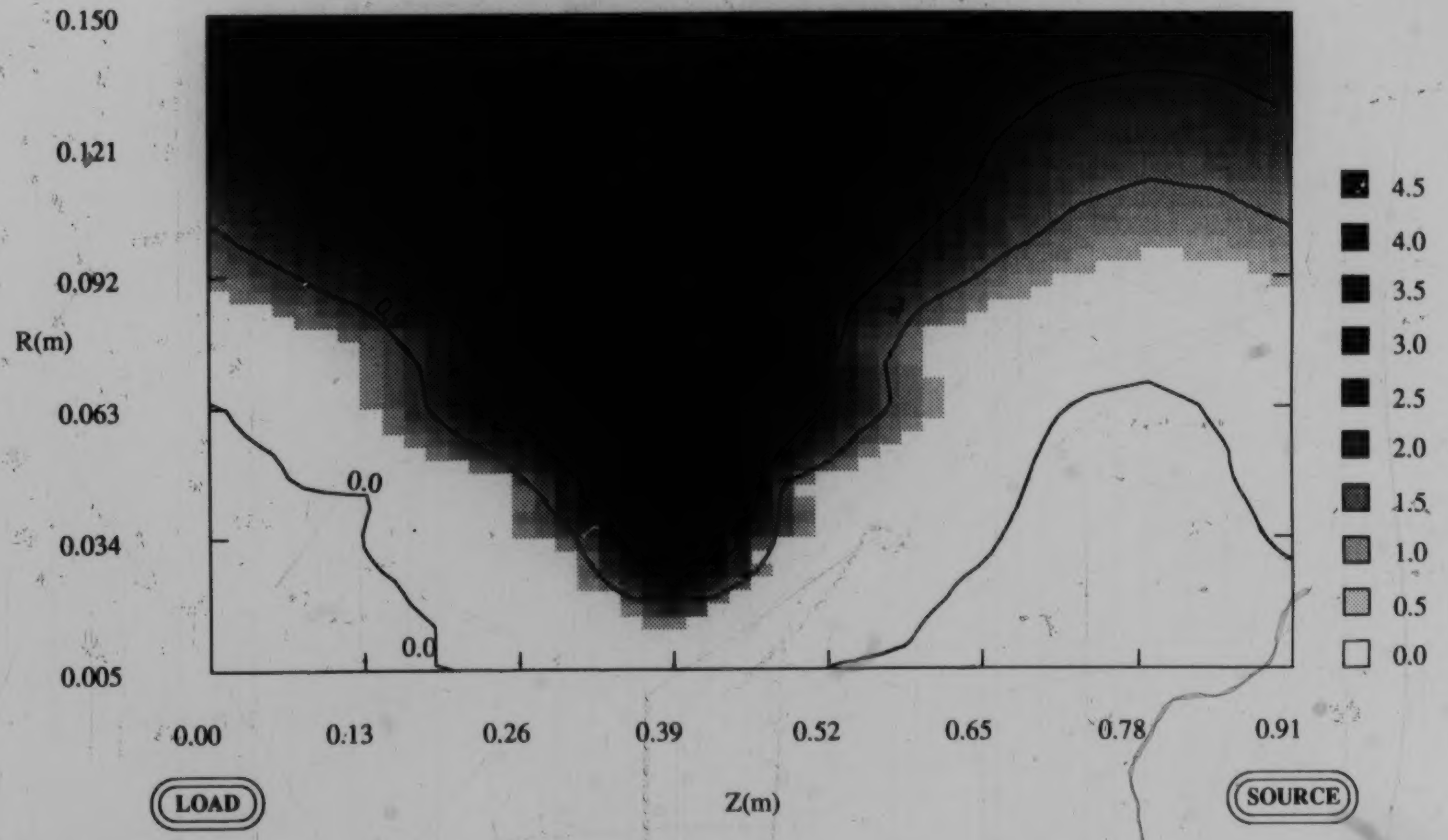

Figure 4.7d TM COPTER simulation mass percent water content vs. position.
Initial conductivity = 0.0205 S/m. Time = 15000 sec.

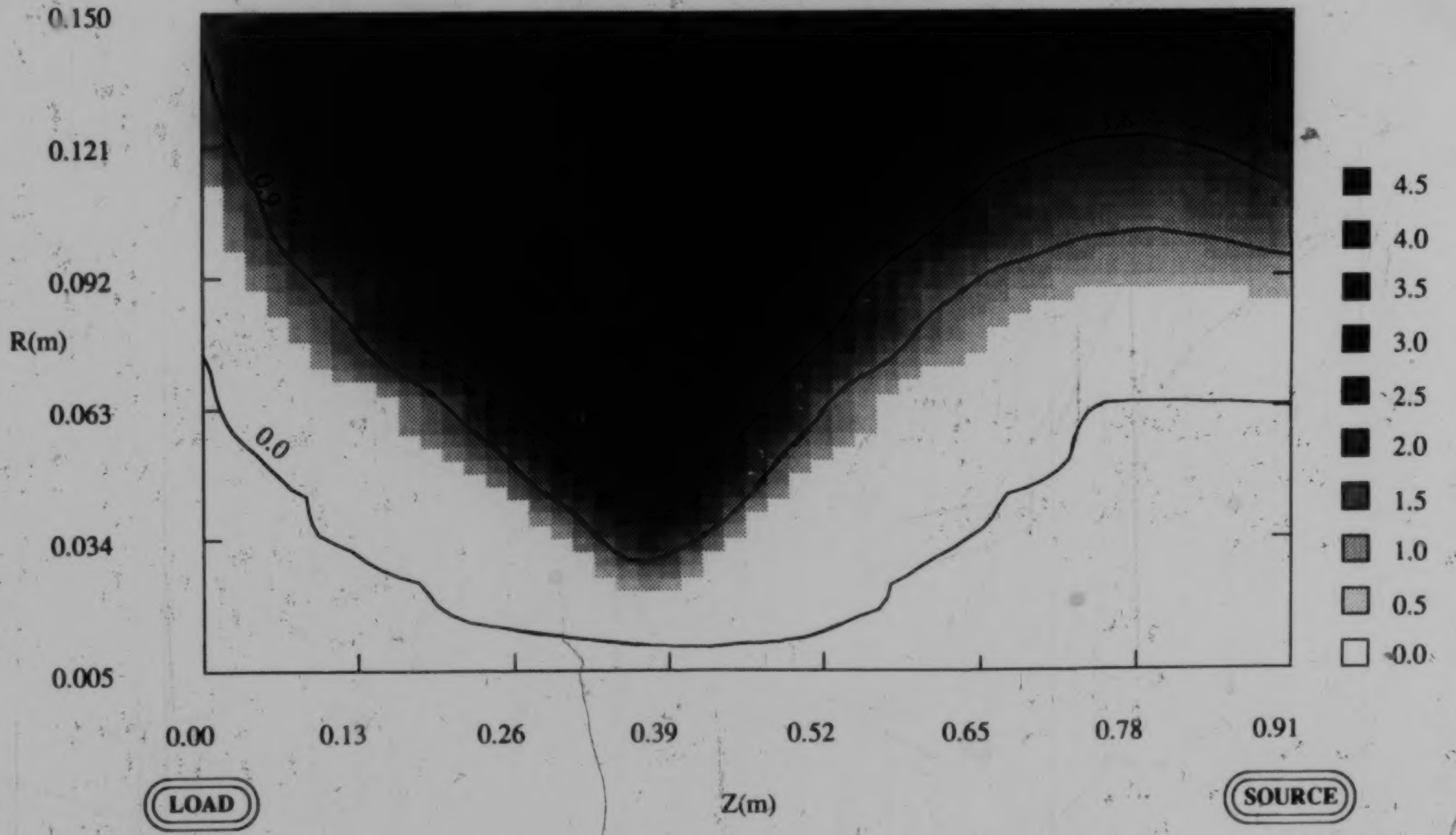

Figure 4.7e TEM COPTER simulation mass percent water content vs. position.
Initial conductivity = 0.052 S/m. Time = 15000 sec.

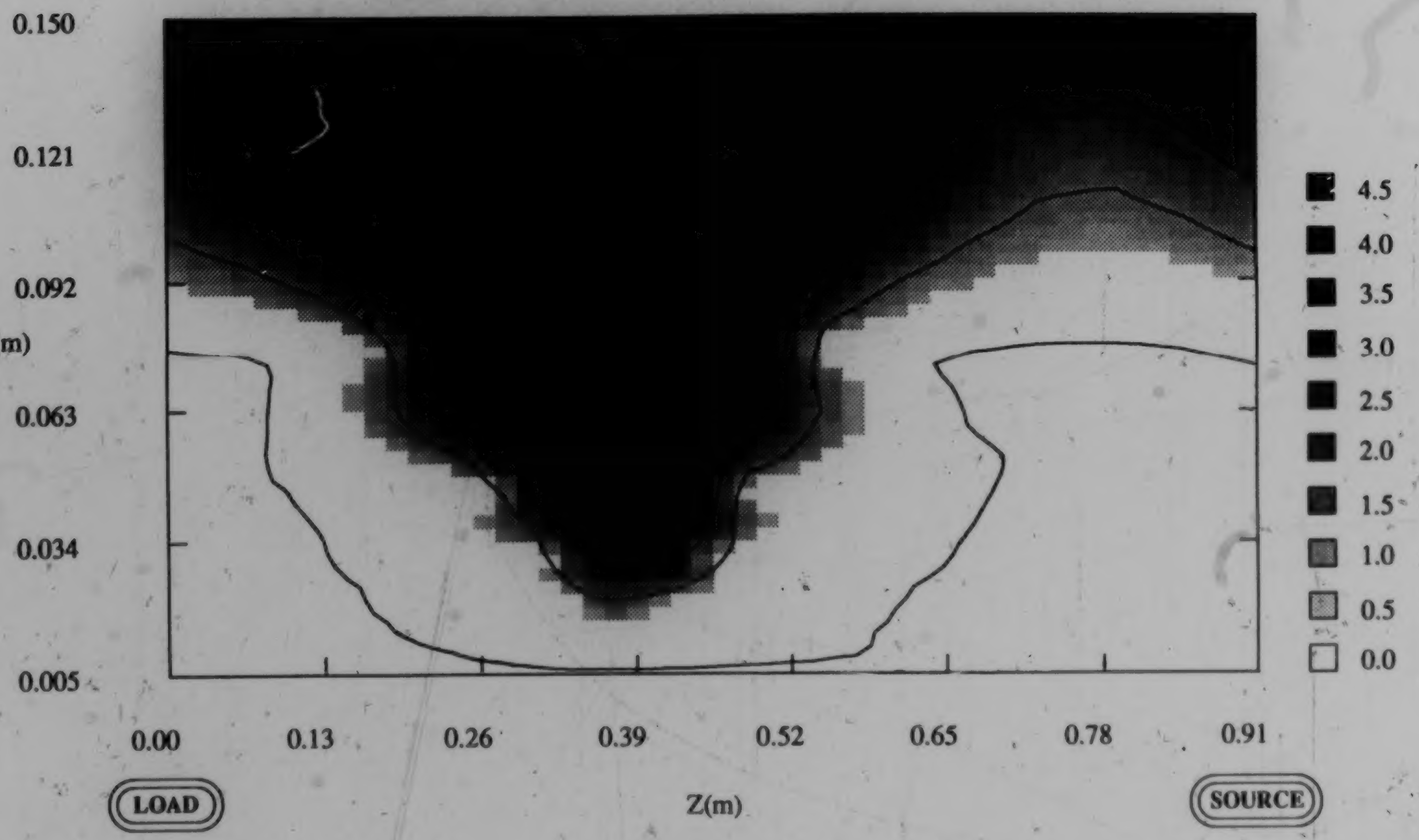

Figure 4.7f TM COPTER simulation mass percent water content vs. position.
Initial conductivity = 0.052 S/m. Time = 15000 sec.

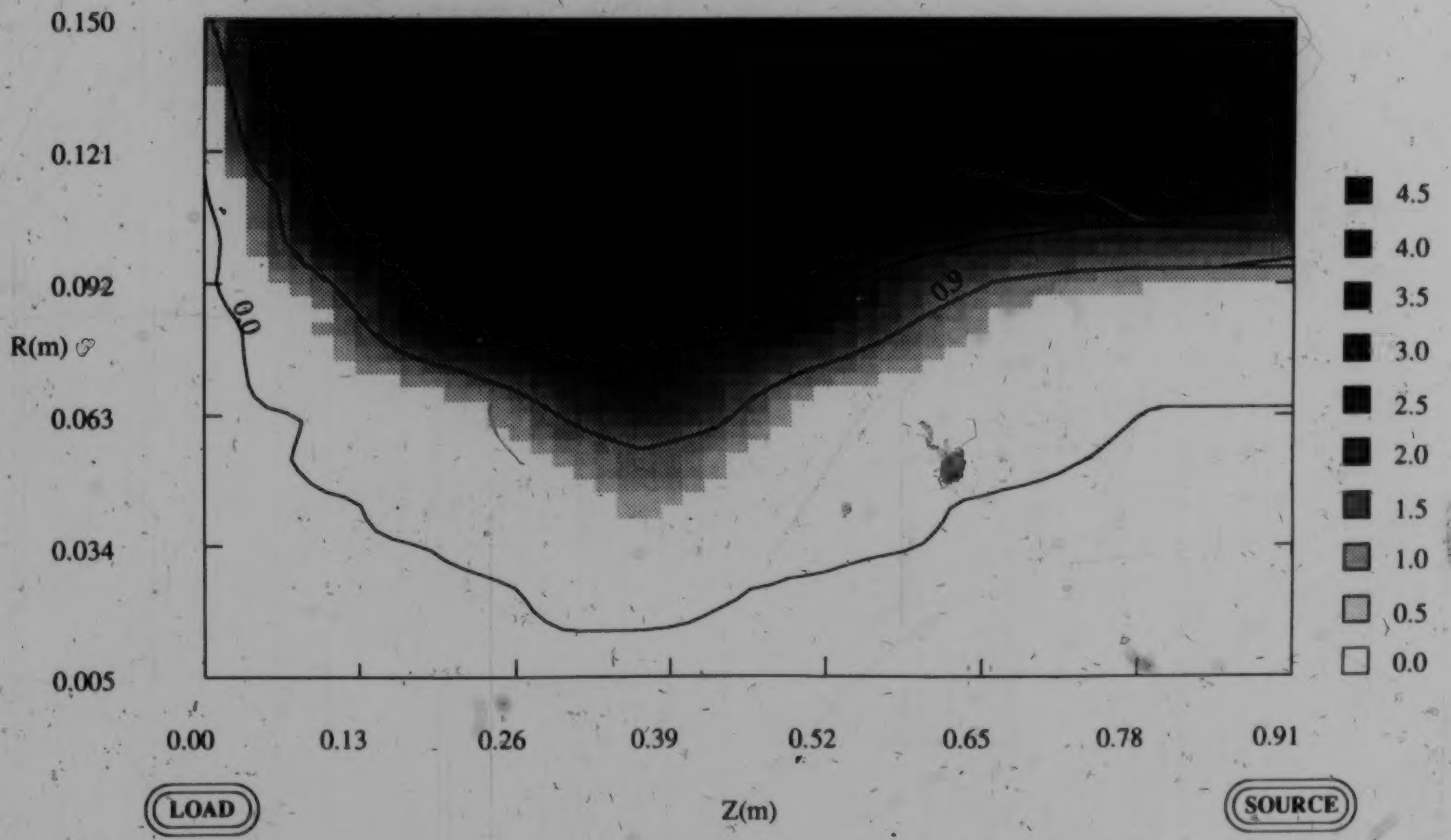

Figure 4.7g TEM COPTER simulation mass percent water content vs. position.
Initial conductivity = 0.069 S/m. Time = 15000 sec.

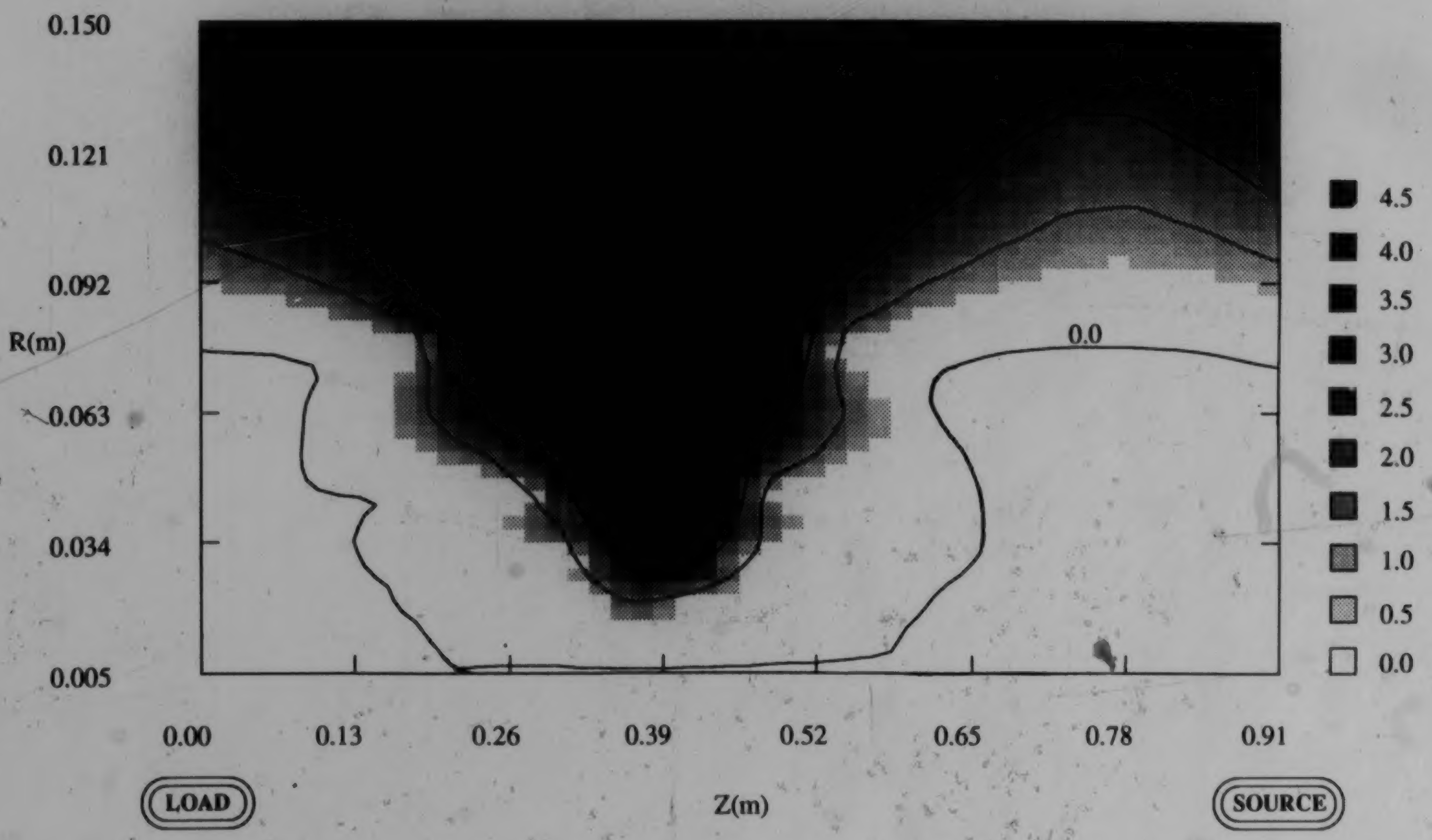

Figure 4.7h TM COPTER simulation mass percent water content vs. position.
Initial conductivity = 0.069 S/m. Time = 15000 sec.

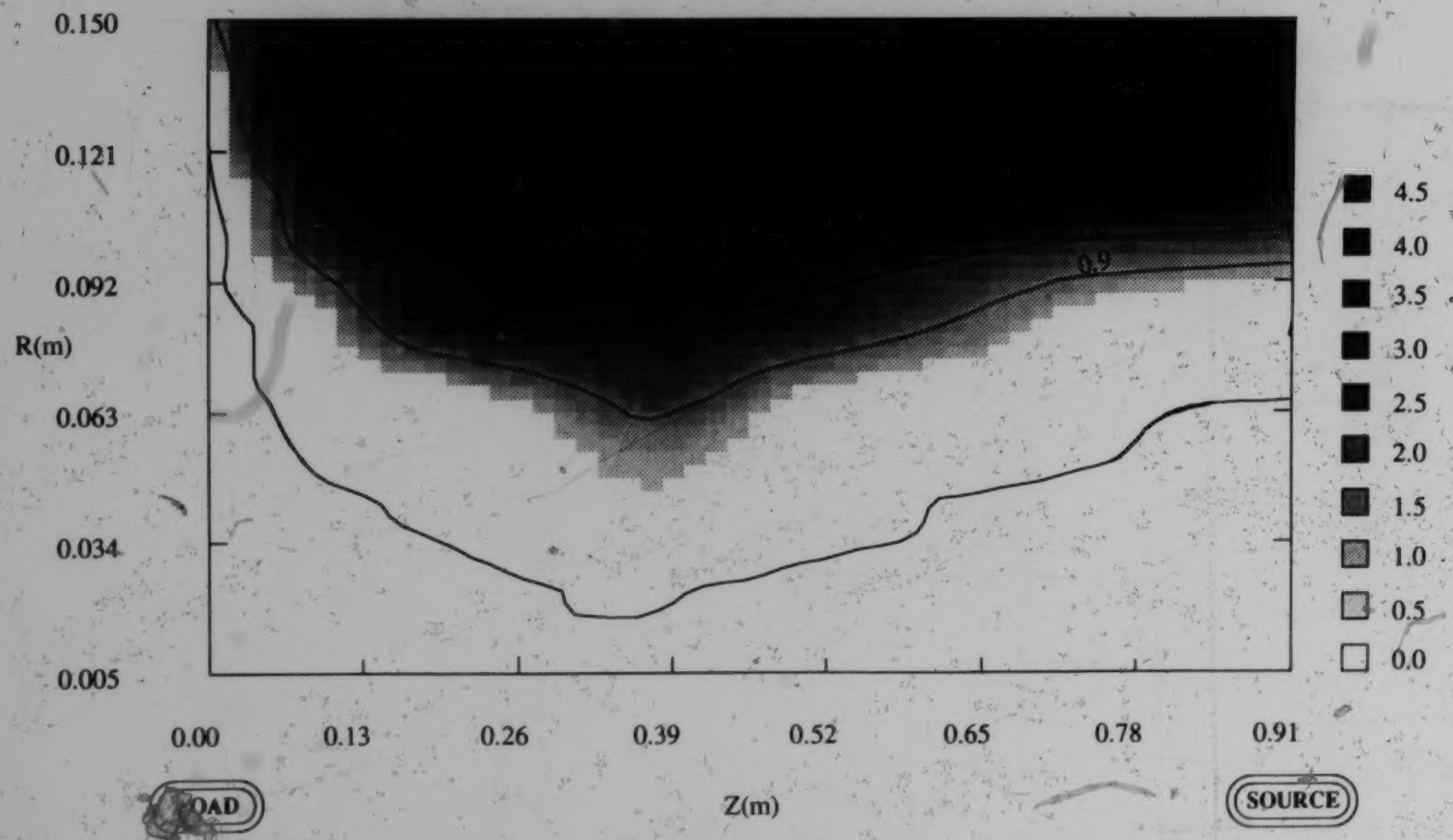

Figure 4.7i TEM COPTER simulation mass percent water content vs. position.
Initial conductivity = 0.205 S/m. Time = 15000 sec.

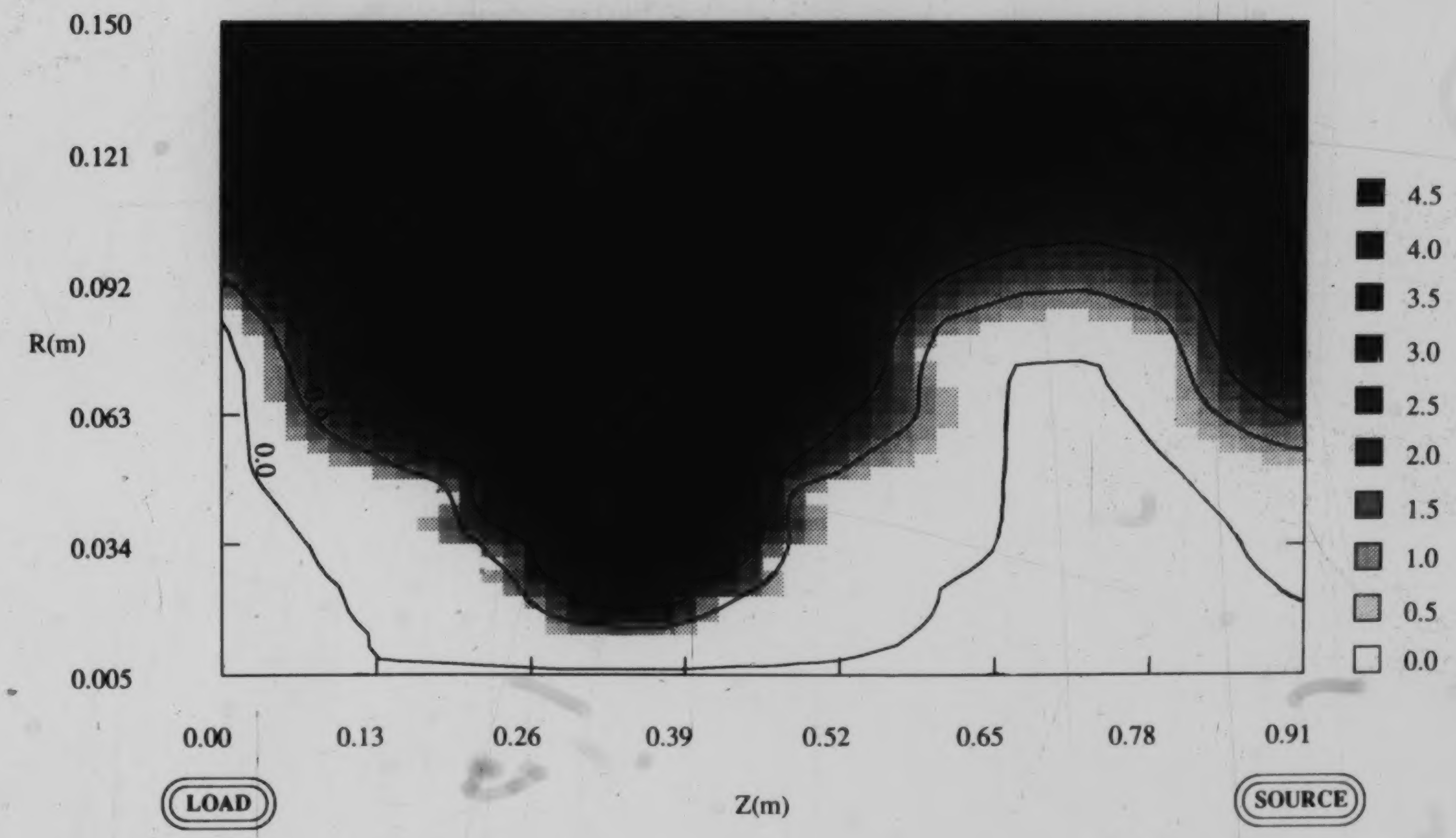

Figure 4.7j TM COPTER simulation mass percent water content vs. position.
Initial conductivity = 0.205 S/m. Time = 15000 sec.

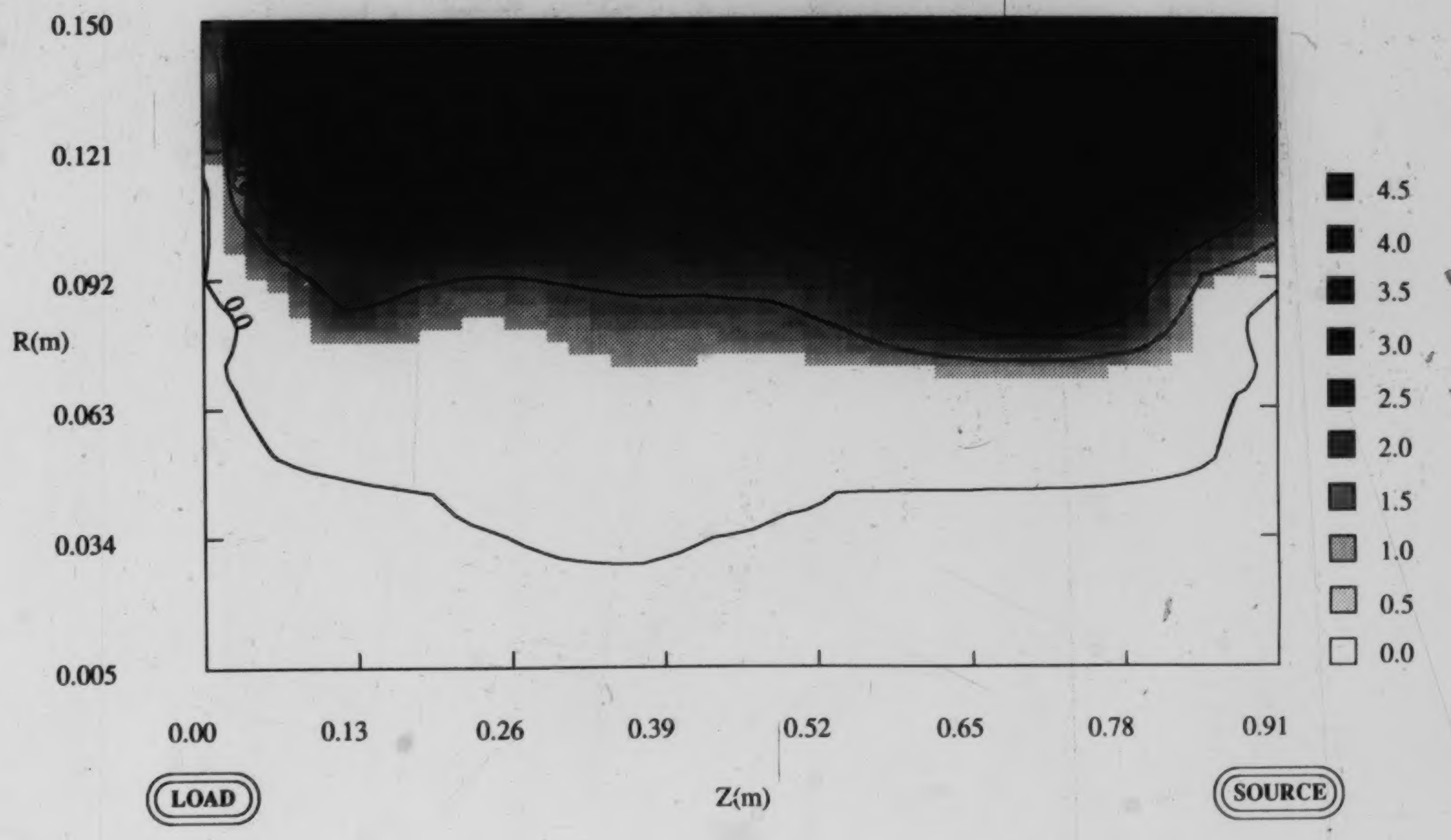

electrical standing wave, but the TM result indicates a more axially uniform pattern, due to the presence of significant axial field components in the wet region. In order to meet electrical boundary conditions, axial field standing waves exist in quadrature with the TEM standing waves along the waveguide. Effectively, the antinodal hot spots of the axial field standing wave occur in the same locations as the TEM field nodal cold spots, thus tending to level the heating irregularities of the TEM standing wave. This process becomes even more apparent in figures 4.7g through 4.7j, which present the results of simulations with initial conductivities of 0.069 S/m and 0.205 S/m (initial wavelengths approximately 0.96 m and 0.65 m) respectively. The TEM approximation is clearly invalid for these simulations unless electrically short, open circuited wave guides were to be employed. The magnitudes of the TEM and axial fields are approximately equal for the case represented in figure 4.7j. Clearly, accounting for the non TEM field components, as performed by the TM electrical solver, represents a necessary measure in the overall solution of the guided wave RF heating problem when wavelength effects must be considered.

McPherson[14] conducted laboratory RF heating experiments at 52 MHz similar to the high initial conductivity simulations and observed that simple TEM field calculations did not substantiate his experimental results. McPherson's calculations predicted the presence of large inhomogeneities in the heating patterns (similar to those of figure 4.7i, for example) due to the presence of standing waves. He observed a much more uniform heating pattern (similar to that of figure 4.7j) in his experimental results. In order to rationalize this discrepancy, he postulated the existence of a self levelling heating phenomenon which would smooth the standing wave patterns once a dielectric coating was present on the waveguide conductors. The transverse impedance at a point on the waveguide is then essentially dominated by the high impedance of the coating, and a transverse current would subsequently be independent of the value of the transverse resistance in the moist medium. The decreased transverse resistance in the moist medium which is associated with a hot spot in the moist medium results in decreased energy deposition into the hot spot by the transverse current, since the current is independent of the transverse resistance. This, in turn, would level the hot spot and facilitate the more uniform heating pattern. It is important to notice that the TEM version of COPTER is capable of simulating the mechanism which would generate this self levelling effect, but in the hundreds of TEM COPTER simulations which have been performed during the course of this project, no self leveling phenomenon has been observed. According to the results presented here, it is the presence of significant axial fields outside the dried coating that results in the beneficial levelling of the standing wave heating patterns which would otherwise be generated by purely TEM fields. It is most probable that the levelling effects which were observed by McPherson were due to the presence of axial field components.

4.4 Comparison With Physical Models

Two RF heating experiments were performed using a longer than previously employed brine-sand filled open circuited coaxial waveguide as a final means of validating the overall performance of the COPTER simulation routine. The experiments are illustrated in plate 4.2 and in figure 4.8. One experiment was performed with a 20 % water saturation brine-sand, while the second was performed with a 10 % water saturation brine-sand. Operational data for both experiments is documented in table 4.3. The experimental procedure was virtually identical to that of the single axial cell COPTER experiment described earlier. In this case, however, the use of an electrically long 0.91 m long, 0.3 m diameter waveguide (item 5 in plate 4.2 and in figure 4.8) meant that wavelength effects would be present, and that it was not possible to assume that only TEM fields were present, as in an electrically short case. Also, because heating occurred on a larger scale, a more powerful Amplifier Research 2000L RF power amplifier (item 2) was used to excite the waveguide. As before, power was delivered to this thermally insulated waveguide apparatus at as high a rate as equipment and safety would permit, so that minimal heat loss was realized, and the approximation of perfect thermal insulation was adequately approached. Periodically, power was removed such that the three thermocouple jigs (item 6), azimuthally spaced at 120° intervals, could be inserted into the brine-sand through small holes in the apparatus, thus facilitating simultaneous temperature measurements with the data acquisition system (item 7) at 27 physical locations within the sand. Again, teflon tubes imbedded in the sand guided the thermocouples into and out of the sand during the measurement. Impedance matching was also performed during the power down period. Unlike the single cell experimental case,

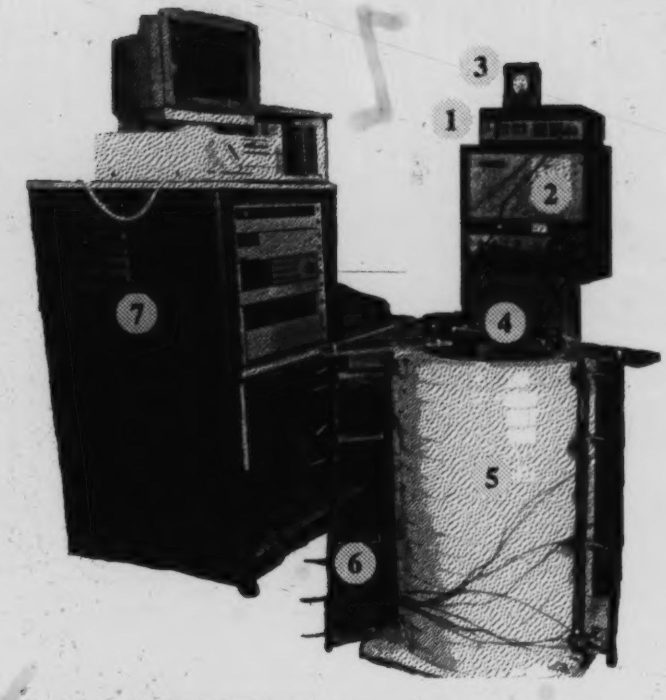

Plate 4.2 Full RF heating experiment apparatus.

	20 % S_w Brine Sand	10 % S_w Brine Sand
Frequency of Operation (MHz)	50	50
Input Power Level (kW)	0.45	0.40
Coaxial Waveguide Length (m)	0.91	0.91
Coaxial Waveguide Diameter (m)	0.30	0.30
Inner ~~Conductor~~ Diameter (m)	0.0095	0.0095
Initial Density (g/cm^3)	1.64	1.60
Initial Thermal Conductivity (W/m°C)	1.73	1.35
Initial Specific Heat (J/g°C)	0.910	0.830
Initial Conductivity (S/m)	0.2	0.064
Initial Loss Tangent	12.4	5.90
Initial Relative Dielectric Constant	5.8	3.9
Smallest Wavelength (m)	0.60	1.1

Table 4.3 Full RF heating experiment medium parameters. Brine sand for the model experiments utilized the same clean tailings pond sand as did the single axial cell experiment. Brine conductivity was 12 S/m in both model cases. Mass percent water content in the models was 4.52 % and 2.31 % for the 20 % S_w and 10 % S_w cases respectively.

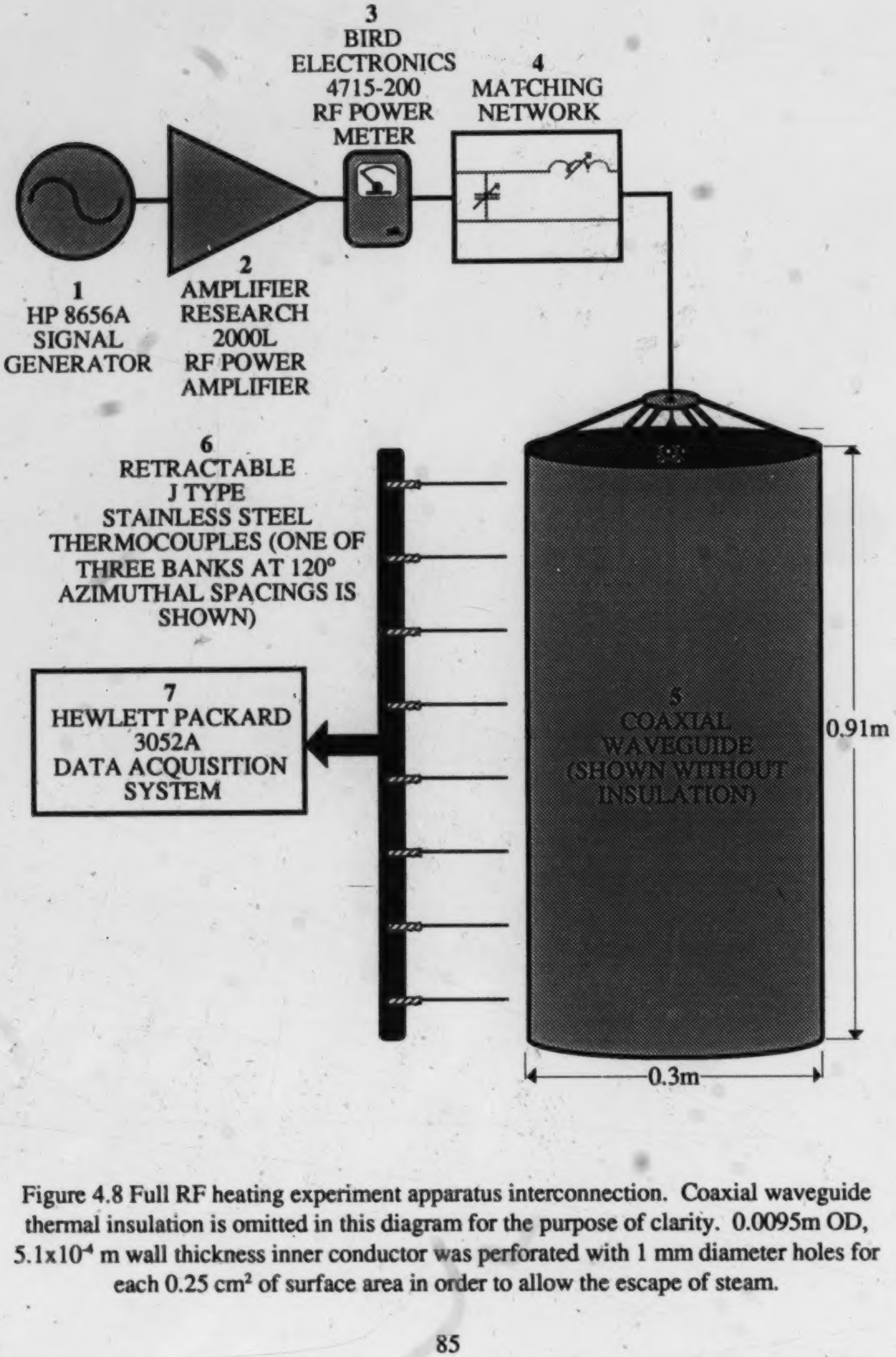
3
BIRD
ELECTRONICS
4715-200
RF POWER
METER
4
MATCHING
NETWORK
1
HP 8656A
SIGNAL
GENERATOR
2
AMPLIFIER
RESEARCH
2000L
RF POWER
AMPLIFIER
6
RETRACTABLE
J TYPE
STAINLESS STEEL
THERMOCOUPLES (ONE OF
THREE BANKS AT 120°
AZIMUTHAL SPACINGS IS
SHOWN)
7
HEWLETT PACKARD
3052A
DATA ACQUISITION
SYSTEM
5
COAXIAL
WAVEGUIDE
(SHOWN WITHOUT
INSULATION)
0.91m
0.3m

Figure 4.8 Full RF heating experiment apparatus interconnection. Coaxial waveguide thermal insulation is omitted in this diagram for the purpose of clarity. 0.0095m OD, 5.1×10^{-4} m wall thickness inner conductor was perforated with 1 mm diameter holes for each 0.25 cm^2 of surface area in order to allow the escape of steam.

the changing input impedance of the waveguide did not require elaborate matching procedures. It is true that a dried coating would first appear on the inner conductor of the waveguide, just as it did in the single cell experiment. Recall that capacitive decoupling brought about by this dried layer created the matching problems in the single cell case. Since any impedance which is measured through a significant electrical length of waveguide will undergo an impedance transformation at the measurement point, the vastly increased electrical length of the waveguide in the full RF heating experiment transformed the capacitive reactance before it could be experienced at the input binding posts.

The temperature results of these experiments are plotted against TM COPTER simulated temperature contours in figure 4.9. The agreement is reasonable except at points which are near to the medium boundaries. Heat loss resulting from imperfect thermal insulation is responsible for these discrepancies. Heating is fairly uniform except for some overheating towards the load, in the dried region, near the inner conductor. This overheating, observed in both the simulated and experimental results, was due to antinodal peaking *within the dried region* at the open circuited load. Axial fields were present which countered the effects of antinodal peaking as previously discussed, but axial fields appear only within the wet lossy outer region and not within dried coatings. Since the dried sand near the inner conductor was almost lossless, and since the radially adjacent wet sand was much more lossy, the boundary between the wet and dry sands could have been considered as an outer conductor to the dried sand. Only TEM fields were present within the resulting low loss inner cylindrical waveguide, and the resulting antinode at the open circuited load provided the observed overheating.

A water content plot is given in figure 4.10 as predicted by TM COPTER at a time corresponding to the end of the full 20 % water saturation experiment. At the end of this experiment, a significant amount of the sand had been dried and encrusted onto the inner conductor due to the heating process. The remaining sand which was adjacent to this dried crust remained quite damp and did not bake itself onto the crusted formation. An abrupt radial moisture gradient was clearly evident. The inner conductor and its encrusted dry sand formation were carefully removed from the coaxial waveguide, and are shown in plate 4.3. This encrusted formation measured approximately 0.05 m in radius. Clearly, the simulated

Figure 4.9a TM COPTER simulation temperature (°C) vs. position.
Initial water saturation level = 20 %. Time = 25000 sec.
Outlined temperatures represent the corresponding experimental temperatures.

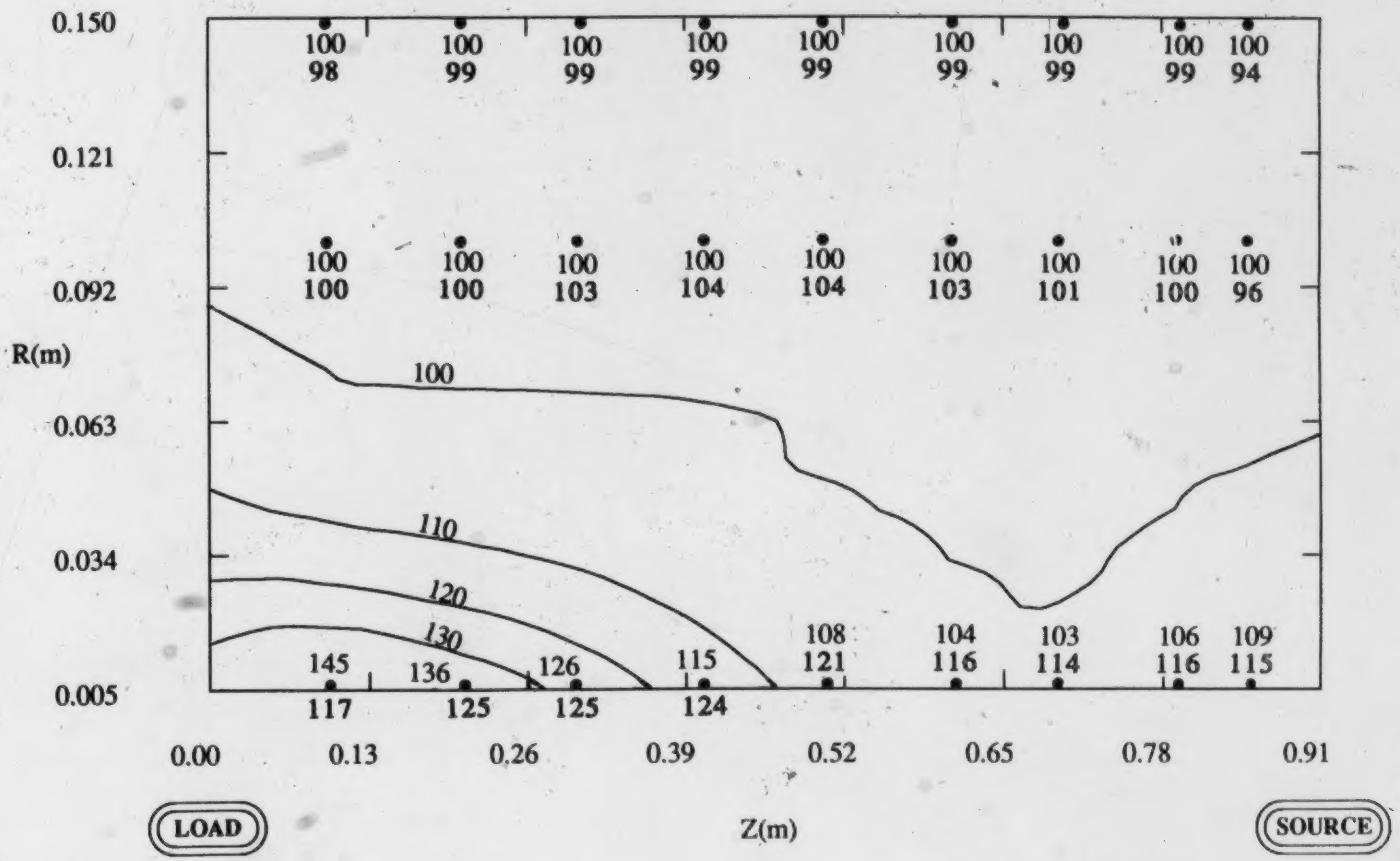

Figure 4.9b TM COPTER simulation temperature (°C) vs. position.
Initial water saturation level = 10 %. Time = 22000 sec.
Outlined temperatures represent the corresponding experimental temperatures.

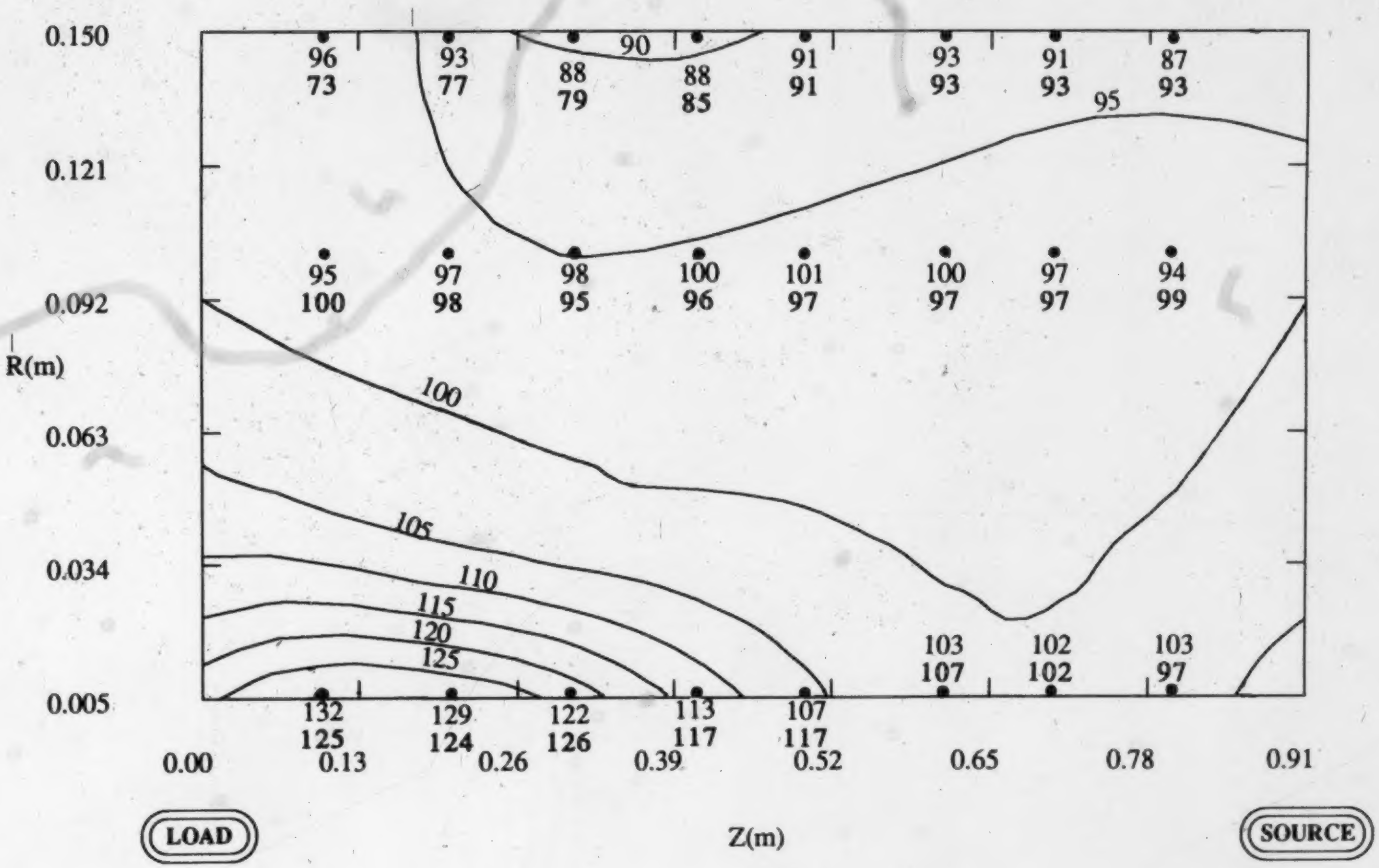

Figure 4.10 TM COPTER simulation mass percent water content vs. position.
Water saturation level = 20 %. Time = 25000 sec.

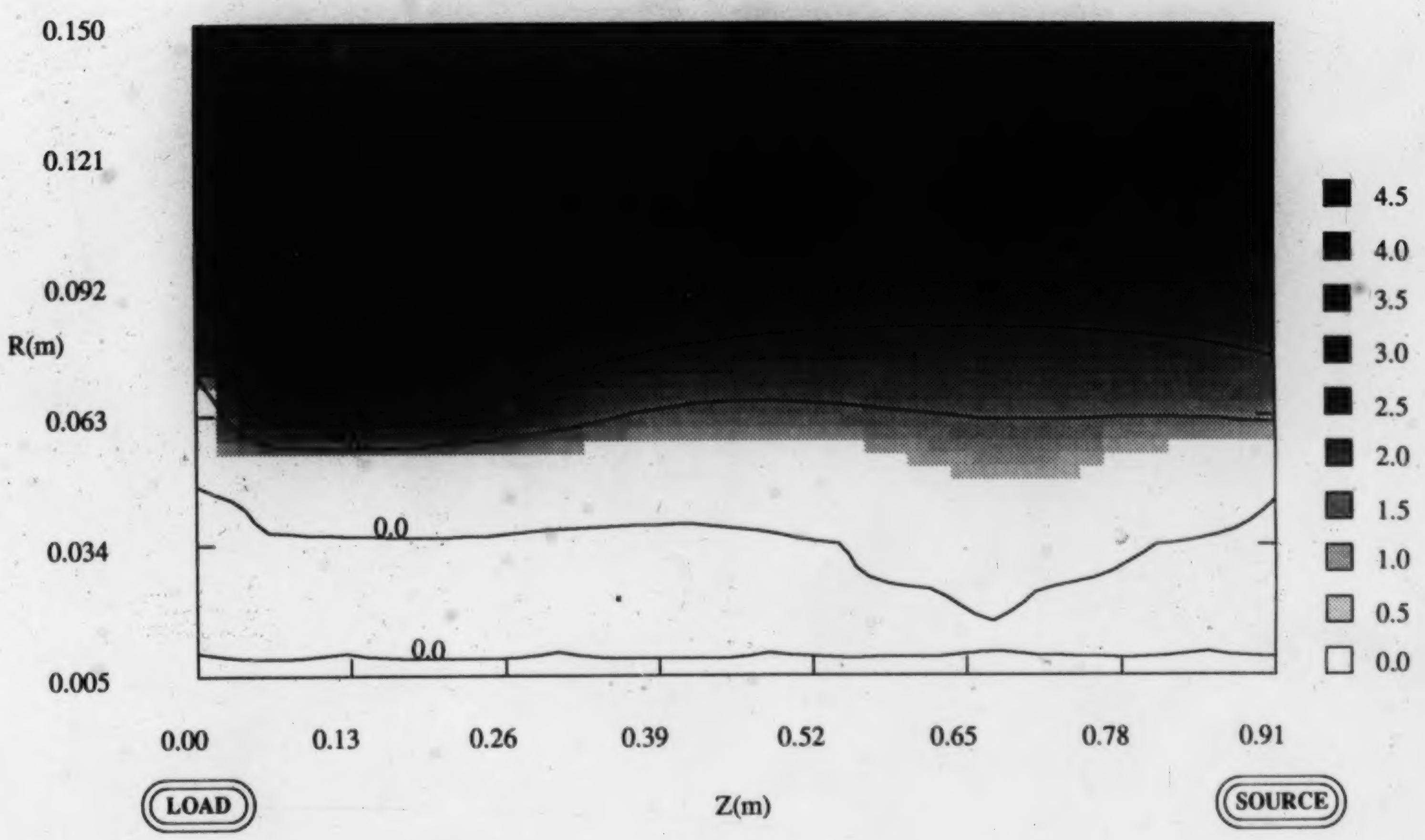

water content plot of figure 4.10 predicts virtually the same dried region dimension about the inner conductor.

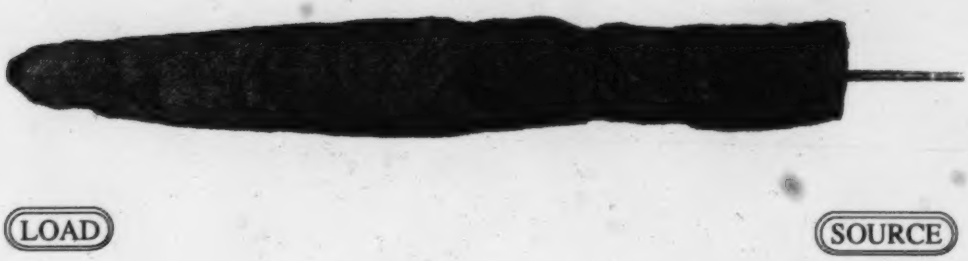

Plate 4.3 Inner conductor encrusted sand formation.

5. Summary of Results Using the Guided Wave Heating Process

The process of development and verification of the COPTER simulation routine has yielded significant insight into the guided wave heating process. Once some comprehension of the important phenomena behind the guided wave heating process, such as conductor coatings, field compositions, and fluid movements, is understood, progress can be made towards the further study and optimization of the process. Uniform energy deposition is usually the main objective of the guided wave heating process. Standard transmission line theory has been employed in order to develop methods for controlling the TEM electric field patterns in low loss cases and very uniform heating is possible[11]. The results of the previous chapter seem to suggest that the presence of non TEM fields will also promote uniformity in the heating process in higher loss cases. In addition, the literature indicates that the electromagnetic flooding process[8] represents a promising method by which very moist porous media may be heated uniformly. This current chapter attempts to qualitatively evaluate the merits of the more promising RF guided wave heating techniques by examining in some greater detail the phenomena which are associated with the techniques.

5.1 The Self Coating Action

Figure 5.1 gives the results of the initial moments of a heating simulation previously presented in Chapter 4. Initial conductivity was 0.205 S/m in the 0.91 m long, 0.3 m diameter coaxial waveguide. As listed in table 4.2, the inner conductor was 0.0095 m in diameter, and an open circuited load was used. Initial mass percent water content versus position is given in figure 5.1a. When RF power was first applied to the moist, homogeneous lossy material within the coaxial guiding structure, concentrated heating occurred near the inner conductor due to the inherent concentration of the electric field lines in this area. In addition, since the guide was not electrically short (starting wavelength was 0.65 m), the excitation field initially deposited most of its energy near the source end of the guide because of attenuation. Initial attenuation was 8.32 Np/m in the simulation, which limited field penetration to approximately 12 cm from the source. The very localized heating which occurred at the inner conductor near the source resulted in local evaporation at an early time

Figure 5.1a TM COPTER simulation mass percent water content vs. position.
Initial conductivity = 0.205 S/m. Time = 0 sec. Frequency = 100 MHz.

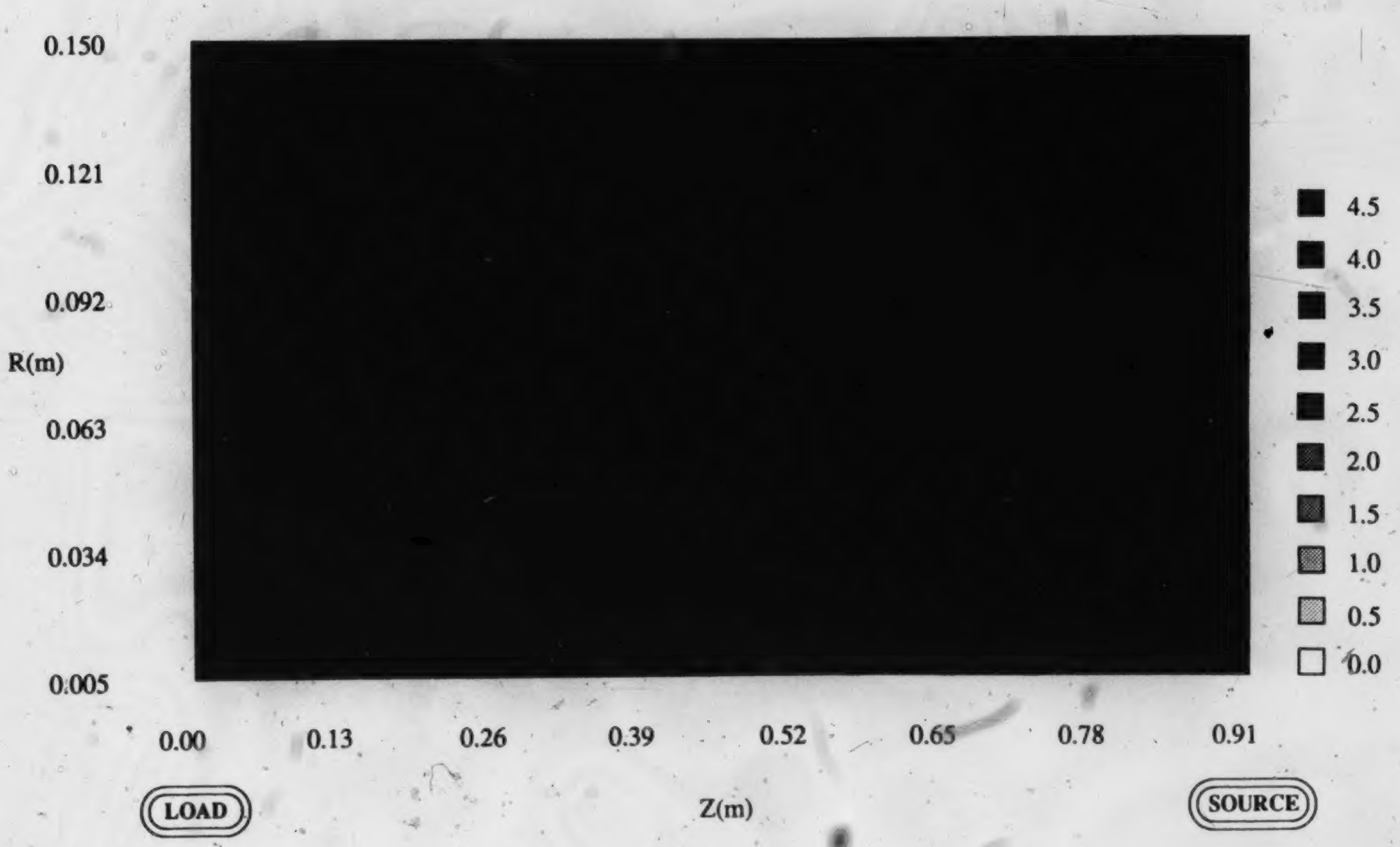

Figure 5.1b TM COPTER simulation mass percent water content vs. position.
Initial conductivity = 0.205S/m. Time = 402 sec. Frequency = 100 MHz.

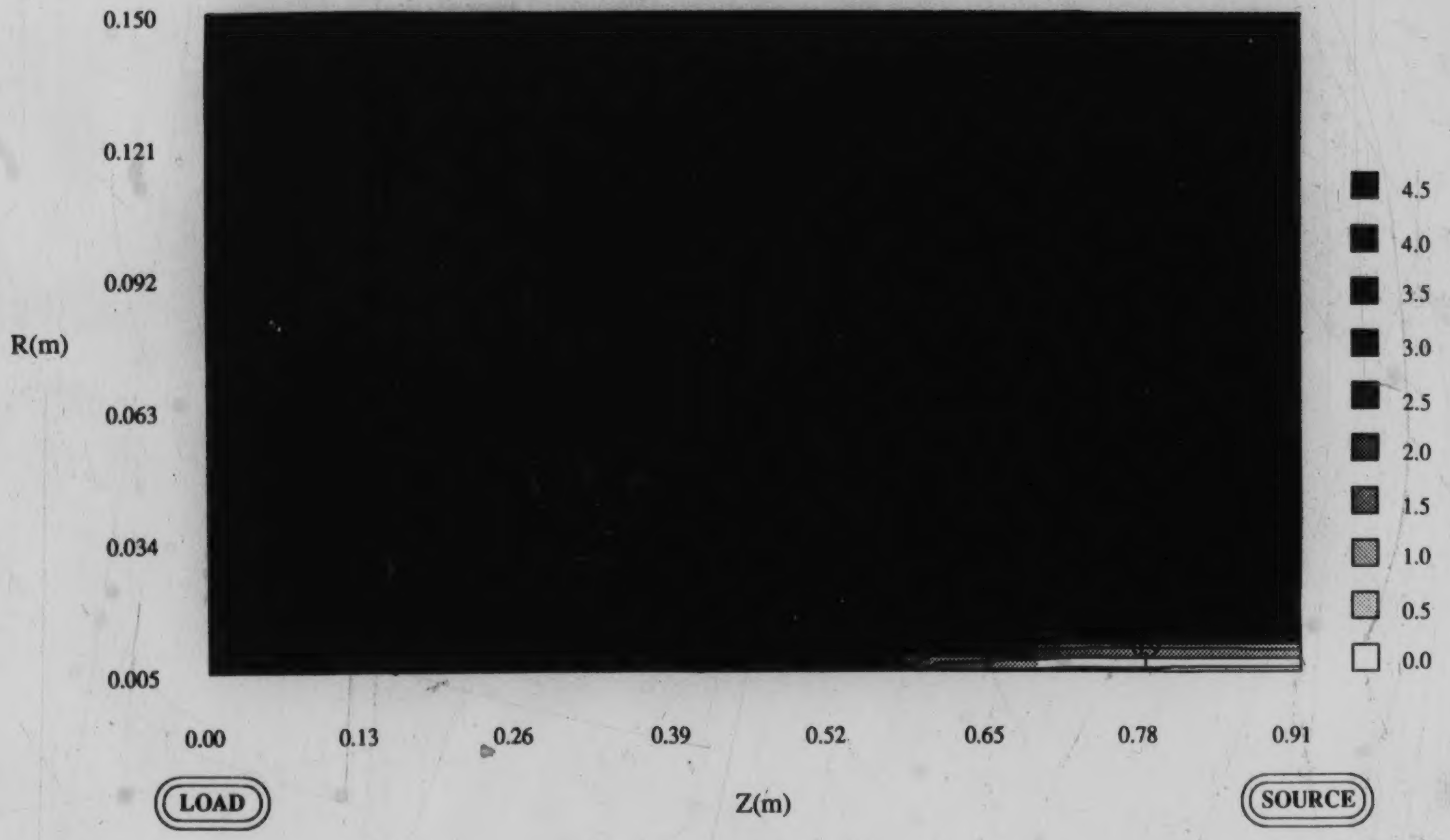

Figure 5.1c TM COPTER simulation mass percent water content vs. position.
Initial conductivity = 0.205S/m. Time = 1171 sec. Frequency = 100 MHz.

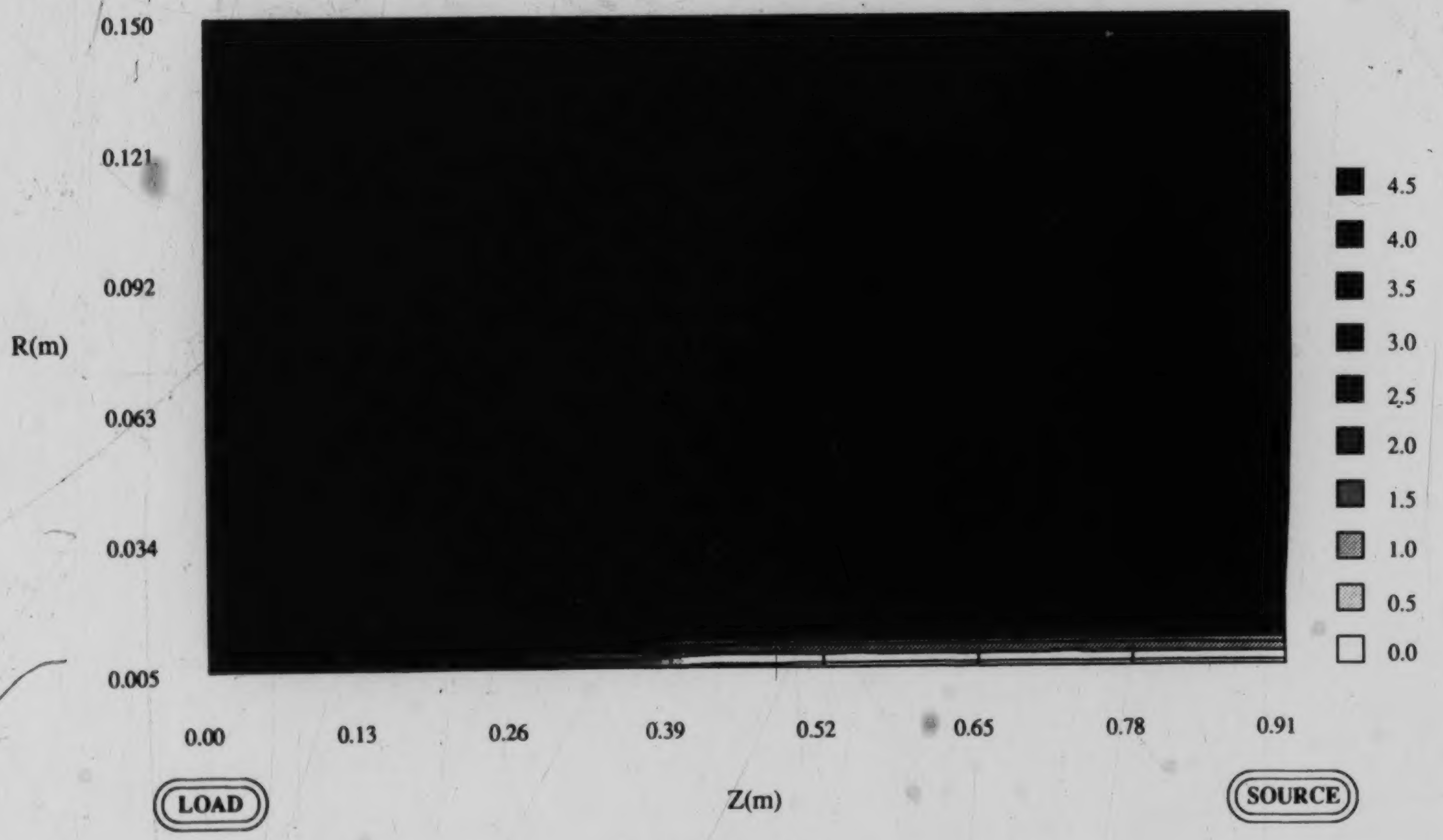

Figure 5.1d TM COPTER simulation mass percent water content vs. position.
Initial conductivity = 0.205S/m. Time = 2445 sec. Frequency = 100 MHz.

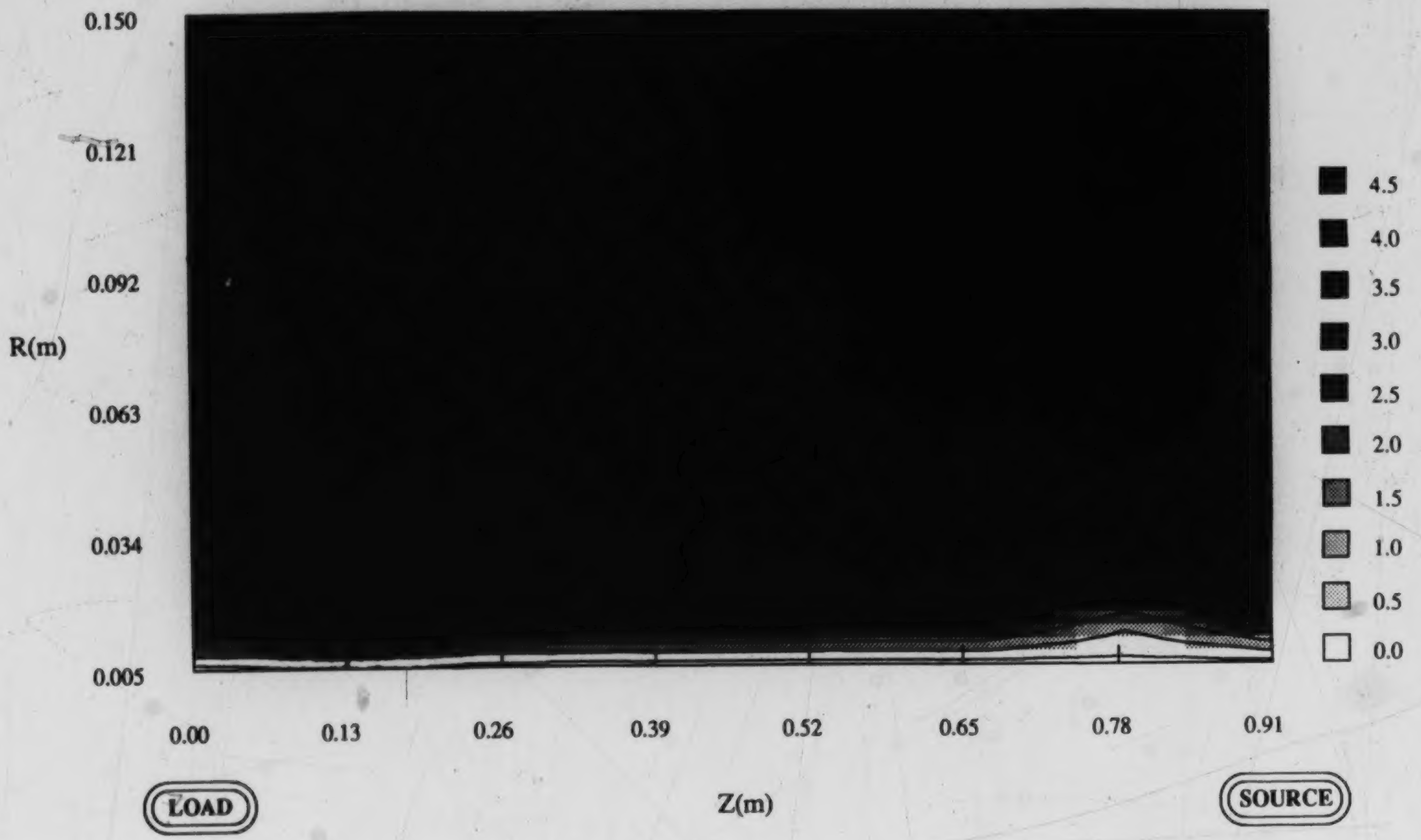

in the heating process. Since the medium had a low water saturation level such that the "steam disappears" approximation was valid and no significant recoupling occurred subsequently due to fluid flow, a thin dried dielectric coating was formed on the inner conductor portion, as shown in figure 5.1b. As previously explained, the line propagation characteristics of the wave in the vicinity of the source were then significantly altered by this coating, even though the remaining majority of the material near the source was still saturated with fluids and was highly lossy. Near the source, the axial attenuation of the wave was drastically reduced by the partial decoupling effect of the thin coating to the extent that it proceeded further down the line without further heating of the volume near the source for the time being. Of course, once the wave impinged upon the next axial slice of homogeneous material, the coaxial geometry once again promoted concentrated heating near the inner conductor, which extended the dried conductor coating into this second axial slice as well. Very quickly, the thin dried coating was then propagated down the entire length of the line, as illustrated in figures 5.1c and 5.1d, while relatively little heating was accomplished in the remaining bulk of the medium, away from the immediate vicinity of the inner conductor.

Because of the coaxial geometry, this phenomenon is almost impossible to avoid at the frequencies of interest if the connate moisture of the medium is sufficiently immobile to prevent resaturation of the dried coating. COPTER, with the "steam disappears" fluid flow coding, is fully capable of simulating the self coating phenomenon. Although very little energy is expended in the coating process, the coating redefines the electrical behavior of the composite medium. An approximate example of the dependence of attenuation factor and wavelength on coating thickness is given in figure 5.2. As illustrated in figure 5.2a, overall attenuation is greatly reduced by a thin coating such that the excitation wave is able to propagate back and forth along the waveguide. Bulk overheating near the source as a result of poor wave penetration is eliminated by the coating, but standing wave problems may then appear since wavelength does not increase rapidly with increases in coating thickness, as shown in figure 5.2b.

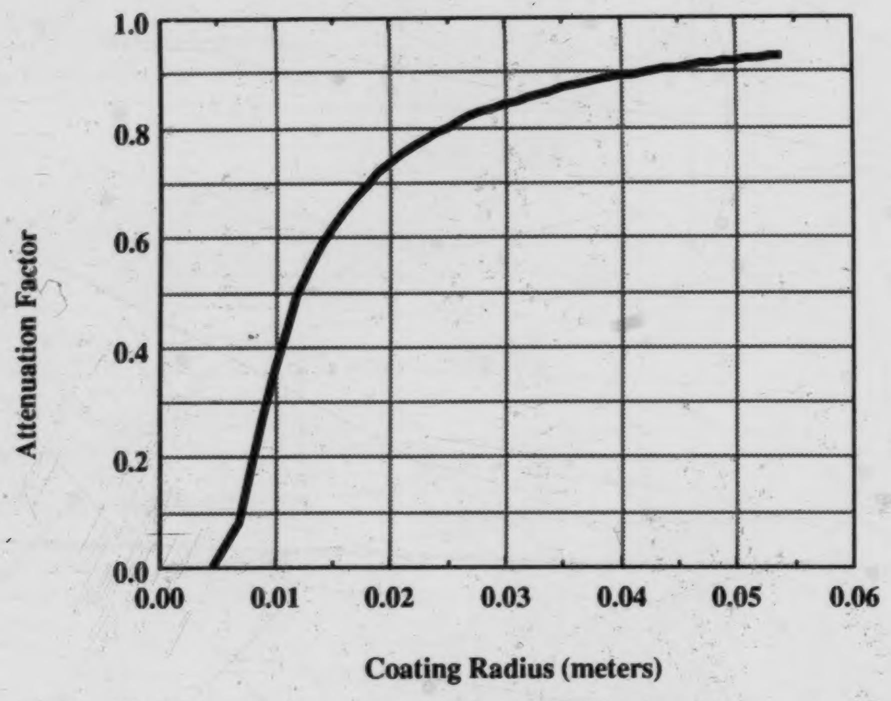

Figure 5.2a Representative attenuation factor (for 1 m length) versus coating radius plot.

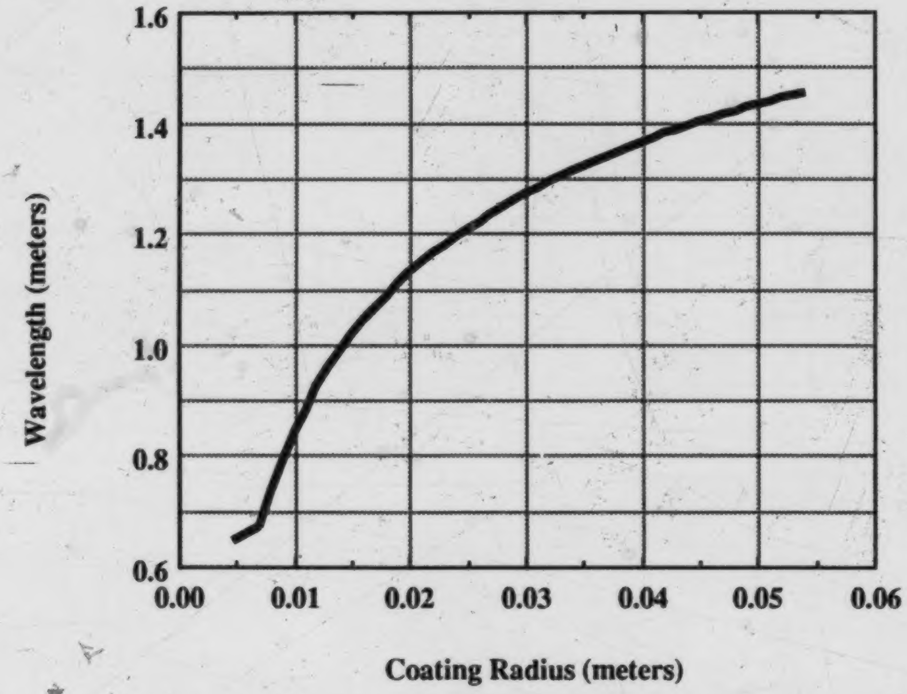

Figure 5.2b Representative wavelength versus coating radius plot.

5.2 Uniform Heating in Low Loss Cases

Electric field peaking and standing waves are frequently experienced in low loss guided wave RF heating applications. These phenomena are prominent enough to warrant research[11] which examines various means of promoting uniform heating in the presence of standing waves. Altering the waveguide load impedance, as well as the excitation frequency and power level during the course of a heating operation are some of the techniques which have been postulated. Elaborate electrode configurations and power feeding methods have also been examined in the quest for uniform guided wave heating of low loss materials. The TEM version of COPTER was used to determine the best method for promoting uniform heating in low loss media in electrically long guides. It was found that the use of matched loads tended to minimize the appearance of non uniform heating patterns, which result from standing waves, to a great extent. However, the best means of providing the uniform heating was found to be by continuous alternation of load impedance during heating from that of an open circuit to a short circuit, on a 50 % duty cycle. Figure 5.3a depicts the water content results of an open circuit low loss heating simulation. Initial conductivity was 0.00205 S/m in the 0.91 m long 0.3 m diameter coaxial waveguide, and initial wavelength was 1.24 m. The remaining simulation parameters are listed in table 4.2. Figure 5.3b gives the water content results of the same simulation, but with a short circuited load instead of an open circuited load. Finally, figure 5.3c depicts the results of the same simulation again, but with the load alternation occurring as described. Virtually perfect heating uniformity was obtained by using the antinodal hot spots which were generated by the opened termination to heat the nodal cold spots which were generated by the shorted termination, and vice versa.

5.3 The Use Of Axial Electric Fields for the Promotion of Uniform Heating

The results of section 5.2 clearly indicate that in RF heating applications which exhibit standing waves, antinodal interleaving techniques represent an effective means of developing uniform heating patterns. If one employs the accepted methods, achieving this antinodal interleaving is not a simple task from a practical viewpoint, however. The field equipment configurations which would be required in order to facilitate dynamic waveguide loading or other such techniques represent significant expense and difficulty since easy

Figure 5.3a TEM COPTER simulation mass percent water content vs. position.
Initial conductivity = 0.00205 S/m. Time = 15000 sec. Termination = open circuit.

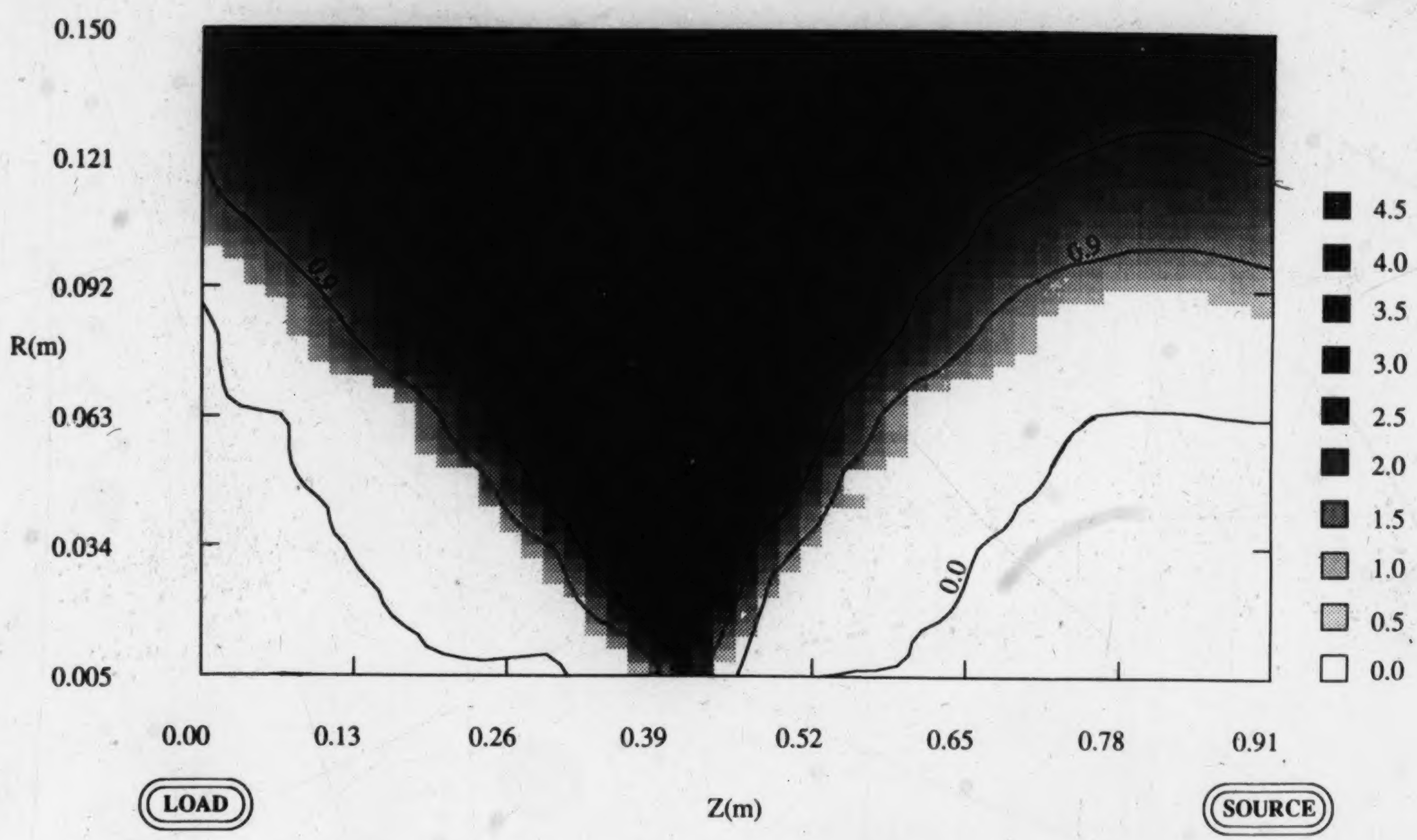

Figure 5.3b TEM COPTER simulation mass percent water content vs. position.
Initial conductivity = 0.00205 S/m. Time = 15000 sec. Termination = short circuit.

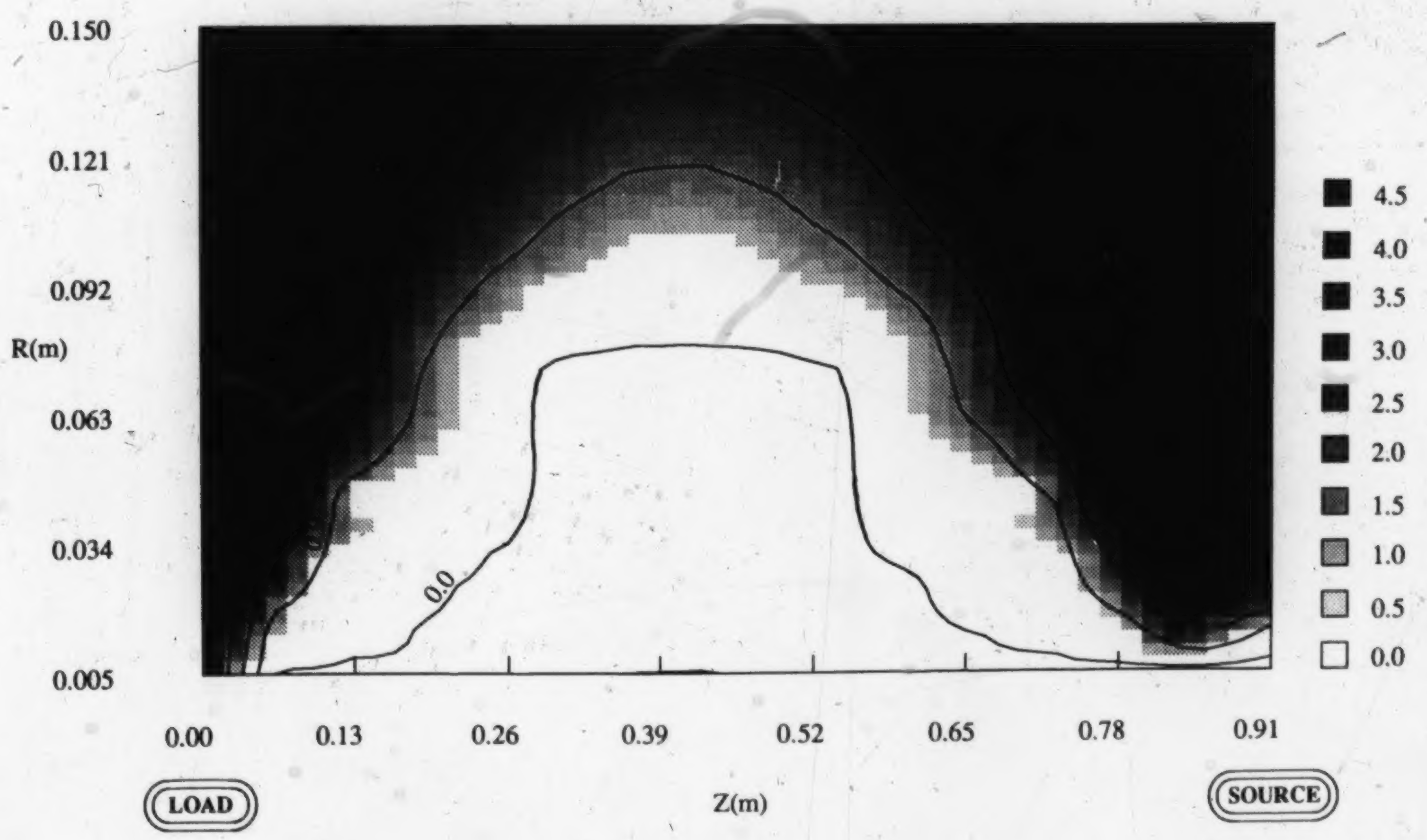

Figure 5.3c TEM COPTER simulation mass percent water content vs. position.
Initial conductivity = 0.00205 S/m. Time = 15000 sec. Termination = alternate open / short circuit.

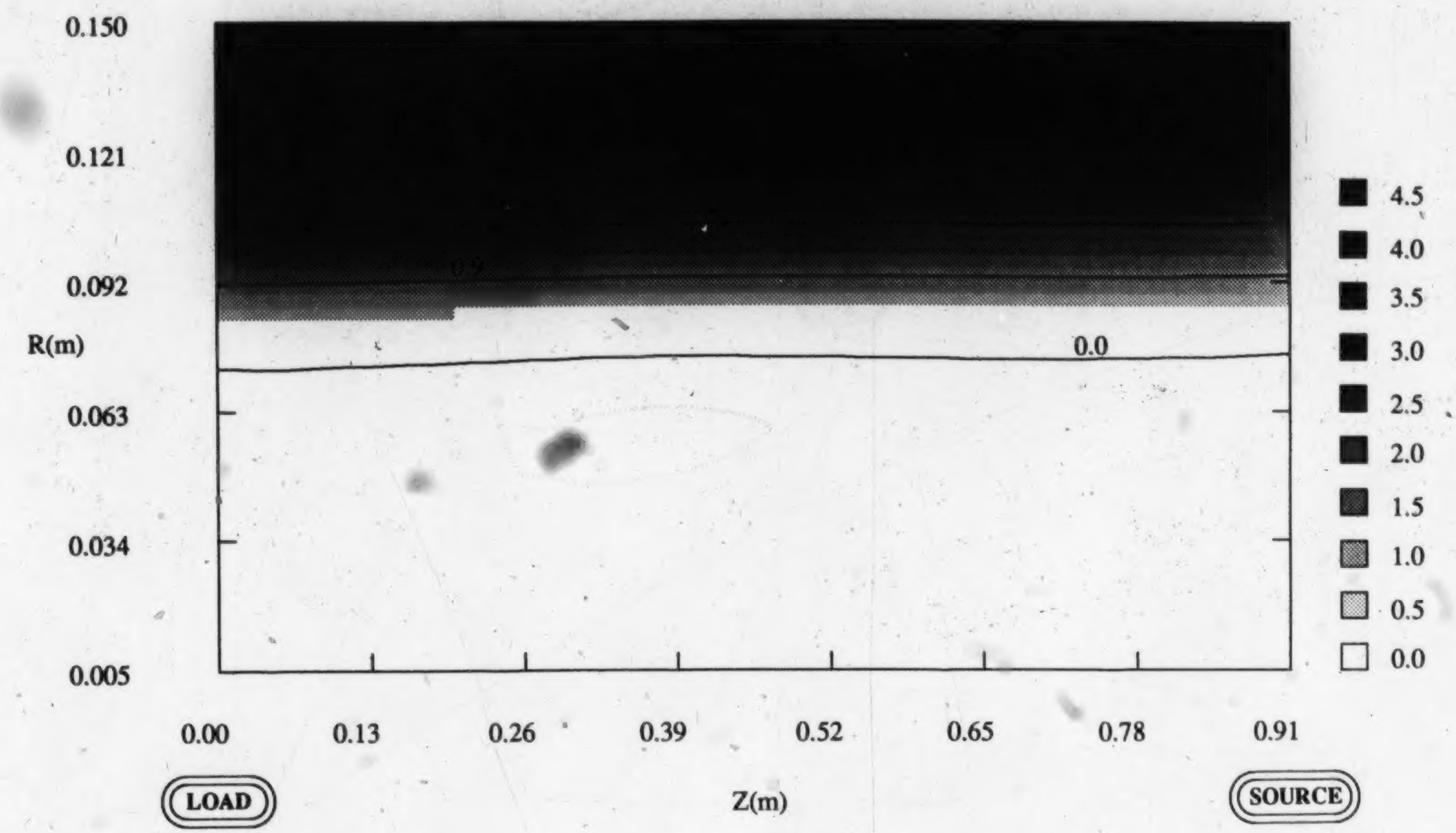

access to the end of the guiding structure is generally not available.

Published literature[11,25] suggests that industry has been performing guided wave heating under the assumption that TEM is the accepted mode of operation. However, the results of the previous chapter indicate that, in cases of higher initial conductivity, the presence of strong axial fields in addition to the TEM fields affects the RF heating in an electrically long guiding structure. Automatic interleaving is obtained between the axial fields and the TEM fields, since they may only exist in quadrature with each other in order to conform to the electrical boundary conditions of the waveguide. The results of the TEM experiment (Appendix A) and of Chapter 4 indicate that axial fields are always generated in the presence of dielectric conductor coatings, and are in fact unavoidable in many practical instances. These dielectric conductor coatings are easily self generated in coaxial waveguides by moisture evaporation, and may be manually installed if the waveguide geometry and fluid mobility do not facilitate their self generation. Rather uniform guided wave heating can often be obtained by merely installing unterminated conductors into the lossy medium, and by then applying power to the conductors at an appropriate RF frequency without further attention, as demonstrated in figure 4.7.

5.4 "Total Evaporation Boring"

Throughout the course of this project, hundreds of COPTER simulations were performed, along with several RF heating experiments. During most of these simulated and experimental events, it was observed that the thin uniform dielectric coating would first form on the entire length of the inner conductor before any significant medium heating would occur. Total evaporation boring did not occur because of this coating, since at the frequencies of interest the line attenuation was greatly reduced by the partial decoupling effect of the coating, and the wave therefore deposited its energy into much more of the lossy medium at a time. Such boring or flooding begins to occur when somewhat higher line attenuation forces the excitation wave to deposit most of its energy nearer to the source, *even after a thin coating begins to form on the inner conductor*. A much thicker dried dielectric zone must therefore develop near the source and progressively further down the line in order to reduce the attenuation and allow the wave to penetrate along the line. An axially tapered coating will form whose thickness occupies a significant portion of the radial dimension of the waveguide. In cases involving the highest levels of line attenuation, total evaporation boring occurs as the dried coating appears entirely between the inner and outer conductors and moves down the line as a solid front with little progressive tapering.

Recall that figure 5.1 showed the early water content results of a 100 MHz, 0.205 S/m TM COPTER heating simulation which is detailed in table 4.2. In this case, a thin dried coating formed near the source and quickly coated the entire inner conductor before any significant heating occurred in the bulk of the guide. With the coating in place, attenuation was small and uniform bulk heating resulted along the line. "Partial evaporation boring" exhibits heating characteristics between those of the self coating action and total evaporation boring, and is created in the presence of only somewhat higher levels of line attenuation. The self coating action can, for the same physical system, be changed to a partial evaporation boring mode of heating by simply increasing the operating frequency, which in turn provides the necessary additional line attenuation. A second simulation was performed using the same parameters, but with 500 MHz excitation, which doubled the initial line attenuation. As illustrated in figure 5.4, the results of this simulation indicate that partial evaporation boring, as a result of the increased line attenuation, was occurring. In this case, however, the use of still higher frequencies would be required to produce the extremely high attenuation which causes total evaporation boring. Again, the water content results are analogous to temperature distribution results.

In some cases, it is possible to experience the high attenuation necessary to establish total evaporation boring in a waveguide without operating at such high excitation frequencies. Based on the experimental evidence of the previous chapter, it is postulated that had the radially inward flow of fluids under the pressures of evaporation and gravity been significant, then an electromagnetic flood would have been observed. It is postulated that even if the excitation frequency is not excessively high, flooding may still take place in materials with high water saturation levels and highly mobile connate water (the "steam disappears" approximation would not be valid). Once an amount of material near the inner conductor is heated to the boiling point of the moisture, pressure begins to build due to the evolution of steam, and gravitational forces to some extent. If the connate fluid mobility is

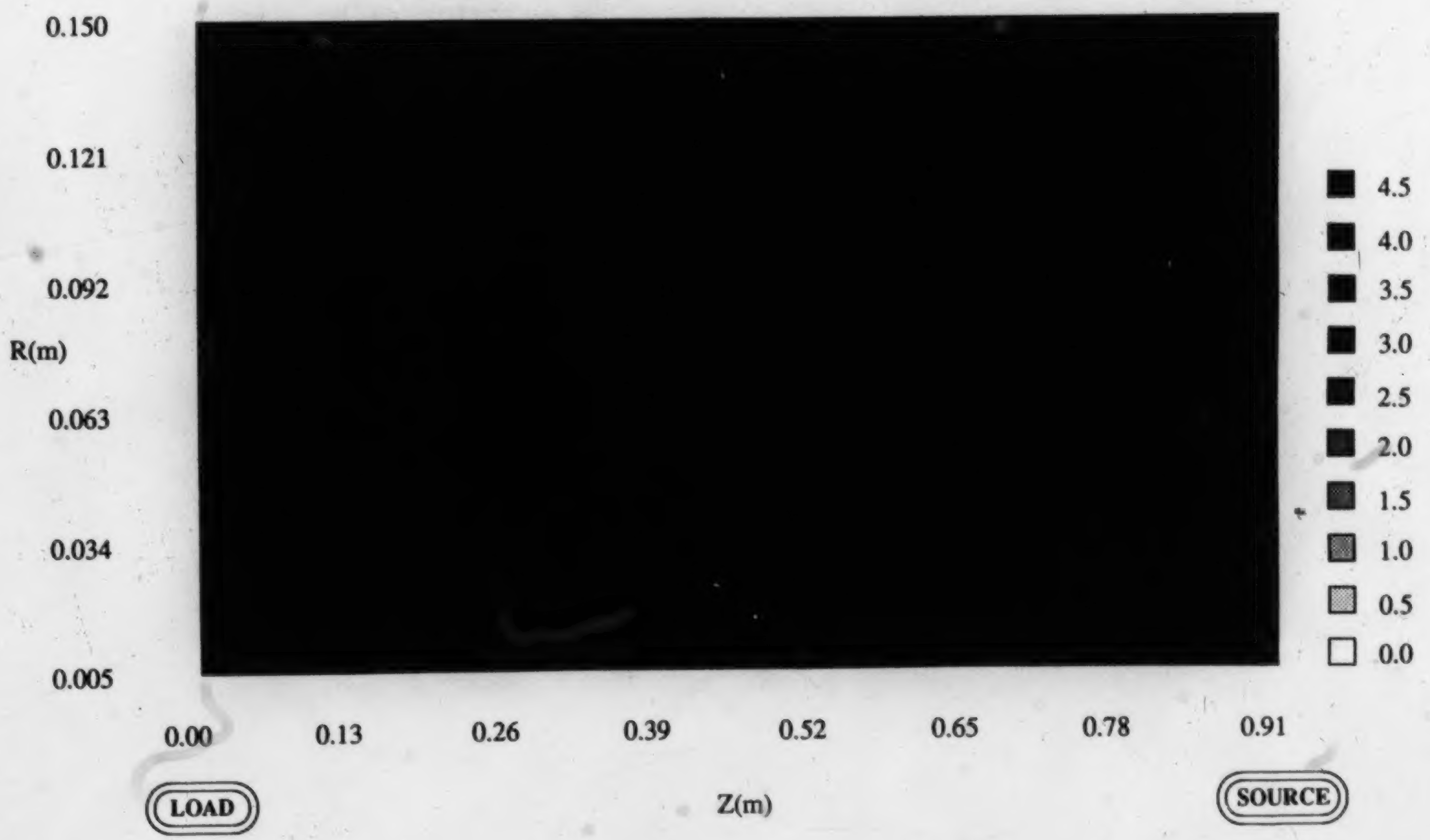

Figure 5.4a TM COPTER simulation mass percent water content vs. position. Initial conductivity = 0.205 S/m. Time = 0 sec. Frequency = 500 MHz.

Figure 5.4b TM COPTER simulation mass percent water content vs. position. Initial conductivity = 0.205S/m. Time = 107 sec. Frequency = 500 MHz.

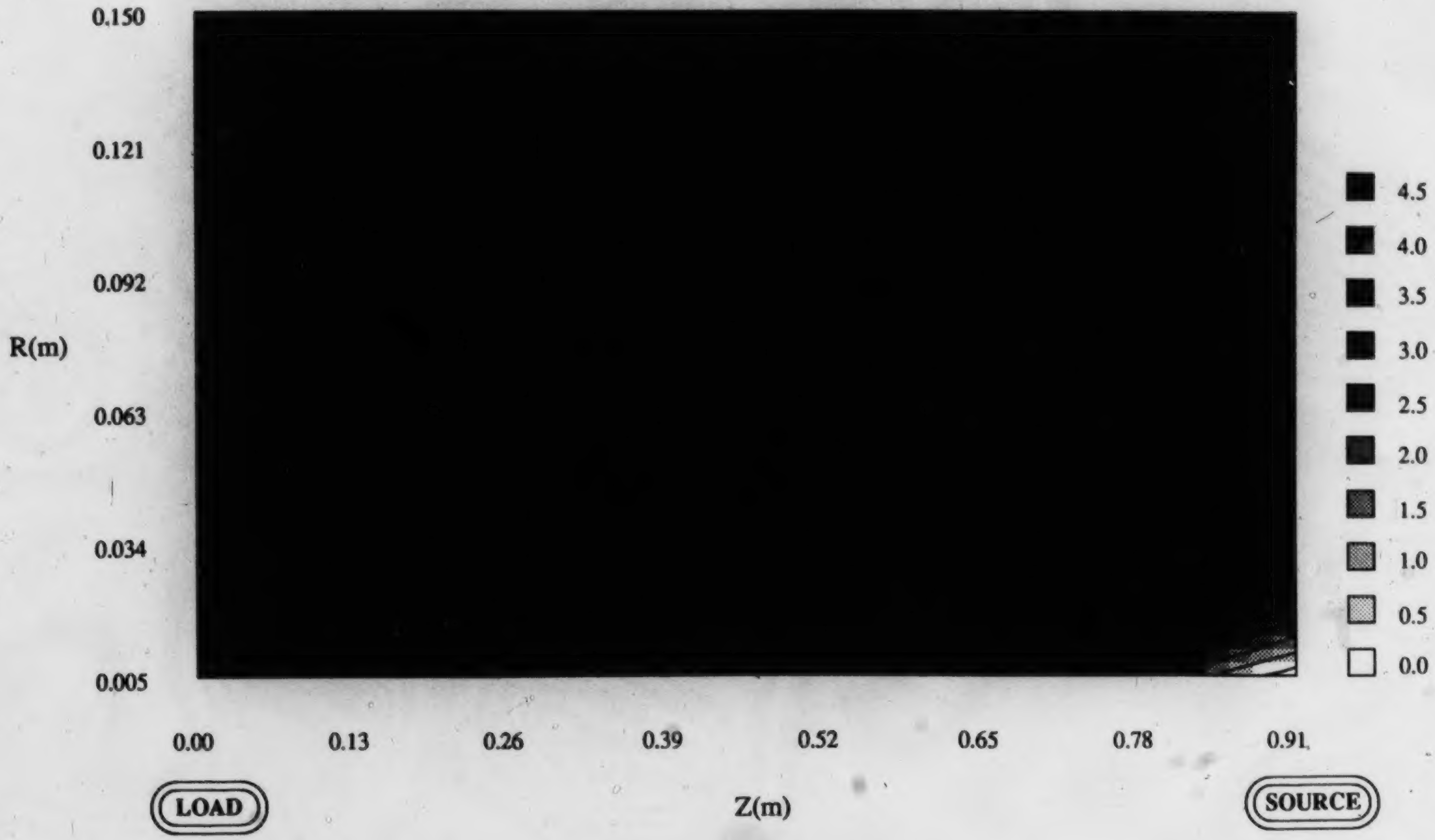

Figure 5.4c TM COPTER simulation mass percent water content vs. position.
Initial conductivity = 0.205S/m. Time = 888 sec. Frequency = 500 MHz.

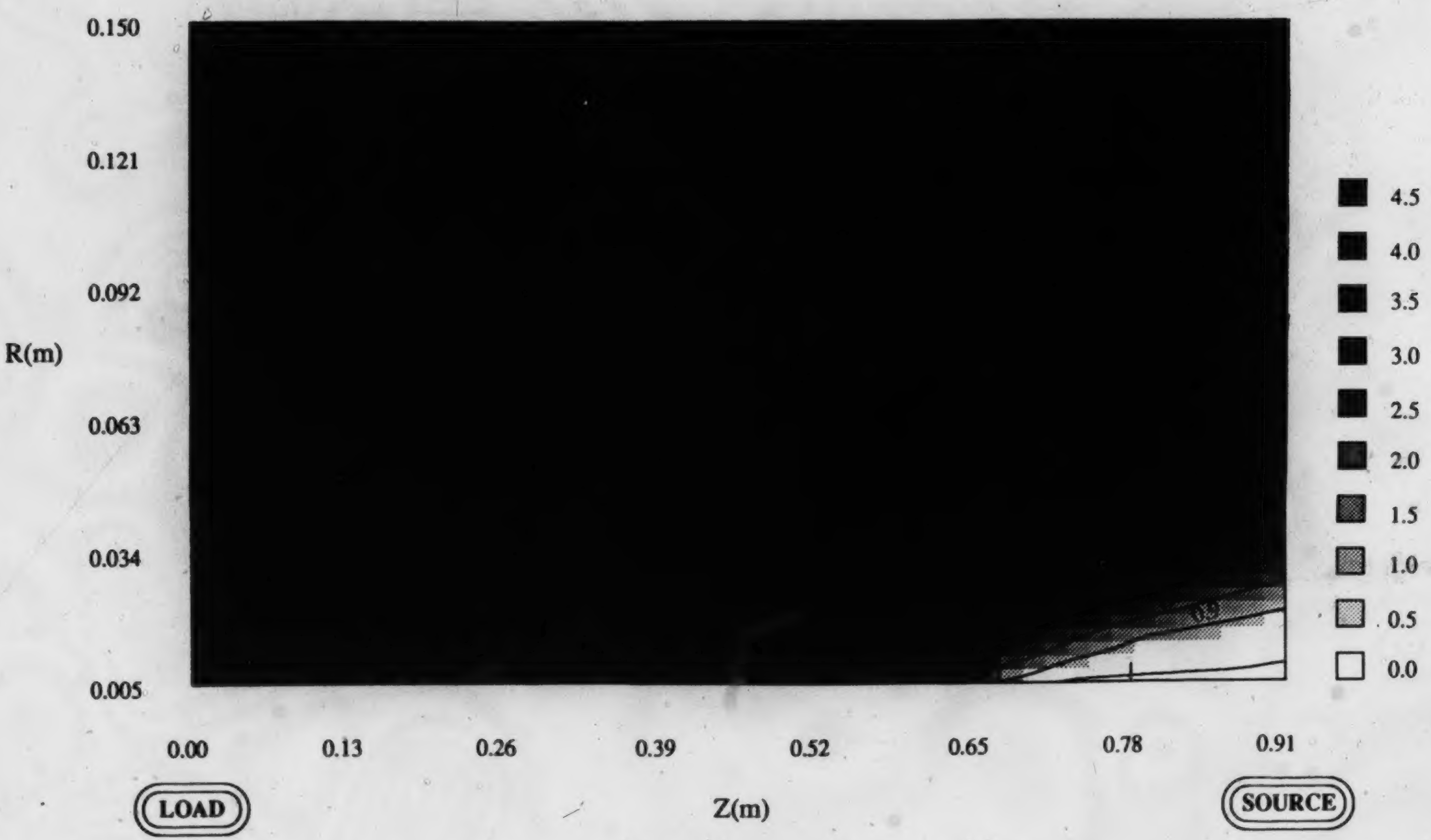

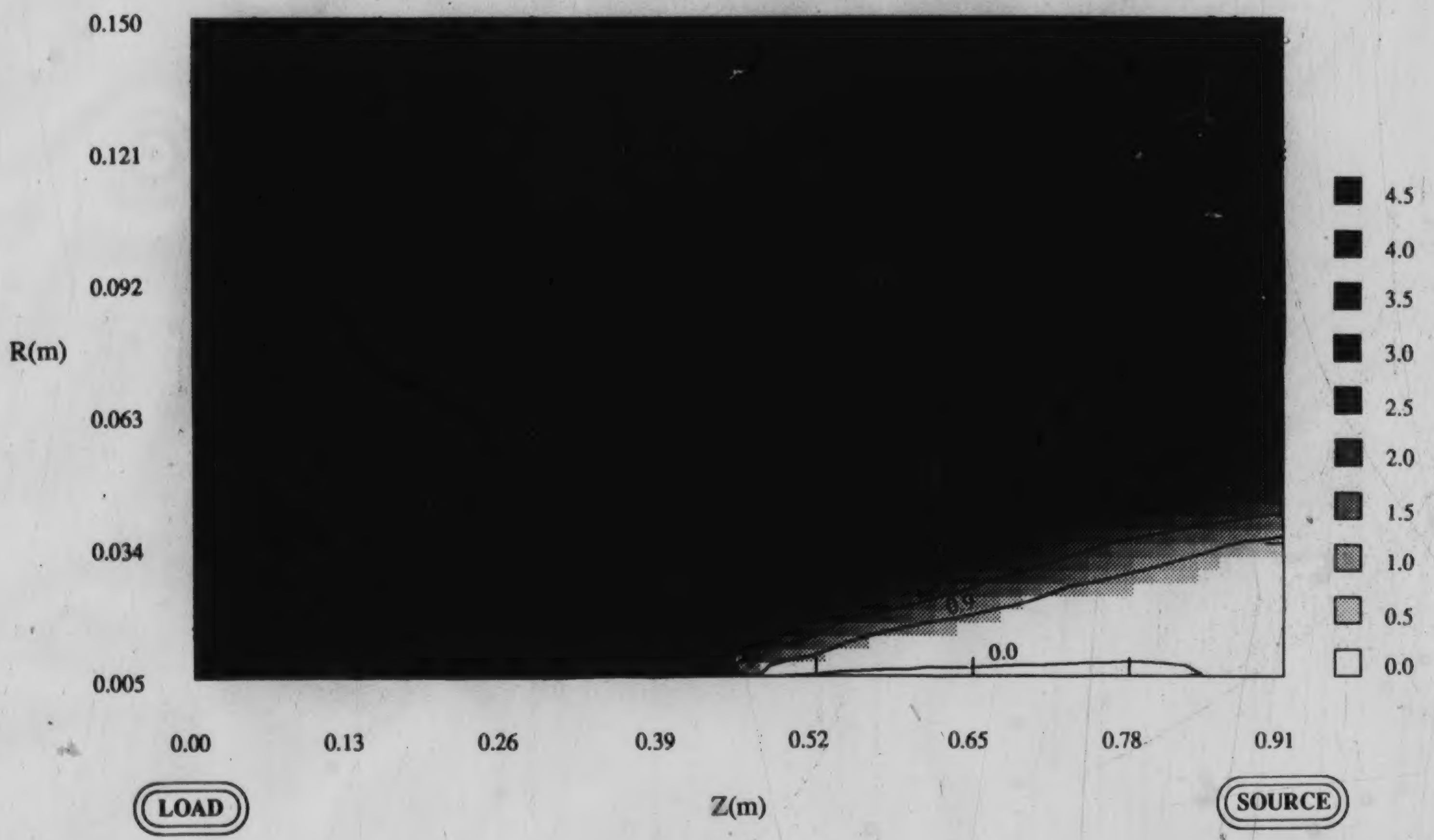

Figure 5.4d TM COPTER simulation mass percent water content vs. position. Initial conductivity = 0.205S/m. Time = 3040 sec. Frequency = 500 MHz.

Figure 5.4e TM COPTER simulation mass percent water content vs. position. Initial conductivity = 0.205S/m. Time = 4843 sec. Frequency = 500 MHz.

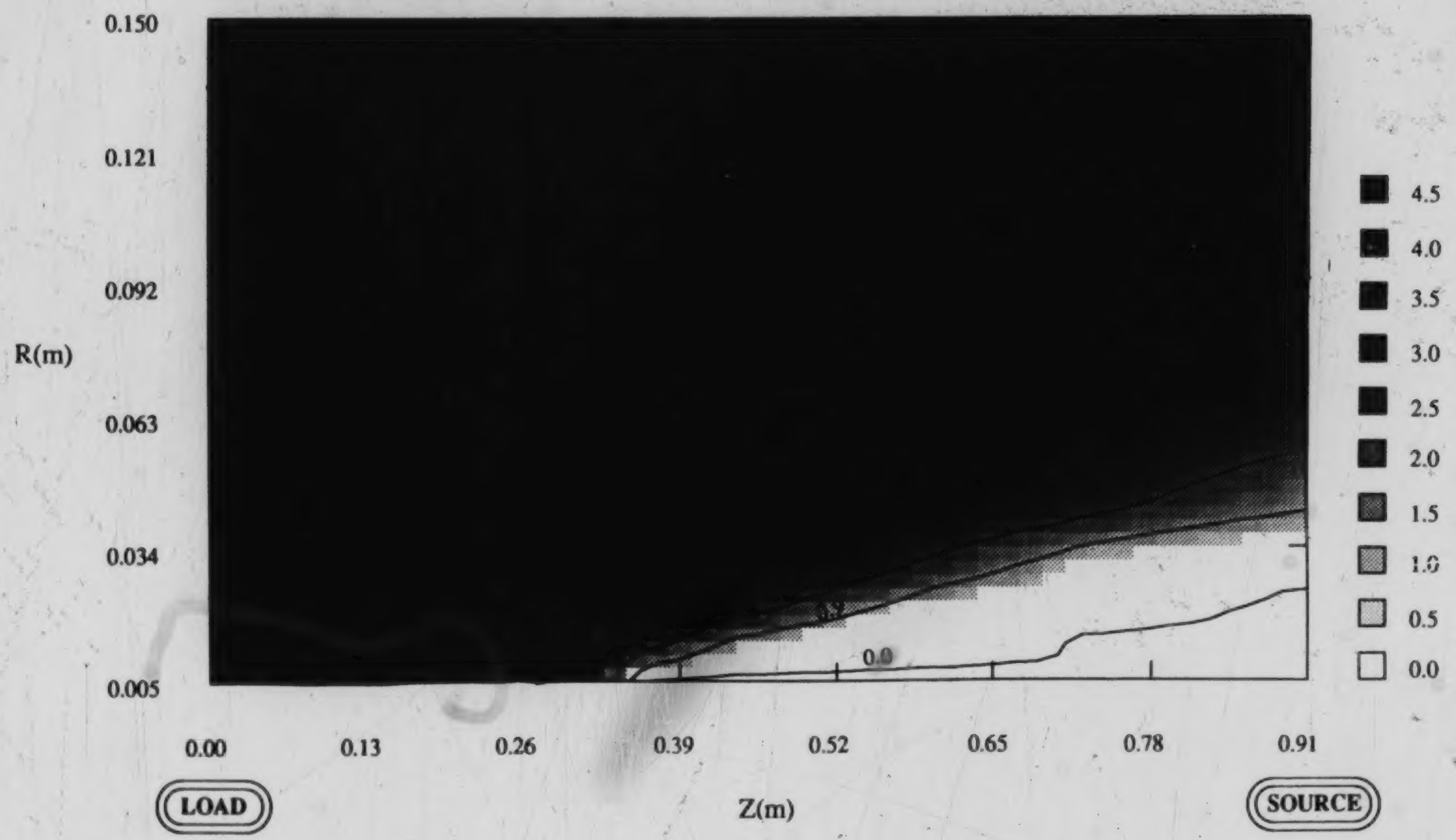

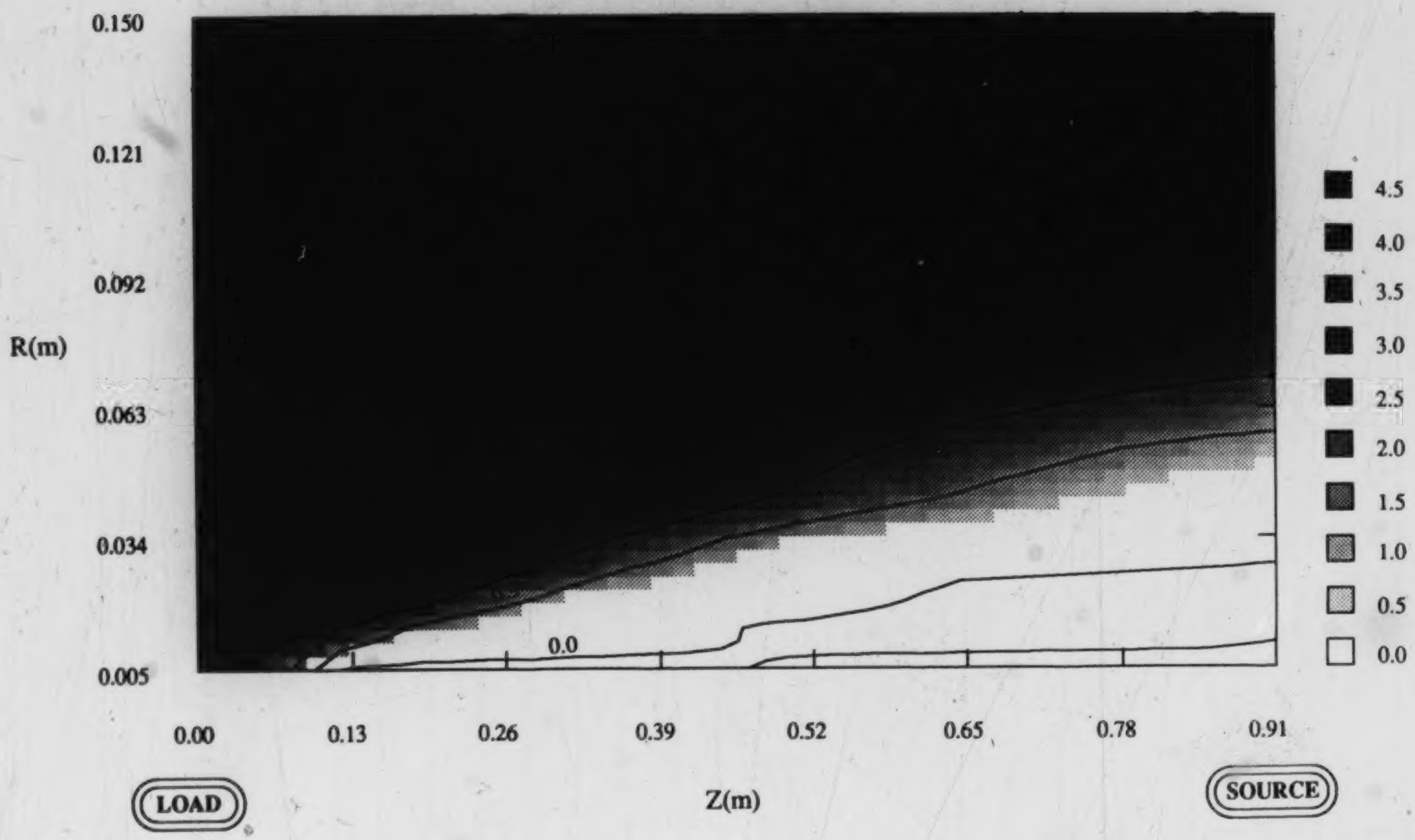

Figure 5.4f TM COPTER simulation mass percent water content vs. position.
Initial conductivity = 0.205S/m. Time = 8788 sec. Frequency = 500 MHz.

such that this pressure drives a large amount of the conductive fluid into the inner conductor as the medium near the conductor begins to evaporate, the conductor will be resaturated and will remain ionically coupled to the medium. A significant line attenuation will be maintained, since the inner conductor is replenished with fluid on an ongoing basis and the dried region cannot develop. This persistent attenuation forces the exciting electromagnetic wave into initially depositing most of its energy near the source, which instigates the electromagnetic flood as previously described. In order to test this postulation, a special "pseudo flow" fluid flow code was developed for COPTER. As a simulation with this coding in place progresses, water which would initially evaporate from a grid which was nearest to the inner conductor would then be removed uniformly from that entire axial slice, instead of from the innermost grid alone. For demonstration purposes only, this mimicks the large radial flow of liquid under the pressures of evaporation, and hence an extremely strong attenuation would be maintained. The water content results of such a simulation, which employed the brine-sand simulation parameters in table 4.2 and an initial conductivity of 0.205 S/m, are illustrated in figure 5.5. It is quite apparent that a simulated total evaporation boring flood was occurring.

It is postulated that the partial evaporation boring experiment conducted successfully by McPherson[14] at 52 MHz, with apparatus comparable to the full 20 % water saturation experiment of Chapter 4, was influenced by the flow of fluids. It is not possible to evaluate the efficiency of the boring processes from the information which has been obtained in this project, but one may conclude that a more complete accounting of fluid movement is necessary if one wishes to study the onset of a flood under a given circumstance.

Figure 5.5a TM COPTER simulation mass percent water content vs. position. Initial conductivity = 0.205 S/m. Time = 0 sec.

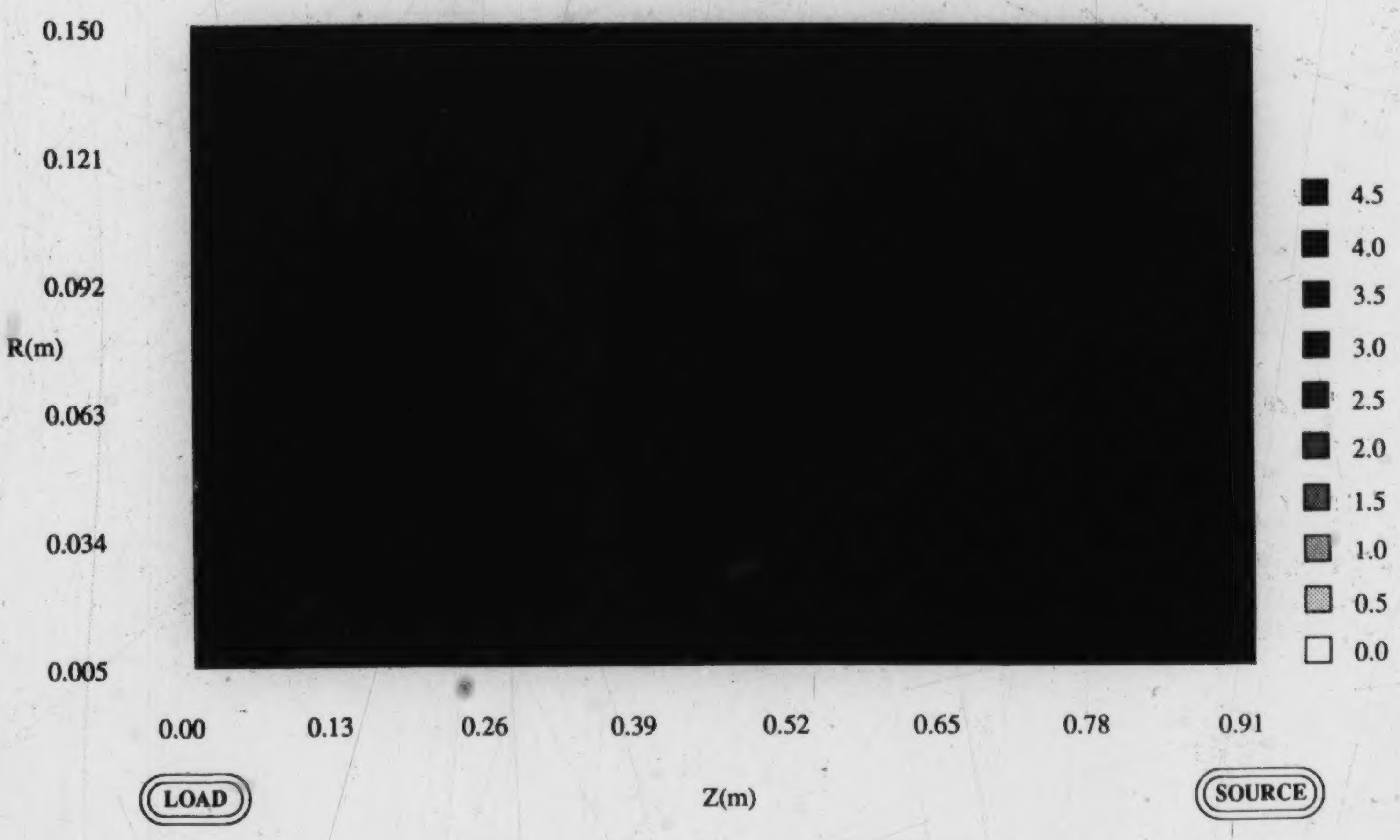

Figure 5.5b TM COPTER simulation mass percent water content vs. position.
Initial conductivity = 0.205 S/m. Time = 471 sec.

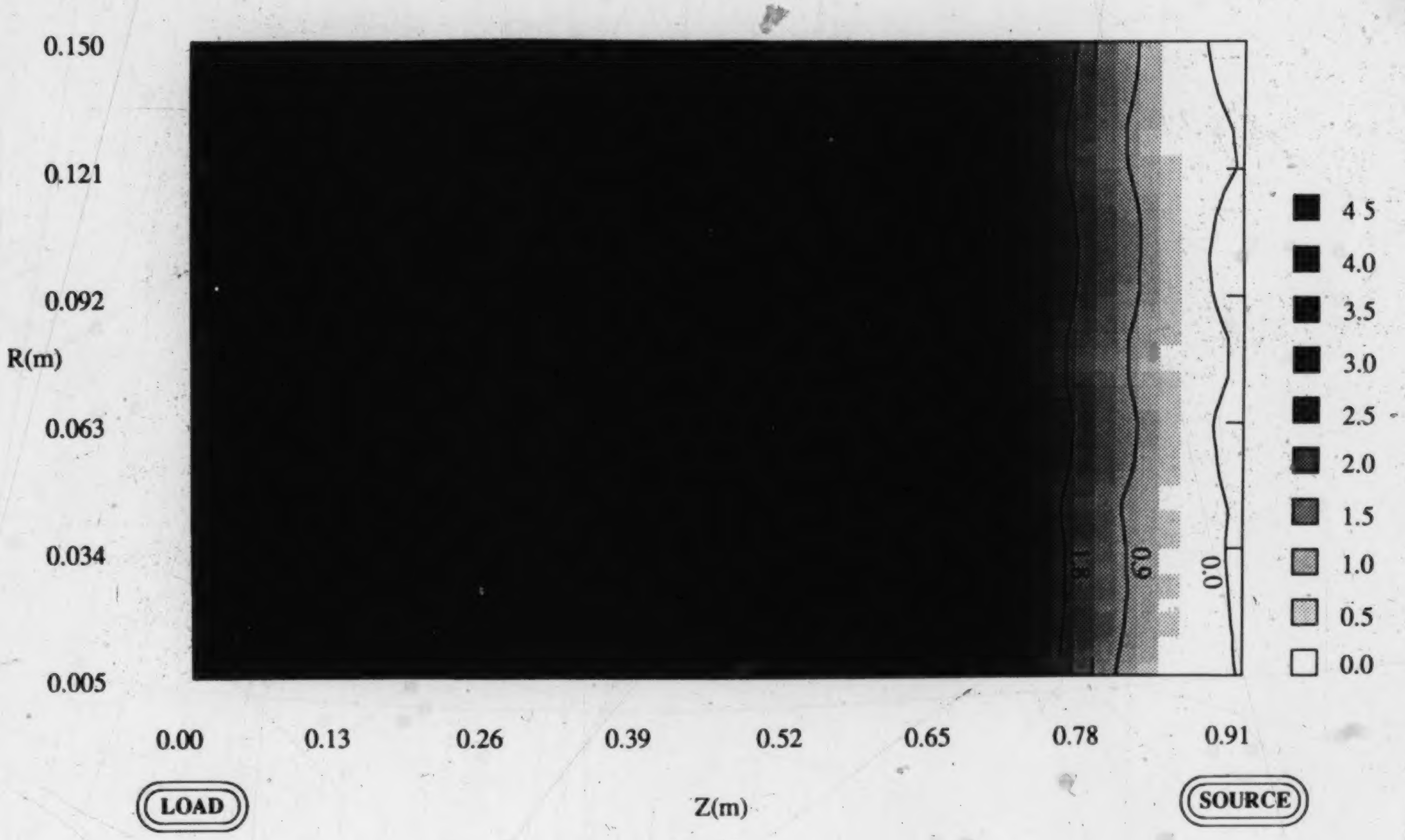

Figure 5.5c TM COPTER simulation mass percent water content vs. position.
Initial conductivity = 0.205 S/m. Time = 9711 sec.

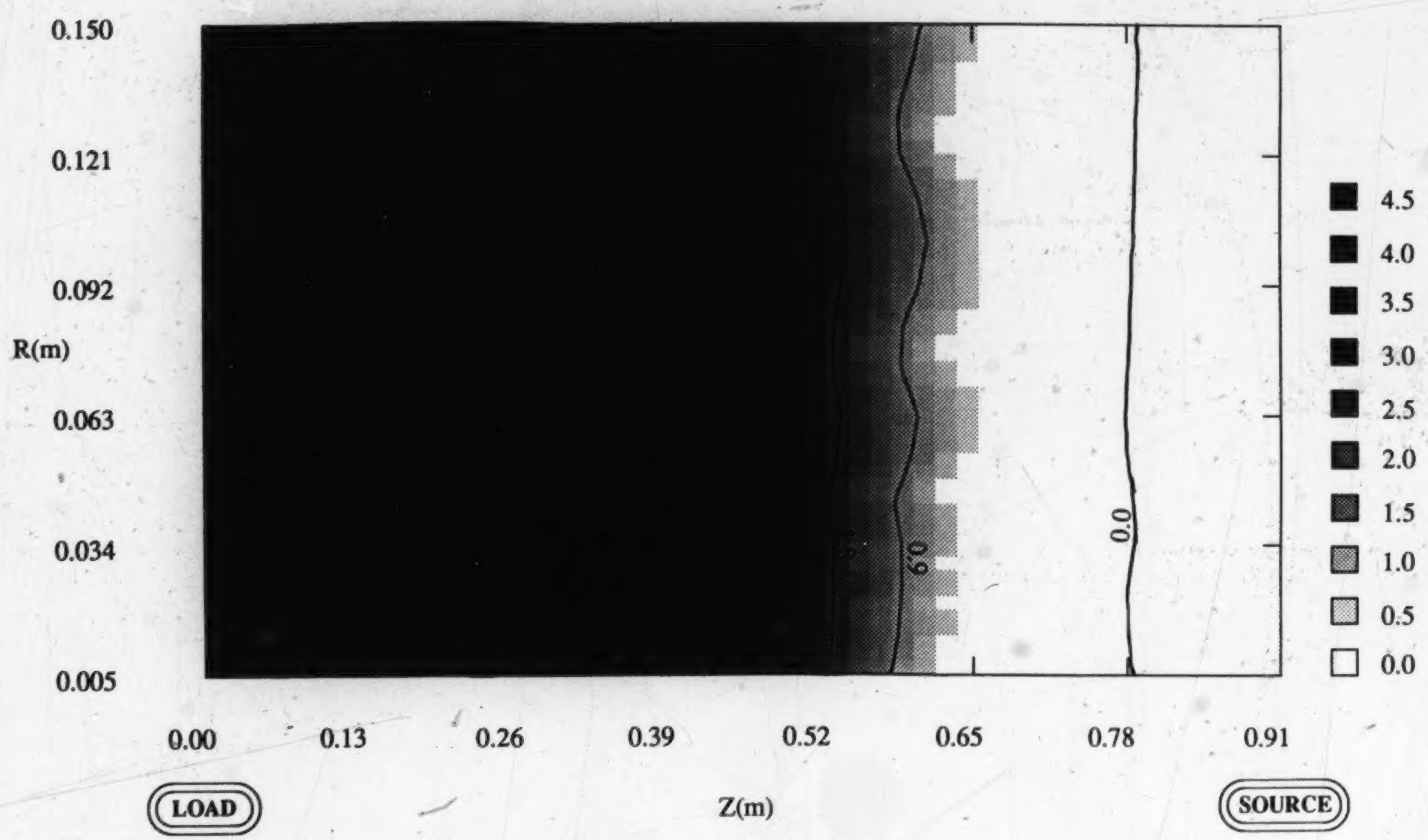

Figure 5.5d TM COPTER simulation mass percent water content vs. position.
Initial conductivity = 0.205 S/m. Time = 14706 sec.

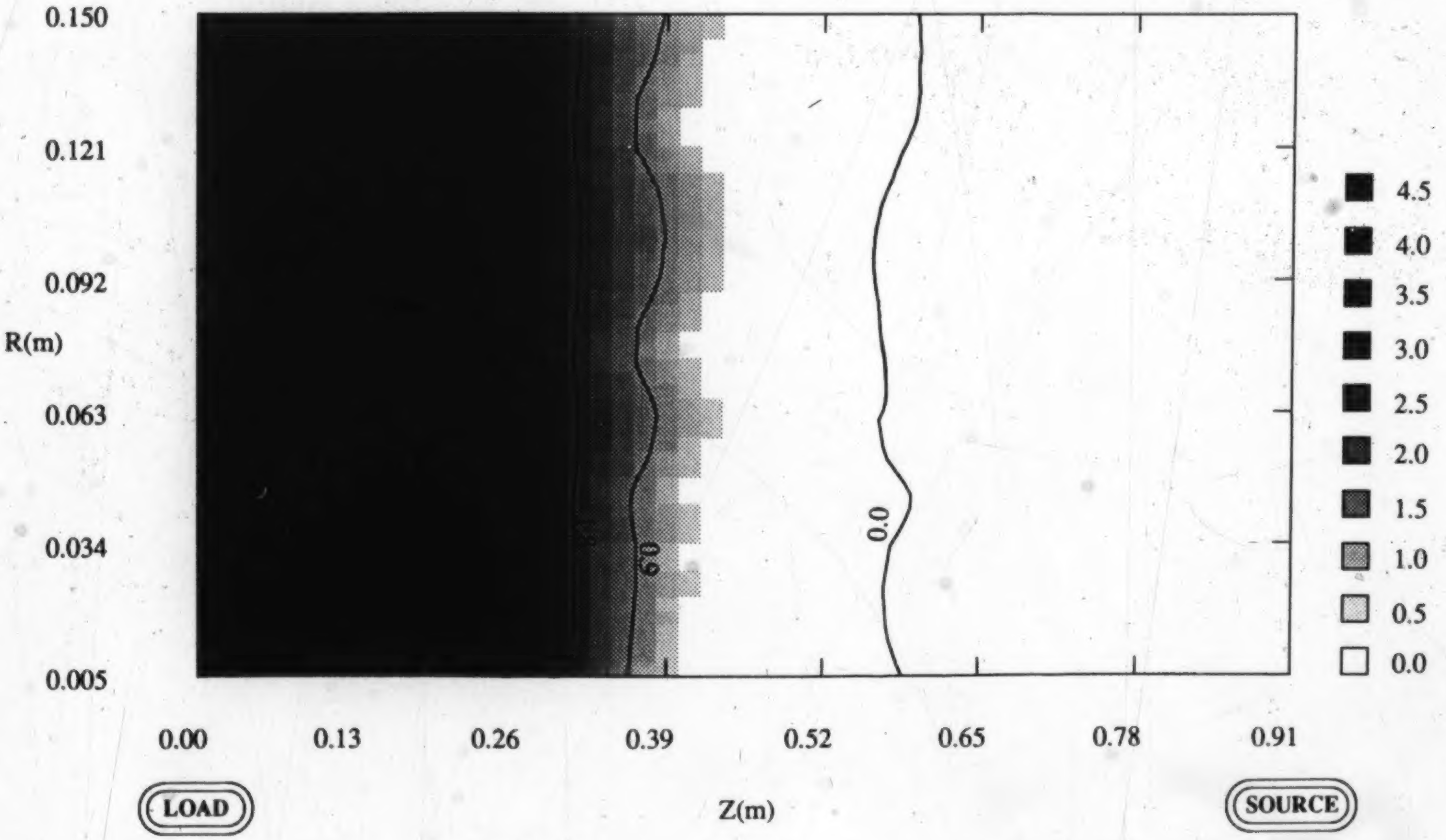

Figure 5.5e TM COPTER simulation mass percent water content vs. position.
Initial conductivity = 0.205 S/m. Time = 19706 sec.

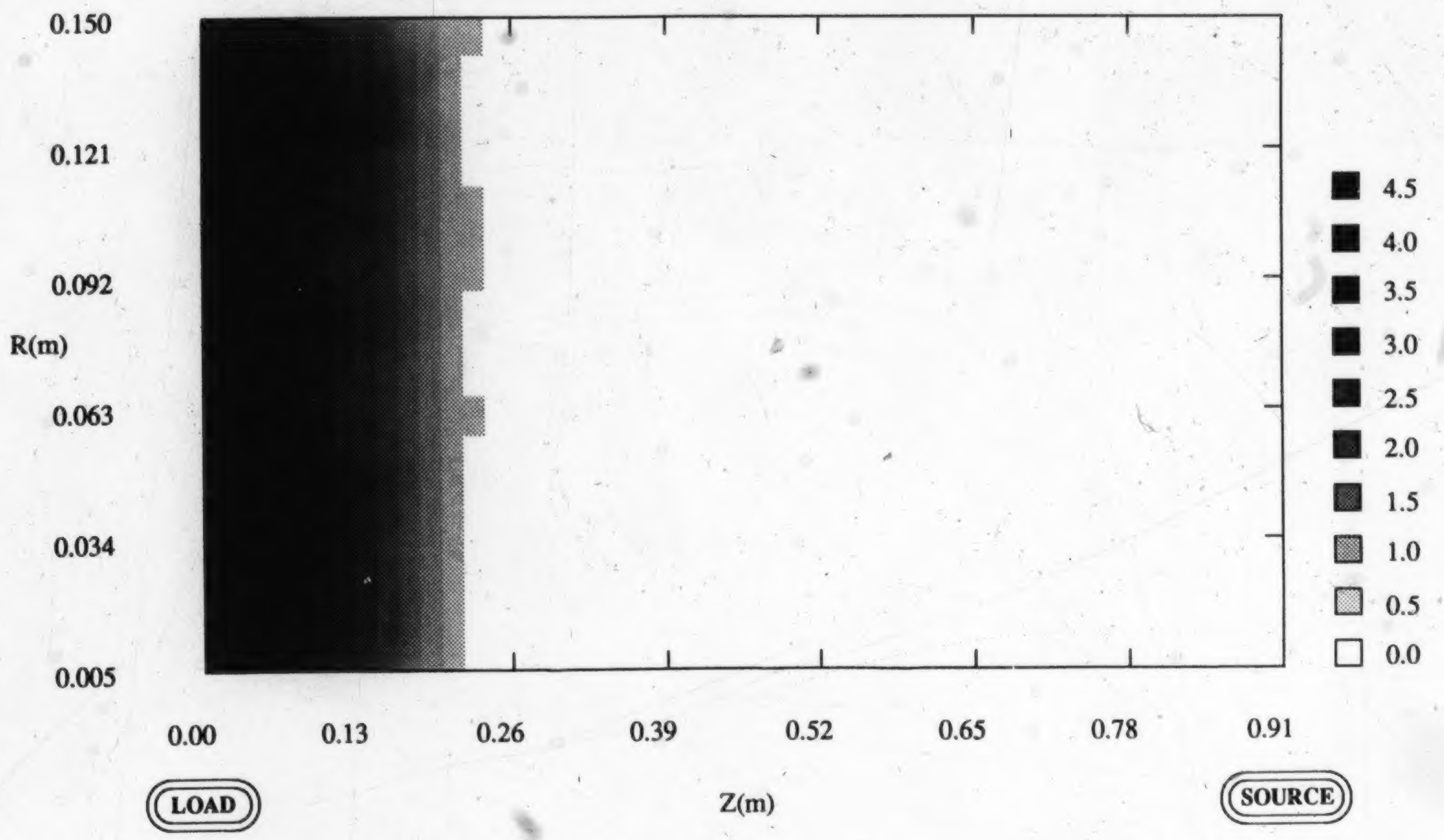

6. Conclusions

The COPTER simulation routine is a reliable means of predicting the RF heating of porous, low moisture, lossy materials within a coaxial guiding structure. The simulation process is accomplished by solving the electrical and thermal problems via a numerical approach. The additional difficulty of simulating the phase change of the connate moisture is accommodated by employing a fully implicit thermal solution procedure. Fluid movements in the medium resulting from the pressures of evaporation and gravity must ordinarily be accounted for in the simulation process. If the moisture saturation level is sufficiently low such that the connate liquid is virtually immobile, however, it is possible to ignore the effects of fluid flow. Flowing liquids may be present in moderately low amounts if enough power is applied such that the radially flowing liquids are evaporated and driven out of the medium before they influence the electrical response. The major effect of flow in this case would otherwise be to slow down the growth of the moisture depleted region surrounding the inner conductor. Under these circumstances, it is also possible to ignore the effects of fluid flow. COPTER employs this insight by assuming that steam simply "disappears", once it has evolved. Although this approximation was used in order to simplify the development and use of COPTER, many field applications which employ electromagnetic heating do contain porous materials with appropriately low moisture levels.

In general, it is not possible to simulate the RF heating of practical materials in a multi-conductor guiding structure by assuming that only TEM fields are present. Dielectric inhomogeneities in the medium, whether manually installed, intrinsically present, or most commonly, as a result of the heating process itself, are likely to be present. A thin electrical inhomogeneity will promote the appearance of strong non TEM axial electric fields. Two versions of COPTER have been developed as a result. TEM COPTER will perform simulations of the coaxial electromagnetic heating of materials which will remain free of axial fields and significant flowing fluids throughout the heating period. If the medium is of a low loss nature, or if an electrically short, open circuited guide is employed in the RF heating process, TEM COPTER will correctly predict the results of the process. TM COPTER, with its full electromagnetic field solution capabilities, may be used to predict the electromagnetic heating of *any* material within a coaxial guiding structure, for which the "steam disappears" fluid flow approximation is valid.

A desirable heating procedure is often one which achieves uniform deposition of energy in the lossy material. Field propagation behavior, such as poor medium penetration and the onset of standing waves, represents the common source of heating non uniformity in the guided wave heating process. Investigations with the TEM COPTER simulator have revealed that the antinodal heating irregularities which predominate in low loss heating cases are most efficiently removed by alternately applying open circuited and short circuited loads to the terminating end of the guide. The poor field penetration which characterizes the RF heating of higher loss materials, such as Athabasca oil sands, is efficiently accommodated by first applying thin uniform dielectric coatings to the waveguide conductors. These coatings, which are also easily self generated in all but the most highly attenuative materials, increase the penetration depth of the impinging RF wave. In many situations, antinodal heating anomalies do not occur with the coatings in place, because of the presence of the axial electric field component in addition to the transverse field component. These components intrinsically exist in quadrature along the waveguide, such that the heating is much more uniform under these circumstances. If high attenuation is sustained during heating due to an extremely high excitation frequency, or to the liberal presence of mobile fluids within the material which prevents the early formation of the thin dry dielectric coating on the conductors, for example, total evaporation boring occurs, as a distinct heat front moves down the waveguide and leaves a dried zone in its wake. A heating process characterized by relatively high levels of attenuation, but not so high as to facilitate total evaporation boring, involves partial evaporation boring, which exhibits properties of both total evaporation boring and the dielectric conductor coating process.

In order to increase the capabilities of the COPTER simulator, it is recommended that a full multiphase fluid flow code be added. This will facilitate a more quantitative examination of the very promising "steam disappears" fluid flow approximation, as well as of the evaporation boring process. An accounting of thermal losses to the surroundings would be of some practical benefit, since one cannot readily install styrofoam insulation onto in situ waveguides. Because of the prohibitively long run times of TM COPTER, some effort to improve the efficiency of the HERZ electrical solver is warranted. The possible replacement of the HERZ direct matrix inverter by complex ADIP, along with compiler optimization procedures, or possibly the use of more specialized computing hardware, should dramatically reduce the run times of TM COPTER. Dynamic grid quantity reselection during the course of a simulation should also help to speed the simulator, since the initial choice of grid quantities for both dimensions must always be quite liberal. Once the dried conductor coating is formed, the field inside the coating is almost purely TEM, and a longer wavelength than initially is present, which relaxes the grid quantity requirements. Finally, in order to facilitate the practical application of COPTER, another version of the simulator should be written in three dimensional cartesian geometry.

References

1. F.S. Chute, F.E. Vermeulen and M.R. Cervenan, Physical Modelling of the Electrical Heating of the Oil Sand Deposits, Final Report AOSTRA Agreement No.31, October, 1978.

2. D. Towson, The Electric Preheat Recovery Process, 2nd International Conference on the Future of Heavy Crude and Tar Sands, Caracas, Venezuela, 7-17 February, 1982, 869.

3. F.S. Chute, F.E. Vermeulen, R.G. McPherson, A.D. Hiebert and J. Fearn, Electromagnetic Heating of Oil Sands, Final Report AOSTRA Agreement No. 296, June, 1985.

4. J.S. Broz, W.T. Savery, J.E. Bridges and G.C. Sresty, Results from a Preliminary Feasibility Study of Electromagnetic Hot Water Flooding for Tar Sands and Heavy Oil, 20th Intersociety Energy Conversion Engineering Conference, Miami Beach, 18-23 August, 1985.

5. J.E. Bridges, G.C. Sresty, H.L. Spencer, R.A. Wattenberger, Electromagnetic Stimulation of Heavy Oil Wells, 3rd International Conference on Heavy Crude and Tar Sands, Long Beach, California, 22-31 July, 1985.

6. D.J. Howling and H.A. Palmer, Method and Apparatus for Combatting Encroachment By In Situ Treated Formations, U.S. Patent No. 4576231, 18 March, 1986.

7. J.E. Bridges, J.J. Krstansky, A Taflove and G. Sresty, The IITRI In Situ RF Fuel Recovery Process, Journal of Microwave Power, 18(1983)3.

8. R.G. McPherson, F.S. Chute and F.E. Vermeulen, The Electromagnetic Flooding Process for In Situ Recovery of Oil From Athabasca Oil Sand, Journal of Microwave Power, 21(1986)129.

9. G.C. Sresty, H. Dev, R.H. Snow and J.E. Bridges, Recovery of Bitumen from Tar Sand Deposits With the Radio Frequency Process, SPE Reservoir Engineering, 1(1986)85.

10. J.S. Osborne, In Situ Oil Shale Process, Canadian Patent No. 1199573, 21 January, 1986.

11. J.E. Bridges and Allen Taflove, Apparatus and Method for In Situ Controlled Heat Processing of Hydrocarbonaceous Formations, U.S. Patent No. 4449585, 22 May, 1984.

12. G.C. Sresty, R.H. Snow and J.E. Bridges, The IITRI RF Process to Recover Bitumen From Tar Sand Deposits - A Progress Report, 2nd International Conference on the Future of Heavy Crude and Tar Sands, Caracas, Venezuela, 7-17 February, 1982, 871.

13. R.G. McPherson, F.S. Chute and F.E. Vermeulen, Recovery of Athabasca Bitumen With The Electromagnetic Flood Process, Journal of Canadian Petroleum Technology, 24(1985)44.

14 R.G. McPherson, High Frequency Electric Heating of the Athabasca Oil Sands, Ph.D. Thesis, University of Alberta, Fall 1985.

15. D.C. Ellinger, Radio Frequency Heating of Low Conductivity Materials with a Semi Cylindrical Solenoid, M.Sc. Thesis, University of Alberta, Spring, 1987.

16. A.D. Hiebert, Modelling of the Electric Preheat Process, Ph.D. Thesis, University of Alberta, Edmonton, Alberta, June, 1986.

17. C.F. Gerald and P.O. Wheatley, Applied Numerical Analysis, Addison Wesley, Section 8.1, (1989).

18. D.S. Burnett, Finite Element Analysis,, Addison Wesley, Section 11.3, (1987).

19. loc. cit. (17), Section 7.11.

20. W.H Press, B.P. Flannery, S.A.Teukolsky, and W.T. Vetterling, Numerical Recipes, Cambridge University Press, Section 2.6, (1988).

21. S.C. Chapra and R.P. Canale, Numerical Methods for Engineers, McGraw Hill, (1988).

22. MPW Shell Version 3.0. Apple Computer Inc. 1985 - 88.

23. A.D. Hiebert, Computer Simulation of In Situ, Low Frequency Electrical Heating of Oil Sand Formations, M.Sc. Thesis, University of Alberta, Edmonton, Alberta, Spring, 1981.

24. F.E. Vermeulen, Applied Electromagnetics Group, Department of Electrical Engineering, University of Alberta, private communication, May 1989.

25. J. Pound, Radio Frequency Heating in the Timber Industry, E.&F.N. SPON Ltd., (1970).

26. R. De Bibhas, Measurement and Analysis of Broadband Dielectric Properties of Brine Saturated Rocks, Proceedings of SPWLA Twenty Sixth Annual Logging Symposium, June 17-20, 1985.

27. G.E. Archie, Electrical Resistivity, An Aid In Core Analysis Interpretation, Bulletin of American Association of Petroleum Geologists, 31(1947)350.

28. F.E. Vermeulen, F.S. Chute, M.R. Cervenan and J. Fearn, Physical Modelling of the Electrical Heating of the Oil Sand Deposits, Final Report AOSTRA Agreement No. 58, June 1982.

29. W.H. Somerton, J.A. Keese and S.L. Chu, Thermal Behavior of Unconsolidated Oil Sands, Society of Petroleum Engineers Journal, 14(1974)513.

30. M.R. Cervenan, F.E. Vermeulen and F.S. Chute, Thermal Conductivity and Specific Heat of Oil Sand Samples, Canadian Journal of Earth Sciences, 18, No. 5, (1981)926.

Appendix A. Selected Results from the TEM Experiment

As discussed in Chapter Two, the TEM experiment illustrates the dependence of axial fields on dielectric conductor coating thickness, applied frequency, and medium conductivity. A brine filled short circuited 0.91 m long, 0.3 m diameter waveguide was used. The inner conductor diameter was 0.0095 m, and all measurements were taken at r = 4.6 cm. Although an open circuited load would allow the demonstration of the existence of predominantly TEM fields for small guide lengths, short circuited loads minimize field fringing. Also, axial field strength is maximized by the shorted load in small guide length cases, thus establishing conservative guidelines for evaluating the validity of the TEM approximation. If the guide length is electrically significant, which is often the case, loading has no bearing on the evaluation of the TEM approximation, since the fields may be examined away from the axial field antinode at the short circuit. Three groups of graphs are given in order to illustrate three specific trends. Group A.1 shows the increasing relative axial field strength with increasing conductor coating thicknesses. Group A.2 depicts how the axial fields are reduced as the applied frequency is increased. The final group, A.3, illustrates the increased axial field content which results from increasing material conductivity. The conductivities of the brines, the operating frequencies, and the outer diameters of the dielectric coatings are indicated on each graph in the format [conductivity \ frequency \ outer diameter].

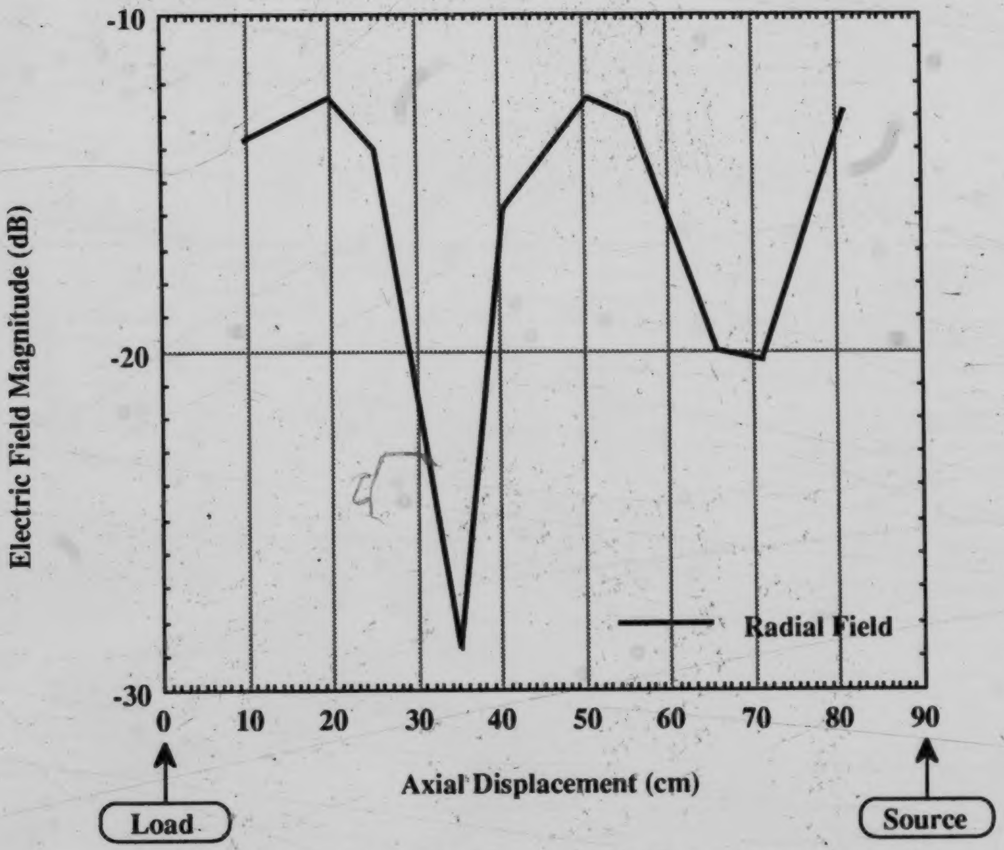

Figure A.1a Relative field magnitudes [1E-3 S/m|50 MHz|9.563 mm].

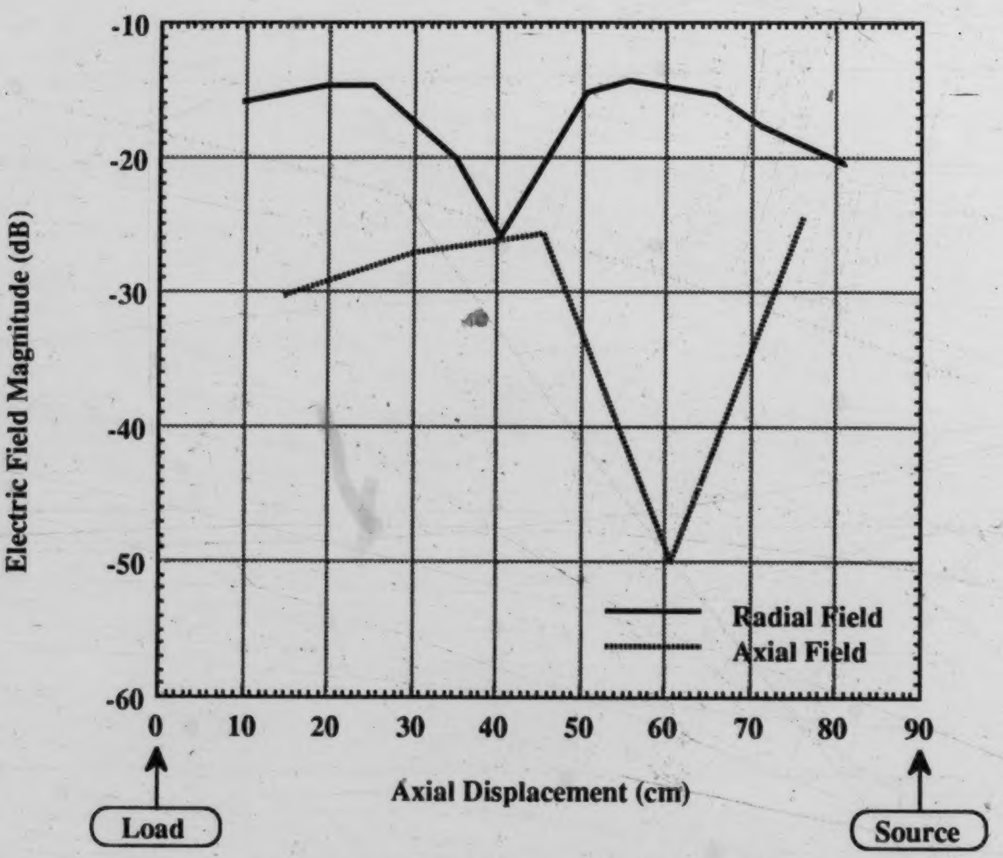

Figure A.1b Relative field magnitudes [1E-3 S/m|50 MHz|9.931 mm].

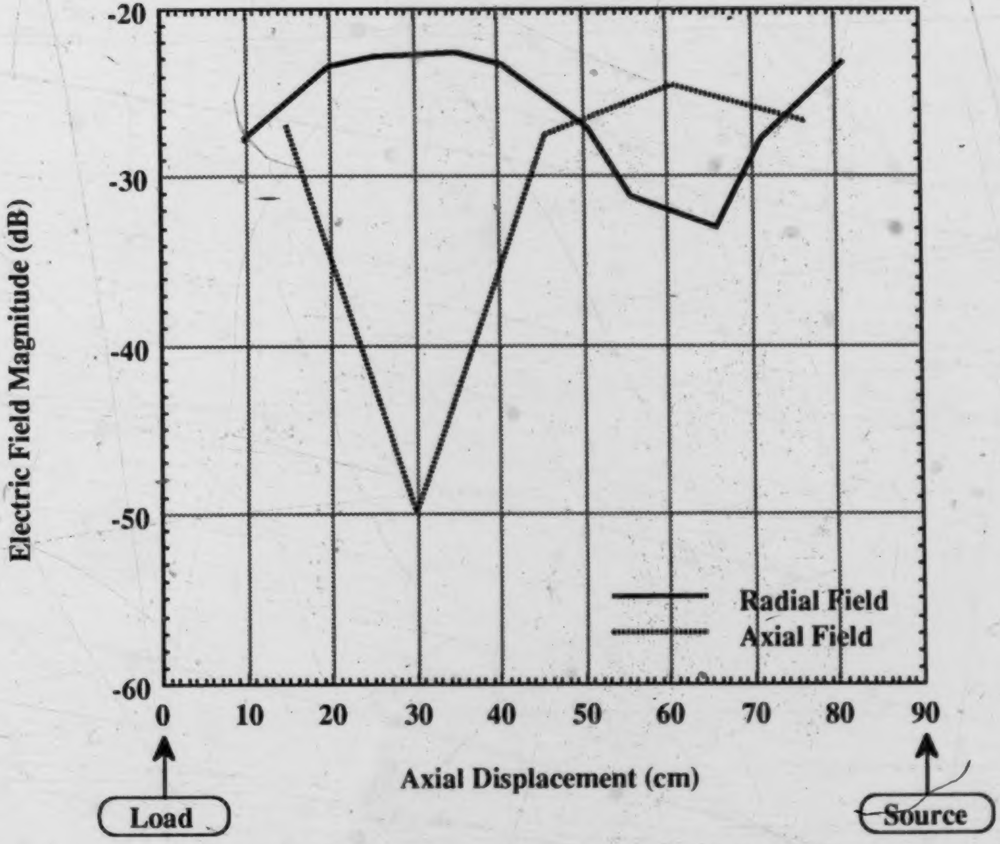

Figure A.1c Relative field magnitudes [1E-3 S/m|50 MHz|12.700 mm].

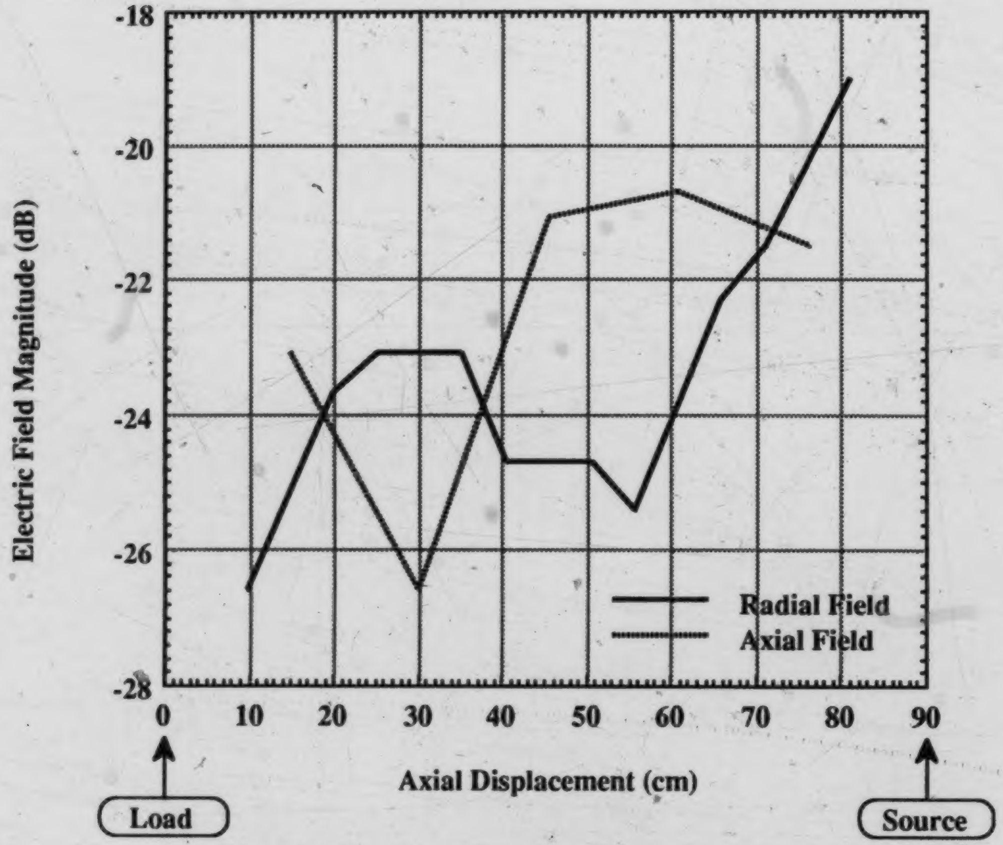

Figure A.2a Relative field magnitudes [1.29 S/m|20 MHz|9.931 mm].

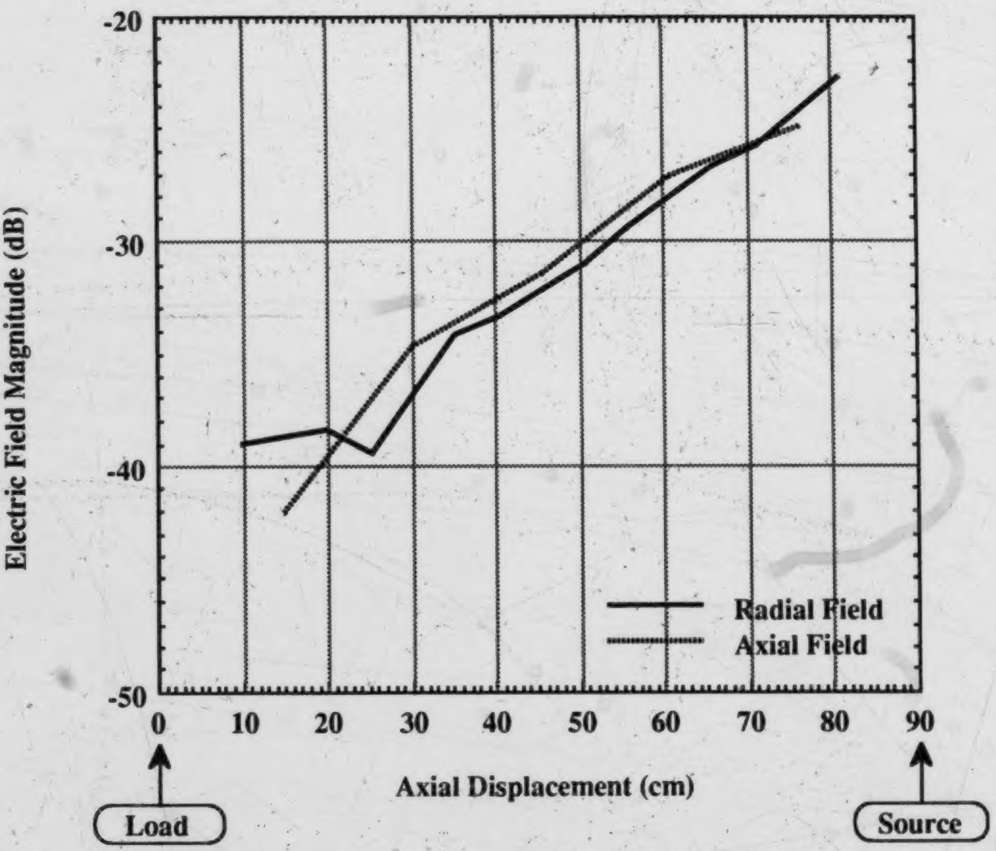

Figure A.2b Relative field magnitudes [1.29 S/m|50 MHz|9.931 mm].

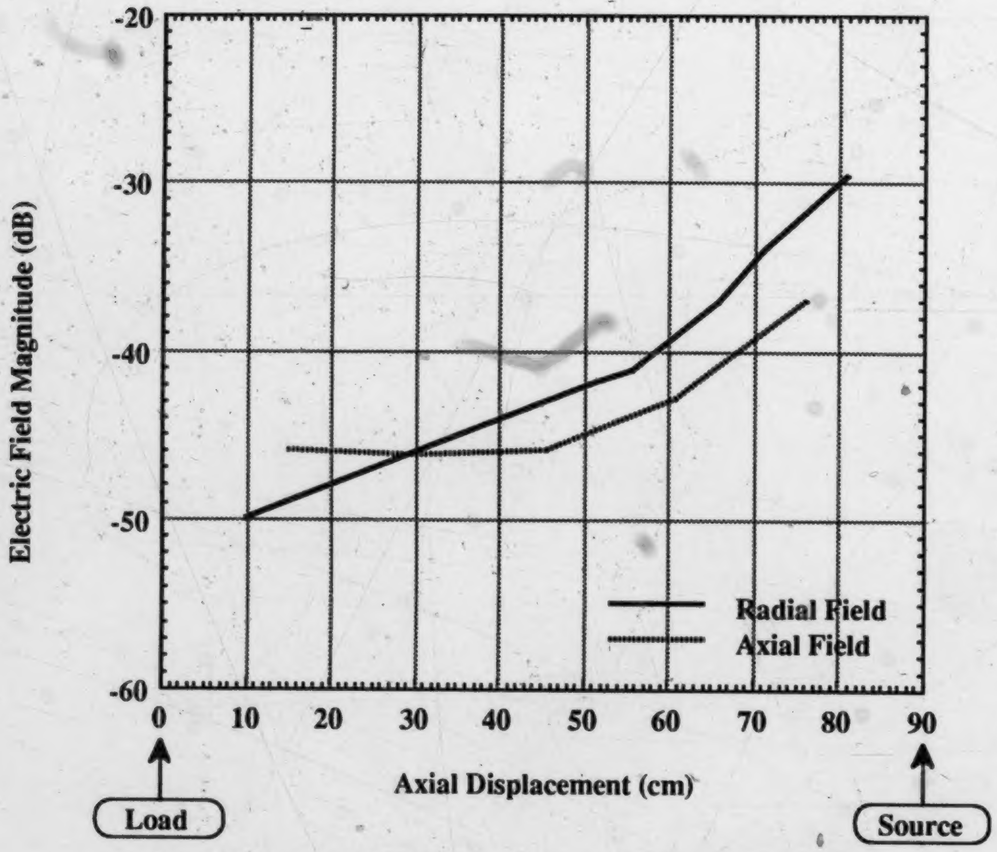

Figure A.2c Relative field magnitudes [1.29 S/m|80 MHz|9.931 mm].

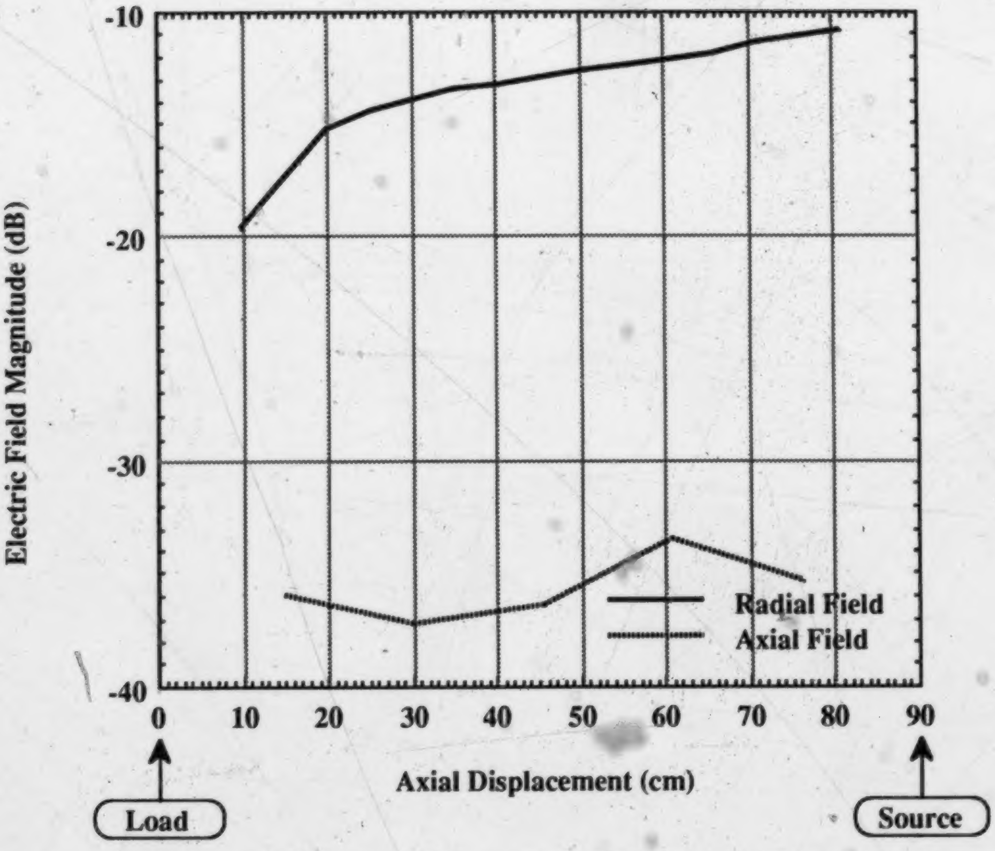

Figure A.3a Relative field magnitudes [1E-3 S/m|2 MHz|9.931 mm].

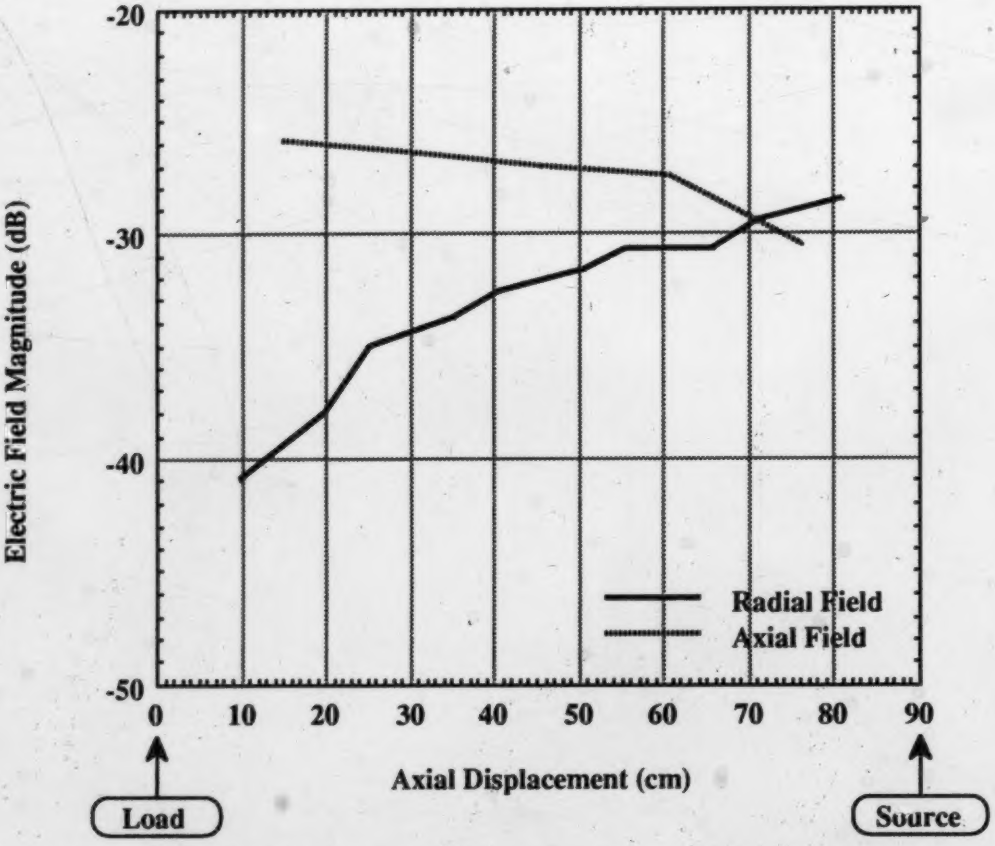

Figure A.3b Relative field magnitudes [0.66 S/m|2 MHz|9.931 mm].

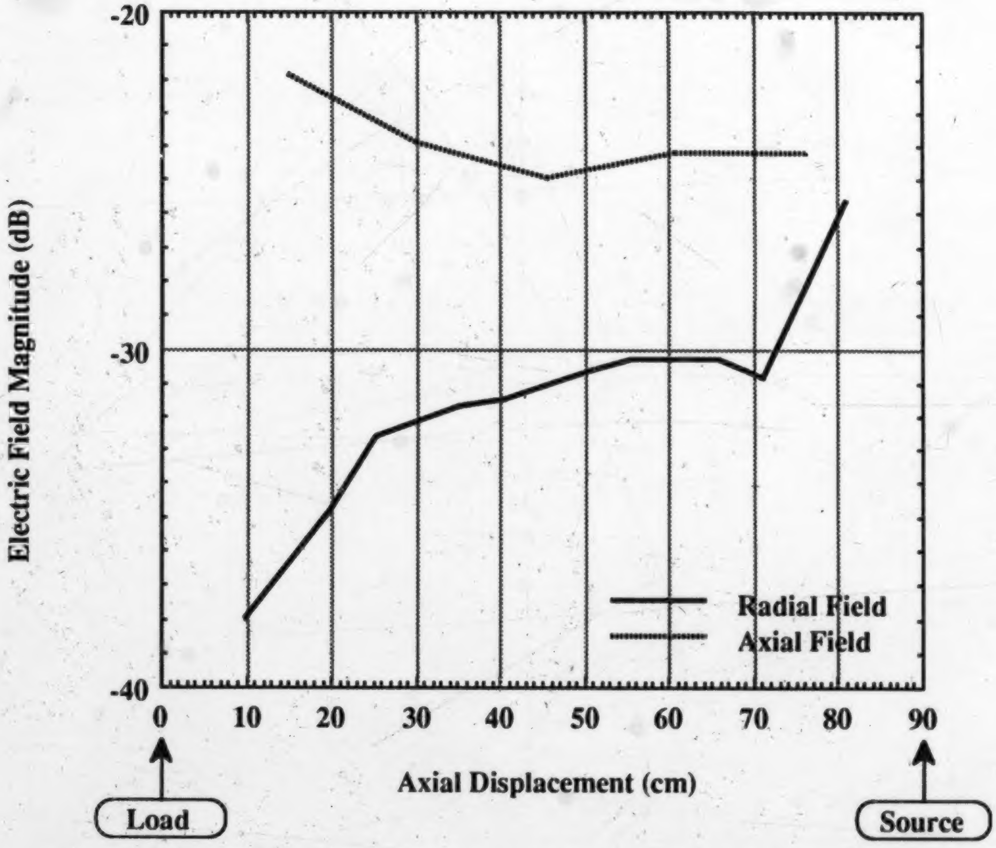

Figure A.3c Relative field magntudes [1.29 S/m|2 MHz|9.931 mm].

Appendix B. Electrical and Thermal Properties of the Model Medium

The electrical and thermal properties of the medium to be heated are of paramount importance in the research efforts to develop effective RF heating schemes. The electrical and thermal properties of oil sand are well documented[3]. Brine-sand was employed for all of the laboratory experiments of this project. Brine-sand is structurally typical of the earth type materials which would most likely be heated using RF methods. In addition, the properties of brine-sand are easily and economically controlled for modelling purposes. The literature contains fragmented listings of brine-sand thermal and electrical properties. The De Bibhas mixing law[26] provides the dielectric constant of a brine-sand mixture for all permutations of the composition of the mixture, but it cannot account for the increased dielectric response of the mixture due to the interfacial phenomena which become significant at frequencies below 20 MHz. The electrical conductivity of brine-sand can be estimated by the Archie-Humble formula[27], but only at low frequencies.

Fortunately, the electrical conductivity and dielectric constant of brine-sand at radio frequencies are easily obtained by packing an amount of the brine-sand into a coaxial capacitor, and by measuring the input impedance of the coaxial capacitor with an RF impedance meter. The conductivity and dielectric constant of the sample may then be obtained via simple calculations. In addition, the temperature and moisture content dependence of the electrical properties of brine-sand are known[28] to be virtually identical to that of oil sand. The simulation routine incorporates this electrical parameter information as follows:

$$\sigma(W,T) = [1+\alpha(T-24)][K_{1C}W^2+K_{1B}W+K_{1A}] \qquad (B.1)$$

where σ is conductivity in siemens per meter, W is mass percent water content, T is temperature in degrees celsius, and α is the temperature dependence factor, with the dimension $^\circ C^{-1}$. The value of α was taken to be $0.024^\circ C^{-1}$ throughout the study. The measured constants K_{1C} and K_{1B} have the units $\%^{-2}$ and $\%^{-1}$ respectively, while K_{1A} is dimensionless. Similarly, the dielectric constant is modelled as:

$$\varepsilon(W) = 8.854\times10^{-12}[K_C W^2 + K_B W + K_A] \qquad \text{(B.2)}$$

where ε is in farads per meter. The constants K_C and K_B have the units $\%^{-2}$ and $\%^{-1}$ respectively, while K_A is dimensionless. The temperature dependence of the dielectric constant has been reported to be approximately one order of magnitude lower than that of the conductivity. In practise, this temperature dependence was found to be negligible.

A temperature independent thermal conductivity for the brine-sand medium can be estimated from Somerton's empirical formula[29], which has been found to be quite accurate for oil free brine-sands[30].

$$k=1.27-2.25\phi+2.886\sqrt{S_w} \qquad \text{(B.3)}$$

where k is in watts per meter per degree celsius. ϕ and S_W represent the fractional porosity and fractional water saturation respectively. It is not possible to assume a constant value of thermal conductivity during RF heating operations. The volumetric heat capacity M_{VOL} of the brine-sand, in joules per cubic meter per degree celsius, can be reliably calculated from a material analysis, using the specific heats of the medium constituents:

$$M_{VOL} = \frac{4.19\, m_W + 0.753 m_S}{v} \qquad \text{(B.4)}$$

Within an arbitrary volume v (cubic meters) of the brine-sand, m_W is the moisture mass in grams, while m_S represents the mass of the solid sand in grams. The specific heat of the moisture is assumed to be equal to that of water, or 4.19 joules per gram per degree celsius, and the specific heat of the solid sand is 0.753 joules per gram per degree celsius. COPTER determines its thermal and electrical lumped element parameters by evaluating these formulae during each time step, using the most current physical properties of the lossy material.

Appendix C TEM COPTER Program Listing

```
C
C
C
C
C                                 TTTTTTTTT    EEEEEE   MMM   MMM
C                                 TTTTTTTTT   EEEEEEEE  MMMM MMMM
C                                    TTT     EEE        MMMMMMMMM
C                                    TTT     EEEEEEEEE  MMM M MMM
C                                    TTT     EEEEEEEEE  MMM   MMM
C                                    TTT     EEE        MMM   MMM
C                                    TTT      EEEEEEEE  MMM   MMM
C                                    TTT       EEEEEE   MMM   MMM
C
C
C
C                   CCCCCC    00000     PPPPPP    TTTTTTTTT    EEEEEE     RRRRRR
C                  CCCCCCC   0000000   PPPPPPPP   TTTTTTTTT   EEEEEEEE   RRRRRRRR
C                 CCC       000   000 PPP   PPP      TTT     EEE        RRR   RRR
C                 CCC       000   000 PPPPPPPPP      TTT     EEEEEEEEE  RRRRRRRR
C                 CCC       000   000 PPPPPPPP       TTT     EEEEEEEEE  RRRRRRRR
C                 CCC       000   000 PPP            TTT     EEE        RRR   RRR
C                  CCCCCCC   0000000  PPP            TTT      EEEEEEEE  RRR   RRR
C                   CCCCCC    00000   PPP            TTT       EEEEEE   RRR   RRR
C
C
C
C
C
C                                  A TWO DIMENSIONAL SIMULATION ROUTINE
C              FOR THE ELECTROMAGNETIC HEATING OF LOW MOISTURE, POROUS, LOSSY MATERIALS
C                                       WITHIN A COAXIAL GUIDING STRUCTURE
C                        UNDER THE ASSUMPTION THAT ONLY TEM FIELDS ARE PRESENT.
C
C                                          WRITTEN BY MIKE MACHAI
C                                          UNIVERSITY OF ALBERTA
C                                  APPLIED ELECTROMAGNETICS LABORATORY
C                                                    1990
C
C
C
C
C
C
C
C
C
C
C
C
C
C
C       VARIABLES DESCRIPTION
C       ---------------------
C
C      M            : Number of grids in the radial direction, including inner and outer conductors.
C      N            : Number of grids in the axial direction, including the thermal insulating grids
C                         at both ends of the coaxial waveguide.
C      I            : Radial index for the grids. Inner conductor grid radial index is "1", outer
C                         conductor grid radial index is "M".
C      J            : Axial index for the grids. Load end thermal insulator grid axial index is "1",
C                         source end thermal insulator grid axial index is "N".
C      MI           : Radial index for the grids which are radially adjacent to the outer conductor.
C      NI           : Axial index for the grids which are axially adjacent to the source end thermal
C                         insulation grids.
C      RAD(I)       : Radial distance, in meters, to the outer radial boundary of the "I"th grid.
C      RR(I)        : Radial distance, in meters, to the center of the "I"th grid.
C      ZZ(J)        : Axial distance, in meters, to the center of the "J"th grid. This axial distance
C                         originates at the extreme load end of the guide and is positive towards the
C                         source.
C      DZ           : Axial dimension, in meters, of the grids.
C      VOL(I)       : Volume of grid (I) in cubic meters.
C      PW(I,J)      : Percentage of the total mass of grid (I,J) which is occupied by moisture.
C      GW(I,J)      : Mass of moisture contained within grid (I,J) in grams.
C      GS(I,J)      : Mass of solid material contained within grid (I,J) in grams.
C      W0           : Initial mass percent water content of the grids.
C      D0           : Initial density of the grids in grams per cubic centimeter.
C      T0           : Initial temperature of the grids, in degrees celcius.
C      T(I,J)       : Temperature of grid (I,J) at the beginning of a timestep, in degrees celcius.
C      TP(I,J)      : Updated temperature of grid (I,J) at the end of a timestep, in degrees celcius.
C      MVOL(I,J)    : Volumetric heat capacity of grid (I,J), in joules per cubic meter per degree
C                         celcius.
C      Q(I,J)       : Electrical power dissipated within grid (I,J), in watts.
C      H(I,J)       : Thermally conductive heat flow into grid (I,J), in watts.
C      GR(I,J)      : Radial thermal conductance between gr'd (I,J) and grid (I-1,J), in watts per
C                         degree celcius.
C      GZ(I,J)      : Axial thermal conductance between grid (I,J) and grid (I,J-1), in watts per
C                         degree celcius.
C      SE(I,J)      : Steam energy developed in grid (1,J), in joules, during a timestep.
C      DSE          : Total steam energy developed in all of the grids, in joules, during a timestep.
```

```
C     TOTSE     : DSE accumulated with time.
C     DETEMP    : Total temperature change energy developed in all of the grids, in joules,
C                   during a timestep.
C     ETEMP     : DETEMP accumulated with time.
C     DE        : Energy which is input to the lossy medium, in joules, during one timestep.
C     EIN       : DE accumulated with time.
C     OMEGA     : Angular frequency of operation, in radians per second.
C     MAXLOP    : Maximum number of iterations for thermal solver implicit recovery scheme.
C     ERR       : Minimum accuracy requirement for thermal solver implicit recovery scheme.
C     DT        : Timestep interval in seconds.
C     ETIME     : Simulation end time, in seconds.
C     PERCNT    : Desired maximum grid relative temperature rise in a given timestep.
C
C
C
C      SUBROUTINE DESCRIPTION
C      ----------------------
C
C      Subroutine PRINT
C        PRINT will output arrays of grid information, along with headings and coordinate
C        locations of the grids. It is used to output the grid power dissipation levels,
C        end of timestep temperatures, and end of timestep mass percent water contents.
C
C      Subroutine OUT
C        OUT prints noncomplex variables, along with appropriate labelling.
C
C      Subroutine COUT
C        COUT prints complex variables,,along with appropriate labelling.
C
C      Subroutine IVOUT
C        IVOUT prints complex line voltages and currents, along with appropriate labelling.
C
C      Subroutine REED
C        REED is used for both inputting and outputting data. The specific function of this
C        subroutine depends on parameter #3 in the call list. A zero as parameter #3 will cause
C        the subroutine to read data, a one is used to write a real number, and a two is used
C        to write an integer. A string of letters in the subroutine call list is used to label
C        output variables.
C
C
C
C*******************************************************************************************
C
C                                  INITIALIZATION AND DIMENSIONING
C
C*******************************************************************************************
C
C>>>>>>>>>> Dimensioning.
C
       DIMENSION RS(32,202),GS(32,202),GW(32,202),GAM(202)
       DIMENSION GZ(32,202),T(32,202),TP(32,202),VOL(32)
       DIMENSION Q(32,202),H(32,202),TH(32,202)
       DIMENSION PW(32,202),RPART(32,202),GWO(32,202)
       COMPLEX ZIN,YIN,CURL(202),CURS(202),ZTERM
       REAL KC,MVOL(32,202),SE(32,202),GR(32,202),RAD(32)
       REAL RR(32),ZZ(202),K1A,K1B,K1C,KA,KB,L,HF,KDC,K3DC
       COMPLEX VIN,IIN,V(202),F,ZED(202),Z,ZCDRY,ZCWET,ZIMET
       INTEGER COUNT,FLAG
       CHARACTER*7 PICT(32,202)
       DATA PI/3.141593/
       DATA ETEMP/0./,EIN/0./,TOTSE/0./
       OPEN (UNIT=1,FILE='INRST',STATUS='OLD')
       OPEN (UNIT=2,FILE='ORST',STATUS='NEW')
       OPEN (UNIT=3,FILE='DATAIN',STATUS='OLD')
       OPEN (UNIT=7,FILE='COPOUT',STATUS='NEW')
       OPEN (UNIT=8,FILE='PLOTIN',STATUS='NEW')
C
C>>>>>>>>>> Input data.
C
C
C
C    REED can read or write depending on call list parameter #3. Setting #3 to zero means
C    subroutine will read in a number, setting it to 1 means it will output a real number,
C    and setting it to 2 will output an integer number.
C
C
       CALL REED('Store run results? 0=no 1=yes   ',SAVE,0)
       CALL REED('Restarted run? 0=no  1=yes      ',RST,0)
       CALL REED('Output tables? 0=no 1=yes       ',TABLE,0)
       ISAVE=IFIX(SAVE)
       IRST=IFIX(RST)
       WRITE(7,1)
     1 FORMAT('1',/,' ',T20,'RUN PARAMETERS',/,' ',T20,14('-')//)
       WRITE(6,2)
     2 FORMAT(' ','*******Begin format free input.*******',/)
       CALL REED('Cooldown?  0=no,1=yes            ',COOLDN,0)
       CALL REED('Dielectric coating? 0=no,1=yes  ',ANS,0)
C
C
C    This following section of the program is passed through twice by a loop, first to input run
C    parameters from the user via an input file (UNIT 3), and the second time to output these
C    parameters to another file (UNIT 7) for storage. I1 and I2 are set to zero for parameter
```

```
C     Input.
C
C
        I1=0
        I2=0
       DO 7 NUM=1,2
        IF(ANS.NE.1)GOTO 3
        CALL REED('Coating dielectric constant.    ',KDC,I1)
        CALL REED('Coating thermal cond.(W/mC)     ',K3DC,I1)
        CALL REED('Coating volumetric heat capacity',VHCC,I1)
    3   CALL REED('Axial steps between data output.',STEP,I2)
        IF(COOLDN.NE.1.0)GOTO 30
        CALL REED('Time of cooldown (seconds).     ',COOLTM,I1)
   30   CALL REED('Timesteps between output.       ',CSTEP,I2)
        CALL REED('Max timestep % temperature rise.',PERCNT,I1)
        CALL REED('Maximum thermal iteration loops.',TLOP,I2)
        CALL REED('Maximum thermal iteration error.',ERR,I1)
        CALL REED('Conductivity constant    C.     ',K1C,I1)
        CALL REED('Conductivity constant    B.     ',K1B,I1)
        CALL REED('Conductivity constant    A.     ',K1A,I1)
        CALL REED('Conductivity temp. constant.    ',ALPHA,I1)
        CALL REED('Dielectric constant  C.         ',KC,I1)
        CALL REED('Dielectric constant  B.         ',KB,I1)
        CALL REED('Dielectric constant  A.         ',KA,I1)
        CALL REED('Vaporization temperature.       ',TS,I1)
        IF(IRST.NE.1)GOTO 18
        IF(NUM.EQ.2)GOTO 19
C
C
C     If the simulation is being restarted from the stored results of another simulation, the
C     relevent data is read back from the file (UNIT 1) containing these stored results.
C
C
        READ(1,28)TO
   28   FORMAT(F7.4)
        READ(1,21)DZ,M,N,TIME,EIN,ETEMP,TOTSE
   21   FORMAT(' ',1PE14.6,2X,I2,1X,I3,2X,1PE14.6,1PE14.6,1PE14.6,1PE14.6)
        READ(1,22)(RAD(I),I=1,M)
   22   FORMAT(' ',1PE14.6)
       DO 26 I=2,M-1
       DO 26 J=2,N-1
        READ(1,36)T(I,J),TP(I,J),GW(I,J),GS(I,J),RPART(I,J)
   36   FORMAT(' ',F12.4)
   26  CONTINUE
        GO TO 19
   18   CALL REED('Initial temperature.            ',TO,I1)
        CALL REED('Initial water content in %.     ',WO,I1)
        CALL REED('Initial density (g/cc)          ',DO,I1)
        CALL REED('Z-direction increment DZ (m)    ',DZ,I1)
   19   CALL REED('Simulation stop time (sec.)     ',ETIME,I1)
        CALL REED('Maximum number of timesteps     ',TMAX,I2)
        I3=6+I1
        WRITE(I3,5)
    5   FORMAT(' ','Sources: 1)Power(W)    2)Current(A)  3)Voltage(V)')
        CALL REED('Source type.                    ',C,I2)
        CALL REED('Source rating (RMS).            ',S0,I1)
        CALL REED('Frequency of operation (Hz).    ',FREQ,I1)
        WRITE(I3,4)
    4   FORMAT(' ','Line Termination = R+jX. (infinity=1E35)')
        CALL REED(' R (ohms).                      ',RTERM,I1)
        CALL REED(' X (-capacitive, +inductive).   ',XTERM,I1)
        IF(IRST.EQ.1)GOTO 23
        WRITE(I3,6)
    6   FORMAT(' ','NOTE: Divisions include boundaries (ie. conductors  &
     + insulators).')
        CALL REED('Number of radial divisions.     ',A,I2)
        CALL REED('Number of axial divisions.      ',B,I2)
C
C
C     Set I1 & I2 for second loop to output run parameters.
C
C
   23   I1=1
    7  I2=2
        IF(IRST.EQ.1)GOTO 24
C
C
C     Variables which are read in by the REED subroutine become real numbers. Certain ones
C     must be treated as integers, and are therefore converted to integers by IFIX.
C
C
        M=IFIX(A)
C
C
C     Input M radii.
C
C
        WRITE(6,8)M
    8   FORMAT(' ','Enter: ',I4,' Radii(m)   starting from center.')
        DO 888 I=1,M
        READ(3,*) RAD(I)
  888   CONTINUE
```

```
      N=IFIX(B)
 24   JSTEP=IFIX(STEP)
      ICSTEP=IFIX(CSTEP)
      MAXT=IFIX(TMAX)
      MO=IFIX(C)
      MAXLOP=IFIX(TLOP)
C
C>>>>>>>>>>> Initialization.
C
C
C
C    Convert densities from g/cc to g/m3, and percentages to decimal form for calculations.
C
C
      PERCNT=PERCNT/100
      IF(IRST.EQ.1)GOTO 25
      DO=DO*1.0E06
      WO=WO/100.
C
  25  M1=M-1
      N1=N-1
C
C
C    Calculate line inductance per axial division.
C
C
      L=2.0E-07*ALOG(RAD(M1)/RAD(1))*DZ
C
C
C    Output line inductance to the UNIT 7 file.
C
C
      CALL REED('Line inductance (per section).  ',L,1)
C
C
C    Output radii values to the UNIT 7 file.
C
C
      WRITE(7,12)RAD(1)
  12  FORMAT(' ','Radial division coordinates(m)=',F9.5)
     DO 11 I=2,M
  11 WRITE(7,9)RAD(I)
   9  FORMAT(' ','                            =',31F9.5)
C
      WRITE(6,455)
 455  FORMAT(' ','EXECUTION BEGINS...')
C
C
C    Calculate angular excitation frequency OMEGA.
C
C
      OMEGA=2*PI*FREQ
C
      ZTERM=CMPLX(RTERM,XTERM)
C
     DO 15 I=2,M1
C
C
C    Calculate grid volumes. No j index is necessary, since all axial grid widths are the same,
C    and there is therefore no difference in the volumes of grids with the same radial index.
C
C
      VOL(I)=PI*DZ*(RAD(I)**2-RAD(I-1)**2)
C
     DO 10 J=2,N1
C
C
C    Initialize grid temperatures, steam energies, water and sand contents.
C
C
      IF(IRST.EQ.1)GOTO 10
C
      T(I,J)=TO
      TP(I,J)=TO
      TH(I,J)=TO
      SE(I,J)=0.0
      IF(AMS.NE.1.OR.I.NE.2)GOTO 16
      GW(I,J)=0.0
      GO TO 17
  16  GW(I,J)=VOL(I)*DO*WO
      GWO(I,J)=GW(I,J)
  17  GS(I,J)=VOL(I)*DO*(1-WO)
      PW(I,J)=100.*GW(I,J)/(GW(I,J)+GS(I,J))
  10 CONTINUE
C
C
C    Calculate radial distances from the center of the inner conductor to the middles of the
C    grids, for use in table headings.
C
C
      RR(I)=(RAD(I)+RAD(I-1))/2.0
C
```

```
C
C    Initialize temperatures and water contents of load and source grids.
C
C
      TP(I,1)=T0
      TP(I,M)=T0
      T(I,1)=T0
      T(I,M)=T0
      TM(I,1)=T0
      TM(I,M)=T0
      GW(I,1)=GW(I,2)
      GW(I,M)=GW(I,M1)
      PW(I,1)=PW(I,2)
      PW(I,M)=PW(I,M1)
C
C
C    Axial thermal conductance of load grids is set to zero, since these grids are thermal
C    insulators.
C
C
  15 GZ(I,1)=0.
C
     DO 20 J=2,M1
C
C
C    Calculate axial displacement from load to center of each grid.
C
C
      ZZ(J)=(2*J-3)/2.0*DZ
C
C
C    Initialize temperatures and water contents for conductor grids.
C
C
      TP(1,J)=T0
      TP(M,J)=T0
      T(1,J)=T0
      T(M,J)=T0
      TM(1,J)=T0
      TM(M,J)=T0
      GW(1,J)=GW(2,J)
      GW(M,J)=GW(M1,J)
      PW(1,J)=PW(2,J)
      PW(M,J)=PW(M1,J)
C
C
C    Set the radial thermal conductance of the inner conductor grids to zero, since the inner
C    conductor is considered to be thermally insulating.
C
C
  20 GR(1,J)=0.
C
      LWG=0
C*************************************************************************************************
C
C                                 MAIN TIME STEP CONTROL LOOP
C
C*************************************************************************************************
      IF(IRST.EQ.1)GOTO 29
C
      TIME=0.0
C
C
C    The program will automatically stop after TIME exceeds ETIME. A maximum number of timesteps
C    MAXT is also specified.
C
C
  29 DO 1000 COUNT=1,MAXT
      FLAG=0
      IF(COOLDN.EQ.1.0.AND.TIME.GE.COOLTM)GOTO 273
C
C>>>>>>>>>>> Calculate lumped element parameters.
C
     DO 100 J=2,M1
      ZED(J)=0.
     DO 100 I=2,M1
C
C
C    Calculate radial (GR) and axial (GZ) thermal admittances for the lossy medium grids.
C
C
      IF(ANS.NE.1.OR.I.NE.2)GOTO 13
      GZ(I,J)=PI*K3DC*(RAD(I)**2-RAD(I-1)**2)/DZ
      GR(I,J)=2.*PI*K3DC*K3*DZ/(K3DC*ALOG((RAD(I+1)+RAD(I))/
     +(2.*RAD(I)))+K3*ALOG(2.*RAD(I)/(RAD(I-1)+RAD(I))))
      GO TO 14
 13   TKIJ=0.4375+2.886*SQRT(GW(I,J)/VOL(I)/373000.)
      IF(I.GE.M1)GOTO 335
      TKIP1J=0.4375+2.886*SQRT(GW(I+1,J)/VOL(I+1)/373000.)
 335  IF(J.GE.M1)GOTO 336
      TKIJP1=0.4375+2.886*SQRT(GW(I,J+1)/VOL(I)/373000.)
 336  GR(I,J)=2*PI*DZ*TKIJ*TKIP1J/(TKIJ*ALOG((RAD(I+1)+RAD(I))
     +/(2.*RAD(I)))+TKIP1J*ALOG(2.*RAD(I)/(RAD(I-1)+RAD(I))))
       GZ(I,J)=2.*PI*TKIJ*TKIJP1/(TKIJ+TKIJP1)*(RAD(I)**2-RAD(I-1)**2)/DZ
C
C
C    Calculate the location of each imaginary grid partition for the double RC circuit.
C
C
  14   RPART(I,J)=SQRT(RAD(I)**2-VOL(I)*GW(I,J)/(PI*DZ*WO*(GW(I,J)+GS(I,J))))
C
C
C    Set the thermal conductances of the outer conductor and source grids to zero, since they
C    are considered to be thermally insulating.
C
C
       GZ(I,M1)=0.
       GR(M1,J)=0.
C
C
C    Calculate the transverse resistances of the wet and dry portions of all medium grids.
C
C
       SIGDRY=K1A*(1.+ALPHA*(T(I,J)-TO))
       SIGWET=(K1C*(WO*100.)**2+K1B*WO*100.+K1A)*(1.+ALPHA*(T(I,J)-TO))
       RDRY=ALOG(RPART(I,J)/RAD(I-1))/(2*PI*SIGDRY*DZ)
       RWET=ALOG(RAD(I)/RPART(I,J))/(2*PI*SIGWET*DZ)
C
C
C     Calculate the transverse capacitances of the wet and dry portions of all medium grids.
C
C
       IF(AMS.NE.1.OR.I.NE.2)GOTO 97
       EPS=KDC
       GO TO 98
  97   EPSDRY=KA*8.854E-12*(1.+0.0*(T(I,J)-TO))
       EPSWET=(KC*(WO*100.)**2+KB*WO*100.+KA)*8.854E-12*(1.+0.0*(T(I,J)-TO))
  98   IF(GW(I,J).EQ.GWO(I,J))THEN
       CDRY=1E20
       GOTO 102
       ENDIF
       CDRY=(2*PI*EPSDRY*DZ)/ALOG(RPART(I,J)/RAD(I-1))
       IF(GW(I,J).EQ.0.0)THEN
       CWET=1E20
       GOTO 101
       ENDIF
 102   CWET=(2*PI*EPSWET*DZ)/ALOG(RAD(I)/RPART(I,J))
C
C
C     Calculate imaginary transverse impedance (ZC) due to the capacitance portions.
C
C
 101   ZCDRY=1.0/CMPLX(0.0,CDRY*OMEGA)
       ZCWET=1.0/CMPLX(0.0,CWET*OMEGA)
C
C     Calculate equivalent transverse impedance (Z) of the double RC circuit for each grid.
C
       Z=RDRY*ZCDRY/(RDRY+ZCDRY)+RWET*ZCWET/(RWET+ZCWET)
C
C
C     Store the real and imaginary transverse impedance components for each grid.
C
       RS(I,J)=REAL(Z)
C
C
C    Sum transverse impedances so that the total transverse impedance ZED from inner to outer
C    conductor is known for all axial line segments.
C
C
  100 ZED(J)=ZED(J)+Z
C
C>>>>>>>>>>> TEM electrical ladder solver.
C
C
C
C    Solve all transverse voltages and currents along the line based on assumed levels at the
C    load.
C
C
       ZTM=CABS(ZTERM)
       ZO=CABS(ZED(2))
       IF(ZTM.GT.ZO)THEN
       V(2)=1.0
       CURS(1)=1.0/(ZTERM+CMPLX(0.0,OMEGA*L/2.))
       CURL(1)=CURS(1)
       V(1)=CURL(1)*ZTERM
       CURS(2)=1.0/ZED(2)
       CURL(2)=CURL(1)+CURS(2)
       ELSE
       CURL(1)=1.0
       CURS(1)=CURL(1)
       V(1)=1.0*ZTERM
       V(2)=V(1)+CMPLX(0.0,OMEGA*L/2.)*CURL(1)
       CURS(2)=V(2)/ZED(2)
```

```
         CURL(2)=CURL(1)+CURS(2)
         ENDIF
        DO 200 J=3,N1
         U(J)=U(J-1)+CURL(J-1)*CMPLX(0.0,OMEGA*L)
         CURS(J)=U(J)/ZED(J)
         CURL(J)=CURL(J-1)+CURS(J)
  200   CONTINUE
         UIN=U(N1)+CURL(N1)*CMPLX(0.0,OMEGA*L/2.)
         IIN=CURL(N1)
C
C
C     Compare the input excitation, which was calculated as per the assumed load levels, to the
C     actual excitation. Derive a correction factor F from the ratio of these two levels and
C     correct the levels along the line. Factor calculation depends on the source nature NO.
C     For constant power source, go to 210, constant current go to 220, constant voltage continue.
C
C
         GOTO(210,220),NO
C
C
C     Constant voltage source.
C.
C
         F=SO/UIN
        DO 205 J=1,N1
         U(J)=U(J)*F
         CURL(J)=CURL(J)*F
         CURS(J)=CURS(J)*F
  205   CONTINUE
         GOTO260
C
C
C     Constant power source.
C
C
  210    F=SQRT(SO/REAL(UIN*CONJG(IIN)))
        DO 211 J=1,N1
         U(J)=U(J)*F
         CURL(J)=CURL(J)*F
         CURS(J)=CURS(J)*F
  211   CONTINUE
         GOTO260
C
C
C     Constant current source.
C
C
  220    F=SO/IIN
        DO 221 J=1,N1
         U(J)=U(J)*F
         CURL(J)=CURL(J)*F
         CURS(J)=CURS(J)*F
  221   CONTINUE
C
C
C     Calculate all input parameters
C
C
  260    VIN=U(N1)+CURL(N1)*CMPLX(0.0,OMEGA*L/2.)
         IIN=CURL(N1)
         PIN=REAL(VIN*CONJG(IIN))
         PTOT=REAL(ZTERM)*CABS(CURL(1))**2
        DO 270 J=2,N1
         PTOT=PTOT+REAL(ZED(J))*CABS(CURS(J))**2
  270   CONTINUE
         ZIN=VIN/IIN
         VIN=1.0/ZIN
C
C>>>>>>>>>>> Prepare for thermal solution.
C
C
C
C     Calculate heating rates.
C
C
  273    QTOT=0.0
         DTMAX=ETIME
        DO 400 J=2,N1
        DO 400 I=2,N1
         Q(I,J)=CABS(CURS(J))**2*RS(I,J)
         IF(COOLDN.NE.1.0.OR.TIME.LT.COOLTM)GOTO 397
         Q(I,J)=0.0
C
  397    QTOT=QTOT+Q(I,J)
C
C
C     Calculate total grid mass for time step.
C
C
         GT=GS(I,J)+GW(I,J)
C
C
```

```
C    MVOL, the grid volumetric heat capacity, must be calculated for each time step since
C    it is a function of water content.
C
C
      IF(ANS.NE.1.OR.I.NE.2)GOTO 398
      MVOL(I,J)=VHCC
      GO TO 399
 398  MVOL(I,J)=(GW(I,J)/GT*4.19+GS(I,J)/GT*.753)
      MVOL(I,J)=MVOL(I,J)*GT/VOL(I)
C
C
C    The time step increment is calculated by examining the net energy into each grid. Higher
C    energy inputs mean faster thermal changes and smaller required time steps. Using an
C    energy balance equation to choose the time step size realizes this algorithm. The smallest
C    time step from the fastest thermally changing grid is used.
C
C
 399  H(I,J)=GR(I-1,J)*(T(I-1,J)-T(I,J))+GR(I,J)*(T(I+1,J)-T(I,J))
      H(I,J)=H(I,J)+GZ(I,J-1)*(T(I,J-1)-T(I,J))
      H(I,J)=H(I,J)+GZ(I,J)*(T(I,J+1)-T(I,J))
      DT=MVOL(I,J)*VOL(I)*PERCNT*T(I,J)/ABS(Q(I,J)+H(I,J))
      IF(DT.LT.DTMAX)THEN
      DTMAX=DT
      END IF
 400 CONTINUE
      DT=DTMAX
      DDT=ETIME-TIME
      IF(DDT.LT.DT)DT=DDT
C
C
C    Increment the total time accumulator.
C
C
C     IF(LUG.EQ.1)DT=10.
      TIME=TIME+DT
      LUG=0
C
C>>>>>>>>>>> Thermal solver.
C
C
C
C    ADI axial swing.
C
C
       INDEX=1
       BET=1.0
      DO 580 I=2,MI
      DO 579 J=2,MI
       IF(TP(I,J).GE.TS.AND.GW(I,J).GT.0.0)GO TO 577
       GAM(J)=(0.-GZ(I,J-1)*DT*0.5)*INDEX/BET
       BET=MVOL(I,J)*VOL(I)+(GZ(I,J)+GZ(I,J-1))*DT*0.5+GZ(I,J-1)*DT*0.5*GAM(J)*INDEX
       TH(I,J)=Q(I,J)*DT*0.5+MVOL(I,J)*VOL(I)*T(I,J)
       TH(I,J)=TH(I,J)+(T(I-1,J)-T(I,J))*GR(I-1,J)*0.5*DT
       TH(I,J)=TH(I,J)+(T(I+1,J)-T(I,J))*GR(I,J)*0.5*DT
       TH(I,J)=TH(I,J)+TS*GZ(I,J-1)*(1-INDEX)*DT*0.5
       IF(TP(I,J+1).EQ.TS.AND.GW(I,J+1).GT.0.0)TH(I,J)=TH(I,J)+GZ(I,J)*DT*0.5*TS
       TH(I,J)=TH(I,J)+GZ(I,J-1)*DT*0.5*TH(I,J-1)*INDEX
       TH(I,J)=TH(I,J)/BET
       INDEX=1
       GO TO 579
 577   TH(I,J)=TS
       INDEX=0
       GAM(J)=0.0
 579 CONTINUE
C
C
C    Back substitution.
C
C
      DO 576 J=MI-1,2,-1
       TH(I,J)=TH(I,J)-GAM(J+1)*TH(I,J+1)
 576 CONTINUE
      DO 580 J=2,MI
       IF(TH(I,J).GE.TS.AND.GW(I,J).GT.0.0)TH(I,J)=TS
 580 CONTINUE
C
C
C    ADI radial swing.
C
C
       INDEX=1
       BET=1.0
      DO 581 J=2,MI
      DO 589 I=2,MI
       IF(TH(I,J).GE.TS.AND.GW(I,J).GT.0.0)GO TO 587
       GAM(I)=(0.-GR(I-1,J)*DT*0.5)*INDEX/BET
       BET=MVOL(I,J)*VOL(I)+(GR(I,J)+GR(I-1,J))*DT*0.5+GR(I-1,J)*DT*0.5*GAM(I)*INDEX
       TP(I,J)=Q(I,J)*DT*0.5+MVOL(I,J)*VOL(I)*TH(I,J)
       TP(I,J)=TP(I,J)+(TH(I,J-1)-TH(I,J))*GZ(I,J-1)*0.5*DT
       TP(I,J)=TP(I,J)+(TH(I,J+1)-TH(I,J))*GZ(I,J)*0.5*DT
       TP(I,J)=TP(I,J)+TS*GR(I-1,J)*(1-INDEX)*DT*0.5
       IF(TH(I+1,J).EQ.TS.AND.GW(I+1,J).GT.0.0)TP(I,J)=TP(I,J)+GR(I,J)*0.5*DT*TS
       TP(I,J)=TP(I,J)+GR(I-1,J)*DT*0.5*TP(I-1,J)*INDEX
       TP(I,J)=TP(I,J)/BET
       INDEX=1
       GO TO 589
  587  TP(I,J)=TS
       INDEX=0
       GAM(I)=0.0
  589  CONTINUE
C
C
C    Back substitution.
C
C
      DO 588 I=MI-1,2,-1
       TP(I,J)=TP(I,J)-GAM(I+1)*TP(I+1,J)
  588 CONTINUE
      DO 581 I=2,MI
       IF(TP(I,J).GE.TS.AND.GW(I,J).GT.0.0)TP(I,J)=TS
       IF(TP(I,J).NE.TS)SE(I,J)=0.0
       IF(TP(I,J).GE.TS.AND.GW(I,J).GT.0.0)LUG=1
  581 CONTINUE
C
       IF(LUG.EQ.0)GOTO 620
C
C
C    Implicit recovery and steam energy calculation.
C
C
      DO 605 FLAG=1,MAXLOP
       TEMP1=0.0
      DO 600 I=2,MI
      DO 600 J=2,MI
       TEMP=TP(I,J)
       IF(GW(I,J).GT.0.0.AND.TP(I,J).EQ.TS)GOTO585
  570  SE(I,J)=0.0
       G=GR(I,J)+GZ(I,J)+GZ(I,J-1)+GR(I-1,J)
       TOP=Q(I,J)*DT+MVOL(I,J)*VOL(I)*T(I,J)
       TOP=TOP+TP(I,J+1)*GZ(I,J)*DT+TP(I+1,J)*GR(I,J)*DT
       TOP=TOP+TP(I,J-1)*GZ(I,J-1)*DT+TP(I-1,J)*GR(I-1,J)*DT
       TP(I,J)=TOP/(MVOL(I,J)*VOL(I)+G*DT)
       GOTO590
  585  TP(I,J)=TS
       HF=(TP(I,J+1)-TP(I,J))*GZ(I,J)+(TP(I,J-1)-TP(I,J))*GZ(I,J-1)
       HF=HF+(TP(I+1,J)-TP(I,J))*GR(I,J)+(TP(I-1,J)-TP(I,J))*GR(I-1,J)
       SE(I,J)=Q(I,J)*DT+HF*DT
       IF(SE(I,J).LT.0.0)GOTO570
  590  TEMP=TEMP-TP(I,J)
       IF(ABS(TEMP).GT.ABS(TEMP1))TEMP1=TEMP
  600 CONTINUE
       IF(ABS(TEMP1).LT.ERR)GOTO620
  605 CONTINUE
       WRITE(6,610)
  610  FORMAT(' ','NO CONVERGENCE-EXECUTION TERMINATED')
  620  CONTINUE
C
C
C    Accumulate input, temperature rise and steam energies.
C
C
       IF(COOLDN.EQ.1.0.AND.TIME.GE.COOLTM)PIN=0.0
       DE=DT*PIN
       EIN=EIN+DE
       DETEMP=0.0
       DSE=0.0
      DO 630 I=2,MI
      DO 630 J=2,MI
       IF(TP(I,J).GT.TS.AND.GW(I,J).GT.0.0)TP(I,J)=TS
       DSE=DSE+SE(I,J)
       DETEMP=DETEMP+(MVOL(I,J)*VOL(I))*(TP(I,J)-T(I,J))
       T(I,J)=TP(I,J)
  630 CONTINUE
       ETEMP=ETEMP+DETEMP
       TOTSE=TOTSE+DSE
C
C
C    Calculate the new water contents of each grid.
C
C
      DO 640 J=2,MI
      DO 640 I=2,MI
       DGW=SE(I,J)/(540.*4.19)
       GW(I,J)=GW(I,J)-DGW
       IF(GW(I,J).LT.0.0)GW(I,J)=0.0
       PW(I,J)=100.*GW(I,J)/(GW(I,J)+GS(I,J))
  640 CONTINUE
C*****************************************************************************
C
C                                      OUTPUT
C
C*****************************************************************************
C
C
```

```
C    As the simulation is running, simulation status information is printed on the screen.
C
C
      WRITE(6,454)COUNT,TIME,DT,FLAG
 454  FORMAT(' ','TIMESTEP #',I4,'   TIME=',1PE14.6,' DT=',1PE14.6,I4)
C
C
C    Time step results are not output to UNIT 7 after each time step.
C    ICSTEP controls the frequency at which time step results are successively output to UNIT 7.
C
C
      SHIF=(1.0*COUNT)/ICSTEP-IFIX((1.0*COUNT)/ICSTEP)
      IF(SHIF.EQ.0.0.OR.TIME.GE.ETIME.OR.COUNT.EQ.1)GOTO900
      GOTO1000
 900  IF(TABLE.EQ.0.0)GOTO 333
C
C
C    Output timestep information heading for UNIT 7 file.
C
C
      WRITE(7,99)COUNT,TIME
  99  FORMAT('1',99('*'),/,'TIMESTEP #',I4,'  TIME = ',1PE14.6,/
     + ' ',36('-')/)
      WRITE(7,905)FLAG
 905  FORMAT(' ','NUMBER OF ITERATIONS=',I3)
C
C
C    Print the input electrical parameters.
C
C
      CALL OUT('Input Power               ',PIN,' Watts  ')
      IF(COOLON.EQ.1.0.AND.TIME.GE.COOLTM)GOTO 919
      CALL OUT('Total Grid Block Power  ',PTOT,' Watts  ')
      WRITE(7,910)
 910  FORMAT(/,' ',T36,'Magnitude',T50,'Phase (deg)'/' ',T35,11('-'
     + ),T49,13('-'))
      CALL COUT('Input Voltage             ',VIN,' Volts  ')
      CALL COUT('Input Current             ',IIN,' Amps   ')
      CALL COUT('Input Impedance           ',ZIN,' Ohms   ')
      WRITE(7,914)REAL(ZIN)
      WRITE(7,913)AIMAG(ZIN)
 914  FORMAT(' ','Input Resistance               = ',1PE14.6,14X,' Ohms')
 913  FORMAT(' ','Input Reactance                = ',1PE14.6,14X,' Ohms')
C     DO 917 J=2,NI
C     DO 917 I=2,MI
C       WRITE(8,916)TP(I,J),PW(I,J),AA(I),ZZ(J)
C 916   FORMAT(' ',F7.3,1X,F6.3,1X,1PE14.6,1X,1PE14.6)
C 917 CONTINUE
C      WRITE(8,918)
C 918  FORMAT(' ',//)
      CALL COUT('Input Admittance          ',YIN,' Mhos   ')
C
C
C    Print line voltages and line currents.
C
C
      CALL IVOUT(NI,V,CURS,ZZ,JSTEP)
C
C
C    Output cumulative energies, temperature, and water content tables.
C
C
 919  CALL PRINT(MI,NI,T,ZZ,AA,'TEMPERATURE DISTRIBUTION',JSTEP)
      CALL PRINT(MI,NI,PW,ZZ,AA,'  % WATER   DISTRIBUTION',JSTEP)
      CALL OUT('Cumulative Temp. Energy ',ETEMP,'Joules  ')
      CALL OUT('Cumulative Steam Energy ',TOTSE,'Joules  ')
      CALL OUT('Total Energy Supplied   ',EIN,'Joules  ')
C
      WRITE(7,920)
 920  FORMAT(' ',/)
 333  CONTINUE
      IF(TIME.GE.ETIME)GOTO1111
1000  CONTINUE
C
C
C    If desired, relevant data will be saved in UNIT 2 file for restarting the simulation
C    after the simulation and has been reached.
C
C
1111  IF(ISAVE.EQ.0)GOTO 1112
      WRITE(2,925)T0
 925  FORMAT(' ',F7.4)
      WRITE(2,923)DZ,M,N,TIME,EIN,ETEMP,TOTSE
 923  FORMAT(' ',1PE14.6,2X,I2,1X,I3,2X,1PE14.6,1PE14.6,
     + 1PE14.6,1PE14.6)
      WRITE(2,921)(RAD(I),I=1,M)
 921  FORMAT(' ',1PE14.6)
     DO 924 I=2,MI
     DO 924 J=2,NI
      WRITE(2,922)T(I,J),TP(I,J),GW(I,J),GS(I,J),APART(I,J)
 922  FORMAT(' ',F12.4)
 924 CONTINUE
 1112  STOP
       END
C
C
C
C************************************************************************************************
C
       SUBROUTINE PRINT(M1,N1,T,Z,R,A,JSTEP)
C
C************************************************************************************************
       CHARACTER*4 A(6)
       CHARACTER*1 DASH
       DATA DASH/'-'/
       DIMENSION T(32,202),Z(202),R(32)
       WRITE(7,10)(A(I),I=1,6)
   10  FORMAT(' '//,' ',T20,6A4/' ',T20,24('-')/)
       WRITE(7,12)
   12  FORMAT(' ',T14,'Radial Direction ------->')
       WRITE(7,15)(R(J),J=2,M1)
   15  FORMAT(' ','   Z\R  ',15('|',F7.3))
       WRITE(7,50)(DASH,J=2,M1)
      DO 20 I1=2,M1,JSTEP
       WRITE(7,40)Z(I1),(T(J,I1),J=2,M1)
   20 WRITE(7,50)(DASH,J=2,M1)
   40  FORMAT(' ',F8.3,15('|',F7.3))
   50  FORMAT(' ','--------',15('+',A1,'------'))
       RETURN
       END
C
C
C
C************************************************************************************************
C
       SUBROUTINE OUT(A,VAL,B)
C
C************************************************************************************************
       CHARACTER*4 A(6),B(2)
       WRITE(7,100)(A(I),I=1,6),VAL,(B(J),J=1,2)
  100  FORMAT(' ',6A4,T30,'= ',1PE14.6,'  ',2A4)
       RETURN
       END
C
C
C
C************************************************************************************************
C
       SUBROUTINE COUT(A,VAL,B)
C
C************************************************************************************************
       CHARACTER*4 A(6),B(2)
       COMPLEX VAL
       DATA PI/3.141593/
       BIG=CABS(VAL)
       PHASE=ATAN2(AIMAG(VAL),REAL(VAL))*180./PI
       WRITE(7,100)(A(I),I=1,6),BIG,PHASE,(B(J),J=1,2)
C 100  FORMAT(' ',6A4,T30,'= ',1PEIC
C
C
C************************************************************************************************
C
       SUBROUTINE REED(A,VAR,P)
C
C************************************************************************************************
       INTEGER P
       CHARACTER*4 A(8)
C
C
C    If P=0 read, P=1 write real, P=2 write integer
C
C
       IF(P.NE.0)GOTO 20
       WRITE(6,10)(A(I),I=1,8)
   10  FORMAT(' ','Enter: ',8A4)
       READ(3,*)VAR
       RETURN
   20  IF(P.EQ.2)GOTO 50
       WRITE(7,30)(A(I),I=1,8),VAR
   30  FORMAT(' ',8A4,' = ',1PE14.6)
       RETURN
   50  JJ=IFIX(VAR)
       WRITE(7,60)(A(I),I=1,8),JJ
   60  FORMAT(' ',8A4,' = ',I4)
       RETURN
       END
C
C
C
C************************************************************************************************
C
       SUBROUTINE IVOUT(N1,V,CURL,ZZ,JSTEP)
C
C************************************************************************************************
       COMPLEX V(202),CURL(202)
      DIMENSION ZZ(202)
      DATA PI/3.141592/
      WRITE(7,40)
 40   FORMAT(//)
      WRITE(7,50)
 50   FORMAT(' ','    Z',T25,'LINE VOLTAGES',T60,'SHUNT CURRENTS',/
     * ' ',T24,15('-'),T59,16('-'))
      WRITE(7,60)
 60   FORMAT(' ','   ---',T20,'Magnitude',T36,'Phase',T59,'Magnitude'
     + ,T74,'Phase'/' ',T19,11('-'),T35,7('-'),T58,11('-'),T73,7('-'))
     DO 100 J1=2,M1,JSTEP
      BIGV=CABS(V(J1))
      BIGI=CABS(CURL(J1))
      PHV=ATAN2(AIMAG(V(J1)),REAL(V(J1)))*180./PI
      PHI=ATAN2(AIMAG(CURL(J1)),REAL(CURL(J1)))*180./PI
100  WRITE(7,200)ZZ(J1),BIGV,PHV,BIGI,PHI
200   FORMAT(' ',F9.4,'  |',T15,1PE14.6,T30,1PE14.6,T55,1PE14.7,T70
     + ,1PE14.7)
      RETURN
      END
```

Appendix D Sample Output From TEM COPTER

```
1
                  RUN PARAMETERS
                  --------------

Axial steps between data output. =    5
Timesteps between output.        =  500
Max timestep % temperature rise. =   5.000000E+00
Maximum thermal iteration loops. = 9999
Maximum thermal iteration error. =   1.000000E-06
Conductivity constant    C.      =   1.190000E-04
Conductivity constant    B.      =   0.000000E+00
Conductivity constant    A.      =   2.000000E-05
Conductivity temp. constant.     =   2.400000E-02
Dielectric constant  C.          =   1.626000E-01
Dielectric constant  B.          =   0.000000E+00
Dielectric constant  A.          =   3.000000E+00
Vaporization temperature.        =   1.000000E+02
Initial temperature.             =   2.400000E+01
Initial water content in %.      =   4.150000E+00
Initial density (g/cc)           =   1.620000E+00
Z-direction increment DZ (m)     =   1.820000E-02
Simulation stop time (sec.)      =   1.500000E+04
Maximum number of timesteps      = 9999
Sources: 1)Power(W)    2)Current(A)  3)Voltage(V)
Source type.                     =    1
Source rating (RMS).             =   8.000000E+02
Frequency of operation (Hz).     =   1.000000E+08
Line Termination = R+jX. (infinity=1E35)
 R (ohms).                       =   0.000000E+00
 X (-capacitive, +inductive).    =   0.000000E+00
NOTE: Divisions include boundaries (ie. conductors  & insulators).
Number of radial divisions.      =   10
Number of axial divisions.       =   52
Line inductance (per section).   =   1.255358E-08
Radial division coordinates(m)=  0.00476
                               =  0.00700
                               =  0.01000
                               =  0.01600
                               =  0.02500
                               =  0.03600
                               =  0.05400
                               =  0.10000
                               =  0.14976
                               =  0.15100
1*************************************************************************************************
TIMESTEP #    1  TIME =   7.244176E-01
----------------------------------------

NUMBER OF ITERATIONS=  0
Input Power                 =   8.000000E+02   Watts
Total Grid Block Power      =   7.999999E+02   Watts

                                Magnitude     Phase (deg)
                                -----------   -------------
Input Voltage               =   6.886871E+02 -8.913062E+01 Volts
Input Current               =   1.498751E+00 -1.283196E+02 Amps
Input Impedance             =   4.595075E+02  3.918899E+01 Ohms
Input Resistance            =   3.561486E+02               Ohms
Input Reactance             =   2.903538E+02               Ohms
Input Admittance            =   2.176243E-03 -3.918899E+01 Mhos


   Z               LINE VOLTAGES                        SHUNT CURRENTS
                  ---------------                      ----------------
  ---          Magnitude       Phase                 Magnitude       Phase
              -----------     -------               ------------   -------
  0.0091  |   3.156266E+01   9.000002E+01           3.3839639E-02  1.7633047E+02
  0.1001  |   3.327118E+02   9.015803E+01           3.5671419E-01  1.7648849E+02
  0.1911  |   5.648548E+02   9.060823E+01           6.0560441E-01  1.7693869E+02
  0.2821  |   6.798981E+02   9.145112E+01           7.2894716E-01  1.7778159E+02
  0.3731  |   6.541787E+02   9.295786E+01           7.0137227E-01  1.7928831E+02
  0.4641  |   4.936880E+02   9.602706E+01           5.2930349E-01 -1.7764255E+02
  0.5551  |   2.354002E+02   1.061769E+02           2.5238237E-01 -1.6749274E+02
  0.6461  |   1.104971E+02  -1.284306E+02           1.1846852E-01 -4.2100182E+01
  0.7371  |   3.862784E+02  -9.839553E+01           4.1414523E-01 -1.2065071E+01
  0.8281  |   5.998058E+02  -9.262003E+01           6.4307678E-01 -6.2895622E+00

                   TEMPERATURE DISTRIBUTION
                   ------------------------

          Radial Direction ------->
  Z\R   |  0.006|  0.009|  0.013|  0.021|  0.030|  0.045|  0.077|  0.125|
--------+-------+-------+-------+-------+-------+-------+-------+-------+
  0.009| 24.082| 24.001| 24.001| 24.000| 24.000| 24.000| 24.000| 24.000|
--------+-------+-------+-------+-------+-------+-------+-------+-------+
  0.100| 24.270| 24.137| 24.059| 24.023| 24.010| 24.005| 24.002| 24.001|
--------+-------+-------+-------+-------+-------+-------+-------+-------+
   0.191| 24.779| 24.396| 24.169| 24.067| 24.030| 24.014| 24.005| 24.002|
--------+-------+-------+-------+-------+-------+-------+-------+-------+
   0.282| 25.128| 24.574| 24.244| 24.098| 24.044| 24.020| 24.007| 24.003|
--------+-------+-------+-------+-------+-------+-------+-------+-------+
   0.373| 25.045| 24.531| 24.226| 24.090| 24.040| 24.019| 24.006| 24.002|
--------+-------+-------+-------+-------+-------+-------+-------+-------+
   0.464| 24.595| 24.302| 24.129| 24.051| 24.023| 24.011| 24.004| 24.001|
--------+-------+-------+-------+-------+-------+-------+-------+-------+
   0.555| 24.135| 24.069| 24.029| 24.012| 24.005| 24.002| 24.001| 24.000|
--------+-------+-------+-------+-------+-------+-------+-------+-------+
   0.646| 24.030| 24.015| 24.006| 24.003| 24.001| 24.001| 24.000| 24.000|
--------+-------+-------+-------+-------+-------+-------+-------+-------+
   0.737| 24.364| 24.185| 24.079| 24.031| 24.014| 24.006| 24.002| 24.001|
--------+-------+-------+-------+-------+-------+-------+-------+-------+
   0.828| 24.878| 24.446| 24.190| 24.076| 24.034| 24.016| 24.005| 24.002|
--------+-------+-------+-------+-------+-------+-------+-------+-------+


                    % WATER   DISTRIBUTION
                    ----------------------

          Radial Direction ------->
   Z\R  |  0.006|  0.009|  0.013|  0.021|  0.030|  0.045|  0.077|  0.125|
--------+-------+-------+-------+-------+-------+-------+-------+-------+
   0.009|  4.150|  4.150|  4.150|  4.150|  4.150|  4.150|  4.150|  4.150|
--------+-------+-------+-------+-------+-------+-------+-------+-------+
   0.100|  4.150|  4.150|  4.150|  4.150|  4.150|  4.150|  4.150|  4.150|
--------+-------+-------+-------+-------+-------+-------+-------+-------+
   0.191|  4.150|  4.150|  4.150|  4.150|  4.150|  4.150|  4.150|  4.150|
--------+-------+-------+-------+-------+-------+-------+-------+-------+
   0.282|  4.150|  4.150|  4.150|  4.150|  4.150|  4.150|  4.150|  4.150|
--------+-------+-------+-------+-------+-------+-------+-------+-------+
   0.373|  4.150|  4.150|  4.150|  4.150|  4.150|  4.150|  4.150|  4.150|
--------+-------+-------+-------+-------+-------+-------+-------+-------+
   0.464|  4.150|  4.150|  4.150|  4.150|  4.150|  4.150|  4.150|  4.150|
--------+-------+-------+-------+-------+-------+-------+-------+-------+
   0.555|  4.150|  4.150|  4.150|  4.150|  4.150|  4.150|  4.150|  4.150|
--------+-------+-------+-------+-------+-------+-------+-------+-------+
   0.646|  4.150|  4.150|  4.150|  4.150|  4.150|  4.150|  4.150|  4.150|
--------+-------+-------+-------+-------+-------+-------+-------+-------+
   0.737|  4.150|  4.150|  4.150|  4.150|  4.150|  4.150|  4.150|  4.150|
--------+-------+-------+-------+-------+-------+-------+-------+-------+
   0.828|  4.150|  4.150|  4.150|  4.150|  4.150|  4.150|  4.190|  4.150|
--------+-------+-------+-------+-------+-------+-------+-------+-------+
Cumulative Temp. Energy     =   5.794877E+02  Joules
Cumulative Steam Energy     =   0.000000E+00  Joules
Total Energy Supplied       =   5.795341E+02  Joules
```